Design Optimisation and Testing of SSM on ASTROSAT and Study of X-ray Transients

by

M.C. Rama Devi
ISRO Satellite Centre, Bangalore

A thesis submitted in partial fulfillment for the degree of Doctor of Philosophy to the

Department of Physics
University of Calicut
Calicut, Kerala

February 2011

Certificate

This is to certify that the thesis titled "**Design Optimisation and Testing of SSM on ASTROSAT and Study of X-ray Transients**" is a bonafide record of the work done by Ms. M.C. Rama Devi under our joint supervision and that no part of it has been included any where previously for the award of any degree, either in this university or any other institution.

Dr. S. Seetha
Head, SAID, SAG
ISRO Satellite Centre
Bangalore

Dr. B.R.S. Babu
Professor, Department of Physics
University of Calicut
Kerala

Declaration of Authorship

I hereby declare that the thesis titled "**Design Optimisation and Testing of SSM on ASTROSAT and Study of X-ray Transients**" is an authentic record of the research work carried out by me under the supervision of Dr. S. Seetha, Head, Space Astronomy & Instrumentation Division (SAID), Space Astronomy Group (SAG), ISRO Satellite Centre, Bangalore and Dr. B.R.S. Babu, Professor, Department of Physics, University of Calicut. No part of this work has formed the basis for award of any other degree or diploma in any university or institution.

M.C. Rama Devi

February 2011

Abstract

ASTROSAT is India's first multiwavelength mission dedicated for astronomy to do observations of different classes of galactic and extragalactic sources in the spectral band of optical to hard X-rays. ASTROSAT is planned for launch in 2011 with five instruments on-board. One of the instruments is the Scanning Sky Monitor (SSM). SSM is an X-ray sky monitor which scans the entire sky in few hours to detect and locate any X-ray transients occurring in its Field Of View (FOV), in the energy range 2 to 10 keV. SSM has a large FOV and imaging of the X-ray sky is done using a coded-mask on the detector. SSM detectors are position-sensitive gas proportional counters. SSM comprises of three identical detectors with the associated electronics for each detector. A coded-mask with a collimator is mounted on top of each detector unit which defines a slightly different FOV for each unit. The three SSM units are mounted on a single rotating platform to scan the sky.

The thesis work presented here includes design optimisation of certain parameters of the gas proportional counters like the cell size, the gas mixture, gas pressure etc. for better performance of SSM detectors to achieve the science objectives. Characterisation of SSM detectors for stability of the output, detection efficiency in the energy range of interest, gas gain at different operating voltage, energy resolution, position resolution etc. are experimentally carried out and the results are discussed. As per the science objective of SSM to detect and locate any X-ray source in its FOV, it is required that the position of every photon incident on SSM detector is derived. The methodology to derive the position of the photon incident on SSM is devised and verified. Position calibration of SSM detectors are carried out experimentally and the anode calibration constants are derived. Various experiments are carried out to verify the calibration constants. Experiment to locate the position of the X-ray source in the FOV of SSM is carried out and found successful. Energy calibration of SSM at different energies in the energy range of interest is done and the spectral response of SSM is generated. The on-board calibration procedure for SSM is planned using the Crab nebula. Using the spectral response for SSM, the pulse height spectrum of the Crab nebula is simulated and the Crab count for SSM is estimated.

SSM detectors can detect and locate the transient X-ray sources, but are not meant for detailed spectral observations. A more detailed observation of these X-ray transient sources are carried out using pointed-mode instruments which have a narrow FOV and observe the sources for a longer duration. Two X-ray transient sources observed by the RXTE mission are studied for spectral and timing properties. The details of the analysis are presented in

this thesis. The two X-ray transients studied here are SLX 1746-331 and Swift J1753.5-0127. The mass estimate for these sources indicate them to be black hole candidates.

Acknowledgements

The research work presented in this thesis was carried out under the guidance of Dr. S. Seetha. I am extremely indebted to my supervisor for her support and guidance all through this thesis phase, for the useful suggestions and discussions at various stages of the work and above all for encouraging me to work independently. Without her timely encouragements this thesis would not have been possible.

I am privileged to acknowledge Dr. P. Sreekumar, whose lively discussions and valuable suggestions have helped a lot towards my thesis work.

I am extremely grateful to Prof.Ravishankar Babu, my thesis guide at the University, for his support and timely suggestions at various phases of this thesis work.

I gratefully acknowledge the help that I have got from all the members of the SSM team through out my thesis phase. I thank, starting from the detector team, Mr. V. C. Babu, Mr. B.N. Ashoka and Mr. Kumar who are involved in making of SSM detectors, without whose effort SSM could not have been made available for my thesis study. I thank the members of the electronics group of SSM, Mr. Ramki, Mr. Murthy, Mrs. Meena, Mr. Ravi Kulkarni, Ms. Prema, Mr. Monoj and Mr. Manjunath for their constant effort to build a low noise and trouble-free electronics system for SSM, without whose support SSM integrated system study would not have been possible. A special thanks to Meena who was there to explain me the details of the electronics for SSM and make me understand the logics and circuits for SSM, without any reluctance. I am grateful to each and every one in the SSM team for all their efforts to make this instrument a success. I am thankful to my friend Ravishankar, who is also part of the SSM team as the software member for SSM, for providing the required codes for the data analysis of SSM and for being there for any help all the time. I also thank my friend Sreejith for his initial support as a team member of SSM for software related issues.

I must acknowledge the friendly and moral support that I have received from Mrs. Lalitha Abraham throughout this thesis phase and for being there for any help all the time. I must express my gratitude towards her for taking the pains to come on holidays and whenever I wanted, to get me the keys of the office for me to work on holidays, without saying a 'NO' even once.

I am thankful to all my friends Ravishankar, Manju, Debbijoy, Sreejith, Shyama, Koshy, Athray, Girish, Sankar, Radhakrishna, Vaishali, Rakhee, Radhika, Bindu, Rajini, Uma, Vivek for the happy moments that I have had all the time. It was simply nice to spend

time together either at the canteen or at a restaurant or in the office. I must acknowledge Rakhee specially for being there to do anything and everything for me.

I thank all the other members of SAG for all the help that I have got throughout this thesis phase. I specially thank Mrs. Padma for her personal support and timely suggestions whenever I needed.

My thanks to my lovely brother, for being there for any support that I needed, for being there to share my joys and pains all the time.

I express my heartfelt thanks to my husband who had the patience to bear with me and spared my time for me to complete my thesis.

Lastly, but most importantly, I express my heartfelt gratitude to my loving parents who always wanted my happiness and had given the utmost importance for my Ph.D. work. They were always there for me, for everything, all the time.

Dedicated to my dear parents...

Contents

List of Figures

List of Tables

List of Publications

- **Refereed Publications**

  1. Optimization of Gas Proportional Counters for Scanning Sky Monitor (SSM) onboard ASTROSAT - **M.C. Ramadevi**, S. Seetha, V.C. Babu, B.N. Ashoka, P. Sreekumar, Advances in Space Research 38 (2006) 3002-3004
  2. The Scanning Sky Monitor (SSM) on ASTROSAT - S. Seetha, **M.C. Ramadevi**, V.C. Babu, M.R. Sharma, N.S.R. Murthy, B.N. Ashoka, K.C. Shyama, R. Kulkarni, G. Meena, P. Sreekumar, Advances in Space Research 38 (2006) 2995-2998
  3. Scanning Sky Monitor, A status report. - S. Seetha, **M.C. Ramadevi** et. al., BASI, 2003, Vol. 31, 485
  4. Slx 1746-311 in outburst - K.C. Shyama, **M.C. Ramadevi**, M. Sudhakar, D. Bhattacharya, P. Sreekumar, S. Seetha, Advances in Space Research 38 (2006) 2788-2790
  5. RXTE observations of a new x-ray transient SWIFT J1753.5-0127 in its low/hard state outburst - **M.C. Ramadevi** and S. Seetha, Mon. Not. R. Astron. Soc. 378, 182188 (2007)

- **Conference Proceedings**

  1. Position-sensitive Proportional Counter for space-based X-ray Imaging Studies - V.C. Babu, S. Seetha, **M.C. Ramadevi**, B.N. Ashoka et. al., Proceedings of DAE-BRNS National Symposium on Compact Nuclear Instruments and Radiation Detectors - 2005

Chapter 1

Introduction

1.1 A brief Overview of X-ray Astronomy

Earth's atmosphere absorbs X-rays and hence, it is required to go beyond the atmosphere to observe the X-ray sources in the sky. First rocket experiment flown under the direction of Herbert Friedman in the Naval Research Laboratory, Washington DC, to observe X-rays from the Sun, revealed the Sun as a powerful source of X-rays. Following this, there were trials to observe X-rays from the moon, produced as a result of fluorescence due to interaction of the X-rays and charged particles, from the Sun, with the lunar surface. A rocket experiment, developed by a group at American Science & Engineering (AS&E) led by Riccardo Giacconi, launched to observe X-rays from the moon, detected the first extra-solar cosmic X-ray source in 1962. Historic discovery of this bright X-ray source Sco X-1 (Giacconi et al., 1962) in the constellation of Scorpius triggered the advent of X-ray astronomy. An optical star of 13th magnitude was found in the same location (Sandage et al., 1966), where the X-ray source Sco X-1 was observed. After the discovery of Sco X-1, X-ray astronomy saw a rapid progress. Many balloon borne experiments to look for such objects bright in X-rays were conducted. Evidence for two weaker sources was found by Herbert Gursky and group in October 1962, which was followed by the identification of one of these sources as the Crab Nebula in 1963 by Stuart Bowyer. In July 1964, high energy X-rays were detected from Crab using a balloon-borne experiment by George Clark. This provided a hint that there are many sources in the sky, bright in X-rays and thus the sky was randomly observed for such sources with rockets and balloon-borne experiments. Although the X-ray sources were discovered, the phenomena responsible for the production of such high energy X-rays releasing large amount of energy were not understood.

Scientists had to wait till 1970, when the first X-ray satellite, UHURU (by the group at AS&E) was launched on December 12, 1970, which did a first survey of the sky for X-ray sources. UHURU discovered its first X-ray source Cen X-3 (Giacconi et al., 1971a), which was found to be pulsating. The X-ray source Cen X-3 was detected twice, earlier in 1967, by two groups from Lawrence Livermore Laboratory, who had derived a rough location. The period of pulsations of Cen X-3 was found to be 4.84 sec. Theoretical explanations for such pulsations indicated that it could be a neutron star that can rotate with such high angular velocity (Charles & Seward (1995) and references therein). Continuous monitoring showed slight variations in the pulse period. It was later discovered that this variation was due to the Doppler shift as the compact star moved in circular orbit with a period of 2.09 days. Further monitoring of the source indicated eclipses of the X-ray source, for 11 hours, once in every 2.09 days of its orbit. This confirmed the X-ray source as an eclipsing binary system. Optical observations of the source revealed the presence of a B type star. All these information put together indicated the X-ray source to be a binary system with a neutron star orbiting its companion, which is a normal star. It was understood that the X-ray emission was due to the accretion of matter from the companion star to the neutron star (which is a compact object with a high gravitational field) and as the matter falling onto the surface of the neutron star gets heated to millions of degree Kelvin, it produces X-ray emission.

Following the discovery of X-ray binaries, there were other X-ray sources observed with various experiments. Among those are the Cataclysmic variables, supernova remnants, hot stars with strong coronal X-ray emission, galaxies, active galactic nuclei etc. Cataclysmic variables (CV) are binary systems with a white dwarf accreting matter from its companion which is a normal star. The first CV, SS Cygni, was discovered in 1973 by Rappaport and colleagues (MIT) using a rocket experiment. Supernova remnants (SNR) are extended objects with or without a compact object at the centre which are formed after supernova explosion during the end stage of a massive star. Crab Nebula was the first SNR discovered in X-rays and it is 10-100 times brighter than the other remnants observed. First observation of strong coronal emission in X-rays was in 1974 from the bright star, Capella. Many more stars were observed with X-ray emission from the corona. It was found that many stars have coronal X-ray emission stronger than the sun. Later with instruments of better sensitivity, extragalactic X-ray sources were discovered. The first extragalactic X-ray source observed was an active galaxy, M87. Active galaxies are galaxies with a supermassive black hole at the centre of the galaxy which accretes the surrounding matter towards it, producing jets from the central part. UHURU observations added many galaxies, AGNs, quasars etc. to the extragalactic X-ray sources catalog. The first sky survey by UHURU led to the catalog

of 339 X-ray sources including X-ray binaries, supernova remnants, active galactic nuclei and clusters of galaxies (Forman et al., 1978).

After the major breakthrough of the discovery of X-ray binary system with the first X-ray satellite UHURU, there were many more satellites launched for the dedicated study of X-ray sources. Immediate follow-up missions were Ariel-V and HEAO-1. Ariel-V did a survey of the galactic plane and many more sources were discovered. First all-sky survey for X-ray sources was done by Kent Wood and collaborators (NRL) after about 20 years of the first X-ray source detection (Wood et al., 1984), using HEAO-1. The catalogue of X-ray sources from the observations of HEAO-1 satellite contained a total of 842 sources. Following this many missions with much better sensitive instruments such as Einstein, EXOSAT, Ginga, ROSAT etc. were launched. The Einstein X-ray telescope (Giacconi et al., 1979) had a sensitivity of an order better than HEAO-1 with a narrow field of view, with which it could observe about 5% of the sky. This was the first mission which conducted detailed study of X-ray sources and also led to a classification of different types of sources. ROSAT made the second all-sky survey in X-rays, particularly soft X-rays, with a better sensitivity (Truemper, 1992). ROSAT deep pointings went upto a sensitivity of an order better than the survey mode and hence helped the discovery of sources which were about 10^7 times fainter than Sco X-1 (Charles & Seward, 1995). This extensive sky survey produced a catalog of about 150,000 sources (Truemper, 1992). EXOSAT (White & Peacock, 1988) of ESA helped timing study of X-ray sources with high time resolution. Quasi-Periodic Oscillation (QPO) in X-ray binaries were discovered using EXOSAT's observations. The observations of the X-ray sky by these satellites provided a better insight of the X-ray sources, such as geometric parameters, mode of X-ray emission and the physics going on in these systems.

Today, missions like RXTE, Chandra, XMM, Suzaku and Swift have resulted in observations of various X-ray sources with unprecedented sensitivity and helped in detailed understanding of various objects. The Chandra X-ray observatory of NASA is known for its excellent imaging capability with high sensitivity in the energy range 0.1-10 keV (Weisskopf et al., 2002). It provides an angular resolution of 0.5 arcsec, which is unmatched till today. Chandra's contributions to X-ray astronomy include study of pulsar wind nebulae, study of abundances in supernova remnants, study of jets from AGNs, study of gaseous regions in nebulae and galaxy clusters, study of density and temperature distribution of hot gas in clusters etc. (Schwartz, 2004). The XMM-Newton observatory of ESA also provides fast imaging and sensitive spectroscopy similar to Chandra in the energy range 0.1-10 keV. Few important contributions of XMM are the discovery of broad spectral lines of iron from accreting black holes and neutron stars, discovery of black holes in globular clusters,

determining the luminosity and temperature of hot gas in galaxy clusters and estimating the mass of the clusters etc. (Schartel & Parmar, 2008). The Japanese mission, Suzaku launched in 2005 had the first X-ray microcalorimeter array in space. One of the important findings of this mission is the pulsar-like behaviour of the rotating magnetized white dwarf in hard X-rays (Terada et al., 2008).

Rossi X-ray Timing Explorer (RXTE) of NASA, another dedicated mission for X-ray astronomy, has very good timing capability along with broad band spectroscopy. Most of the X-ray sources are accreting objects and the X-ray emission from these systems are variable at different time scales. Timing study of these sources reveal many aspects of the system like orbital parameters, the accretion process happening in these systems etc. The very large collecting area of RXTE provides good photon statistics for doing timing study. The mission which contributed most to study the X-ray binaries in the recent years has been the RXTE. The All Sky Monitor (ASM Levine et al. (1996)) on RXTE has been monitoring the X-ray sky for transient sources and increased the number of sources in the source catalog. It is the first experience to provide sky monitoring on a daily basis and this kind of continuous monitoring supports the study of long term variations in the observed sources. The large area Proportional Counter Unit (PCU Jahoda et al. (1996)) has provided unprecedented timing study of X-ray binaries. The High Energy X-ray Timing Explorer (HEXTE Rothschild et al. (1998) has provided spectra at hard X-rays upto 180 keV. The important science contributions from this mission are the discovery of kilohertz QPO in low-mass X-ray binaries (van der Klis et al., 1996), the periodic variability on the surface of neutron stars during thermonuclear X-ray bursts (Strohmayer et al., 1996) etc.

India started its X-ray astronomy program with balloon borne and rocket borne experiments. Amongst few of the astronomy experiments flown, the IXAE on IRS-P3 gave interesting results on the time variability of X-ray binaries (Agrawal P.C. et al., 2007). India is planning to have a dedicated multiwavelength mission for astronomy, to be launched in 2011, which is named 'ASTROSAT', which has five instruments on-board for observations of different classes of galactic and extragalactic sources (Agrawal P.C., 2004, 2006). Section 1.9 gives an overview of ASTROSAT. One of the instruments on-board ASTROSAT is an X-ray sky monitor called Scanning Sky Monitor (SSM) (Seetha et al., 2006, Seetha S., 2003). This thesis describes the design optimization and calibration of gas proportional counters for SSM. With the knowledge gained from the present study a design for future X-ray sky monitor is proposed at the end. The thesis also includes detailed spectral and timing study of select X-ray transient sources based on observations conducted by RXTE (Rossi X-ray Transient Explorer). The following sections give a brief overview of the processes causing the X-ray emission in these X-ray sources, X-ray transient sources and binaries and the

kind of variabilities observed in these systems. Details of galactic black hole systems such as the spectral and timing studies are also discussed.

1.2 Accretion

Accretion proves to be the most efficient process of energy release, in which the gravitational potential energy of the accreted matter is converted to orbital kinetic energy and eventually into heat which is radiated away in the form of electromagnetic radiation. It is the "gravity" which is envisaged to power the most luminous objects in the universe. Astrophysical objects like the X-ray Binaries (XRBs), the Active Galactic Nuclei (AGN) etc. are believed to be powered by accretion. For an object of mass M and radius R, the gravitational potential energy released by the accretion of a mass m on to its surface is given as

$$\Delta E_{acc} = \frac{GMm}{R} \tag{1.1}$$

where G is the gravitational constant. Equation 1.1 shows that the efficiency of accretion in the release of energy is strongly dependent on the compactness of the accreting object, which is a function of the mass to radius ratio. If the accreting object is a neutron star with radius R = 10 km and mass M $\simeq$ 2 $M_{\odot}$, the gravitational potential energy released due to accretion is about 2.7 $\times$ 10^{20} ergs per accreted gram. The energy released from burning of Hydrogen to Helium is ΔE = 0.007mc^2, which is about 6 $\times$ 10^{18} ergs per gram (Frank et al., 2002), which is about (1/20) of the energy released by accretion. However, the efficiency of accretion is low for low compactness (M/R) parameter. For example, in a white dwarf with mass M $\sim$ 1 $M_{\odot}$, the energy released by nuclear burning is more efficient than accretion by factors of 25-50 (Frank et al., 2002). Therefore, accretion is efficient in systems which contain a neutron star or a black hole as the compact object. It has been proven from observations that many X-ray sources exist where accretion plays the major role in X-ray emission.

The luminosity produced due to accretion in X-ray sources, depends on the mass accretion rate $\dot{M}$ (which is the rate at which the matter is accreted by the compact object from its surrounding) and the luminosity produced due to accretion is given by

$$L_{acc} = \frac{GM\dot{M}}{R} \tag{1.2}$$

where R is the radius of the compact object, G is the gravitational constant and M is the mass of the accreting compact object and $\dot{M}$ is the mass accretion rate. The luminosity

can also be expressed as

$$L = \eta \dot{M} c^2 \tag{1.3}$$

where η is the efficiency, η = GM/c^2, is ∼0.1 for a neutron star, ∼0.06 to 0.42 for black holes and ∼0.001 for white dwarfs (Charles & Seward, 1995).

There are X-ray binary systems (which are discussed in detail in section 1.4), which contain a black hole or a neutron star as the compact object along with a companion star, orbiting about the centre of mass. These X-ray binary systems constitute the brightest class of galactic X-ray sources in the sky. Their X-ray luminosities range from 10^{36} to 10^{38} ergs/sec.

1.2.1 The Eddington Limit

The Eddington limit, also called the Eddington luminosity, is the point at which the luminosity emitted by a star or active galaxy is so high that the radiation pressure starts blowing off the outer layers of the object. In X-ray binary systems, the Eddington limit is the maximum luminosity from the system produced due to the matter accreted on to the compact object, beyond which the luminosity becomes high enough for the radiation pressure to overcome the gravitational potential of the compact object and the accretion is stopped. The pressure exerted by the electromagnetic radiation on the accreted material is proportional to the flux F of the radiation. The Eddington luminosity can be estimated by equating the inward force of gravity and the radiation pressure acting outwards (Charles & Seward, 1995, Longair, 1994) and is given as

$$L_E = \frac{4\pi G M m_p c}{\sigma_0} \tag{1.4}$$

where σ_0 is the Thomson scattering cross-section, M is the mass of the compact object, m$_p$ is the mass of the proton, c is the velocity of light. Substituting the values of the constants in equation 1.4, the Eddington luminosity is given as

$$L_E = 1.3 \times 10^{38} (M/M_\odot) erg/s \tag{1.5}$$

Thus, a neutron star of mass 1.5 M$_\odot$ can produce a luminosity of ∼2×10^{38} erg s^{-1} due to accretion.

1.2.2 Accretion Disks

The accreted matter flowing towards the compact object cannot fall straight on to the surface of the object, as this matter will have an angular momentum associated with it. Therefore, it takes a circular Keplerian path around the accreting object. The continuous stream of matter captured from the companion will follow a sequence of circular orbits with the Keplerian angular velocity given by $\Omega_k(R) = (GM/R^3)^{1/2}$, about the compact object and hence forming a disk (Frank et al. (2002) and references therein). For the accreted matter to move inwards closer to the compact object, it must lose energy and angular momentum. The means for the loss of angular momentum is viscous force that acts as the frictional force between two adjacent layers with a velocity gradient. This results in the dissipation of heat, part of which is eventually radiated. The surface temperature of the thin disc due to viscous heat dissipation is given by Frank et al. (2002) and references therein.

$$T = \left(\frac{3GM\dot{m}}{8\pi R^3 \sigma} \left[1 - \left(\frac{R_*}{R} \right)^{1/2} \right] \right)^{1/4} \tag{1.6}$$

where M is the mass of the accreting object, $\dot{m}$ is the rate of accreted matter, R is the radius of the layer of the accretion disk which is emitting radiation, R_* is the radius of the accreting object and σ is the Stefan-Boltzmann constant. For non-magnetic white dwarfs and neutron star systems, the inner radius of the accretion disk R_{in} becomes equal to R_*. Different layers in the accretion disk have different temperatures and the emission from each one of them can be approximated to black body emission. The total emission from the disk is proportional to the surface area of the disk. Therefore, the emission from the disk is the integrated emission from each layer, where emission from each layer is given as surface area of the layer at temperature, T $\times$ the blackbody emission at that temperature. Therefore the total intensity can be given as

$$I(\nu) = \int_{r_{in}}^{r_{max}} 2\pi r B[T(r), \nu] dr \tag{1.7}$$

where B(T,ν) is the Planck function given as $B_\nu \propto \nu^3 [exp(h\nu/kT) - 1]^{-1}$. As the accretion disk is a combination of many black body spectra at different layers which are at different temperatures, it is approximated to a single multi-color black body. The theory of steady thin disk was first introduced by Shakura & Sunyaev (1973). However, the accretion disk is not found to be steady always. There are different timescales on which the disk varies. Also, in addition to variabilities in the X-ray emission from the accretion disk, there are other kinds of variabilities observed in these binaries. Accretion disks have been studied since the

discovery of binaries and many theories have sprung up on accretion disks to explain the observational results from the astrophysical systems.

1.3 X-ray emission processes in accreting systems

The X-ray emission in these accreting systems occur at regions very close to the compact object, where the accreted matter is heated to millions of degree Kelvin. There are different physical processes of X-ray emission that can happen in these systems. The process of emission can be black-body radiation from the inner regions of the accretion disk around the compact object, from the surface of the accreting neutron star, thermal bremsstrahlung from the hot optically thin plasma surrounding the compact object, line emission from the hot accreted material around the compact object, inverse compton scattering from the hot corona around the compact object and synchrotron radiation in case of highly magnetized neutron star system. The emission spectra observed from these sources can contain one or more processes of X-ray emission, depending on the nature of the compact object and the companion star. Studying the energy spectra helps in understanding the physical picture of the systems. The energy spectra of the outbursts at different instances give detailed information on the physical processes which produce these sudden outbursts. Thus, these X-ray binary systems serve as promising candidates to study "accretion".

X-ray flux varies on different time scales for different classes of objects due to various reasons. The light curve (a plot of Intensity vs Time) of these objects contains information of time-dependent behavior of accretion processes in the disks (Chen et al., 1997) and other processes going on in the systems. The variation in the X-ray intensity of these binary systems depends on the interaction of accretion flows with the compact object, which is either a neutron star or a black hole. In the case of the neutron star systems, it also depends on how strong the magnetic field of the neutron star is, either a weakly magnetized (B$\sim 10^9$ G) neutron star or a strongly magnetized one (B$\sim 10^{12}$ G). These systems are distinguished by their observational properties such as pulsations, types of outbursts, types of variabilities, spectral signatures etc. One of the important observational manifestations is the presence of pulsations (discussed in 1.7.1) in the light curve of the binary system, which is a clear signature of the presence of a strongly magnetized neutron star. Another important observational feature to distinguish between a weakly magnetized neutron star and a black hole system is the presence of type I X-ray bursts, which are thought to be thermo-nuclear flashes (discussed in 1.6.2) that occur due to burning of Helium layer on the surface of the neutron star.

1.4 X-ray Binaries

An X-ray binary system consists of a normal star transferring matter on to a compact object which might be a neutron star or a black hole. The compact star can also be a white dwarf and such binary systems are called cataclysmic variables (CV). The compact object accretes matter from the companion through Roche Lobe overflow (Roche Lobe: area around the star up to which its gravitational field is present) or through stellar wind accretion. The matter accreted from the companion star flows on to the compact star under the influence of its gravitational potential. As the inflowing matter has with it an angular momentum associated, it spirals on to the compact star forming an accretion disk. The violent collisions between the particles in the inflowing matter heat the gas to very high temperatures of about 10^7 K to 10^8 K. In this process the gravitational potential energy of the infalling matter is converted to kinetic energy and eventually into radiation in the form of X-rays. The main factors which determine the emission property of the X-ray binary systems are the nature of the compact object and the companion star, the mass of the compact object and the mass accretion rate. In addition to these, there are other factors such as the geometry of the accretion flow, the properties of the companion star like the mass loss by Roche Lobe overflow or stellar wind, the orbital parameters of the binary system, the strength of the magnetic field of the compact object if it is a neutron star etc. A detailed discussion of X-ray Binaries can be found in Lewin et al. (1995).

X-ray binaries are important objects to study, as they are promising candidates to understand the physical mechanisms of accretion. They also serve as good examples to study the nature of the exotic compact objects at relative proximity compared to the extragalactic sources. Some of these systems are transient in nature. Although these systems have been studied extensively over the last few decades, still many questions remain unanswered. This includes determining system parameters like mass of the compact star and companion star, orbital parameters of the system, understanding the complex physics processes that take place during different phases of the outburst, evolution of these systems, the link between these and other similar systems like Ultra-Luminous-X-ray Objects (ULX, which are believed to be black hole binary systems hosting intermediate mass black holes of mass $\sim 100 M_\odot$), Active Galactic Nuclei (AGN) etc. in which accretion plays the prime role.

1.4.1 Types of X-ray Binaries

X-ray Binaries are broadly classified into two categories depending on the mass of the companion star.

High Mass X-ray Binaries (HMXBs)

In High Mass X-ray Binaries, the companion star has a mass $\geq 10M_{\odot}$ and is an early type star with a powerful stellar wind by which it looses its mass. It is generally a supergiant with spectral type earlier than B, or an O type star (Charles & Coe, 2006, Van Paradijs & McClintock, 1995). The mass transfer on to the compact star happens through this stellar wind and it is called 'wind-fed' accretion in X-ray binary systems. These are generally young binary systems and the companion star is an early type Be star or a super-giant. The compact star in these systems are mostly neutron stars. If the compact star is a NS, it is most probable that the NS possesses very high magnetic field of the order of $\sim 10^{12}$ G. In such cases, the accretion is funneled to the poles of the star through magnetic field lines, thus producing X-ray pulses as the star rotates when the magnetic and rotation axes are not aligned. Thus, the light curve of these sources show pulsations. The spectra of HMXBs are generally hard with a flat energy spectra.

Low Mass X-ray Binaries (LMXB)

In LMXBs, the companion star is usually a late type star with mass $\leq 2M_{\odot}$. It is typically a main sequence star and evolves by filling its Roche-lobe (Charles & Coe, 2006, Van Paradijs & McClintock, 1995). The matter is transferred on to the compact object by Roche-lobe overflow. The accreted matter has angular momentum and so forms a circular disk around the compact object. This is called the accretion disk in the system. In LMXBs, the ratio of X-ray to optical flux $\gg 1$. In most of the systems, it has been very difficult to identify the optical counter part as the companion star is very faint, and the X-ray emission dominates in the system. The X-ray spectra of these systems are generally soft and are dominated by disk emission. Different types of x-ray outbursts are observed from these transient sources and these are discussed in section 1.6.

1.5 Galactic Black Hole Systems

X-ray binary systems which host a black hole as the compact object are called Black Hole Binaries (BHBs, in cases where the compact object is confirmed to be a black hole) or Black Hole Candidates (BHCs, in cases where the compact object is yet to confirmed to be a black hole, but show significant features of the presence of a black hole). There are 20 confirmed black hole binary systems and few tens of black hole candidates in our galaxy (McClintock & Remillard, 2006). The spectral and timing studies of two such systems are discussed in detail in chapter 5 of this thesis. Black Hole binaries or candidates are a class

of brightest X-ray sources in the sky. The mass estimate of the compact objects in these systems are obtained by optical spectroscopic studies of the companion star and the mass of the companion is estimated. By knowing the radial velocity amplitude K and the orbital period P, the mass function can be calculated using the equation 1.8. As the mass of the companion is known, the mass of the compact object can be estimated using the mass function.

$$f(M) = \frac{PK^3}{2\pi G} = \frac{{M_x}^3 sin^3 i}{(M_x + M_1)^2} \tag{1.8}$$

where M_x is the mass of the compact object, M_1 is the mass of the companion star and 'i' is the inclination angle of the orbital plane of the binary system with respect to the line of sight (Charles & Coe, 2006). However, the mass of the compact object estimated by this method has caveats due to the value of 'i' considered in equation 1.8, which is complicated to estimate for an X-ray binary system.

Mass estimate of black holes in these binaries using the equation 1.8 is possible only if the optical counterpart can be observed. In cases where the optical counterpart is not identified, detailed spectral studies in the X-ray band help in estimating the mass and spin of the black holes. The relativistic iron lines from the inner accretion disks around black holes are good probes of strong gravitational effects including understanding of spins of the black holes (Miller (2007) and references therein). Presently, there are 20 confirmed black hole binaries in our galaxy, with a possibility of $\sim 10^9$ black holes not yet discovered (Remillard & McClintock, 2006).

Black Hole transients are known to undergo outbursts which are caused due to variation in accretion of matter on to it, from the companion star. McClintock & Remillard (2006) give a very detailed discussion of Black hole binaries and their properties observed. There are both persistent and transient black hole systems identified today. Few of the persistent black hole systems which show continuous emission all the time are GRS 1915+105, Cygnus X-1, GX 339-4, LMC X-1 etc. Transient systems are found to undergo outbursts occasionally and the recurrence periods are mostly random and vary from months to years. Most of the outbursts are classified to have different spectral states during different stages of the outburst.

1.5.1 Spectral studies of Black hole systems

The energy spectra of the black hole binaries have been known to consist basically of two components, the thermal and the non-thermal, varying in different proportions according to different stages of the outburst. The thermal component is modelled with a multicolor

blackbody, which is the contribution of the inner accretion disk emission in the soft X-rays of about 1 keV. The non-thermal component is generally modelled with a power law, which is given by N(E)=E^{Γ}, where Γ is called the photon index. This component extends to hard X-rays upto about 100 keV. The spectra of black hole binaries were first distinguished from that of the neutron star binary systems by Tanaka & Lewin (1995). The contribution to the total flux from the system varies in different proportions at different spectral states. State Transitions in the spectra are observed during these outbursts. There are five distinct spectral/temporal states defined in the spectral band of 1-10 keV (McClintock & Remillard (2006) and references therein). They are (1) the high/soft (HS), a high intensity state dominated by thermal emission from the accretion disk, (2) the low/hard (LH) state, a low luminosity state dominated by power law emission and rapid variability, and (3) the quiescent state, the extremely faint state also dominated by power law emission and the two other intermediate states which are (4) the very high (VH) state and (5) the intermediate state which occur between the first two states mentioned here. These transient systems are found to be in quiescent state for a longer time and state transitions occur during an outburst. When an outburst occurs, the system changes its spectral state from low/hard state to the high/soft state. The system is mostly in the high/soft state during the peak of the burst and then it may transit back to steep power law state and then back to the low/hard state during the decay of the burst. Figure 1.1 shows the spectral states during a canonical outburst of a black hole system Cygnus X-1. The spectral states are classified

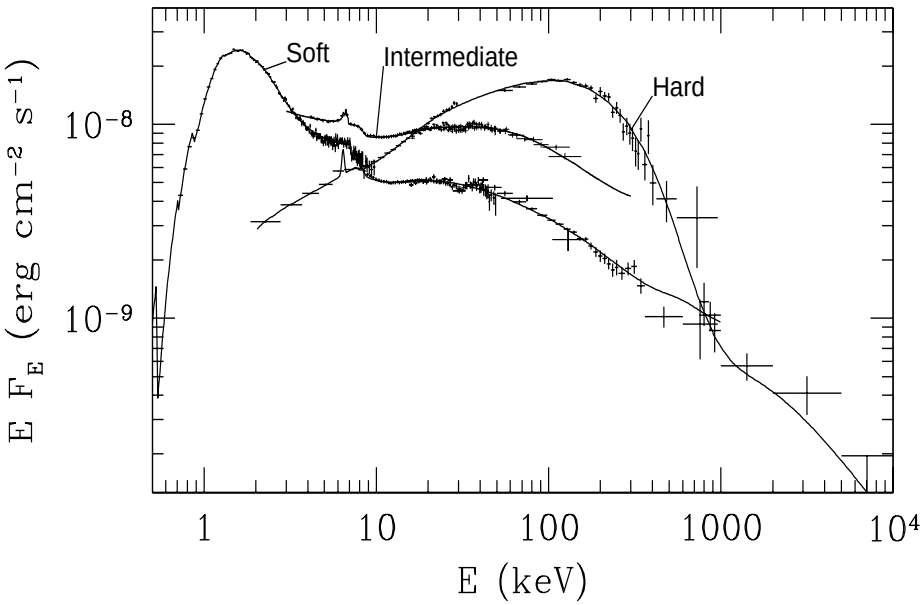

FIGURE 1.1: Different spectral states of a black hole source Cygnus X-1 during an outburst (Gierlinski et al., 1999)

according to the following criteria recently.(Remillard & McClintock, 2006).

- Thermal state, defined by
  - disk flux fraction (f) > 0.75 (disk-dominated flux)
  - power in PDS r < 0.075 and
  - QPO rms amplitude, if present < 0.005 (low continuum power in PDS and weak QPOs)
- Hard state, defined by
  - f < 0.2 (power-law-dominated flux)
  - spectral index: $1.4 < \Gamma < 2.1$, and
  - r > 0.1 (high continuum power)
- Steep power-law (SPL) state, defined by
  - either f < 0.8 with a QPO present (QPO rms amplitude, a > 0.01) or f < 0.5 with no QPOs
  - spectral index $\Gamma > 2.4$
  - r < 0.15

Different spectral states of black hole systems are also discussed in Homan & Belloni (2005).

1.5.2 Timing studies of Black hole systems

One of the best techniques to study the near vicinity of a black hole is studying the rapid variations in the X-ray emission from the system (McClintock & Remillard, 2006, van der Klis, 2006). The commonly used analysis tool for studying the variabilities in the light curve is the power density spectrum (PDS) (Leahy et al., 1983). The PDS of black hole binaries are known to have a broad-band continuum spectra with distinct features called the QPOs (discussed in section 1.7.2). These QPOs can be fitted with Lorentzians, in addition to a number of broad Lorentzians to fit the continuum (Belloni et al., 2002).

QPOs play a key role in probing strong gravitational field regions very close to the black holes. Correlated timing and spectral studies of the black hole binaries can be a promising method to estimate the mass and spin of the central compact object in X-ray binary systems. Figure 1.2 shows the correlation between the energy spectra and the power density spectra at different stages of the outburst of the black hole binary system GRO J1650-40 (Remillard & McClintock, 2006).

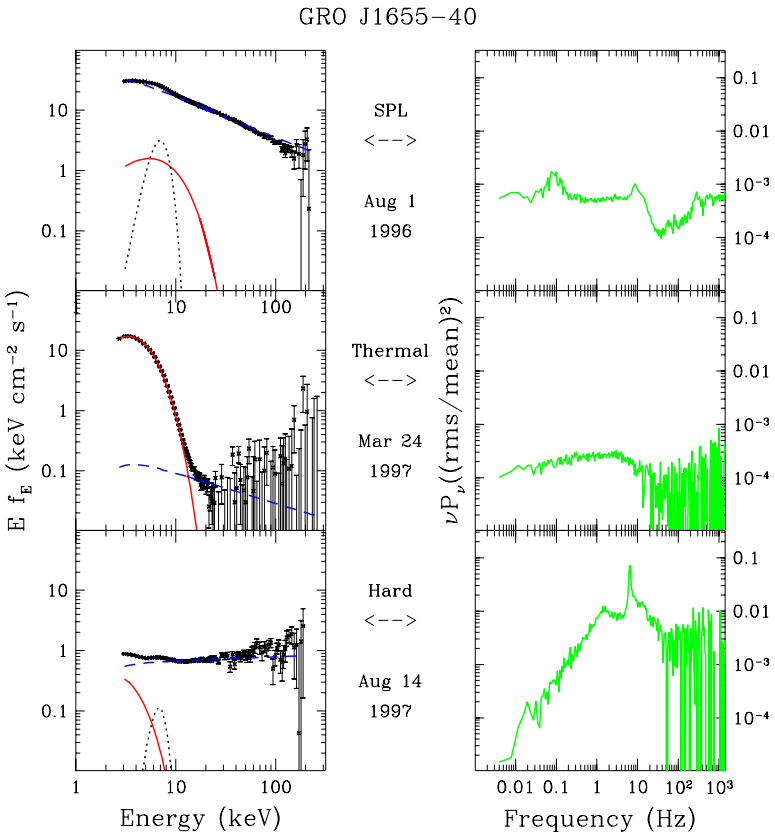

FIGURE 1.2: Correlation between the energy spectra and power density spectra for an outburst of the black hole binary GRO J1650-40, at different states of the outburst (Remillard & McClintock, 2006)

1.6 X-ray transients

X-ray binaries are the brightest class of X-ray sources in the sky. Amongst these X-ray binaries, some are transient sources and some of them are persistent sources. The transient X-ray sources exhibit variabilities in their intensities, by factors of few tens or hundreds over time. These transient sources are usually below the detection threshold of many X-ray instruments, but brighten in intensity by many factors during an outburst. Such an outburst reaches its peak intensity over a week or so and decays back to background level over a time scale of few months. These transient sources allow us to study the nature of variability in their X-ray emission and processes taking place over a large dynamic scale. A review of transient X-ray sources can be found in Tanaka & Shibazaki (1996)

These transients can be classified into soft and hard X-ray transients according to the energy

band in which they flare up. Soft X-ray Transients (SXT), which are also known as X-ray Novae, contain either a black hole or a neutron star accreting matter from its companion star by Roche Lobe overflow. These transients are found to be in quiescence for long periods of time ranging from 0.5 to 50 years before they undergo transient outbursts (Zand (1992). LMXBs are found to be soft X-ray transients which have most of the X-ray emission in the soft X-ray band 2 to 10 keV and the HMXBs are found to be hard X-ray transients that emit in X-rays > 15 keV. Hard X-ray transients are mostly, systems that have highly magnetized neutron stars as the accreting objects and some of them are in highly eccentric orbits. The accretion process is by capture of the stellar wind of the massive companion star. Similar to soft and hard, there is another classification of X-ray transients: slow and fast X-ray transients. Slow transients are those which flare up in intensity with a rise time of few days and decay to the quiescent phase in months timescale. Fast X-ray transients are those with timescales between a minute and a day (Heise & Jean in't, 2006).

There are various kinds of variabilities observed in these transient X-ray sources. The intensity of the X-ray flux emitted by these sources vary at different timescales and are evident in the light curve. The variabilities are different for different mechanisms driving them and these are discussed in the following sections.

1.6.1 Transient outbursts

Soft X-ray transients are found to exhibit X-ray outbursts once in a while, which are called transient outbursts. The X-ray source is in quiescence for most of the time and undergoes an outburst with increase in intensity by at least a factor of 10. These outbursts are also called type II bursts. Type II bursts have typical rise time of few days and decay time of few months. The recurrence time-scales and the duration of these outbursts vary from system to system. For example, in a binary system which has a white dwarf as the compact object and a low-mass companion star, the recurrence time scales would be weeks to months and the duration of the burst can last for days. And in a system where the compact object is a neutron star or a black hole, the recurrence timescales can vary from months to tens of years and the duration can be for months (King, 2006). The light curves can have different profiles, which can be an indication of the physical process driving the outbursts (Chen et al., 1997). The profiles of the outbursts can also vary from one to another in the same system. The cause for these outbursts from a transient X-ray binary system is most likely due to instabilities in the accretion flow in the disk. Other causes can be the instability of the envelope of the mass-losing companion star, which increases the mass accretion rate giving rise to a higher X-ray emission and other instabilities in the system.

1.6.2 X-ray bursts

X-ray bursts are thermo-nuclear flashes occurring on the surface of the neutron star which lasts from few seconds to minutes. When a weakly magnetized neutron star accretes matter from its companion, the matter gets onto the surface of the neutron star, from the accretion disc and produces a layer of hydrogen which burns steadily, producing helium. The density and temperature of the helium layer increases and reaches a critical value at which helium starts burning to form carbon. The burning of helium is an unstable process leading to a thermonuclear flash on the surface of the neutron star. These thermonuclear bursts are called type I bursts and are observed only in the binary systems which have neutron star as the compact object. The rise time of the bursts vary from less than a second to tens of seconds and the decay time range from few tens of seconds to minutes. The recurrent time scales depend on the fuel accumulation for several hours to days, which is followed by successive bursts. Type I bursts are observed only in neutron star binary systems, as these bursts occur on the surface of the star and are not observed in black hole binary systems as there is no hard surface for a black hole. These bursts are one of the important signatures of a binary system and hence can be definitely identified to have a neutron star as the compact object. The type I X-ray bursts were first discovered independently by Grindlay et al. (1976) and Belian et al. (1976).

The spectra during type I bursts are found to be black body spectra which cools slowly with the decay of the burst. Calculations show that the radius of the emitting region is about 10 to 15 km, which matches with the theoretically predicted radius of a neutron star. An extensive discussion of these X-ray bursts are given in Lewin et al. (1995) and references therein.

1.6.3 Superbursts

Superbursts are outbursts similar to type I bursts, but are of comparatively longer duration (of the order of hours), larger fluence level and longer recurrence periods. These bursts are about 1000 times longer and more energetic than the standard type I bursts and hence are given the name superbursts (Strohmayer & Bildsten, 2006). Their spectra are similar to the thermonuclear bursts with a thermal spectra, cooling during the decay of the burst. Cornelisse et al. (2000) reported the first discovery of superbursts in the source 4U 1735-44, which had been observed to show type I bursts. Unstable burning of the Carbon layer is proposed to be the cause for the superburst and this forms a likely explanation for the high amount of fluences emitted during the burst.

1.7 Variabilities observed in X-ray binary systems

In addition to the different kinds of outbursts which are transient in nature, other kinds of variabilities have been observed in X-ray binary systems. These include pulsations, Quasi-periodic oscillations, rapid variability and long-term orbital modulations in the light curve of the X-ray binary systems. These variabilities in the light curve can be periodic or quasi-periodic or even random in nature. However, unlike the transient outbursts which occur at longer timescales of months to years, these variabilities are found in timescales ranging from milliseconds to days. The following sections discuss these variabilities in X-ray binary systems.

1.7.1 Pulsations

Periodic pulsations were first discovered (Giacconi et al., 1971b) in the X-ray light curve of X-ray binary systems. When a highly magnetised neutron star (with B $\sim 10^{12}$ G) accretes matter from its companion star, the matter is funneled by the magnetic field of the neutron star at the Alfven radius (radius at which the magnetic pressure is equal to the ram pressure of the accreting gas) (Ghosh & Lamb (1979) and references therein). When the spin frequency of the neutron star is smaller than the orbital frequency of the accreted matter, the accreted matter gets channeled along the field lines onto the poles of the neutron star (Psaltis (2006) and references therein). As the matter falls onto the magnetic poles, X-rays are produced. If the magnetic axis and the rotation axis of the neutron star are not aligned, then the emission from the poles of the star are seen as pulsations when the light beam crosses the observer's line of sight. These pulsars which show pulsations due to the matter accreted from the respective companion stars are called accretion-powered pulsars. In these accretion-powered pulsars, the neutron star can either spin-up or spin-down with time, ie. the period of the neutron star can either decrease or increase respectively. When the companion star is losing matter that accretes onto the neutron star, the angular momentum is transferred by the accreting matter to the neutron star and vice versa.

1.7.2 Quasi Periodic Oscillations

There has been correlated study of spectral and timing of these transient sources to understand the physics of the variabilities. Quasi Periodic Oscillations (QPOs), as the name suggests are quasi-periodic in nature which are one of the aperiodic variabilities observed in these sources. QPOs could be due to emission from hot clumps of matter orbiting in

the accretion disk around the central compact object (Sunyaev, 1973). QPOs can also be due to aperiodic emission for hot spots on the accretion disk. QPOs are generally found in LMXBs. These are found as broad symmetric peaks in the power spectrum of an X-ray binary system along with the broad noise spectrum. van der Klis (1995) gives a detailed study of QPOs in binary systems.

1.7.3 Rapid variability

The transfer of matter towards the compact object occurs by forming an accretion disk in which matter moves in near-Keplerian orbits. However, the geometry of the accretion flow very close to the compact object (at the innermost orbits of the disk) is very uncertain. The inner radius of the accretion disk close to the compact object varies according to the nature of the compact object. Instabilities in the accretion region can give rise to rapid fluctuations in the X-ray emission of the system. These fluctuations are aperiodic in nature and give rise to different frequencies in the power density spectrum (PDS). The PDS follows a power law within a range of frequencies and is given by $P(\nu) = A\nu^{-\alpha}$, where ν is the frequency, α is the power-law index and A is the normalization constant. A detailed discussion on rapid aperiodic variability in XRBs is given by van der Klis (1995).

1.7.4 Orbital modulations and long-term variations

The light curve of few of the X-ray binary systems indicate the signature of orbital modulations which could be due to eclipses or periodic Doppler shift of the pulse arrival times (Charles & Seward, 1995). Especially in the case of HMXBs, where the compact object is a neutron star, the pulses from the X-ray pulsar can be Doppler shifted. Eclipses are possible mostly in HMXBs where the X-ray source (the compact object) is eclipsed by the huge companion star.

Long term variabilities of accreting black holes and weakly magnetized neutron stars are typically aperiodic and reflect the variable nature of the mass-transfer and accretion processes due to highly elliptical orbits. There are variabilities caused by the reflection of the X-ray photons off the binary companion. Long term variations in the light curve of an X-ray binary system can also be caused due to the precession of the accretion disk or warping of the accretion disk (van der Klis (1995) and references therein)

1.8 X-ray Sky Monitors

The X-ray sky is extremely variable with various kinds of sources discussed above. The brightest class of objects amongst these are X-ray binaries which are generally transient sources with variabilities of different timescales. The X-ray emission from these systems are due to accretion process, which is a phenomenon present at all scales in the universe. Study of these x-ray binary systems largely helps understanding accretion. In order to study these transient X-ray binary systems, it is necessary to monitor these sources continuously to detect them when they exhibit outburst so that detailed timing and spectral studies can be done on these sources. Efficient monitoring of these sources, which are spread over the vast sky, is possible only with an instrument with a large field of view, which are called All Sky Monitors. The large FOV is required because these transients are not predictable.

1.8.1 Key Objectives of All Sky Monitors

The two main objectives of an All Sky Monitor is to serve as an alert for any transient in the X-ray sky giving alerts for other instruments to do further studies and to continuously monitor the X-ray source to study their long-term variabilities. These two objectives render X-ray All Sky Monitors, still in demand in X-ray astronomy, for long-term study of the sources. All Sky Monitors (ASMs) are important to study the X-ray sky in various aspects, which may not be possible with pointed mode instruments. The probability of a serendipitous discovery of any new X-ray source is high with an ASM as it has a large FOV to keep monitoring the sky continuously. About 90% of the black hole candidates are X-ray transients (McClintock & Remillard, 2006). Most of them are discovered by RXTE-ASM and Ginga-ASM (Negoro (2009) and references therein). Many of the X-ray transient sources have been studied in detail by pointed mode instruments, after getting a transient alert notification from the ASMs monitoring the sky. A detailed observation of X-ray transient sources during the rise and decay phases of an outburst has helped in understanding these systems better. A better understanding of "accretion" with many theories and observations has happened with the help of ASMs indirectly.

Since the ASMs have large FOV, most of the bright X-ray sources can be monitored continuously to study the long-term variations in them such as the orbital modulations in case of X-ray binary systems, rapid variabilities occurring in the systems etc. The orbital parameters of X-ray binary systems like the period of orbit of the stars, the pulsations if any

TABLE 1.1: List of X-ray Sky Monitors flown in different missions (details collected from HEASARC website: http://heasarc.gsfc.nasa.gov/docs/observatories.html)

Mission	Instrument used	FOV	Energy range	Year of launch and operation
Vela-5B	Scintillation X-ray detectors	6.1°× 6.1° FWHM	3-12 keV	1969-1979
Ariel-5	pin hole camera with position sensitive proportional counters (two units)	5°× 5°	2-20 keV	1974-1980
Hakucho	first japanese exclusively to monitor the X-ray sky, 10 proportional counters	∼50°× 1.7°	0.1-0.2 keV and 1.5-30 keV	1979-1985
Ginga	Large area proportional counter	1° × 180°	1-20 keV	1987-1991
Granat	All Sky monitor	All sky FOV	6-120 keV	1989-1998
CGRO	Burst Alert and Transient Source Experiment (BATSE)	non-collimated	20-1000 keV	1991-2000
RXTE	All Sky Monitor, which uses three units of proportional counters	12° × 110°	2-10 keV	1995 - till date
BeppoSAX	Wide Field Camera	20° × 20°	2-30 keV	1996 - 2002
HETE-2	Wide Field X-ray Monitor (WXM)	5.5°× 5.5°-	2-25 keV	2000 - 2001
Integral	Joint European X-ray Monitor (JEM-X)	FOV 4.8°	3-35 keV	2002-2008
Swift	Burst Alert Telescope (BAT); wide field coded-mask imager	FOV 1.4 sr	15-150 keV	2004 - till date
MAXI at ISS	MAXI; 12 proportional counter units and CCDs	1.5° × 160°	0.5-30 keV	2009 - till date

in neutron star systems, eclipses in binary systems, etc. have been known for various systems by long-term monitoring with ASMs. ASMs have helped periodic and quasi-periodic long-term variability study of X-ray binaries.

The catalogue of known X-ray sources can be updated with ASMs and the knowledge of different kinds of X-ray sources and their population can help the overall understanding of X-ray sky. All ASMs flown till date have contributed to the existing catalog of sources, some have done a major contribution whereas some have added few to it. The search for new X-ray sources will continue with instruments of better sensitivity in the future years.

1.8.2 Basic design of ASM

The basic requirement of an ASM is that it has to keep monitoring the sky for any variabilities in the intensity of the X-ray sources as well as do long-term observations of the known sources. The ASM has to be sensitive enough with good angular resolution, so that it detects faint sources without any source confusion. These requirements drive the design of an ASM. The important parameters to be considered for design of an ASM are 1. Duty cycle of sky coverage, 2. Angular resolution, 3. Sensitivity and 4. Temporal resolution. A detailed discussion of sky monitors can be found in Holt & Priedhorsky (1987).

The classic techniques to do all sky monitoring are the pinhole camera, a detector with rotation modulation collimator and the scanned slat collimator (Doty, 1988). Each of these techniques have their own advantages and limitations. In the case of pinhole camera, the spatial resolution can be good but the sensitivity would be poor due to less number of photon detected due to the small aperture. And in the case of scanned slat collimator, the number of photons detected are more at the cost of spatial resolution due to mechanical constraints. The detector with scanning collimator also has low duty cycle and low sensitivity. The instrument is scanned in two perpendicular directions across the source and the position where the peak intensity is detected gives the position of the source. One of the ASMs which used a scanning collimator to scan the X-ray sky was the ASM on Ginga (Makino, 1987, Turner et al., 1989). A detector with rotation modulation collimator will have low temporal resolution and duty cycle(Mertz, 1968, Schnopper et al., 1980). In modulation collimator designs, the positional accuracy for a source is achieved at the cost of sensitivity (Fraser, 1989). Few of the ASMs which used a modulation collimator are ASMs on Ariel-5, SAS-3, Hakucho, Granat etc.

In recent years, another technique of optimum sky monitoring has been introduced which gives sufficient duty cycle, angular resolution, temporal resolution and sensitivity. This technique uses "Coded-mask-imaging", where the instrument constitutes of a coded-mask, a detector and an appropriate algorithm for reconstruction technique. Coded-mask imaging has become prevalent in the last two decades due to the availability of fast computing techniques for deconvolution. The details of coded-mask imaging are given in Zand (1992) and references therein. Section 3.1.3 in chapter 3 discusses the principles of coded-mask imaging. Scanning Sky Monitor (SSM) on ASTROSAT also employs coded-mask imaging technique to view the X-ray sky.

There are many sky monitors flown till date which have helped the discovery of various transient objects and a large number of X-ray binary systems. In particular, the first sky

survey was done by UHURU which produced a catalog of 339 X-ray sources (Forman et al., 1978). The first All sky survey was done by HEAO-1 (Wood et al., 1984) which listed a total of 842 sources. The second All sky survey was done by ROSAT which had a sensitivity of an order better than HEAO-1 and hence could detect sources which were 10^7 fainter than Sco X-1 (Charles & Seward, 1995). ROSAT, HEAO-1 etc. carried out all sky surveys with the pointed mode instruments (with narrow field of view) carried on-board. ROSAT produced a catalog of X-ray sources which contained 150,000 sources (Truemper, 1992). Amongst all the sky monitors flown till date, the Wide Field Camera (WFC) on BeppoSAX (Jager et al., 1997) and the All Sky Monitor (ASM) on RXTE (Levine et al., 1996) has provided unprecedented long-term view of the X-ray sky that opened up new discovery space in the study of these transients (Strohmayer & Bildsten, 2006). Table 1.1 gives the list of all sky monitors flown in different missions. It may be noted that most of the X-ray sky monitors are gas proportional counters as it is relatively easier to have large area detectors with wide FOV with these type of detectors, compared to other kinds of detectors. Another important aspect is that most of the missions flown into space for X-ray astronomy studies have either a sky monitor or an all sky survey instrument in them. The X-ray satellites Ariel-5, Ginga, RXTE, BeppoSAX, HETE-2 and Maxi carried sky monitors. It is required to have a sky monitor in a mission, as this instrument would act like the eye of the mission to look at the wide X-ray sky for any interesting phenomena occurring in the vast sky, while the other pointed mode instruments would be doing a detailed observations on a particular source.

Today, in addition to the ASM on RXTE, the Monitor of All sky X-ray Image (MAXI)(Matsuoka et al., 2009), which is a Japanese instrument is installed on the Japanese Experiment Module - Exposed Facility (JEM-EF) on the International Space Station (ISS) and is doing an all sky survey every 96 minutes. MAXI, launched in 2009, is a dedicated instrument for all sky survey in the energy band 0.5-30 keV. MAXI has two types of detectors, proportional counters for the energy range 2-30 keV and CCDs to observe in the energy range 0.5-12 keV. The whole sky is monitored every 96 minutes as the ISS makes one orbit around the earth.

1.9 Motivation and Objective of the present studies

ASTROSAT (Agrawal P.C., 2004) is India's first multi-wavelength mission dedicated for the studies of different classes of galactic and extragalactic sources like stars, neutron stars, black holes, galaxies etc. ASTROSAT will have five instruments on-board, spanning the visible, near ultra violet, far ultra violet, soft and hard (low and high energy) X-rays of

the electromagnetic spectrum. The instruments planned on-board are Ultra Violet Imaging Telescope (UVIT), Large Area Xenon-filled Proportional Counters (LAXPC), Soft X-ray Telescope (SXT), Cadmium Zinc Telluride Imager (CZTI) and Scanning Sky Monitor (SSM). Except SSM, all the other are pointed-mode instruments to do specific study of the celestial sources that are observed and have a relatively smaller field of view (FOV) ranging from about less than a degree to few degrees. A more detailed note of the mission can be found in the site "http://meghnad.iucaa.ernet.in/∼astrosat/". The pointed-mode instruments do one or more of spectral, timing and/or imaging of the source observed. The SSM, as the name suggests is an instrument to scan the sky for monitoring X-ray transients. The Scanning Sky Monitor(SSM) on ASTROSAT is a position-sensitive gas filled proportional counter with a wide field of view. It has a large FOV so that it monitors a large part of the sky at an instant and alerts the science community if an X-ray transient occurs. The angular resolution is ∼10 arcmin, which is achieved by having a coded-mask on the top of the detector. It not only gives an alert but also the location of the source undergoing the outburst with a temporal resolution of about 1 ms. The SSM scans the sky in few hours to detect and locate transient x-ray sources in the outburst phase, in the energy band of 2 to 10 keV. This information is broadcast to the scientific community so that a detailed study of the source may be pursued by other instruments in all possible wavebands by coordinated observations.

The work presented in this thesis is based on both instrumentation and archival X-ray data analysis. The instrumentation deals basically with the design and calibration of position-sensitive gas proportional counters for the X-ray sky monitor (SSM) on-board ASTROSAT. This part of the work includes a detailed study of the design parameters for the X-ray sky monitor and optimization of these parameters for the better performance of the instrument. An important aspect of the instrumentation is the calibration of the instrument, both on-ground and in-flight. Different techniques are devised to do the calibration study of the instrument. It includes the detailed calibration in both positional and spectral domain so as to achieve the science objectives of the mission. The data analysis and study part discusses the study of the transient sources using RXTE data, which includes a detailed study of both spectral and timing studies of the X-ray sources.

The first chapter gives an introduction to both X-ray sources and the instrumentation required to do a monitoring of such sources. Chapter 2 gives the details of the design optimization of certain parameters such as the cell size, gas mixture, the gas gain for Scanning Sky Monitor. Chapter 3 gives the complete picture of SSM and the experiments carried out with the implementation of the design parameters described in chapter 2. It also discusses the details of positional calibration of SSM. Chapter 4 gives the details of

the development of the instrument response and the procedure for on-board calibration of SSM. Chapter 5 discusses the X-ray data analysis of two black hole candidates. Chapter 6 summarizes the entire work along with a short discussion on a possible future sky monitor, based on the knowledge gained from the present work.

Chapter 2

Design optimisation of X-ray detectors for SSM

2.1 Introduction

Gas proportional counters were introduced in late 1940s (Knoll, 2000). The basic proportional counter development dates back to period of counter development by Rutherford and Geiger in 1908 and gas ionization studies by J.J. Thomson in 1899 (Fraser, 1989). Gas proportional counters are the improved version of ionization chambers, where the operating voltage of the detector is such that the amplitude of the output pulse is proportional to the energy of the incident photon. These detectors have been the 'workhorses' of X-ray astronomy (Fraser, 1989) in the initial years, when X-ray astronomy gained momentum after the first discovery of the X-ray source in 1961 (Giacconi & Gursky, 1974). V. Hess detected and discovered Cosmic rays using a gaseous detector (Pfeffermann (2008) and references therein). The physics of gas-filled proportional counters is discussed in detail by Curran and Craggs in 1949, Rossi and Staub in 1949 and Wilkinson in 1950 (Fraser, 1989). Multi-wire proportional counters were constructed and operated by Charpak and his collaborators in 1967-68 (Charpak et al., 1968, Sauli, 1977), for which Georges Charpak was awarded the nobel prize in Physics in 1992. Later came the new detectors based on the concept of gas detectors, like the gas scintillation proportional counter, the microstrip gas detector, micro pattern gas detectors, the gas electron multipliers etc. In the new era where semiconductor detectors are gaining momentum, gas-filled proportional counters still survive due to the fact that large area detectors are relatively easily possible only with these gas-filled counters. The detectors for Scanning Sky Monitors are gas-filled position sensitive

proportional counters. The characteristics and design optimisation of different parameters of these detectors are discussed in this chapter.

2.1.1 Basic principle of operation of gas proportional counters

A simple proportional counter has an anode at the centre surrounded by a cathode of large radius. The cathode forms a cylindrical sealed tube, inside which the gas is filled. The gas acts as the detection medium for the incident X-ray photons, which enter the detector through an entrance window. The cathode can be a thick Aluminium cylinder and there is an opening in the cylinder for the window which can be an aluminized Mylar sheet or a thin Beryllium foil of typical thickness 25 microns. The window is thin enough to allow the X-ray photon to enter inside the detector chamber and thick enough not to allow the gas to leak outside the detector chamber. Figure 2.1 shows the picture of a cylindrical proportional counter with the anode at the centre and the cathode surrounding it forming the detector chamber, which will be filled with detection gas. The anode is given a very high voltage of the order of kiloVolts and the cathode is at zero potential with respect to the anode.

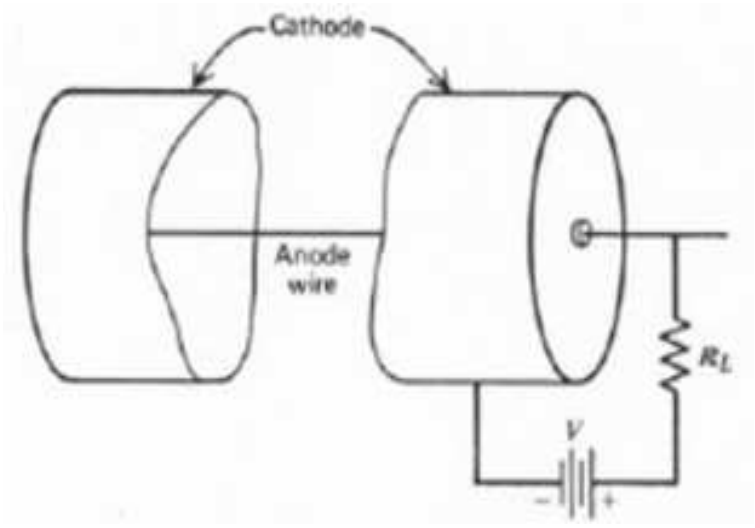

FIGURE 2.1: A simple proportional counter

When an X-ray photon enters the detector chamber, it interacts with gas atoms by the process of photoelectric absorption and produces a photoelectron, followed by the emission of a fluorescent photon or an Auger electron. The energetic photoelectron and the Auger electron interact further with other atoms of the gas and produces a number of primary

electron-ion pairs These primary electrons drift towards the anode which is at a positive potential. As these electrons drift towards the anode, they interact with other atoms in the gas and produce secondary electron-ion pairs, which result in further collisions giving rise to an avalanche effect which is called gas multiplication. The factor of amplification of the intial number of primary electrons to produce the final charge cloud is called the gas multiplication factor. The electrons produced as a result of gas multiplication are collected at the anode and the ions produced during the avalanche drift towards the cathode resulting in induced charge at the anode. In gas-filled proportional counters, the amplitude of output pulse for an incident photon depends on the gas multiplication factor which amplifies the primary charge to produce a signal above the noise level (Knoll, 2000). The amplitude of the output pulse gives a measure of energy of the incident photon. When the fluorescent photon escapes completely out of the gas volume, a significant fraction of the energy of the incident photon is lost which results in an output pulse of lower amplitude. Such pulses show up as an escape peak in the pulse-height spectrum (pulse-height spectrum is a plot of number of pulses of different amplitudes as a function of amplitude).

Position-sensitive proportional counters are those which have a resistive anode, which has a sufficient resistance per unit length, of the order of few kiloOhms per mm. The total charge collected for an incident photon gets divided according to the resistance it sees on either side of the wire. The charge is readout on either side of the anode as output. The ratio of the amplitude of the output pulses on either side of the anode gives the measure of the position of the photon along the anode wire and the sum of the amplitudes gives the energy of the photon.

2.1.2 Detection Efficiency

Detection efficiency of a detector is defined by the fraction of photons detected by it to the number of photons incident on the detector. Detection efficiency depends on various factors like interaction cross section of the photon in the detection medium, geometric area of detector, type of radiation incident and energy of the incident particle/photon. Detection efficiency depends on the probability of transmission of photons through the window and the probability of absorption of photons in the active volume of the gas detector. The detection efficiency is calculated as follows. The probability of transmission of photons through a material of thickness t is given by $\mathrm{N}/N_0 = \mathrm{e}^{-\mu_w t}$ where μ_w is the linear attenuation coefficient of the window material with the units of cm^{-1}, N is the transmitted number of photons and N_0 is the incident number of photons (Knoll, 2000, Tsoulfanidis, 1995). The probability of absorption of photons in a volume of gas is given by (1-probability of

transmission of the photons), ie. 1-e$^{-\mu_g x}$ where x is the depth of the volume of gas and μ_g is the linear attenuation coefficient of the gas. The linear attenuation coefficient (μ) is given as the sum of attenuation coefficient due to photo-electric effect, Compton scattering and pair production for any material at a particular energy. In general, the process of detection in proportional counters is by photoelectric absorption. The photoelectric absorption cross section varies approximately as $Z^5/E_\gamma^{3.5}$, where Z is the atomic number of the absorber atom and E_γ is the energy of the incident photon.

Hence, the probability of detection of photons in the volume of gas of depth 'x' after passing through the window of thickness 't' is given by the product of probability of transmission through the window and the probability of absorption of photons in the volume of gas. Therefore, the detection probability is given as

$$D[E] = N/N_0 = e^{-\mu_w t} * 1 - e^{-\mu_g x} \tag{2.1}$$

where μ_w is the linear attenuation coefficient of the window and μ_g is that of the gas. The detection efficiency can also be given in terms of effective area of detector at different energies. The effective area is expressed as
Effective area = Geometrical area of the detector * Detection Efficiency

The required photon detection efficiency in the energy range of interest determines the choice of gas, its pressure and the active region thickness. The maximum angle of incidence of x-rays and the active region thickness determine the parallax error (error in the position of the incident photon for oblique incidences). It is required that the detection efficiency of the SSM detectors be $\geq$20% in the energy band of interest. Factors determining the efficiency of the gas proportional counter are the gas mixture, gas pressure, window material and the thickness of the window and the depth of the detection medium.

2.1.3 Gas Gain

The gas multiplication factor discussed in section 2.1.1 is also called the gas gain of the detector. The gas gain depends on various factors like the operating voltage, the anode radius, cathode radius (which is the cell size), gas pressure and gas mixture. By tuning the above said factors, optimum gas gain can be chosen for a detector. Proportional counters are usually operated at high gas gains relative to other type of radiation detectors and they are second to the Gieger Muller counters (invented in 1928 by Geiger and Muller (Knoll, 2000), before the proportional counters) which operate at the highest gas gain. In position sensitive proportional counters, the position sensing is done along the length of the resistive

anode wires. The nominal gas gain at which the proportional counters are operated is about 10^4 to 10^5. For gas gains beyond 10^6, the counter is supposed to operate in the Geiger Muller region where the proportionality is lost. For gas gains beyond 10^8, discharges can take place (Sauli, 1977). Therefore, we prefer to have a gas gain of about few times 10^4. Gas gain calculations for SSM detectors using simulations are discussed in section 2.4.2. The gas gain should not be too high, ie. $\geq 10^6$ as this could lead to discharge effects when a large amount of charge is deposited in the detector. Many operating specifications like the energy resolution, position resolution, life-time of the detector etc. are dependent on the gas gain of the detector. It is necessary to choose an optimum value for the gas gain to have a better performance of the detector.

2.2 Description of SSM instrument

Scanning Sky Monitor (SSM) constitutes of three almost-identical one-dimensional position sensitive proportional counters. All three detectors are mounted on a single platform, which can be rotated to scan the sky. SSM scans the sky every few hours to detect and locate X-ray transient sources (which are discussed in detail in Chapter 1). The position-sensitive proportional counters for Scanning Sky Monitor(SSM) are multi-celled and multi-layered. The top layer consists of position-sensitive anode wires surrounded by wire-walled cathodes forming individual cells. The bottom layer consists of conductive wires and this layer along with the side cells in the top layer forms the veto layer, which is used for charge particle background rejection. Figure 2.4 gives the schematic of wire-module in SSM.

2.3 Design optimisation

The characteristics of x-ray proportional counters such as detection efficiency, gas gain, energy resolution, position resolution, timing resolution, sensitivity etc. can be optimised by optimising the parameters like cell size, anode radius, gas mixture, gas pressure, detector operating voltage, window material, window thickness etc. Optimisation of these parameters for SSM are discussed in the following sections.

2.4 Cell design

It is preferred to have a cell of cylindrical geometry as shown in figure 2.2, so that the electric field in the cell will have a radial dependence. The gas multiplication takes place very close to the anode and hence will be independent of position of absorption of photon. SSM cell consists of an anode at the centre surrounded by a square-shaped wire-walled cathode on three sides and a window on the top at zero potential, which is an approximation to a cell of cylindrical geometry. SSM cells are square-shaped so that many number of cells can be accommodated adjacent to each other for a large detection area, without any loss of space, which is not the case if the cells are of cylindrical geometry. The surface field on the anode controls the gas gain of the signal and the drift field controls the velocity and direction of the electron drift. The use of the wire-walled cathode between the anodes, make each cell independent of the other and reduces the chances of signal sharing by two anodes for a single photon incidence.

In designing the cell configuration and the operating voltage, one has to meet various requirements:

1. Uniformity of the electric field in the cell about the anode
2. Sufficient gas gain has to be achieved within the proportionality region of operation
3. Minimum parallax error for incidence of a photon at an oblique angle

It is required that the cell be thick enough so as to have a better detection efficiency and small enough to have a sufficient gas gain and minimum parallax error (discussed in section 2.4.3) in determining the position of the incident photon. The lower limit for the cell depth is given by the requirement of detection efficiency as well as mechanical constraints in making the wire module. The upper limit is given by the required gas gain and a tolerable limit on the parallax error.

2.4.1 Cell Size for SSM

The choice of cell size is defined with respect to the required gas gain. The gas gain for the detector is preferred to be few times 10^4. Gas gain of a cell depends on the electric field at positions very close to the anode and can be calculated if the field is known. Electric field inside an SSM cell is simulated using GARFIELD (Veenhoff, 1984), which is a software to simulate gas chambers. Electric fields are derived using GARFIELD simulations for different cell sizes and the gas gains are calculated as described in the following section.

2.4.2 Calculation of the gas gain using the derived electric field values from GARFIELD simulations:

Gas multiplication requires large values of electric field. For a cylindrical geometry, the electric field at a distance **r** from the anode is given by

$$E(r) = \frac{V}{r \ln (b/a)} \tag{2.2}$$

where

V is the voltage difference between the anode and the cathode

a is the anode radius

b is the cathode radius and

r is the distance from the surface of the anode.

As discussed in section 2.4, SSM cell is an approximation to cylindrical geometry. Using GARFIELD we can derive the value of electric field at a point within a cell. For example, for a cylindrical cell with an anode of diameter 25 microns and a cathode of diameter 1.2 cm, the electric field at a distance of 3 times the anode radius from the center is derived to be 64790 V/cm. Theoretical calculation of the value of E for this cell geometry using the equation 2.2 gives the same value and hence the simulations are found to match with the calculated result.

The layout of cylindrical cell simulated using GARFIELD is shown on the left in figure 2.2 and the electric field inside the cell is shown on the right in the same figure. The electric field in the region about 20 times the anode radius around the anode is shown in figure 2.3.

SSM cells are square shaped with wire-walled cathode around the anode at the centre of the cell. The left panel of figure 2.4 shows the schematic picture of SSM wire module which has all the 20 cells with wire-walled cathode and anodes at the centre of each cell. The right panel of figure 2.4 shows the electric field contours inside the SSM cell simulated using GARFIELD to study the electric field inside the cell. Electric field value inside the cell at a distance of three times the anode radius from the centre of the cell is found to be 62596 V/cm.

Diethorn formula for calculating the gas multiplication factor is given by

$$\ln M = \frac{V}{\ln (b/a)} \frac{\ln 2}{\Delta V} (\ln \frac{V}{p\, a \ln (b/a)} - \ln K) \tag{2.3}$$

where

M is the gas gain

V is the applied voltage

a is the anode radius

b is the cathode radius

p is the pressure of the gas in atmospheres

ΔV is the potential difference through which an electron moves between successive ionizing events

and

K is the minimum value of **E/p** below which multiplication cannot occur.

Both ΔV and **K** are constants for any given fill gas.

Now, for a cylindrical geometry, equation 2.3 can be written by substituting equation 2.2 in it as,

$$\ln M = E\, r\, \frac{\ln 2}{\Delta V}\, (\ln \frac{E\, r}{p\, a} - \ln K) \tag{2.4}$$

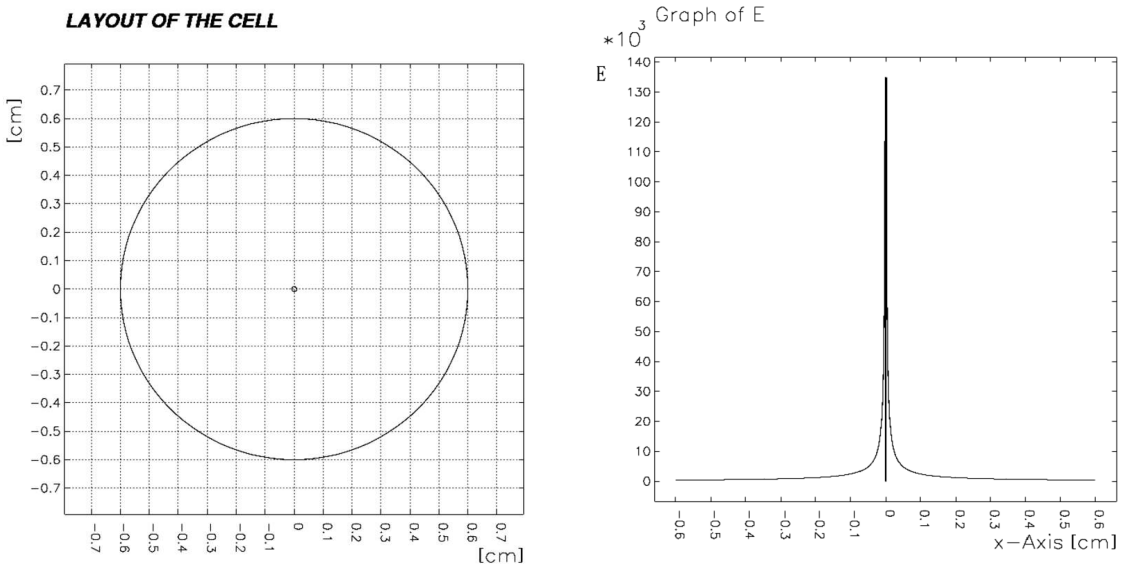

FIGURE 2.2: Cylindrical cell simulated using GARFIELD is shown on the left and the electric field inside the cell is shown on the right

Thus by knowing the value of E at any **r** within the multiplication region, we can calculate the gas gain using the formula given by equation 2.4. Not only for a cylindrical geometry, but for any other geometry of the cell in which the multiplication region can be approximated to that of a cylindrical geometry, the above formula can be used to calculate the gas gain for the applied voltage. It is also to be noted that the value of 'E' times 'r' (Er) is constant

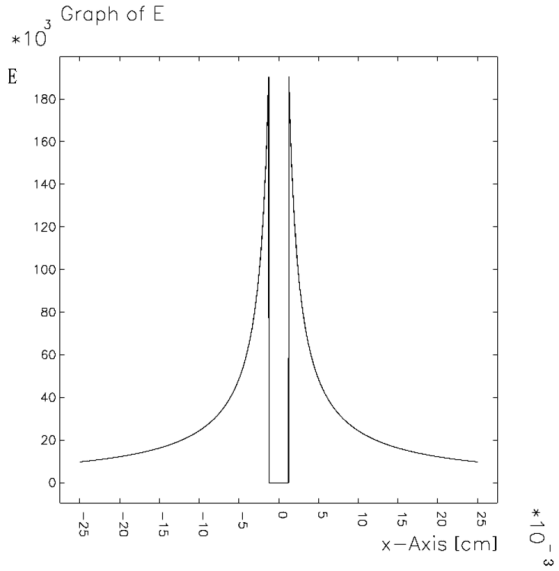

FIGURE 2.3: Electric field around the anode at regions about 20 times the anode radius

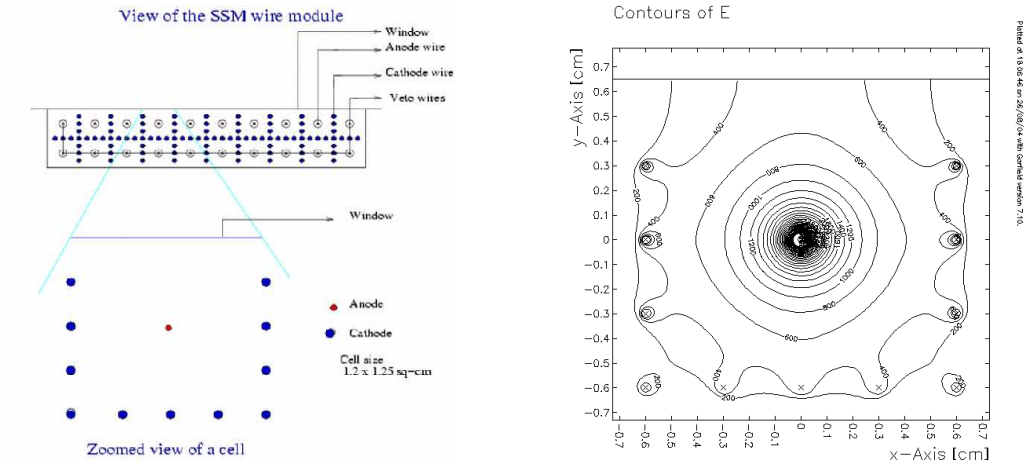

FIGURE 2.4: The arrangement of the cells in the SSM detector is shown at the top-left and a blown-up view of one of the cells is shown at the bottom-left and an SSM cell simulated using GARFIELD with the contours of the electric field is shown at the right.

within the gas multiplication region which is the region few times the anode radius from the surface of the anode. Figure 2.5 shows Er as a function of r.

The gas gain of a cell depends very much on its size which is the cathode diameter of the cell. Smaller the cell size better is the gas gain at the cost of detection efficiency at the high energy end. Figure 2.6 shows the dependence of gasgain on cell size for a square shaped cell. SSM cells are of size 1.2 x 1.2 sq-cm, which give sufficient gas gain with anode of diameter 25 microns at 1500 V. Figure 2.4 shows the ssm-cell with wire-walled cathode. Here, it can be seen that the SSM cell-size is given as 1.2×1.25 cm^2, as the window on the top of each cell is placed 0.05cm above the 1.2 cm depth of the cell. The gas gain very close to the anode is not affected by the 0.05 cm space which is away from the anode. Hence the SSM cells are of size 1.2×1.25 cm^2.

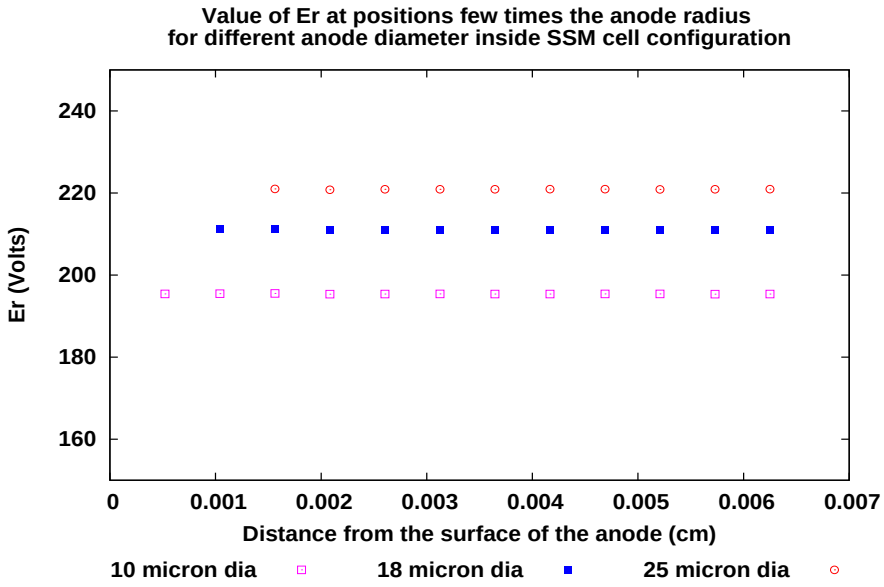

FIGURE 2.5: 'Er' as a function of 'r'.

The depth of each position-sensitive cell is 1.25 cm with a window at the top and wire-walled cathodes on the other three sides with the anode wire at the centre. The gas gain for SSM cell with an anode of diameter 25 microns at an operating voltage of 1500 volts is 8675 with respect to P-10 gas and 13690 with respect to the gas mixture of 20% Xe + 80% P-10 at a gas pressure of 1 atm. This is calculated using Diethorn formula as given by equation 2.4.

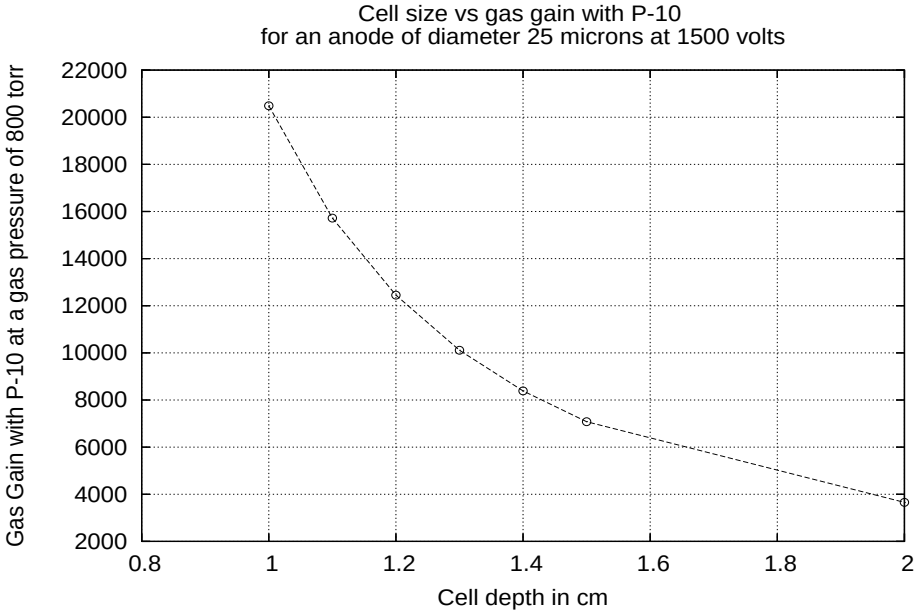

FIGURE 2.6: Gas gain vs Cell size

2.4.3 Parallax error

The error caused in determining the position of an incident photon at incidence angles other than normal incidence with respect to the window of the cell is called 'parallax error'. Every incident photon of a particular energy has a mean free path, the distance at which it gets absorbed in the detector volume. Let 'l' be the mean free path of a photon of energy E. Now, for a normal incidence, the photon is absorbed at a depth of 'l' inside the cell. For an oblique incidence, at an incidence angle θ, with respect to the normal to the detector plane, the photon traverses a distance 'l' inside the cell, but the depth from the window inside the cell at which it gets absorbed is given by r = l $\times$ cos θ. Figure 2.7 explains this better. The parallax error is given by Δx = tan θ $\times$ Δy, where θ is the incidence angle, Δy=(d - (l $\times$ cos θ)) and d is half the cell-depth, which is 0.6 cm for SSM. Therefore, Δx = tan θ $\times$ (0.6 - (l $\times$ cos θ)). The FOV of the SSM detector is $\sim 22^\circ \times 100^\circ$ at FWZM and is $\sim 11^\circ \times 90^\circ$ at FWHM. Considering the θ to be 0 for normal incidence, the maximum angle of incidence of a photon at high inclinations is $\pm 11^\circ$ at FWZM and it is $\pm 5^\circ$ at FWHM.

Considering the FOV at FWHM, the maximum incidence angle with respect to the normal to the window is $\pm 5^\circ$. For an incidence angle of $\pm 5^\circ$ and for a high energy photon which gets detected at the maximum possible depth of 1.2 cm inside SSM cell, the parallax error turns out to be 0.52 mm, which is lesser than the expected position resolution at that high energy $\sim$ 10 keV. This parallax error in determining the position of the detected photon will be included in the error estimation for the position of the incident photon. However, the

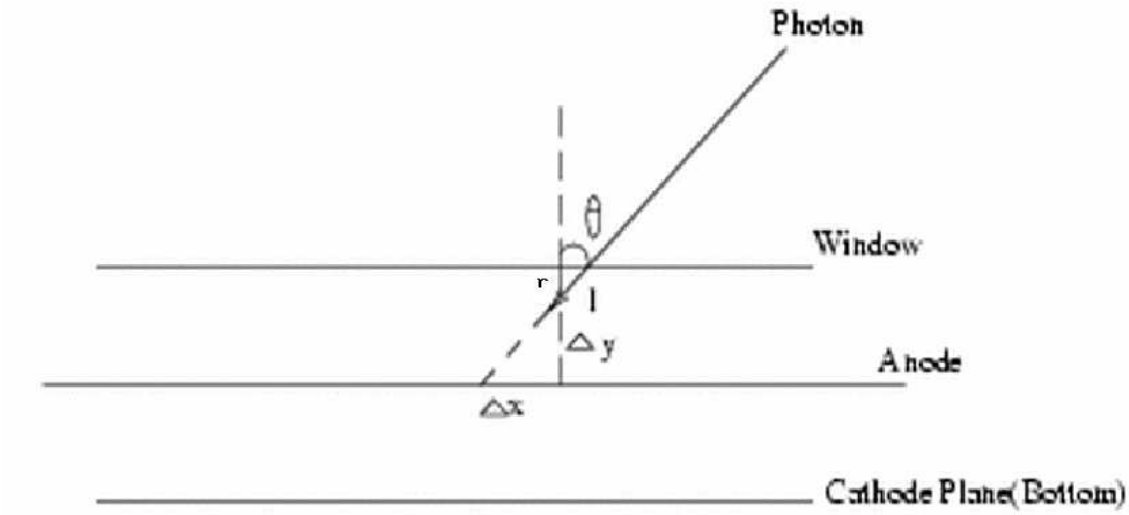

FIGURE 2.7: The figure shows the incidence of a photon in a cell at an angle θ.

probability of detecting a photon with such high parallax is less as the detection efficiency at higher energies in the energy range of interest is only ∼20%.

2.5 Gas Mixture

Gas mixture is one of the prime components of a proportional counter which determines detection efficiency, sensitivity of the detector, gas gain, energy resolution, life time etc. A gas mixture which gives a high gain operation with good proportionality at low operating voltage along with good detection efficiency is preferred.

2.5.1 Detection Efficiency

It is required that SSM has high detection efficiency in the energy range of interest, which is 2 to 10 keV. Detection efficiency not only depends on the cell depth, but also on the gas mixture used, pressure of the gas mixture, window material, thickness of the window and the effective area for photon detection. The choice of gas mixture for SSM in the perspective

of detection efficiency would be Xenon + a quench gas, as Xenon has a relatively higher atomic number amongst the inert gases used for proportional counters. The disadvantage in using Xenon as the detector gas is its susceptibility to contamination (Ramsey & Agrawal, 1988). Also, to use Xenon as the detector gas, the operating voltage has to be higher to have a sufficient gas gain. P-10, which is a mixture of 90%Ar + 10%CH_4, is a commonly used detection gas in proportional counters. However, the detection efficiency of P-10 is much lower than Xe gas mixtures, as can be seen in figure 2.8. Therefore, to have a reasonable detection efficiency at the high energy end (i.e. at 10 keV) and a sufficient gas gain at a lower operating voltage, a gas mixture of Argon and Xenon is chosen. The percentage of Xenon to be used is determined as per the requirement that the detection efficiency be atleast $\geq 20\%$ at the extreme ends of the energy range of interest. It is found that the gas mixture of 25%Xe + 75%P-10 satisfies this requirement (Ramadevi et al., 2006). Figure 2.8 shows the comparison of detection efficiencies for different gas mixtures with different proportions of Xe and Ar.

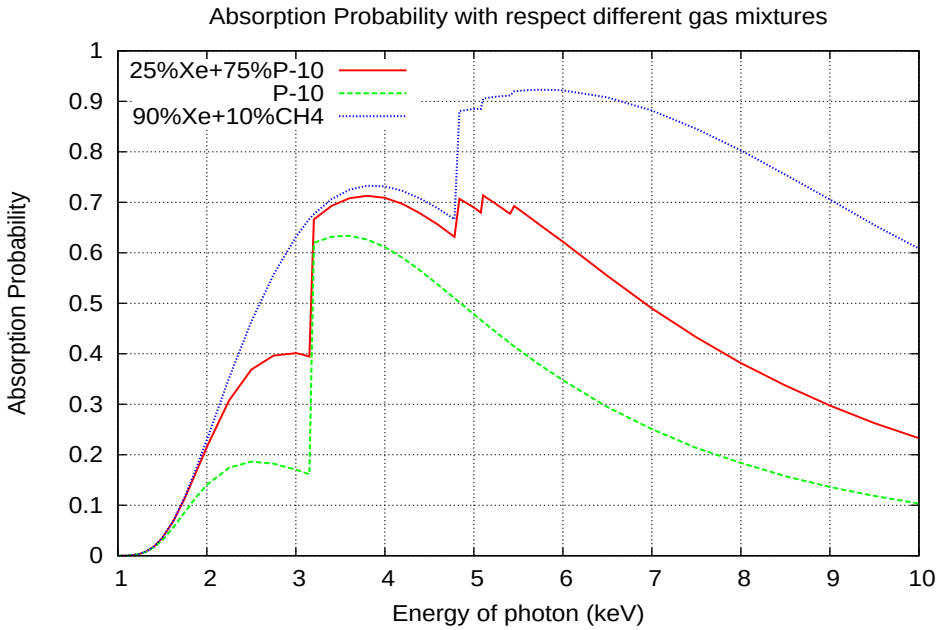

FIGURE 2.8: Absorption Probability for 90% Argon+10% CH4, 90% Xe+10% CH4 and 25%Xe + 75%P-10 for an active cell depth of 12 mm, including the window transmission for an aluminized Mylar window of thickness 25 microns

It can be seen in figure 2.8 that the detection efficiency with respect to the gas mixture of 25% Xe + 75% P-10 at 6 keV is about two times greater than that of P-10 (90% Ar + 10% CH4).

2.5.2 Gas Gain

It had been shown in earlier literature that the gas gain increases with the addition of Xenon with Argon up to about 10% concentration of Xenon and then decreases (Fuzesy, 1972). For a Xenon concentration of about 27%, the gas gain equals to that of a 0% Xenon concentration and with a further increase in Xenon, the gas gain further decreases (Fuzesy, 1972). It is required to have both better detection efficiency and better gas gain. Higher the Xenon concentration better is the detection efficiency. A higher Xenon concentration, just less than 27% gives better gas gain compared to P-10 gas, which has 0% Xe concentration.

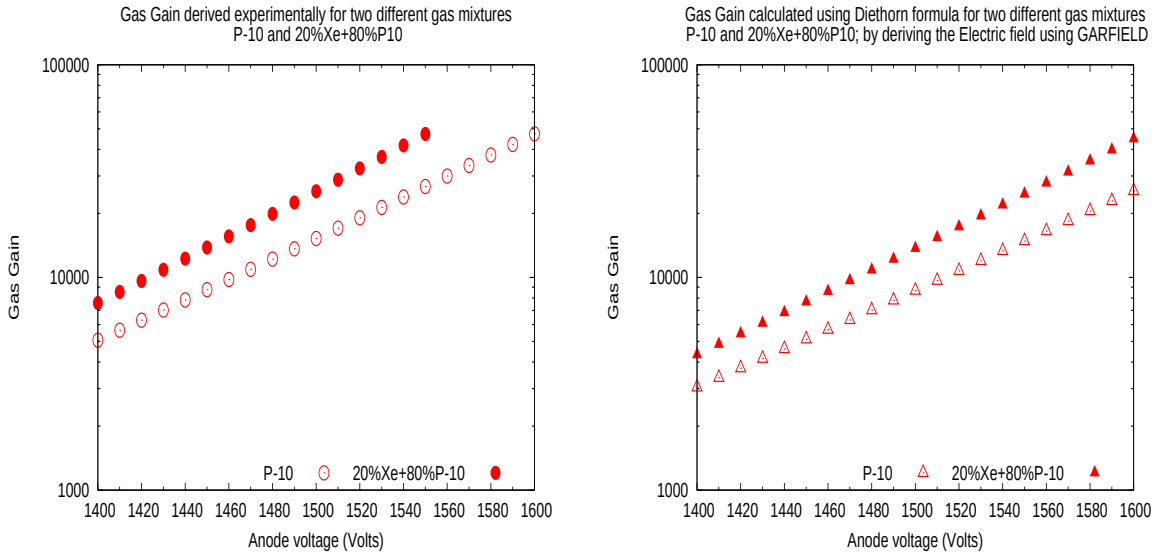

FIGURE 2.9: Comparison of gas gains for two different gas mixtures, experimentally (shown on the left) and theoretically (shown on the right)

SSM detector was tested with three different gas mixtures: P-10 (with 0% Xe concentration, a gas mixture of 20% Xe + 80% P-10 and a gas mixture of 25% Xe + 75% P-10. It was experimentally found that the gas mixture 25%Xe + 75%P-10 gives a higher gain than P-10, which agrees with relative gas gains quoted in Fuzesy (1972). Therefore, a gas mixture of 25%Xe + 75%P-10 is chosen as the detector gas, which gives a better detection efficiency and greater gas gain than that with respect to P-10 for a particular operating voltage (Ramadevi et al., 2006). The gas gain for SSM cell with an anode of diameter 25 microns at an operating voltage of 1500 volts is 8675 for P-10 gas and 13690 for the gas mixture of 20% Xe + 80% P-10 at a gas pressure of 1 atm. The gas gain for the gas mixture 25%Xe + 75%P-10 is very close to that of 20% Xe + 80% P-10 for the same gas pressure and operating

voltage. Theoretical calculations are carried out using Diethorn formula (for the two gas mixtures for which the Diethorn parameters are available) with the values of electric field in the cell derived using GARFIELD. Figure 2.9 shows the comparison of the gas gains of the two different gas mixtures both experimentally and theoretically. It can be seen that the ratio between the gas gains calculated theoretically is found to be consistent with that derived experimentally. The difference found in the absolute values of the gas gains derived theoretically and experimentally for the two gas mixtures could be due to the differences in the assumed HV value for gas gain calculations and the actual HV value fed to the anodes in the experiments.

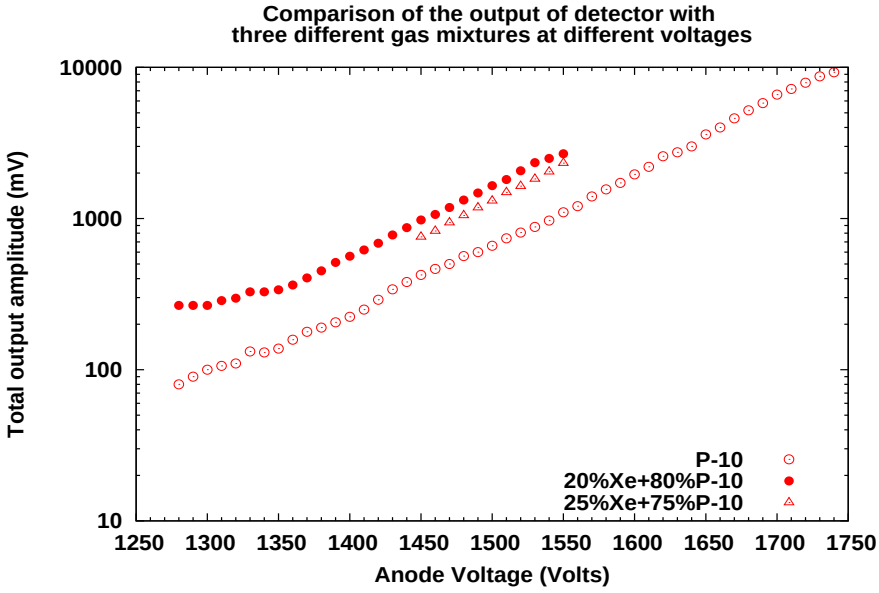

FIGURE 2.10: Comparison of the total output of the detector for three different gas mixtures at 1500 Volts operating voltage

Experimental Verification:

SSM detector was tested with three different gas mixtures, P-10, a gas mixture of 20% Xe + 80% P-10 and a gas mixture of 25% Xe + 75% P-10. Figure 2.10 shows the experimental results showing the comparison of the output of a detector for the three different gas mixtures. The gas gains are calculated from the experimental results. The ratio of the gas gains of the gas mixture of 20%Xe + 80%P-10 to that of P-10, from the theoretical and experimental measures are 1.76 and 1.93 $\pm$ 0.08 respectively, for an anode of diameter 25 microns. Similarly, with respect to an anode of diameter 10 microns, the ratio of the gas gains from theoretical and experimental measures are 2.47 and 2.84 $\pm$ 0.09 respectively.

Gas mixture	Anode diameter	Ratio of Gas Gain with respect to P-10	
		Theoretical	Experimental
20%Xe + 80%P-10	25 micron	1.76	1.93 ± 0.08
20%Xe + 80%P-10	10 micron	2.47	2.84 ± 0.09
25%Xe + 75%P-10	25 micron	-	1.46
25%Xe + 75%P-10	10 micron	-	2.30

TABLE 2.1: Table gives the ratio of the gas gain of two different gas mixtures with respect to P-10 for two anode wires of different diameters

The gas gain of gas mixture of 25%Xe + 75%P-10 is greater by about 1.46 times than that of pure P-10 for a particular operating voltage, for an anode of diameter 25 microns and is about 2.3 times for an anode of diameter 10 microns. Table 2.1 gives the ratio of gas gains of the two gas mixtures 20% Xe + 80% P-10 and 25% Xe + 75% P-10, with respect to that of P-10. The theoretical values for the gas gain of 25% Xe + 75% P-10 is not calculated in table 2.1, as the Diethorn gas constants for this gas mixture is not available.

2.5.3 Energy Resolution:

One of the prime factors which determines the energy resolution is the gas mixture and the quench gas added to it. It is the ionization potential of the quench gas which plays the role. This ionization potential of the quench gas has to be just equal or less than the energy of the metastable state of the primary gas (the noble gas, Ar or Xe) in the detector, so that it collisionally de-excites the primary gas atoms by dissociating itself, thereby preventing the emission of unwanted UV photons, to ensure better energy resolution. It has been experimentally proved that methane serves to be a better quench gas with Xenon rather than with Argon in perspective of better energy resolution (Ramsey & Agrawal, 1988).

Experimental Verification:

It is experimentally found that the energy resolution with respect to the gas mixture 25% Xe + 75% P-10 is about 17-18% at 5.9 keV, which is better than that with respect to P-10 which is about 19-20% at the same energy. It is to be noted that here it is a mixture of Ar and Xe with methane which is compared to that of pure P-10. It is the addition of 25% Xe to P-10 which has enhanced the energy resolution by about 1-2% at 5.9 keV.

2.6 Gas Pressure

The detection efficiency can be improved by increasing the pressure of the gas. Higher the pressure, greater is the detection efficiency. This is because the linear attenuation coefficient which is equal to the photoelectric cross section of a photon is directly proportional to the number density which is in turn proportional to the pressure of the gas. Figure 2.11 shows the detection efficiency of SSM for two different gas pressures. The upper limit for the pressure is given by the tolerance of the window to higher pressures. The bulging of the window increases with the pressure inside the chamber. The gas pressure for SSM detectors is 800 torr, for which the bulge in the window is ∼1 mm. GARFIELD simulations show that the electric field is not disturbed in the multiplication region for a window-bulge of 1mm. Improving the detection efficiency by increasing the pressure of the gas in the detector would be at the cost of the gas gain. Higher the gas pressure, lower is the gas gain. Figure 2.12 shows the gas gain for three different gas mixtures as a function of pressure. The gas gains at different gas pressures for different gas mixtures, shown in figure 2.12 are calculated using the electric field value estimated using GARFIELD for SSM cell.

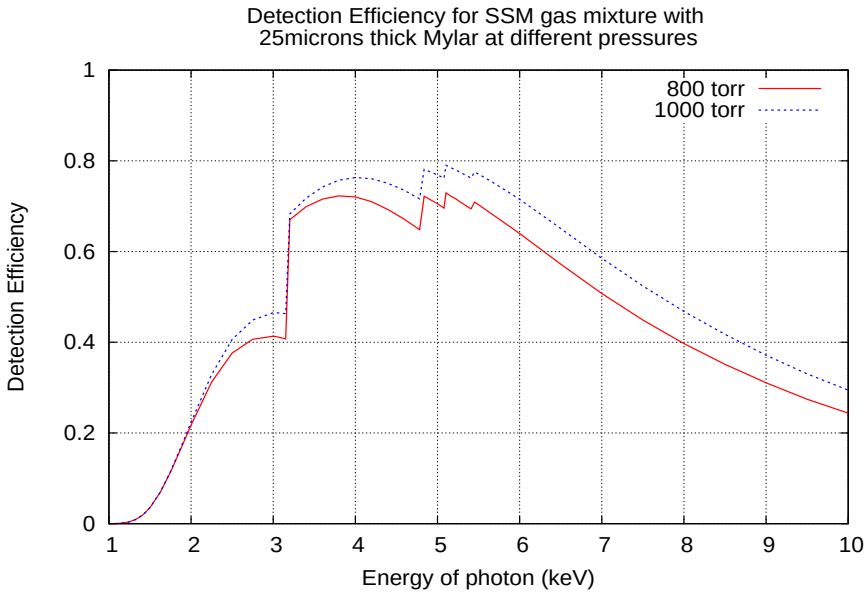

FIGURE 2.11: Detection efficiency (theoretical) for 25%Xe + 75%P-10 at two different pressures, 800 torr and 1000 torr, for SSM cell

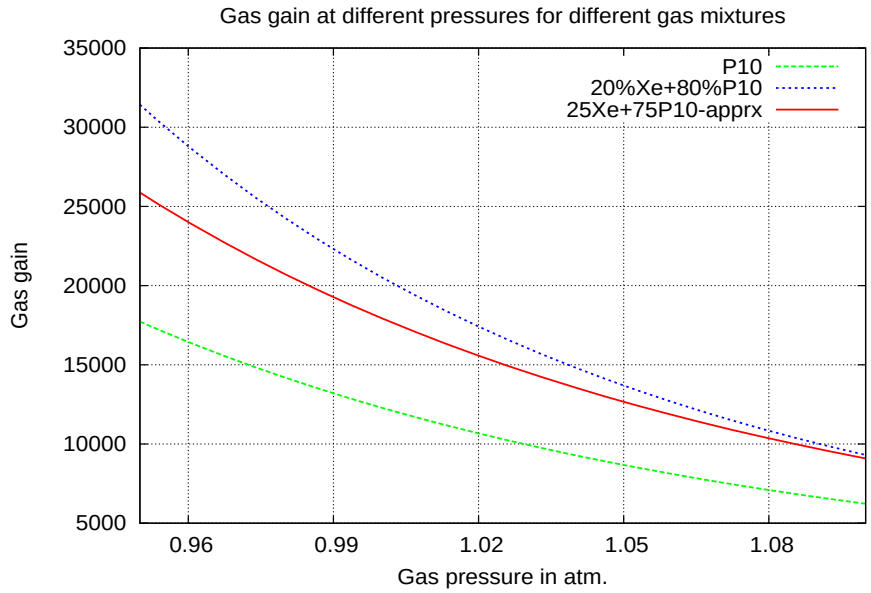

FIGURE 2.12: Gas gain as a function of pressure

At higher pressures, the position resolution is better (Fraser, 1989, Hamburg, 2001).However, the bulge in the window increases at higher pressures, which is not preferred. It is also taken into consideration that the gas pressure is not less than the atmospheric pressure, so that the window of the detector does not bulge inwards and break the wires inside it. So, the SSM detectors are filled at 800 torr pressure which is slightly higher than the atmospheric pressure.

2.7 Anode Wire

Anode wire is one of the important components of the detector. It is required that the anode be a resistive wire, for position sensing by charge division method. Gas gain of the detector depends on the diameter of the anode wire. The parameters of the anode wire like the diameter, the material, resistance per unit length, operating voltage supplied to it etc. determines the characteristics of the detector like gas gain, position resolution etc.

2.7.1 Choice of anode wire

Diameter of the anode wire is required to be of the order of few microns to give very high electric field values for a nominal operating voltage of about 1500 V (Knoll, 2000). The electric field within the cell is related to the anode radius as in equation 2.2. This implies

that smaller the diameter, higher is the gas gain of the detector. Figure 2.13 shows the gas gain as a function of anode radius with respect to P-10 gas at a pressure of 800 torr, calculated using Diethorn formula as given by equation 2.4.

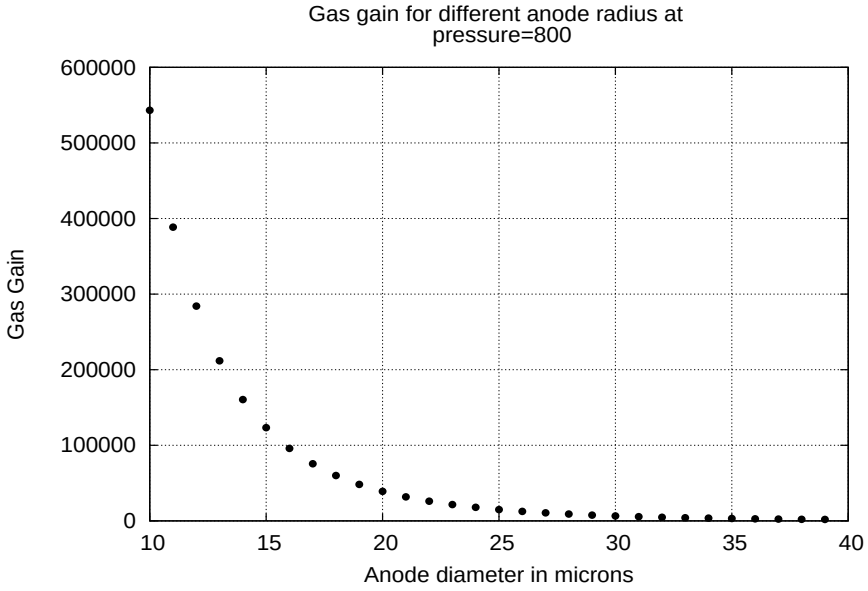

FIGURE 2.13: Gas gain as a function of anode radius

Anode wire of relatively greater diameter is preferred in view of aging effects. For example, for a particular gas gain of about 50000, the aging rate would likely be 20% less for an anode of diameter 25 microns compared to that of a 20 microns anode, as the current remains the same while the wire surface area is increased by 25% (Fischer et al., 1986). For a position-sensitive proportional counter it is necessary that the anode wire is resistive. The resistance per unit length of the wire should be sufficient enough of the order of kiloOhms, to give a good position resolution. As a choice of resistive anode wires, carbon-coated quartz wires, graphite wires are available. The graphite wires are preferred to carbon-coated quartz wires as the carbon-coating on the quartz can be eroded off at very high count rates and also the effect of polymerization can cause polymer chains get deposited on the carbon-coating. However, the graphite wires are available only with lesser resistance per unit length as compared to carbon-coated quartz wires. The resistance per unit length of graphite wires are of the order of 100 Ohm per mm as compared to kiloOhm per mm in carbon-coated quartz wires. Better position resolution is obtained when the total resistance of the wire is of hundreds of kiloOhms. Therefore, Carbon-coated-quartz wires of diameter 25 microns

are used as anode wires in SSM detectors as graphite wires of appropriate resistance and diameter are not available.

2.7.2 Aging of the wire

Free-radical polymerization is considered the dominating mechanism in wire chamber aging (Hamburg, 2001). During gas avalanches many molecules break up in collisions with electrons, de-excitation of atoms, and UV-absorption processes. While most ionization processes require electron energies greater than 10 eV, the breaking of covalent molecular bonds and formation of free radicals require only 3-4 eV, and can lead to a higher concentration of free-radicals than that of ions in the gaseous discharges (Hamburg, 2001). Since free radicals are chemically very active they will either recombine to form the original molecules or other volatile species, or may start to form new cross-linked molecular structures of increasing molecular weight. When this polymerization chain becomes large enough for condensation to occur, it will bond itself to the electrode surface. This results in increase in the diameter of the anode and hence the gas gain decreases when an incident photon gets detected at those positions where the polymerization has occurred.

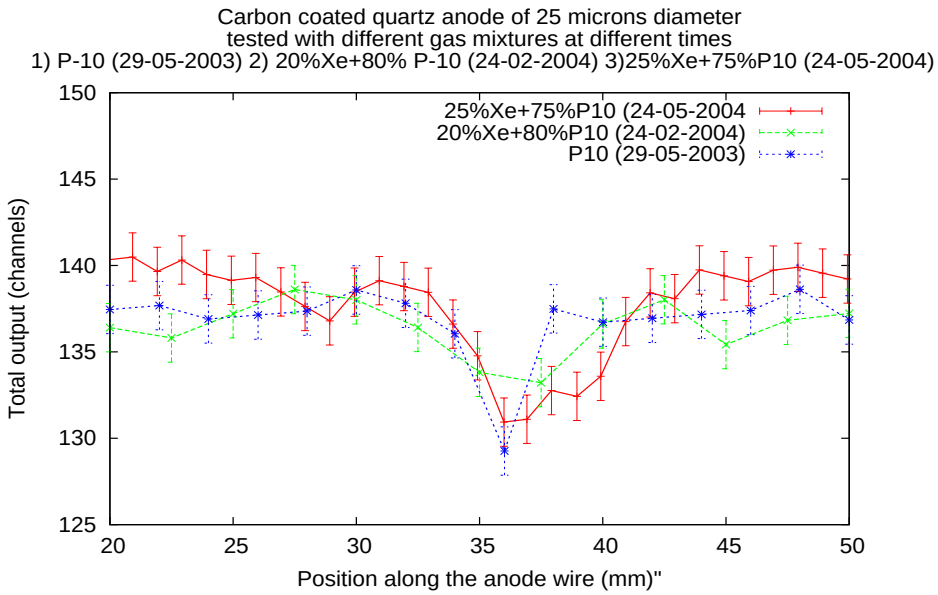

FIGURE 2.14: Aging effect seen in one of the anodes due to long term irradiation with collimated radioactive source ^{55}Fe at about the centre of the wire. Here the total outputs with respect to different gas mixtures are scaled to the same level to compare the degradation effect and the central region of the anode wire.

Experimental result

A carbon-coated quartz wire of diameter 25 microns and 8 kΩ resistance per mm showed aging effect over long term irradiation tests on it. The anode which showed a decrease in the output for collimated ^{55}Fe source placed at a particular position on it, was found to give a further degraded output with time. The dip in the total output curve, at about the central part of the anode, at a particular position was found to widen with time. This aging of the anode wire depends on the total charge collected on the anode due to irradiation. Tests were done with three different gas mixtures at different epochs. Figure 2.14 shows the decrease in the total output at about the centre of the anode due to aging effects caused due to long term irradiation of the wire with collimated radioactive isotope ^{55}Fe. The decrease in the output could be due to deposition of polymer chains on the anode. The aging effect observed could be a combined effect of aging of gas and carbon-coated resistive anode wire in the detector. An estimate of total charge collected at the anode at the central position, where the aging is observed, over a period of 14 months for an integration time of 10 minutes each day with ^{55}Fe (5.9 keV) source is found to be about 10^{-5} C. As the surface quality of the wire also has an influence on aging (Blinov, 2001), it is required that the anode wires be visually inspected before being wired. However, once SSM detectors are flown on-board a satellite, the aging of the anodes can only be indirectly known from gain of the detectors. Calibration of the detectors are done by observing a standard source such as the Crab nebula and any deviations in the estimated position of the source from the expected, due to aging or any other cause, is corrected using the updated calibration factor.

2.7.3 Operating voltage vs gas gain

Gas gain of the detector depends very much on the operating voltage. Figure 2.15 shows the dependence of gas gain on the operating voltage of the detector. The detector performance depends on the operating voltage applied to the anode. The operating voltage of the detector should be chosen such that the detector is operated in the proportionality region (Knoll, 2000). The operation of proportional counters at high charge levels results in both a decrease in the detector lifetime because of the formation of polymerization deposits on the anode wire and an increased susceptibility to space charge effects at high count rates. The energy resolution degrades at very high gas gains (Ramsey & Agrawal, 1988). The position resolution capability can also be degraded at high charge levels greater than 1 pC, particularly when the operating gas pressure is increased Charpak et al. (1968). Therefore, it is necessary that the detector be operated in the proportionality region.

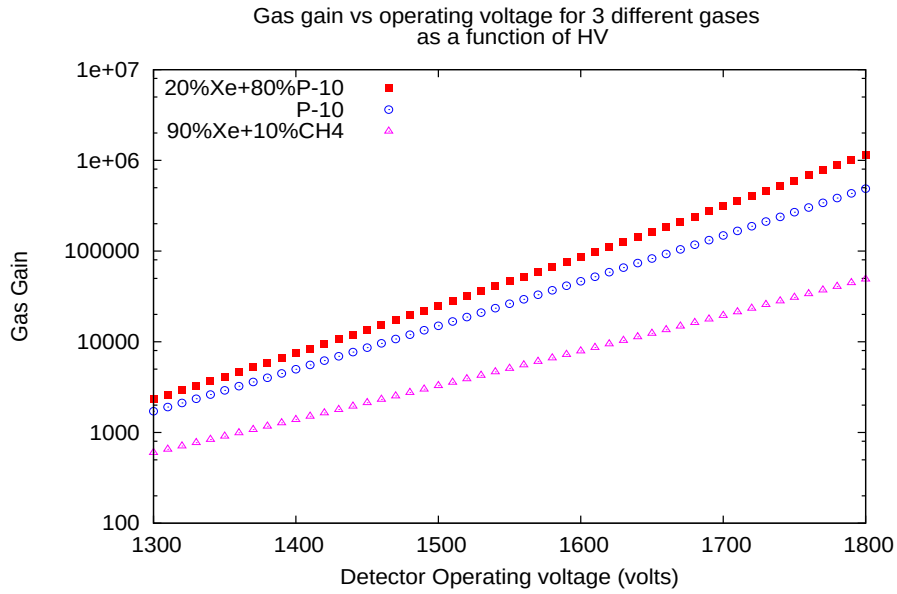

FIGURE 2.15: Gas gain as a function of operating voltage with respect to three different gas mixtures

2.8 Window Material and thickness of the window:

Window of the proportional counter is required to be thin enough to help in better detection efficiency at low energies and thick enough to prevent leakage of the pressurised gas from inside the detector chamber. It should have a conductive surface inside the chamber so as to act as the cathode plane at the top, along its side. The window material of the detector plays the key role in detection efficiencies at lower energies (ie. less than or about 3 keV). The high energy photons are not attenuated by the thin window, whereas the low energy photons (less than or about 3 keV) are attenuated. The transmission probability of the photons through the window is preferred to be higher to have a higher detection efficiency.

Given the option to choose between a Be window and a Mylar window, it is found that the Be window of 50 microns thickness is better than a Mylar window of 25 microns thickness. Figure 2.16 shows the detection efficiency with respect to two different window materials, Be window and Mylar window, for the gas mixture 25%Xe + 75%P-10. It can be seen that at 2 keV, the Be window of thickness 50 microns affords 1.7 times the detection efficiency with respect to that of a Mylar window of thickness 25 microns. However, micropore-free Be windows of large areas have to be test selected and handling large area Be sheets are hazardous. Therefore, Mylar window is chosen for SSM.

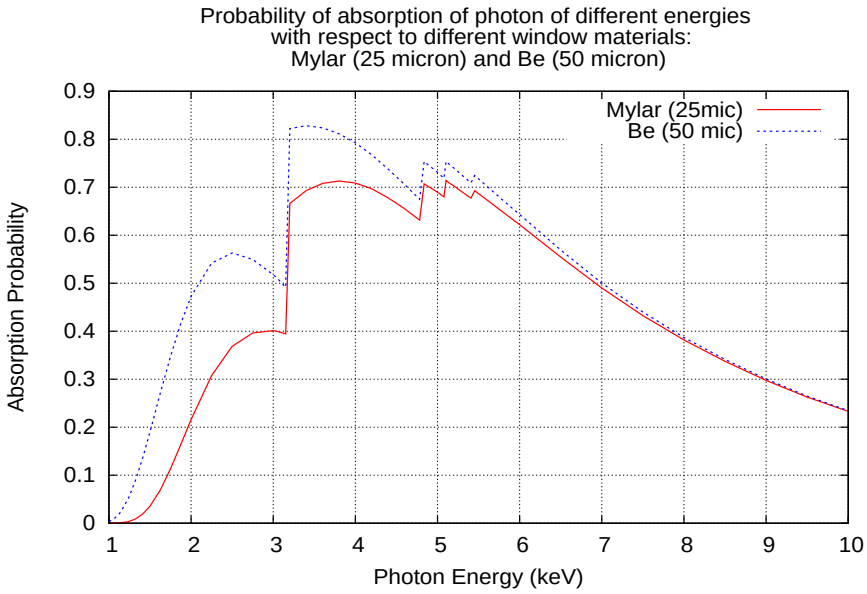

FIGURE 2.16: X-ray detection efficiency in 25%Xe + 75%P-10 gas mixture, for two different window materials, Be of 50 microns thickness and Mylar of 25 microns, for an active region thickness of 12 mm

2.9 Quench Gas

Quench gas plays a prominent role in certain aspects of the detector like gas gain, energy resolution, aging effects etc. Quench gases are those which are added to the primary gas in a detector to ensure stable operation at high gas gains. A pure Argon-filled counter does not allow gains in excess of 10^3 to 10^4 without entering into a permanent discharge operation (Sauli, 1977). Addition of even small amounts of a polyatomic quencher to the noble gas changes the operation of a counter completely. As these quenchers have lower ionization potential that results in a very efficient suppression of secondary photon emission the addition of these quenchers help in gains in excess of 10^6 to be obtained before discharge. The gas gain varies with the percentage of the quench gas used in the gas mixture. The key parameter in choosing a quench gas is its ionization potential.

The quench gas should be chosen appropriately as per the requirements of the operation of the detector. It is the energy resolution which is given the first priority of all the operational characteristics of the detector, it is better to go for the mixtures of argon + 10% propane or xenon + 10% propylene (Ramsey & Agrawal, 1988). Carbon-di-oxide returns the poorest results in all aspects except aging. The quoted instability of operation of argon-CO_2 based counters at high gains limits its use (Sauli, 1977).
Moreover, CO_2 diffuses out through the Mylar window.

In SSM we, therefore use CH_4 as the quench gas. The only disadvantage in using CH_4 as the quench gas is the polymerization effects that lead to faster aging of the detector, at higher count rates. This effect is more pronounced if the anode wire has a carbon-coating on it. In the astrophysical context, where we have very less photon count rate, it is reasonable to have CH_4 as the quench gas. Therefore, the quench gas used in SSM is CH_4 and it is 7.5%CH_4 along with 25%Xe and 67.5% Ar.

2.10 End-effects

In proportional counters, the gas gain is very high towards the ends of the anodes due to the zero potential wall of the wire-module, compared to that at the centre, when no field tubes are used in the design. The electric field at the ends of the anodes in the detector gets distorted and increases towards the ends due to the zero-potential walls at the ends. The gas gain is also high at the ends due to high electric field. This effect of variation in the electric field configuration at the ends of the anode is called the end effect in gas proportional counters (Cockroft & Curran, 1951, Heiberg, 1968).

SSM detector is a multi-celled, multi-layered proportional counter with position-sensing resistive anodes. The position sensing is done along the 60 mm length of the resistive anode wires. The effective length of the anode wires in the detector is 60 mm. Since it is required that the response of the detector be uniform throughout the anode length and the detector be free of discharge effects at the ends at times of very high energy deposition rates, these end-effects have to be minimised.

2.10.1 Problems due to end effects

- Detector life is at risk due to discharge effects at the ends of the anode due to high gas gain for an incident photon or a charged particle at the ends. The discharge effect is more probable for high energy deposition rates.
- Complications in deriving the energy of the incident photon, as the response of the detector is different towards the ends of the anode.

2.10.2 Solutions for end-effects

Conductive field tubes of larger diameters are usually used to reduce the electric field at the ends of the anodes, where these ends are not used for photon detection. In SSM, the

kel-F insulator insulates the anode from the cathode. The kel-F is made to protrude inside the gas chamber from zero-potential walls of the wire module so that the geometric ends of the effective anode length (the length of the anode that is used to detect valid events) is kept away from zero-potential walls. The optimum length of the insulator, with the consideration for mechanical constraints, is determined by simulations using Maxwell-2D software (for electric field simulations) for different lengths of the field tube.

2.10.3 MAXWELL 2D for electric field simulations

MAXWELL 2D is a simulation software to simulate electrostatic and magnetostatic fields for 2D cross sections of different geometries (http://www.ansoft.com/products/em/maxwell/).

2.10.4 Experimental and Simulation results showing the end effects in an SSM cell

The anodes in lab model of SSM detector are tested at every 1 mm from one end (0 mm) to the other (60 mm), with a collimated ^{55}Fe radioactive source placed close to the window. It has been observed that the total output increases towards the ends of the anodes as compared to the central region. Figure 2.17 shows the end effects seen in one of the SSM detectors in which the anode length is 60 mm with the zero-potential walls right next to the ends of the anode. The total output is increased by almost a factor of 2 at the ends compared to that at the central region of the anode. This effect has to be minimized to protect the detector from any discharge effect for large deposition of charge at the ends of the anode.

MAXWELL 2D simulation software is used to simulate the electric field configuration from one end to the other end of the wire. Different configurations of kel-F protrusions inside the chamber are simulated. The longitudinal cross-section of one such configuration of the SSM cell is shown in figure 2.18. The blue coloured boundaries are the walls of the wire-module, the green coloured region is the kel-F which insulates the red coloured anode from the blue coloured zero-potential walls. The top and bottom of the cell which are brown coloured are also at zero potential. The electric field along the anode length is simulated for different kel-F protrusion lengths inside the wire-module and also for no kel-F protrusion where the end effects are very large. The simulated electric field for no kel-F protrusion configuration is shown in figure 2.19 and figure 2.20 shows the electric field configurations for different kel-F protrusion along with no kel-F protrusion. From figure 2.20 it can be seen that the

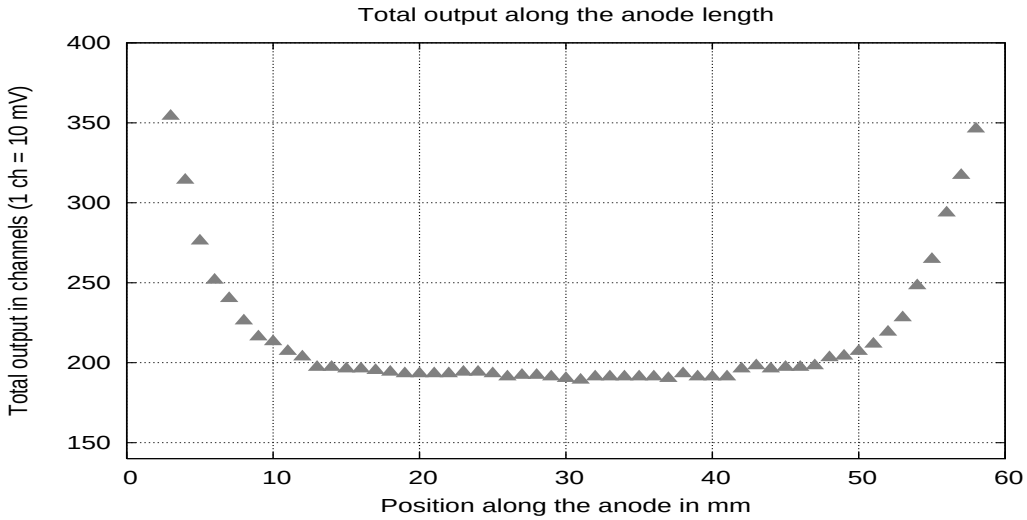

FIGURE 2.17: End effects seen in one of the anodes in an SSM detector; experimental result.

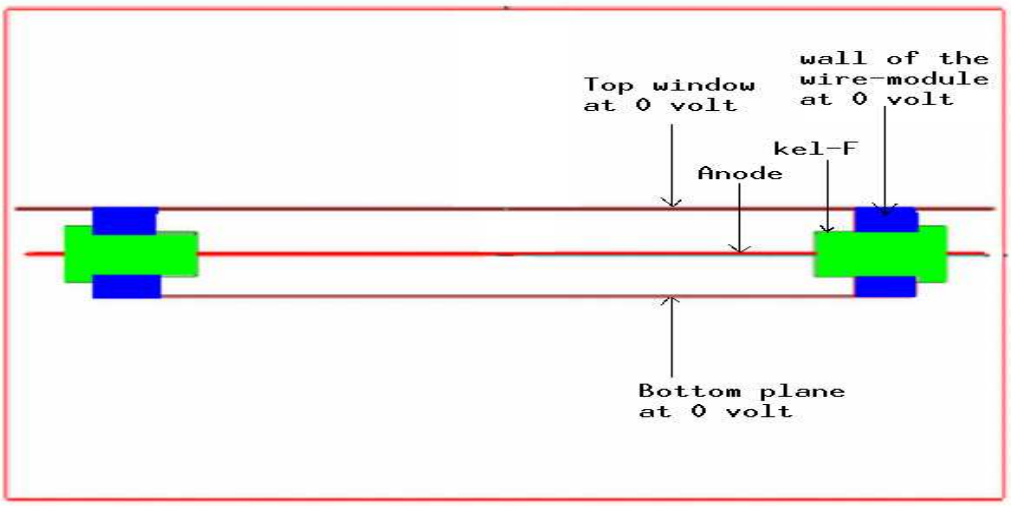

FIGURE 2.18: Longitudinal view of the SSM cell with a 4mm kel-F protrusion inside the wire-module.

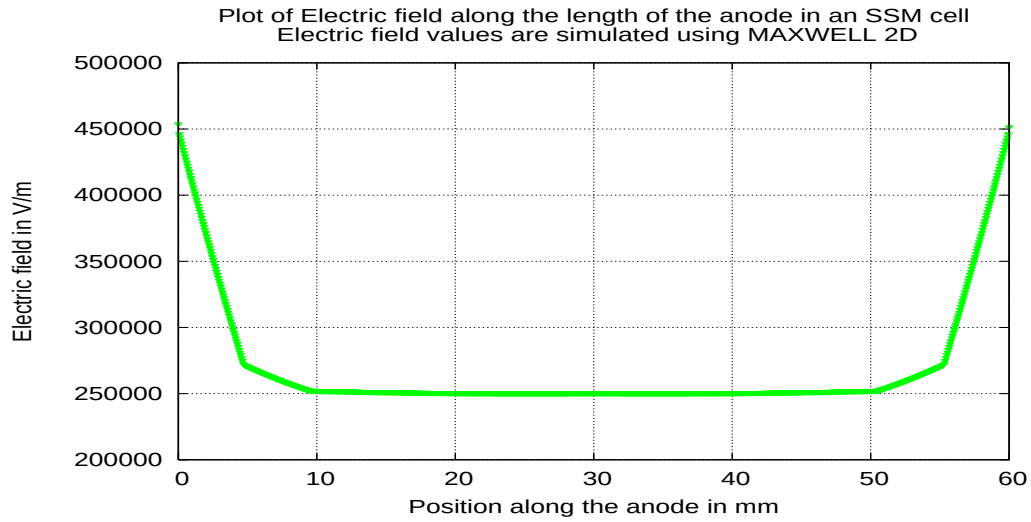

FIGURE 2.19: End effects simulated using MAXWELL 2D for an anode of length 60 mm with the zero-potential walls at the ends of the anode.

configuration with 4 mm kel-F protrusion shows the most minimised end effect towards the ends of the anode compared to other configurations.

The absolute values of these simulations cannot be considered for comparisons with the experimental results since these are done only for the 2-dimensional cross section of the SSM cell. The MAXWELL 3D software to simulate the electric field for 3D geometries would be the right choice for these simulations. Since the MAXWELL 3D software is not available with us now and also that it is only a relative behaviour of the electric field that we need, we have done these simulations with MAXWELL 2D.

2.10.5 Inference from simulations using Maxwell 2D

The end effects in the SSM detectors can be reduced by having the protrusion of kel-F insulator inside the wire-module by 3 or 4 mm. Minimising the end effects helps in having a uniform response for an incident photon throughout the entire 60 mm length of the anode wire. The gas gain can also be maintained the same almost for the entire length. From these simulations we have chosen the 4mm kel-F protrusion to be the optimum value and given as input for the fabrication of the SSM qualification model and flight models.

Figure 2.21 shows the photo of the wire module of lab model of SSM which has no kel-F protrusion where the end-effects have been observed as shown in figure 2.17. Figure 2.22 shows the photo of the wire module of SSM qualification model which has 4 mm protrusion

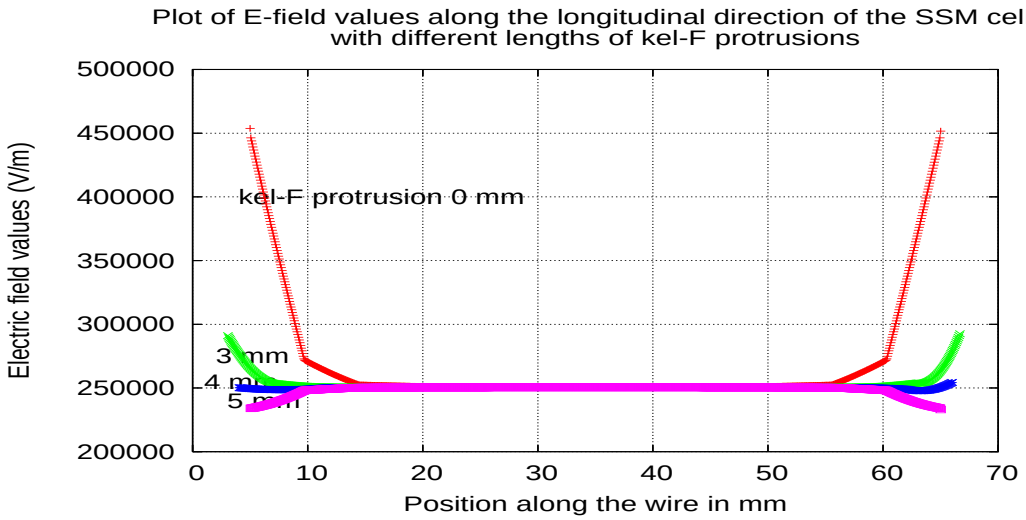

FIGURE 2.20: Simulated electric field for different kel-F protrusions inside the wire-module.

of kel-F inside the wire module. One of the anodes in this detector with 4 mm protrusion of kel-F is tested with collimated ^{55}Fe radioactive source from one end to the other. Figure 2.23 shows the result of the experiment.

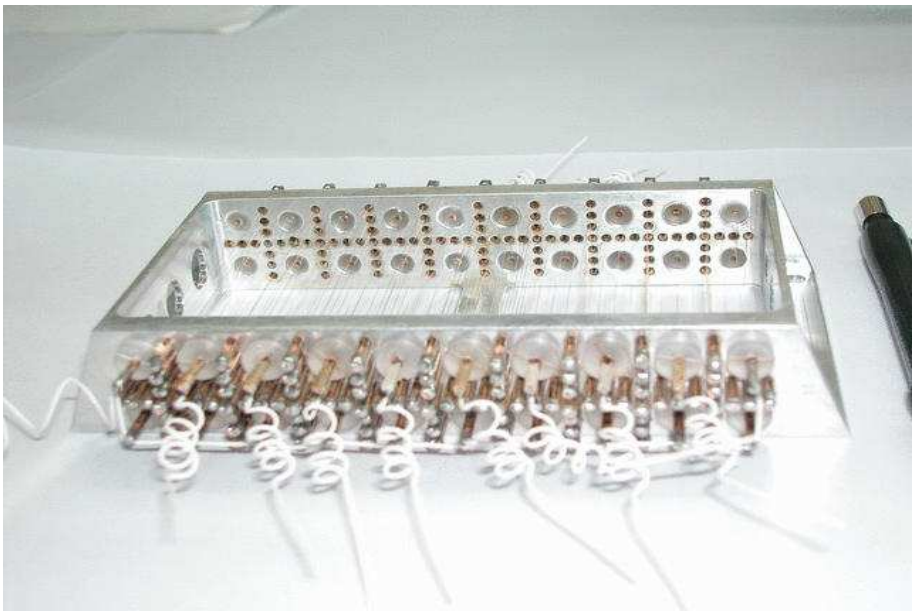

FIGURE 2.21: Photo of the wire module of SSM without any kel-F protrusion.

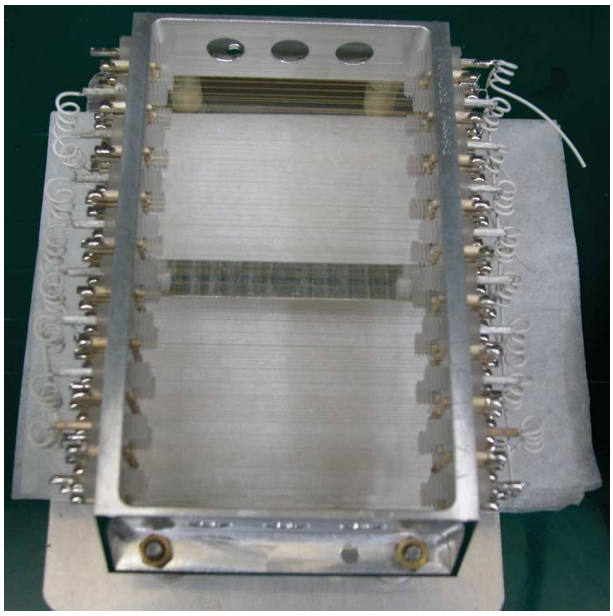

FIGURE 2.22: Photo of the wire module of SSM with 4 mm kel-F protrusion inside.

2.10.6 Experimental verification for minimization of end-effects

SSM detector with 4mm kel-F protrusion inside the wire module was made and tested from one end of the wire to the other end with a collimated ^{55}Fe radioactive source of energy 5.9 keV. Figure 2.23 shows the results of the tests carried out on one of the wires within the detector with 4mm kel-F protrusion. The end effects are found to be minimized drastically compared to the previous configuration where there was no kel-F protrusion inside the wire module. Thus, the end-effects are minimized in SSM detectors. Most of the wires in the detector with 4 mm kel-F protrusion show minimized end-effects. However, some of the ends of the anodes show a decreased output compared to the central region. This results in the reduction of the detection area available for photon detection. The geometric area of SSM is 60 $\times$ 96 mm^2, which is 5760 mm^2. The detection area available after excluding an average of 5 mm on either side of the anodes (due to end-effects) is 50 $\times$ 96 mm^2, which is 4800 mm^2. The 4 mm protrusion of kel-F was chosen on the basis of 2-D simulations. A 3D simulation of the same would have been more realistic and it is planned to do a detailed 3D simulation for more accurate results.

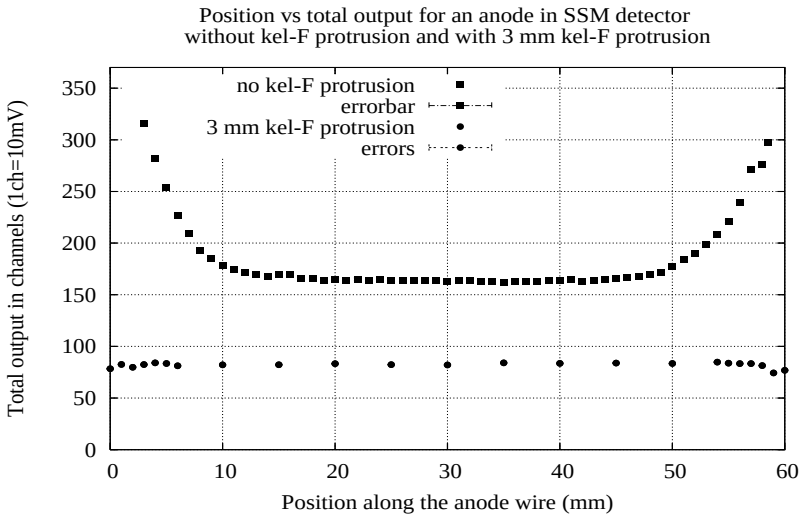

FIGURE 2.23: Experimental result showing the total output from one end to the other for two different configurations: one without any kel-F protrusion, another with 4mm kel-F protrusion with minimized end effects

2.11 SSM configuration

SSM detectors are made with the optimized parameters as discussed in the previous sections. SSM detector consists of 20 cells, in two layers, each acting as an independent proportional counter unit. Each cell is of size 1.2 × 1.2 sq-cm, ie. 1.2 cm depth and 1.2 cm spacing between the anodes of each cell. The anodes are carbon-coated quartz wires of diameter 25

Detector	Position-sensitive gas proportional counter
Gas mixture	25% Xe + 75% P-10
Gas pressure	800 torr
Anode wire	Carbon coated quartz
Cathode wire	Gold-coated tungsten
Anode diameter	25 microns
Cathode wire diameter	75 microns
Cell size	1.2 × 1.25 sq_cm
Operating Voltage	1500 Volts
Window	Aluminized Mylar
Window thickness	25 microns

TABLE 2.2: Parameters for SSM

microns. The effective length of the anode wire used for photon detection is 60 mm. The cathodes are gold-coated tungsten wires of diameter 75 microns. The anode is surrounded by wire-walled cathode on three sides and by the aluminized Mylar window on the top side

through which the X-ray photons enter the cell. The central 8 cells in the top layer are to detect the photons from the celestial X-ray sources and the bottom 10 cells including the side cells in the top layer act as veto cells to detect and reject background charged particles as well as photons of energies outside the energy range of interest of the instrument. Figure 2.4 shows the schematic view of the wire module for SSM with all the 20 cells in two layers. The gas mixture used in the detector is 25% Xe + 75% P-10 at a gas pressure of 800 torr. Table 2.2 gives the optimized parameters for SSM.

Chapter 3

Implementation of design parameters and Calibration of SSM

SSM detectors are made with the optimized parameters discussed in the previous chapter. The principle of operation of the detector for measurement of energy and position of the incident photon is briefly discussed in this chapter. The characteristics of the detector like stability, detection efficiency, gas gain at different operating voltages, energy resolution, position resolution etc. are experimentally studied. A detailed description of the experiments and the results obtained are discussed in the following sections. Characterisation of the instrument with respect to its science objectives with few experiments is also discussed.

3.1 Brief overview of the SSM detector with coded-mask and electronics

SSM consists of three almost-identical one dimensional position-sensitive gas-filled proportional counters with a one-dimensional coded-mask on each detector. Each SSM is mounted to have a different Field of View (FOV) in the sky, with overlap of some part of the FOV with the others. The three SSMs are arranged such that there is one SSM at the centre and two on the sides canted with a 45° angle. The SSM detector at the centre is called the Central SSM, which has a FOV of 22.1°× 100° (FWZM) and the two SSM detectors on the sides are called Edge SSMs with an FOV of 26.8°× 100° (FWZM) each. All the three SSM detectors are mounted on a single platform which can rotate. The whole unit is rotated from 5° to 355°, in steps of 10° to scan the sky in step-and-stare mode.

SSM consists of three major elements: the detector, the electronics and the imaging system (coded-mask). The details of each of these elements is discussed in the following subsections.

3.1.1 Detector system

As discussed in the previous chapter, the detectors for SSM are position sensitive gas-filled proportional counters. The parameters which define the characteristics of position-sensitive gas-filled proportional counters are discussed in the previous chapter. SSM detector consists of multiple cells and are double layered. There are totally 20 independent cells (in two layers, 10 in each layer) which act as proportional counter units. Each cell consists of a central anode and wire-walled cathode surrounding it. The central eight cells in the top layer consist of position-sensitive anode wires which are carbon-coated quartz, that are resistive (with 8 kΩ/mm or 4 kΩ/mm) anodes. The cells in the bottom layer along with the end-cells in the top layer have conductive wires as anodes which are gold-coated tungsten and these form the veto layer for charge particle rejection. All anodes are powered with a high voltage (HV) of about 1500 volts with respect to that of the cathodes which are at zero potential. The geometric length of the anode in each cell is 62 mm, out of which 60 mm is available for charge collection due to photon incidence. The end-effects at the ends of the anodes are minimized largely. However, some of the anodes are still found to have some effect at the ends and hence, the effective length is about 50 mm leaving a maximum of 5mm on either sides due to end-effects in the detector. These cells with the anode at the centre and wire-walled cathode around them form the wire-module of SSM. The wire-module is enclosed in a gas-filled chamber having an entrance window thin enough to allow the incident X-ray photons into the counter. Figure 3.1 shows the schematic view of the cells inside an SSM detector and figure 3.2 shows the photo of the wire module inside the detector.

Principle of operation:

Principle of photon detection, measurement of its energy and position of incidence in SSM detector is discussed in section 2.1.1 for position-sensitive proportional counters. In a position-sensitive detector the anode being resistive, the charge is proportionately divided between the two ends of the anode, depending on the position where the charge cloud is collected along the anode wire. This charge is converted into voltage using a charge sensitive preamplifier at both the ends of the anode. The corresponding voltage pulses at either ends of the anode are referred to as left and right outputs of the anode. Figure 3.1 shows a photon incident on one of the wires and the corresponding left and right outputs produced in that particular anode which detects the photon. The total amplitude of both

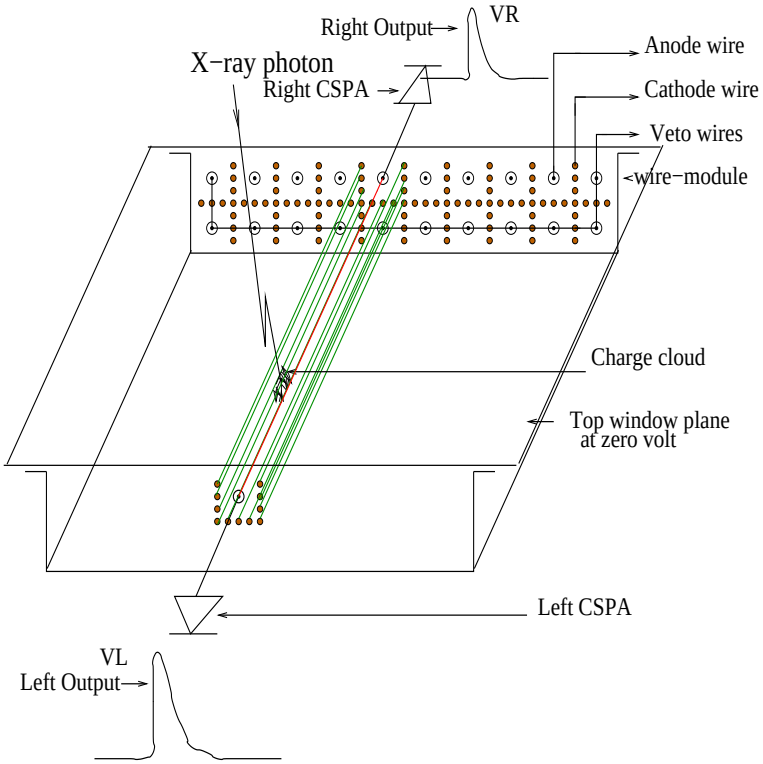

FIGURE 3.1: Schematic picture of wire module of SSM, with a photon incidence on an anode; 3D view of only one of the anodes is shown here for clarity of the picture

the outputs is proportional to the energy of the incident photon. The position (P) of the incident photon on the detector plane is derived using the amplitudes of the left and the right output pulses taken out at the ends of an anode. The details of deriving the position of an incident photon is discussed in section 3.4.

The information that we get about every photon that is incident on the detector are 1. Time of arrival 2. Energy and 3. Position of incidence. All the three parameters are measured using the electronics system of SSM, discussed in section 3.1.2.

3.1.2 Electronics System

The Electronics system for SSM consists of three units: (a) Charge Sensitive Pre-Amplifiers (CSPA) and post amplifiers (PA), (b) Front end electronics consisting of low voltage DC-DCs, HV programmer, logic unit for LLD/ULD/event-analysis, peak detectors, ADC, etc and (c) the Processing Electronics (PE) consisting of FPGA based system for event processing, buffer memory, telecommand and telemetry interfaces and the interface circuits for data transfer to Data Handling package. The detector is powered using High Voltage

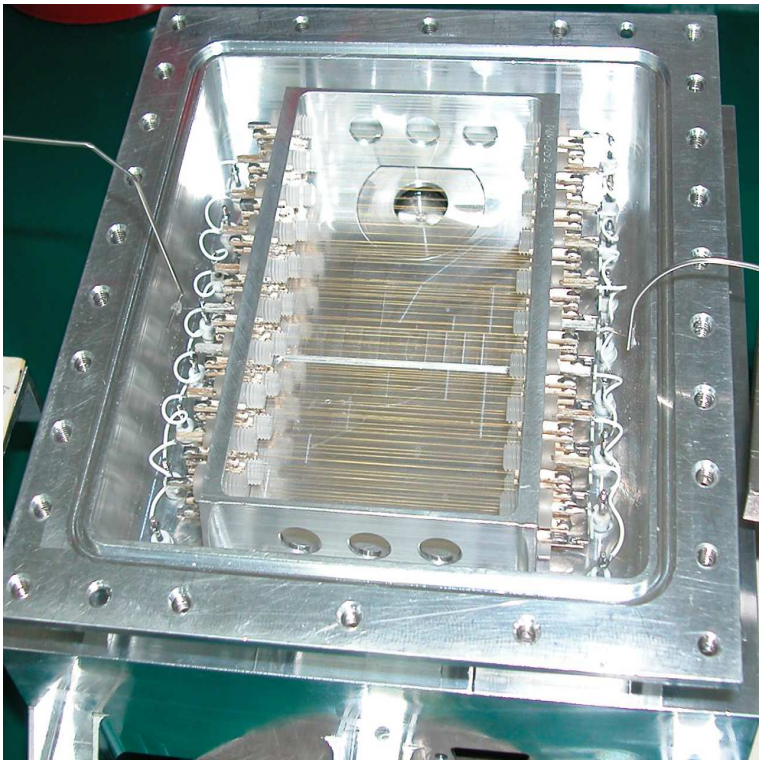

FIGURE 3.2: Photo of wire-module inside the detector chamber

distribution unit mounted behind the detector. Figure 3.3 shows the block diagram of the detector with the electronics.

Processing of an event:

The charge collected at the anode for every incident photon is converted to a voltage pulse using a CSPA on either sides of the anode. Thus, for every photon incidence on an anode wire, there are left and right outputs from either ends of the anode, fed to the respective CSPAs and converted to voltage pulses termed 'L' and 'R' respectively. The CSPA output is further shaped and amplified. There are seventeen such chains for each SSM detector unit, sixteen of them are connected to both ends of eight anodes and one of them is connected to the veto layer. The front end logic unit processes signals from each of these chains. Event outputs between Lower Level Discriminator (LLD) and Upper Level Discriminator (ULD) are accepted for processing. Charge particle rejection is done by the technique called anti-coincidence, where the event is rejected when (a) signals are present in both the top anode layer as well as the bottom veto layer simultaneously, or (b) more than one anode having an output pulse simultaneously. The amplitude of every accepted event is measured and digitised and then the Analog-to-Digital Converter (ADC) output of each event, both left

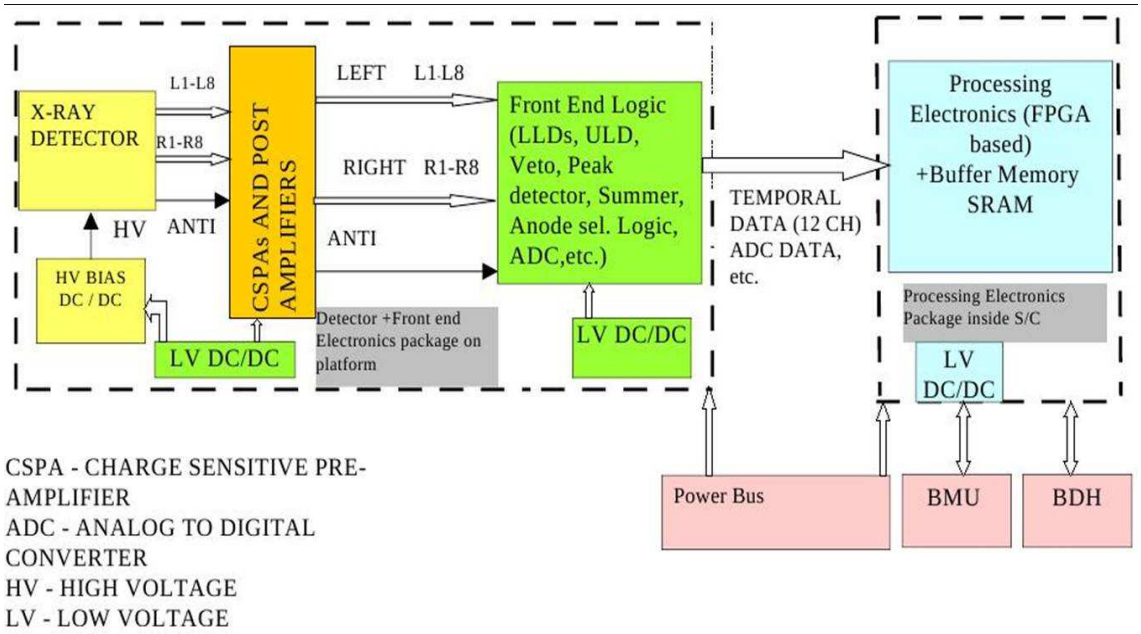

FIGURE 3.3: Block diagram for SSM electronics including the detector

and right sides, are sent to the PE unit. In addition there are several channels for count rates from the anodes and veto, which are also sent to the PE. The PE which is an FPGA-based (Field Programmable Gate Array) unit accepts these events, stores them in buffer memory and interfaces with the Data Handling system of the spacecraft. The PE also acts as both telecommand and telemetry interface for the complete SSM electronics system. The time of incidence of every photon is tagged with the event by the PE using an on-board SSM clock. This clock is periodically matched and stored with the spacecraft Bus Management Unit (BMU) clock for conversion to Universal Time (UT) on ground. In addition, the electronics system also has circuitry for sensing and reducing High Voltage within high charge particle regions based on command-set thresholds and also for corona sensing with auto-shutoff. Data from the PE is sent from the buffer memory through Data Handling and stored in the main spacecraft Solid State Recorder (SSR) package for readout during visibilities. The detector and front end electronics packages are mounted on a rotating platform on the anti-sun-side of the spacecraft whereas the processing electronics is mounted inside the S/C. A flexible cable bunch is used between the packages.

3.1.3 Imaging System

SSM has a large FOV and coded-mask imaging technique is used in SSM. Coded-mask is an advanced version of a pin hole camera with multiple pin holes arranged randomly. In a pin-hole camera, the photons entering the pin hole form an image of the object. However, the sensitivity of the instrument will be limited by the small size of the pin hole. The sensitivity can be improved by having a number of pinholes, but the arrangement of the pin holes has to be random, so that the shadow of the pinholes on the detector plane cast by the each source in the sky is unique. This random pattern pin hole is referred to as a coded-mask (Zand, 1992).

Basic principle of Coded-mask imaging The three principal components of coded-mask imager are a coded-mask, a position-sensitive detector and a reconstruction technique. A coded-mask is a plate with closed (opaque) and open (transparent) elements for the photons to pass through and cast the shadow of the mask on the detector plane, as they get detected. The photons from a source in a particular direction in the sky cast the shadow of the mask on the detector plane. The shadow will have the same pattern as the mask, but shifted appropriately with respect to the direction of the source. Similarly, for a number of sources at different locations in the sky, the shifted mask patterns (corresponding to the different directions of the sources) get accumulated on the detector. The accumulated image of the coded-mask with respect to different sources at different locations in the sky has the information of the position and intensity of the sources. The image in the detector has to be deconvolved to reconstruct the sky image. It is important that every position in the sky is encoded on the detector in a unique way. This implies that the mask pattern should be selected appropriately that the autocorrelation function of the pattern should contain a single peak and flat side-lobes. In other words, this can be stated that for a single source casting the shadow of the mask on the detector, the decoded image should have a single peak corresponding to the single source in the field of view.

The quality of imaging depends on the type of mask pattern, the design of the detector, the spatial resolution of the detector and the decoding or the reconstruction technique used. The mask pattern should be chosen such that it satisfies two conditions: 1. The autocorrelation function of the pattern should give a single peak with flat side-lobes. 2. It is necessary that the mask pattern has $\geq$50% transparency so that the signal to noise ratio is better than the 3σ limits. The imaging is better when a complete image of the mask is created for every observed position of the sky. The design of the instrument takes care of this. The distance between the detector and the mask has to be chosen appropriately such

that the image of a complete basic pattern of the mask is obtained for every observed source position in the sky, within the field of view of the instrument defined by its collimator. The spatial resolution of the detector should be half of the minimum size of the elements in the mask for good imaging quality. A detailed study of coded-mask imaging can be found in the Ph.D. thesis by Zand (1992).

The coded-mask for SSM is one dimensional. The minimum size of an element (open or close) in SSM coded-mask is 0.95 mm. Six different coded mask patterns are used in SSM detector, with 50% transparency. The six mask patterns are joined along the length and the resulting complete coded-mask plate is shown in figure 3.4.

FIGURE 3.4: Coded-mask for SSM with six patterns in it

3.2 Characterisation of SSM detectors

The position sensitive proportional counters have to be qualified for certain characteristics before it is considered for the SSM experiment The important parameters to be studied are the stability of the detector, its detection efficiency, gas gain at the operating voltage, energy resolution and position resolution. Experiments are carried out to test for these parameters in detail. The SSM detectors are calibrated at different energies to understand the spectral response. The main objective of SSM is to detect and locate transient sources and hence deriving the position of the X-ray source in the field of view is of prime importance. Experiments are carried out to arrive at a methodology to derive the position of the X-ray source in the FOV of SSM. The positional calibration of SSM is carried out with various kinds of experiments. Details of different experiments on SSM for the study of various parameters are discussed in the following sections.

3.2.1 Stability

Stability of a detector means that its total output which is the sum of the left and the right output amplitudes for a photon of particular energy incident on the detector should remain

constant over a period of time. The first step to characterize the detector is to look for the stability of the detector, as this instrument SSM is to be flown on-board and has to survive the mission lifetime of about few years. The stability of the detector can be affected by various factors: degradation of the gas mixture due to contaminants, leak of gas from the detector, aging of the anode wires, high voltage fluctuations etc. The contamination of the gas mixture can lead to reduced output whereas the leak of gas from the detector leads to an increase in the total output. Aging of the anode wires can also lead to a reduced output and high voltage fluctuations can result in an increase or decrease in the total output of the anode.

One of the SSM detectors is tested for stability for over a period of few years. Figure 3.5 shows the stable output of one of the SSM detectors tested with ^{55}Fe (which is a source of 5.9 keV X-rays). The total output is given in Channels which is a measure of voltage (1Ch=10mV). The variation in the total output is found to be within $\pm$ 2% (Seetha et al., 2006).

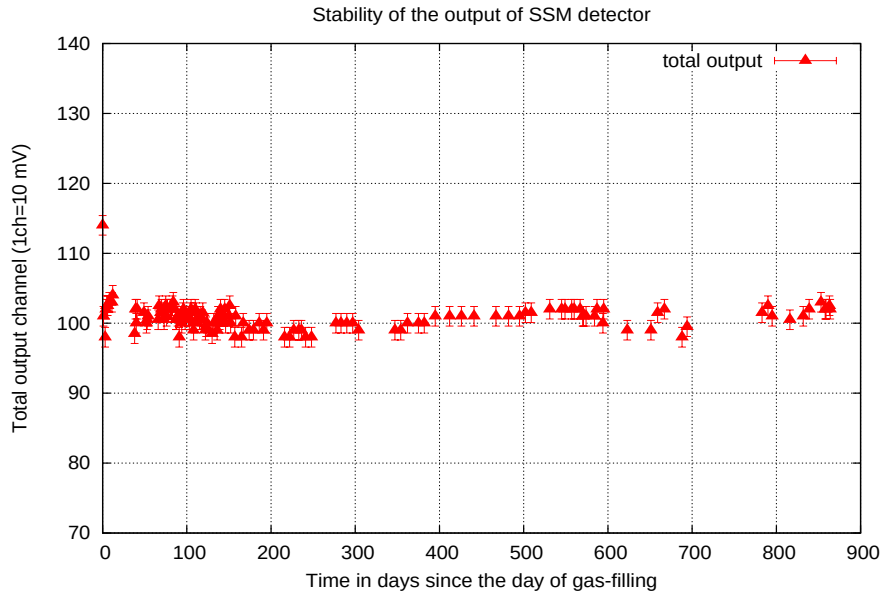

FIGURE 3.5: Plot showing the stability of SSM detector over a period of 2.5 years.

In the laboratory on ground, in order to maintain the purity of the gas inside the detector, it is subjected to window-side evacuation everyday, where the window of the detector is connected to the vacuum pump (or the whole detector is put inside a vacuum chamber), so that any contaminant such as water molecule or O_2 which has entered the detector through the window can be removed. This kind of evacuation is not required while the detector is on-board a satellite in the orbit around the earth, as there is a pressure gradient due to

vacuum in space and there is no chance of the degradation of gas purity due to external contaminants. However, any micro-pore leak in the detector, which is not observed in the experiments in the lab, or which occurs due to meteorite hits, can yield to a detectable leak, when the detector is in near vacuum condition in space. In such cases when an on-board leak is detected from the data collected on-board and analysed here on ground, the HV is tuned by tele-commands, such that the gas gains are brought back to nominal values. Therefore, it is important that, when the SSM detectors are made here in the laboratory, great care is to be taken so that there is no leak present in the detectors. All the detectors are tested for stability by monitoring the total output for a monochromatic source ^{55}Fe for about two weeks initially and if found stable, they are qualified for further integration with other electronics units and studied for other parameters.

3.2.2 Detection Efficiency

Detection efficiency of a detector is defined in section 2.1.2 of chapter 2. Determining the detection efficiency of the detector experimentally, requires a source whose absolute count rate is known. The estimate of the count rate from the radioactive source ^{55}Fe (5.9 keV) from its strength can have errors in it. Therefore, the X-ray source has to be calibrated before it is used to determine the detection efficiency of the detector. Si-PIN detector which has a 99% efficiency at 6 keV is used to calibrate the X-ray source which is then used to determine the detection efficiency of the detector.

SSM detector is irradiated with the radioactive source ^{55}Fe placed at a height of 30 cm from the detector plane, such that it illuminates the entire detector area. The time of integration of the data is 15 minutes. In the same way, SiPIN detector is also irradiated with ^{55}Fe source for 15 minutes of integration time. The data from both the detectors are analysed to get the integrated counts in the energy spectra and the count rates recorded in both the detectors are calculated. The formula given in equation 3.1 is used to derive the detection efficiency of SSM at 5.9 keV.

$$DE_{SSM} = \frac{Cntrate_{SSM}}{Cntrate_{SiPIN}} \times DE_{SiPIN} \times \frac{Area_{SiPIN}}{Area_{SSM}} \tag{3.1}$$

where, DE_{SSM} is the Detection Efficiency of SSM detector, DE_{SiPIN} is the Detection Efficiency of SiPIN detector, $Cntrate_{SSM}$ is the count rate recorded in SSM detector for ^{55}Fe radioactive source at 5.9 keV, $Cntrate_{SiPIN}$ is the count rate recorded in SiPIN detector for ^{55}Fe, $Area_{SSM}$ is the area of SSM detector and $Area_{SiPIN}$ is the area of SiPIN

detector. The Detection Efficiency of the SiPIN detector used for this study is 99% at 6 keV. Area of the SiPIN detector is 4.44 mm^2. The geometric area of SSM is 60 × 96 mm^2. However, the detection area of SSM-Qualification model detector is 50 × 96 mm^2, which is 4800 mm^2, which is due to exclusion of an average of 5 mm on either sides of the anode where the counts registered are almost zero due to end-effects. The maximum detection area of SSM detector is 60 × 96 mm^2, which is 5760 mm^2. Considering the maximum area of the SSM detector gives the lower limit on the detection efficiency calculated.

Figure 3.6 gives the comparison between the theoretically estimated detection efficiencies of both the detectors, the SiPIN and SSM detectors. Detection efficiency of SSM at 5.9 keV derived experimentally is also plotted in the same figure. The lower limit on the data point is derived considering the total geometric area of the SSM detector and the upper limit is got by propogating the poissonian error on the counts detected in both the detectors.

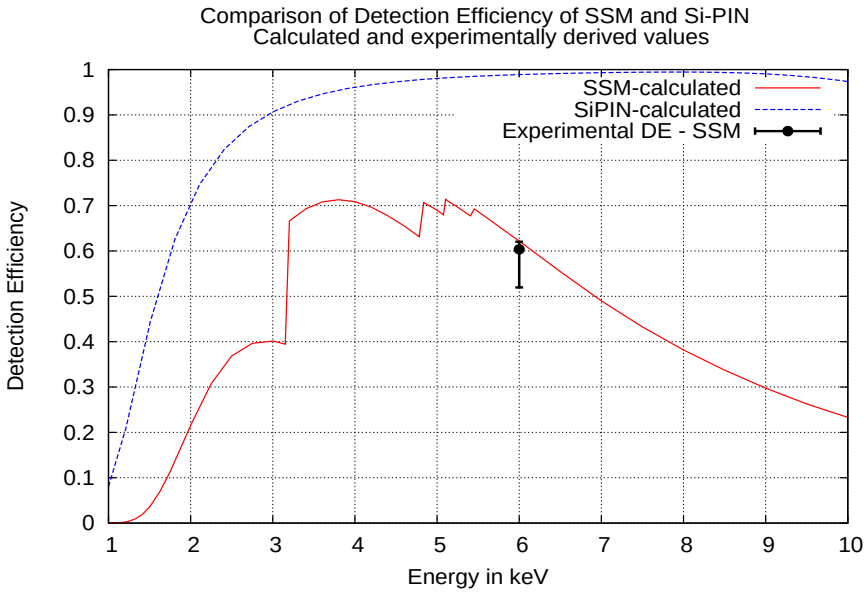

FIGURE 3.6: Comparison of theoretically estimated and experimentally derived values of detection efficiencies of SSM and Si-PIN detectors

3.2.3 Operating voltage

It is required that the detector be operated in its proportional region of operation so that the total output of the detector (which is proportional to the charge collected at the anode) is proportional to the energy of the incident photon. SSM detectors are tested for the proportional region of operation and a particular operating voltage is chosen such that the gas gain is about 10^4. The tests are done with a monochromatic source ^{55}Fe which produces

X-rays of energy 5.9 keV. Figure 3.7 shows the total output of SSM detector as a function of operating voltage.

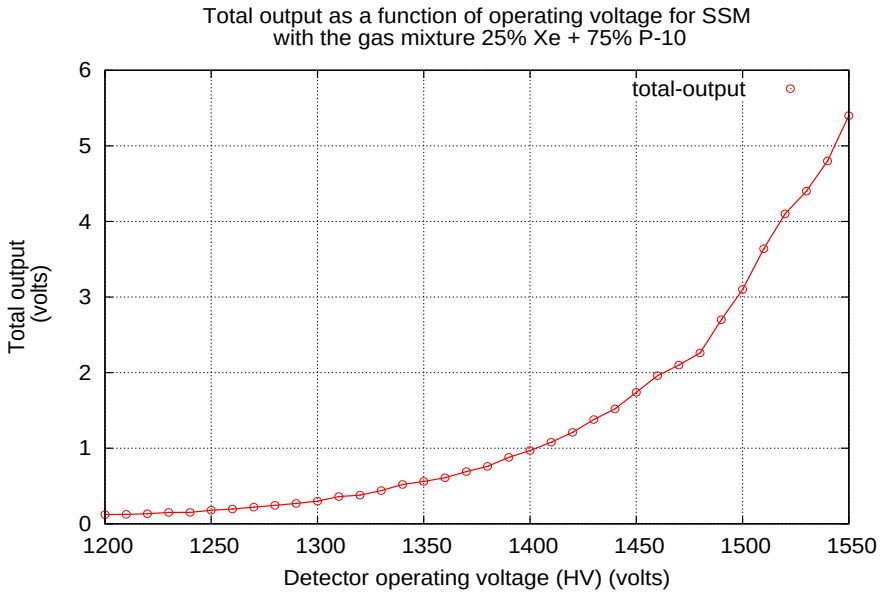

FIGURE 3.7: Total output as a function of operating voltage for one of the SSM detectors

A high voltage of 1500 volts gives a gas gain of about 13000 for the SSM cell geometry for the gas mixture of 25%Xe+75%P-10. Thus, SSM detectors are operated at 1500 Volts where the gas gain is sufficient enough to produce a total output voltage of 3 Volts for a photon of 5.9 keV incident on the detector. The energy resolution and position resolution are found to be satisfactory at this operating voltage, details of which are discussed in the following sections.

3.2.4 Energy Resolution

One of the important characteristics of a radiation detector is its response to a monoenergetic source of radiation. The pulse height spectrum, which is the distribution of pulses of different amplitudes binned into channels, is generally a Gaussian for gas proportional counters. This is called the response function of the detector for the particular X-ray energy incident on it. Ideally, the pulse height spectrum should be a delta function for a monoenergetic X-ray source. The observed pulse height spectrum for a monoenergetic source is a Gaussian and has a definite width, which defines the energy resolution of the detector. The width indicates the fluctuations in the amplitude of every output pulse for every monoenergetic photon detected in the detector. The Full Width at Half Maximum (FWHM) of

the pulse height spectrum (which is a Gaussian) is defined as the width of the distribution at the ordinate with half of the maximum counts of the peak of the Gaussian. The energy resolution of a detector is defined as the FWHM divided by the centroid (peak) of the Gaussian. This dimensionless fraction is generally expressed in percentage.

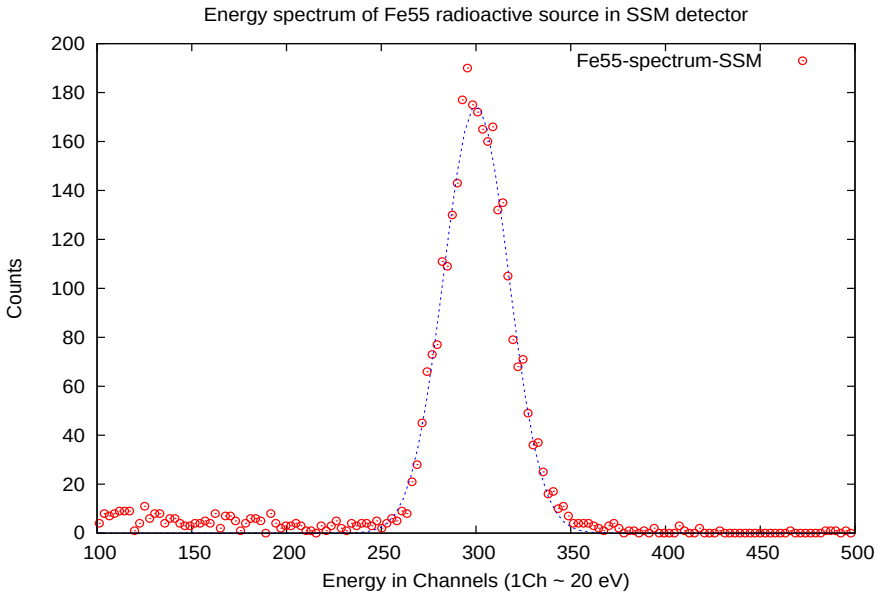

FIGURE 3.8: Energy spectrum of ^{55}Fe radioactive source as seen in SSM detector

The important factors that contribute to the width of the pulse height spectrum are the statistical fluctuations in the number of primary electron-ion pairs produced when the incident photon is absorbed in the detector medium, the statistical fluctuations in the charge produced during the avalanche process, the random noise due to the electronics of the system and the drift in the operating characteristics of the detector system. In the above mentioned factors, the statistical fluctuations in the number of primary electron-ion pairs plays the prime role in causing the width in the pulse height spectrum. Larger the width of the spectrum, poorer is the energy resolution. Energy resolution gives the measure of the capability of the detector to resolve between two different photon energies. Energy resolution for SSM is about 18% at 6 keV. Thus the energy resolution is about 1 keV at 6 keV, which is an order poorer compared to semiconductor detectors. Figure 3.8 shows the energy spectrum of a radioactive source ^{55}Fe for SSM detector.

Since the objective of SSM is to scan a large part of the sky and detect and locate X-ray transient sources, energy resolution is not a critical parameter. However, calibration of the detector at different energies is required to derive the spectral response and the position resolution at different energies. So also, identification of the energy of each photon detected

is required to derive the count rate in different energy bands, which are used to calculate hardness ratio (ratio of the fluxes in two different energy bands [hard-Xray-band/soft-Xray-band] which will be used to understand the nature of X-ray source observed) of the source that will be observed by SSM. The details of calibrating the detector at different energies is discussed in section 4.4.

3.2.5 Position Resolution

Position resolution is one of the important parameters for SSM, as the objective of SSM is to detect and locate X-ray transients in the sky. Position resolution for any imaging proportional counters can be given in terms of FWHM which is a quadratic sum of at least four independent parameters as given in equation 3.2 (Fraser, 1989).

$$\Delta x = 2.36[(\Delta x_r)^2 + (\Delta x_d)^2 + (\Delta x_t)^2 + (\Delta x_n)^2]^{1/2} \tag{3.2}$$

where Δx_r is the contribution from the ranges of photoelectron and Auger electron, which depends on the energy of the incident photon and the pressure of the gas in the detector. The Δx_d is the contribution of lateral diffusion in the drift space of the counter and depends

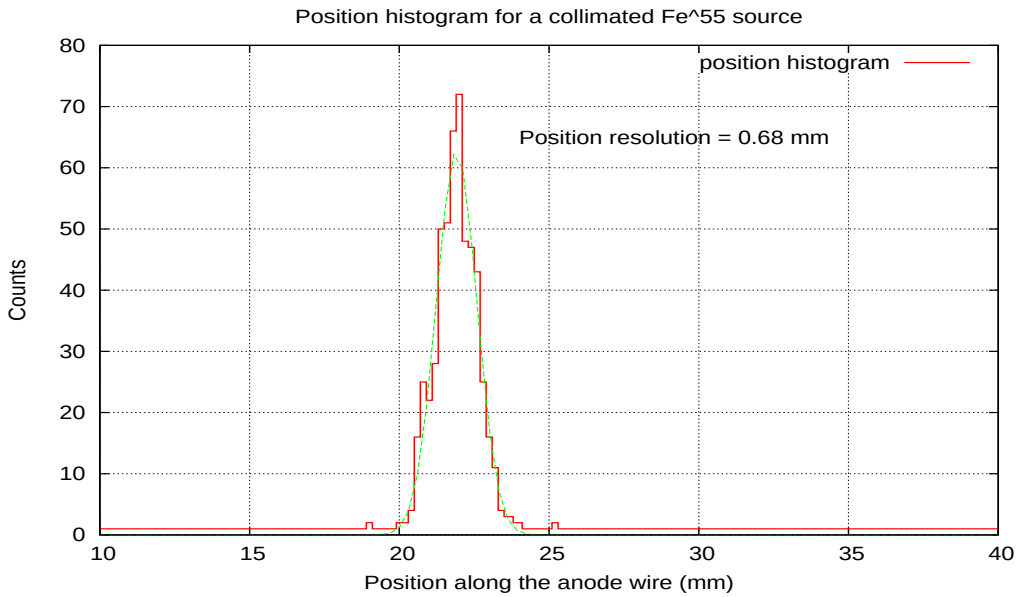

FIGURE 3.9: Position histogram at 6 keV, with radioactive source ^{55}Fe

on the statistics of the initial number of primary electron-ion pairs (N). Diffusion effects are more prominent in position resolution at low energies, as the value of N is small. The

Δx_t is the result of parallax effects due to oblique incidence of the X-rays into the detector and Δx_n is the contribution of the noise in the readout unit. Position resolution is better at higher gas pressures (Fraser, 1989).

It is required that the position resolution be about half the size of the smallest element in the coded-mask (Zand, 1992). Figure 3.9 shows the position histogram for a collimated ^{55}Fe radioactive source, placed on one of the anodes in SSM detector. The position resolution is ∼0.68 mm at 6 keV. The position resolution is given after removing the beam-width of the X-ray source from quadrature. The details of deriving the position resolution is discussed in section 3.6.

3.2.6 Uniformity of the anode wire

Anode wires chosen for SSM are 25 microns diameter Carbon-coated Quartz wires. The anodes are of length 60 mm. Every anode can have some non-uniformities along its length. These non-uniformities show up in the total output of the anode for collimated source placed at every 1mm along the length of the wire. The variation in the total output could be due to the variations in the diameter of the anode wire.

It is required that the anode wire has a uniform diameter throughout its entire length for the gas gain to be a constant and hence the total output be constant for a particular energy of the X-rays incident on it. The collimated ^{55}Fe source is placed at every 1 mm of the anode wire at its ends (in order to look for any variation due to end effects) and at every 5 mm at the central regions (as this region is less likely to have large variations in the total output) and the total outputs are measured. The collimated ^{55}Fe source is placed close to the window of the detector and the data is acquired for about a minute for all the positions along the anode wire. Figure 3.10 shows the variations in the total output along the entire length of the anode. All the anode wires are tested at different positions over the entire length of 60 mm.

It can be seen that all the anodes do not have a uniform output throughout the entire length. These variations in the total output of each anode are due to variations in the gas gain which are attributed to the non-uniformities in the diameter of the anode wires and to end-effects at the ends of the anode. The variations in the total output at different positions along the anodes are typically ±2% (Seetha et al., 2006), except for few positions. Maximum variations are found to be about ±5% along the anode. These variations in the total output are within the limits of energy resolution of the output for a photon of particular energy and hence are within the tolerable limit. The anode wires are inspected

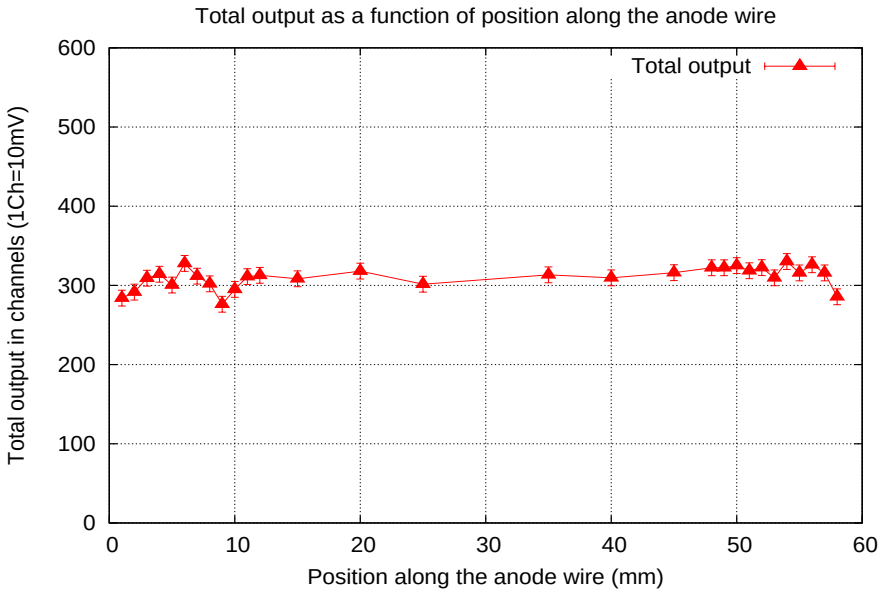

FIGURE 3.10: Plot showing the total output at different positions along the anode wire

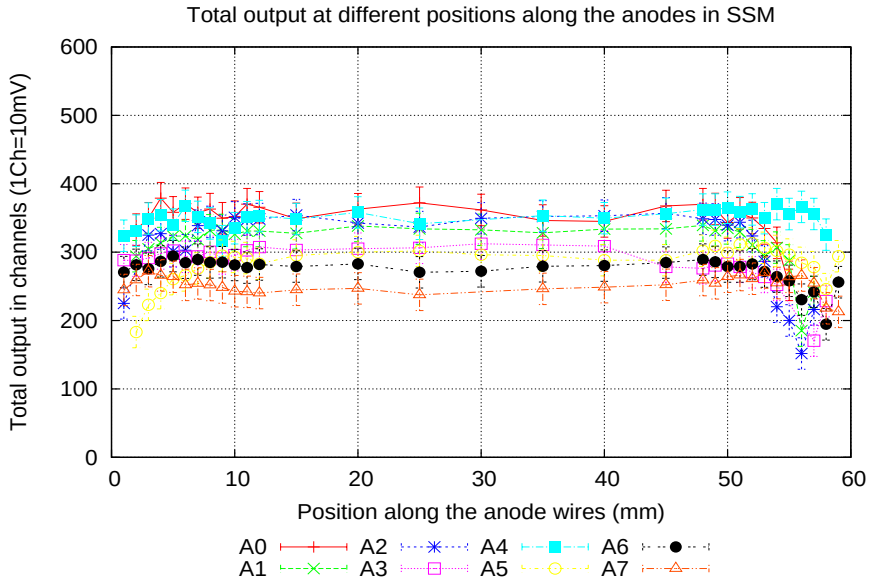

FIGURE 3.11: Plot showing the total output of all the anodes in SSM-Qualification model detector at different positions along the anode wire

visually for any non-uniformity in the diameter, before being wired in the wire module, so that such non-uniformities along the anode wires be minimized as much as possible. In SSM, the energy resolution is 18% at 6 keV which corresponds to a total output of 300 channels (=3 Volts). Therefore, the FWHM is 54 channels which results in sigma of ∼23 channels, which gives the variation threshold for the total output. The errors on the total output plotted in figures 3.11 and 3.12 are ±23 channels.

It is preferred that all the eight anodes give a total output of 300 channels at 6 keV. Therefore, the post amplifier of the respective anodes are fine-tuned to the appropriate gain settings so that the total output is very close to 3 Volts (or 300 channels). Figure 3.12 shows the total output of the anodes after fine tuning of the post amplifiers, so that the total output is within the resolution limits, which are shown as thick black lines in the plot.

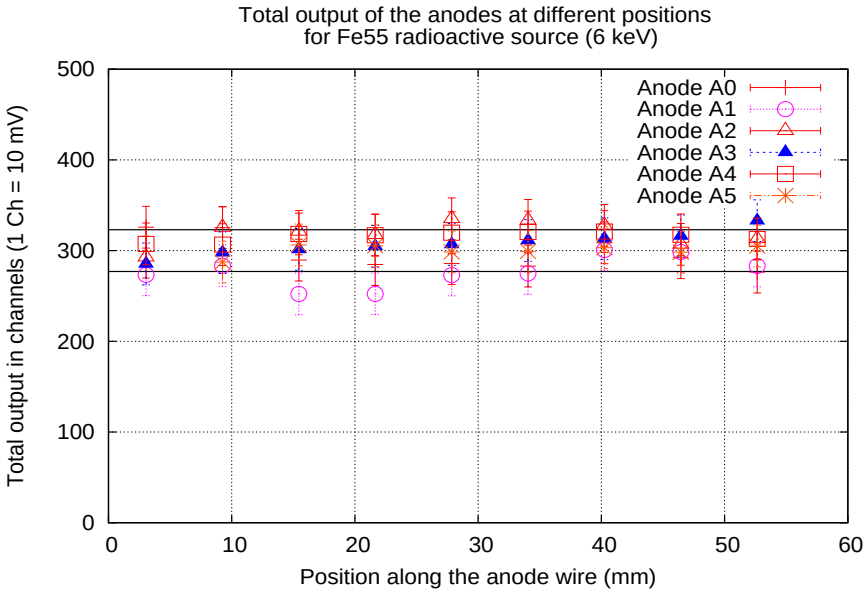

FIGURE 3.12: Plot showing the total output of the anodes after fine-tuning of the post amplifier gain

3.3 Working Principle of SSM

SSM is a position sensitive detector. In a position sensitive proportional counter, the position of an incident photon is derived by the principle of charge division method. The anode wires have significant resistance per unit length, so the charge collected at the anode is divided between the amplifiers at either ends of the anode, as per the resistance seen by the

charge. The anodes in SSM are resistive wires, which have a resistance of 8 kΩ per mm. The proportion of division is related to the position of the incident photon, that is, the ratio of the charge read out on either sides is directly proportional to the position of the incident photon. Ideally, the position of the incident x-ray photon is given by the equation 3.3

$$P = [(Q_L - Q_R)/(Q_L + Q_R)] * (L/2) \tag{3.3}$$

where P is the position of the x-ray incidence, and L is the length of the anode wire. The total charge is divided into Q_L and Q_R according to the resistance seen by it on either sides, where Q_L is the charge read out at the left end and Q_R is the charge read out at the right end. In practice, deriving the position of the incident photon is not that straight forward. The details of deriving the position of the incident photon is discussed in section 3.4.

3.4 Deriving the position of the incident photon

Equation 3.3 gives the position of an incident photon, where the length of the anode wire is required to derive the position. The actual length of the anode wire may not be the same as that of the mechanical dimensions of the wire module. This is because, the anode wires are glued, using conductive silver epoxy, to the conductive grooves placed inside the insulator (kel-F) which is in turn inserted into the wire-module of the detector. Since the anode wires are glued, the start and end points of the resistive wire which defines the length, varies from wire to wire. Thus, it is not possible to get the length of the anode wire from the mechanical dimensions of the detector. Therefore, it is necessary to know the electrical length of the anode wire (which is the length seen by the charge cloud) to derive the position of photons incident on the detector.

3.4.1 Deriving the length of the anodes from the measured outputs

It is necessary to know the electrical start and end points of the resistive anode wires inside the wire module, to derive the actual electrical length of the anodes. Studying the ratio of the left and right output pulses for a collimated X-ray source placed at different positions along the wire helps in estimating the electrical end points of the anodes. Tests were conducted with collimated ^{55}Fe source placed at every 1 mm of the anodes, for the entire length(from 2 mm to 58 mm with respect to the detector plane). The positions at which the collimated ^{55}Fe source is placed along the anodes at every 1 mm are defined as per the geometric or the mechanical co-ordinate of the detector.

The data acquired for every position contains the left and right amplitudes of every photon incident on the anode wire at that position. The charge ratio which is the ratio of the left output to the total output for every photon is calculated and binned to get a spectrum of charge ratio. The peak of this charge-ratio spectrum is considered as the charge ratio value for that particular position. Similarly the charge ratio for all the positions along the anode is derived. The charge ratio values are plotted against the geometric positions (assumed position, i.e the position with respect to the detector co-ordinate) along the wire. This data is fitted with a straight line (y = mx + c), where y is the geometric/mechanical position and x is the charge ratio (L/(L+R)). The absolute value of the slope of the straight line fit gives the actual length of the anode (the electrical length) as seen by the charge cloud. The intercept gives the extended length of the anode beyond the geometric end point (beyond 60 mm) of the anode wire.

Similarly, the procedure explained above is followed using the charge ratio of the right output to the total output. The straight line fit to the charge ratio vs position gives the length of the anode wire which should be the same as that derived from the charge-ratio of left to total output. The intercept of the line gives the extended length of the anode beyond the geometric start point (beyond 0 mm) of the anode wire.

The intercepts obtained from the fits of both options of the charge ratios (L/(L+R) or R/(L+R)) give the extended length of the anode wires at both the ends of the anode.

If the charge ratio is (left/total), the slope is negative slope and the absolute value of the slope is the actual length of the anode and the intercept is equal to 60 mm plus the length of the wire beyond 60 mm at the right end. For example, for the anode 1, the intercept with respect to (left/total) vs position is 61.8 +/- 0.11 and the intercept with respect to (right/total) vs position is -11.66 +/- 0.14 as shown in figure 3.13 and 3.14. This means that the actual (electrical) start point of the wire is -11.66 mm and not 0 mm and the (electrical) end point of the anode is not 60 mm, but 61.8 mm. Similarly, straight line fitting to all the eight anode wire data sets give the actual electrical length of the wire, along with the offsets in the start and end points of the anodes. Figure 3.13 shows the plots of source position (which is the geometric position) as a function of charge ratio (right output/total output) and the straight line fits to the data, for all the eight anodes in the engineering model of SSM where the geometric length of the anodes are 60 mm. Similarly figure 3.14 shows the plots of source position as a function of charge ratio (left-output/total-output) and the straight line fits to the data for all the anodes. Figure 3.15 shows the overlayed plots of figures 3.13 and 3.14, so that the lengths of the anodes with the start and end points (the intercepts) within the wire module is shown clearly. Figure 3.16 shows the experimentally

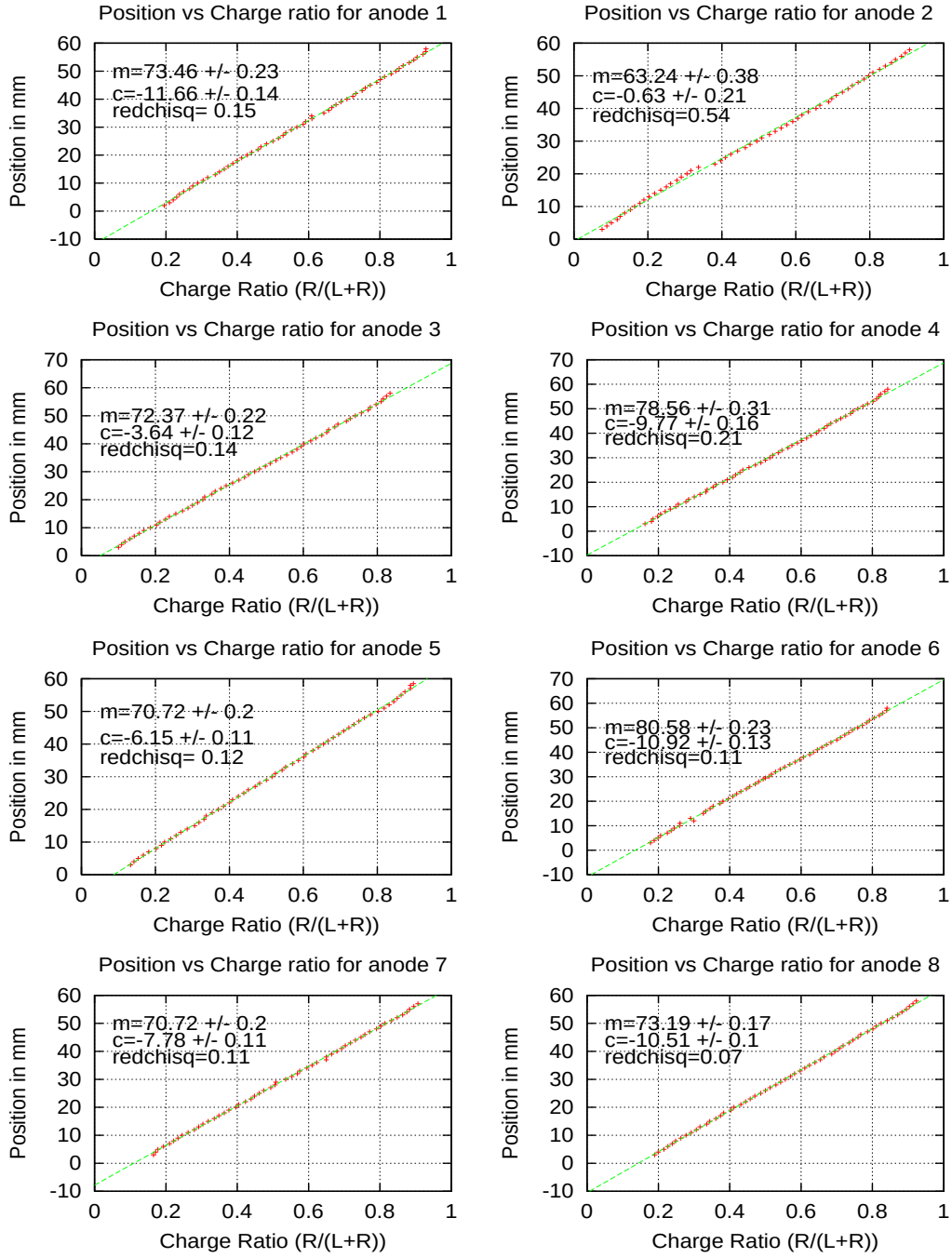

FIGURE 3.13: Figure shows the plots of charge ratio (right/total) vs position on the anodes in SSM detector.

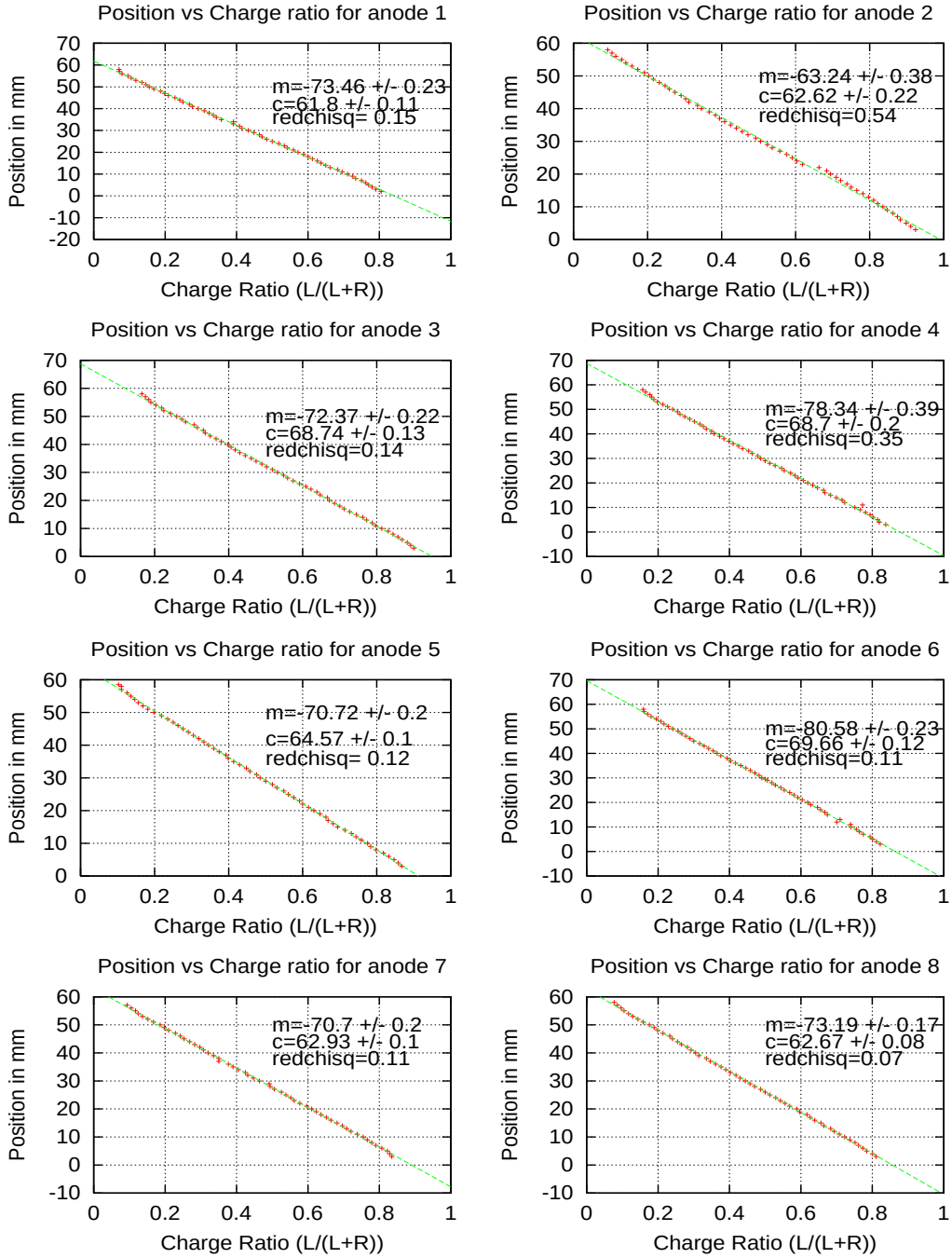

FIGURE 3.14: Figure shows the plots of charge ratio (left/total) vs position on the anodes in SSM detector.

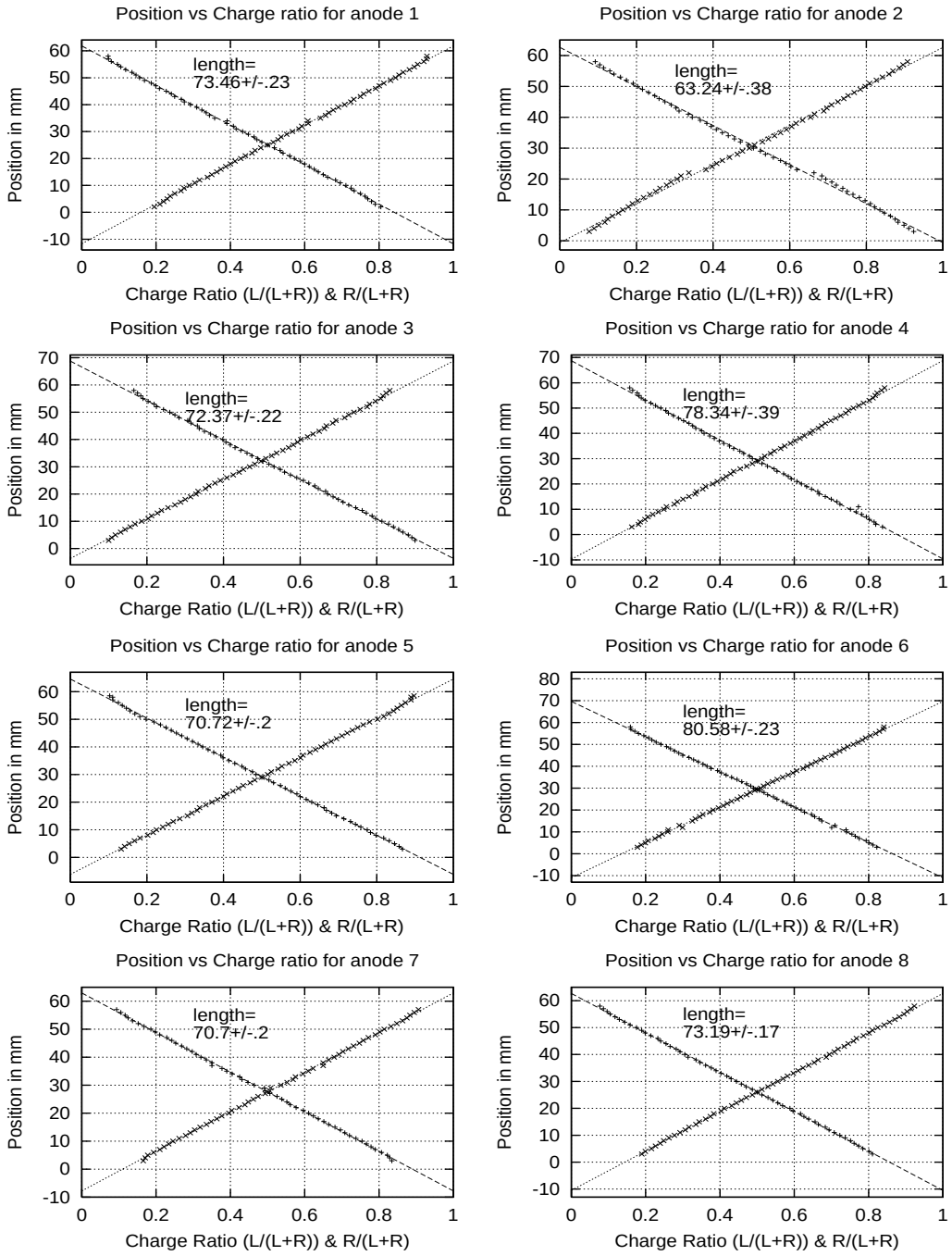

FIGURE 3.15: Figure shows the actual length of all the anodes in the engineering model of SSM detector. The Y-axis between the two intercepts of the straight lines give the length of the anodes and the intercepts give the electrical start and end points of the anode wires.

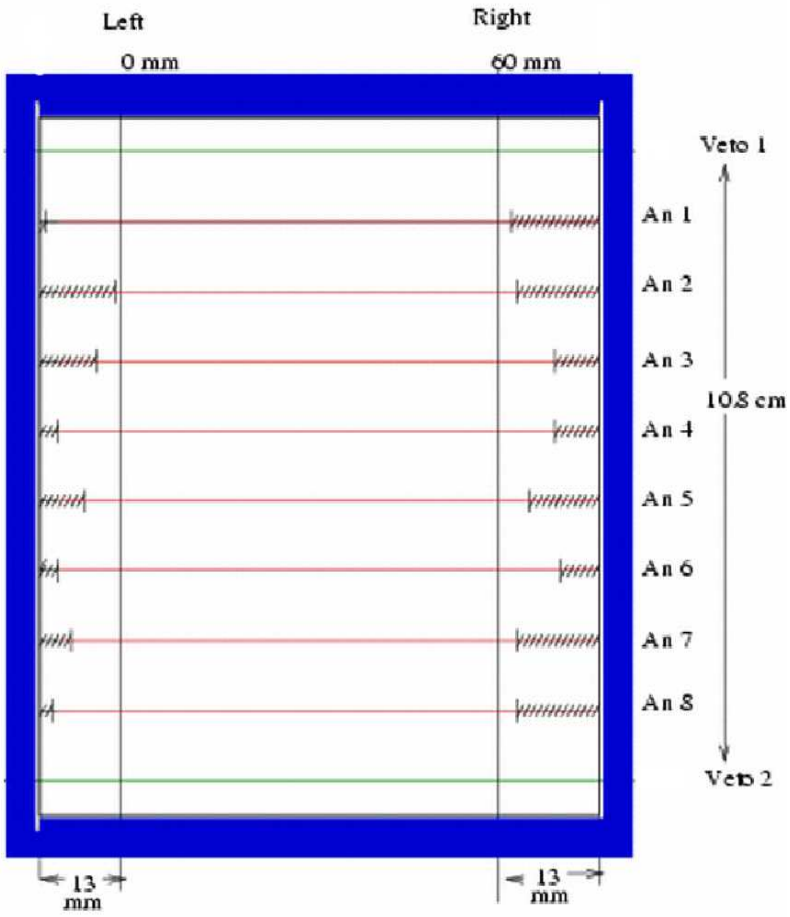

FIGURE 3.16: Figure shows the schematic of the wire module of SSM with the electrical start and end points of the anodes and geometric start (0mm) and end (60mm) of the anodes.

derived schematic of the wire module of one of the SSM detectors, with the actual start and end points of all the anodes. The shaded part of the anodes indicate the contact of the wire with the silver epoxy. The red lines are the 8 anodes and the two green lines are the veto wires. Table 3.1 gives the actual length of the anode wires and the start and end points at both the ends of the anodes.

The calculated length, which can be termed as the electrical length, of the anode wires are different from the geometrically defined length. This results in deviations in the actual positions from the theoretically expected position as calculated by equation 3.3, for every incident photon. The electrical position of the incident photon is different from the geometric position of incidence. The correction factors to convert the electrical position to geometric position are called the anode calibration constants. Every anode has its calibration constants and the position of every photon incident on an anode is calculated using

Anode num.	Actual length in mm	Start point(Left) in mm	End point(Right) in mm
1	73.46 +/- .23	-11.66 +/- .14	61.8 +/- .11
2	63.24 +/- .38	-0.63 +/- .21	62.62 +/- .22
3	72.37 +/- .22	-3.64 +/- .12	68.74 +/- .13
4	78.56 +/- .31	-9.77 +/- .16	68.7 +/- .2
5	70.72 +/- .2	-6.15 +/- .11	64.57 +/- .1
6	80.58 +/- .23	-10.92 +/- .13	69.66 +/- .12
7	70.72 +/- .2	-7.78 +/- .11	62.93 +/- .1
8	73.19 +/- .17	-10.51 +/- .1	62.67 +/- .08

TABLE 3.1: Table gives the actual length of the anodes and the actual start and end points on either ends for the engineering model of SSM.

the respective anode calibration constants using the equation 3.4.

$$P = A * (CR) + B \tag{3.4}$$

where P is the geometric position along the anode wire, CR is the charge ratio (either (left/total or right/total or (L-R)/(L+R), which is used in SSM), A and B are the anode calibration constants. This way of deriving the calibration constants for all the anodes in the detector is the position calibration of the detector. Section 3.6 discusses the step by step procedure and the details of position calibration of SSM.

3.5 Calibration of SSM detectors

SSM detectors are calibrated for position and energy response and also for detection efficiency at various energies. The details of on-ground calibration with the experiments conducted on the detectors are discussed in the following sections. The plans for on-board calibration are discussed in the next chapter. There is no radio-active source placed in SSM for on-board calibration. The Crab nebula, which is a standard celestial calibration source, can be used for on-board calibration. The Crab nebula is generally used for on-board calibration as its energy spectrum does not vary with time. Details of on-board calibration of SSM using Crab is discussed in section 4.7 of chapter 4. The following sections discuss about the position calibration of SSM.

3.6 Positional Calibration

The position of a photon incident on the detector is determined from the ratio of the charge collected on either sides of the anode. It has been observed that for photons incident at the geometric centre of the anode, the left and the right output amplitudes are not the same and hence the calculated position using the charge ratio from the output pulses using the equation 3.3, does not match with the geometric position, as discussed in section 3.4.1. Therefore, it is required to calibrate the detector for its positional response and to get the correction factor, which are called the anode calibration constants, with respect to every anode in the detector. The anode wires are tested at every 1 mm along the length with collimated ^{55}Fe source and the non-uniformity is studied. In addition, the data from these tests are used to derive the anode calibration constants. Various experiments are carried out to verify the derived calibration constants. The details of the experiments and the results are discussed. The steps involved in positional calibration are discussed in the following sections.

3.6.1 Deriving the anode calibration constants

The collimated ^{55}Fe source is placed at every 1mm position of the anodes and the data is acquired for two minutes each. The data contains the left and right amplitude values for all the photons detected on the anode. For every photon incidence, using the left and the right outputs measured, the charge ratio (L-R)/(L+R), which is termed as observed-charge ratio, is calculated. The distribution of observed-charge ratio for a collimated beam of X-rays, at a particular position along the anode, is a Gaussian as shown in figure 3.17. This distribution is fit using Gaussian function and the peak of the distribution (called the observed-charge-ratio peak) is estimated for different source positions along the anode wire. Figure 3.17 shows the plot of counts-vs-charge ratio at different positions along the anode wire, which are fitted with Gaussian function, to derive the peak value of observed-charge ratio corresponding to that position. Thus, the observed-charge-ratio for different positions along the anode is derived.

Now, the geometric source position is plotted as a function of observed-charge-ratio peak. This data is fitted with a straight line as shown in figure 3.18. The constants derived from the straight line fit to the data gives the calibration constants for the anode. In this way, the calibration constants of all the eight anodes in SSM detector are derived. Figure 3.18 shows the fit to derive the anode constants for one of the anodes.

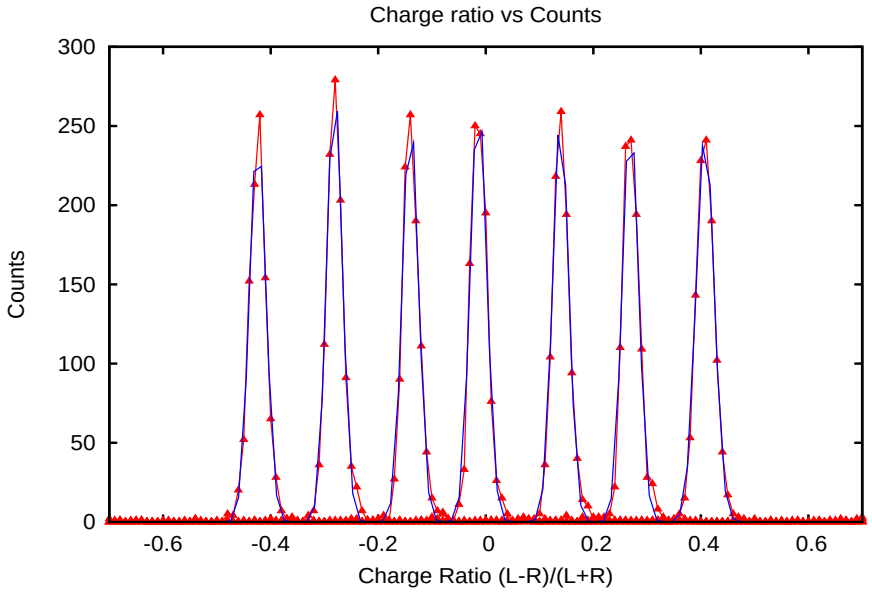

FIGURE 3.17: Distribution of counts as a function of observed-charge-ratio and the respective Gaussian fit functions

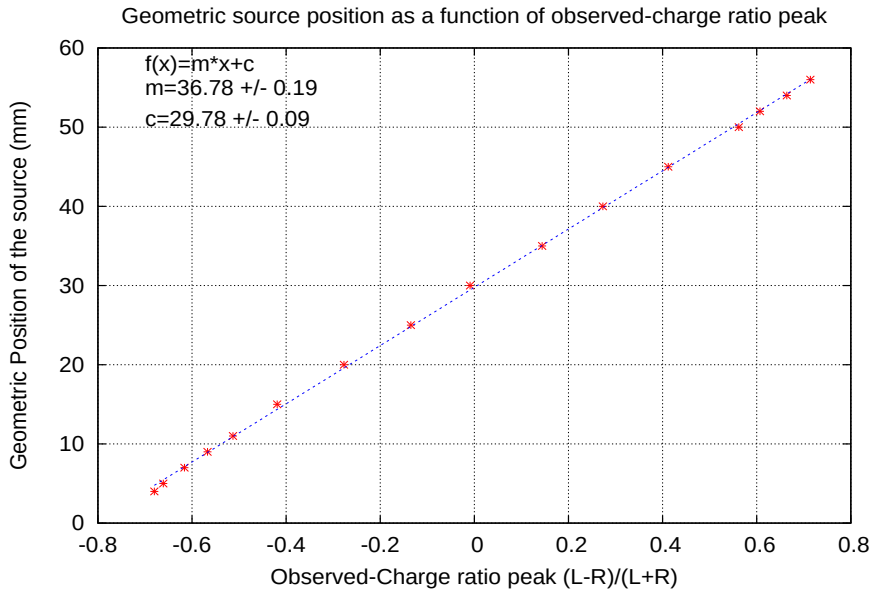

FIGURE 3.18: Straight line fit done on position-vs-observed-charge ratio peak to derive the anode constants

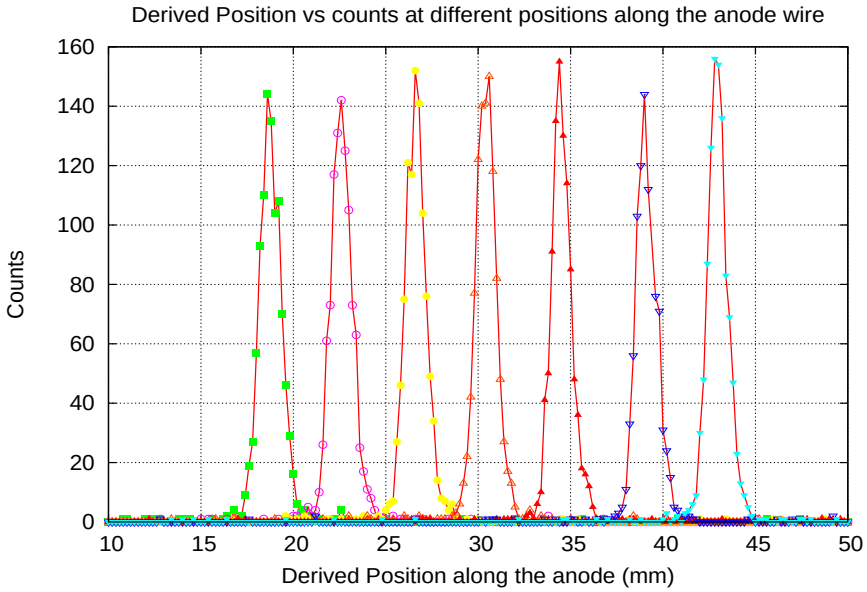

FIGURE 3.19: Position (derived position) vs counts at different positions along an anode wire

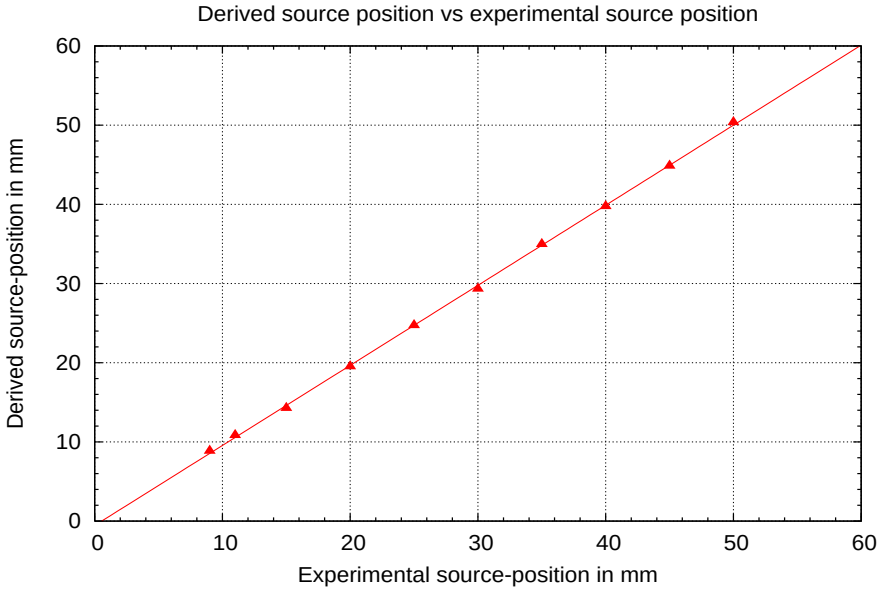

FIGURE 3.20: Plot showing the comparison between derived and experimental source position at different positions along the anode wire.

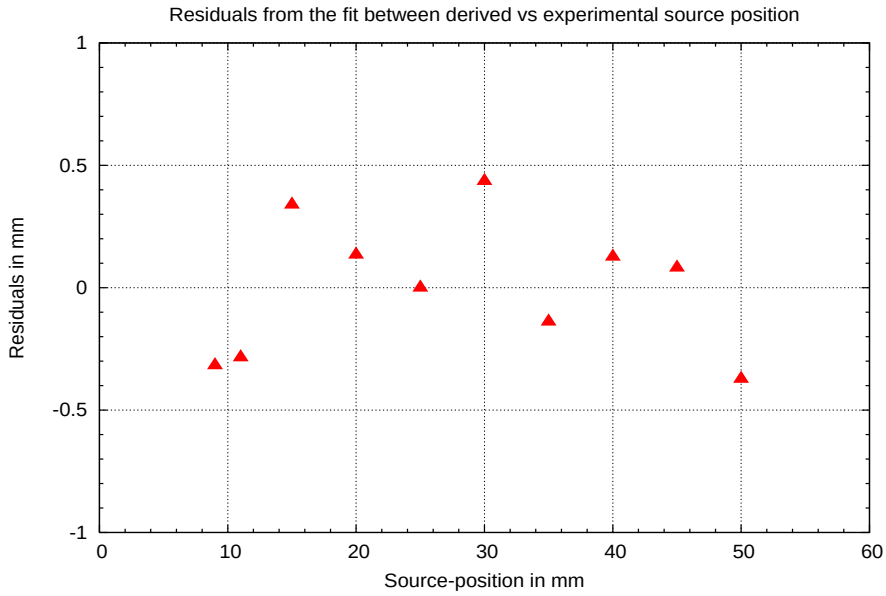

FIGURE 3.21: Deviations of the derived positions from the experimental source positions along the anode wire.

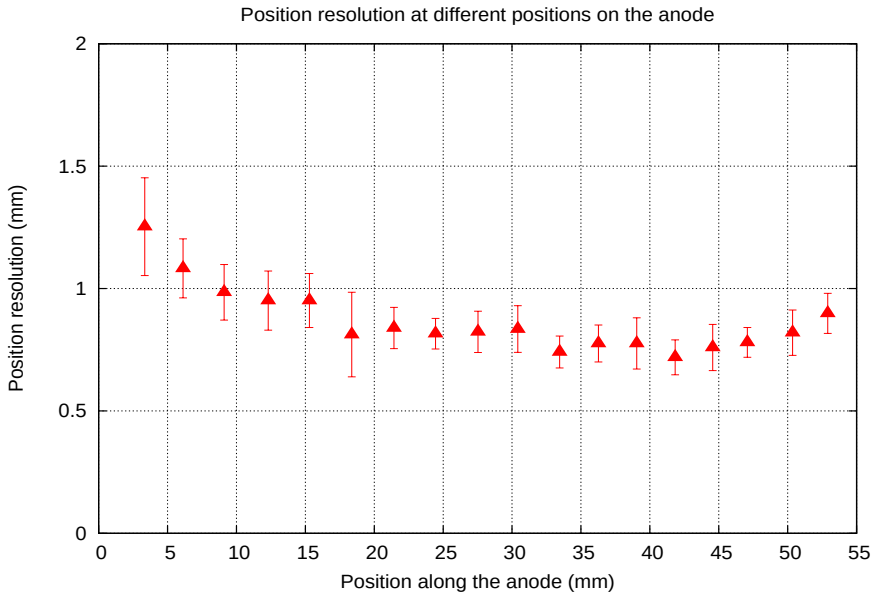

FIGURE 3.22: Position resolution at 6 keV photon energy, at different positions along the anode wire; this is derived from the Gaussian fits made on the position-spectra shown in figure 3.19

Calibration constants are derived for all the anodes and these are used to calculate the position of every photon hitting the detector plane. Using these constants, the position spectra are derived for the collimated source placed at different positions along the anode wire. Figure 3.19 gives the distribution of counts against different positions for collimated ^{55}Fe source placed at different positions along the anode wire. Fitting these position spectra with Gaussian function gives the position resolution, which is the FWHM of the Gaussian, at different positions along the anode wire. Figure 3.22 gives the variation in position resolution at different positions along the anode wire.

It is required to verify the derived calibration constants. Therefore, from the fits of the position spectra shown in figure 3.19 the position peaks are estimated and compared with the defined geometric positions of the collimated source. Figure 3.20 shows the comparison of the derived vs experimental source positions. This data is fit with a straight line to estimate the deviations in the derived positions from the experimental source positions. The deviations are shown in figure 3.21. These deviations in the position from the experimental source position is within the position resolution of the detector and hence it is within the tolerable limit.

3.6.2 Verification of the derived calibration constants

It is necessary to verify the calibration constants derived for the detector as per the positional response of the detector. The comparison of the derived source position to the geometric source position as shown in figure 3.20 in the previous section, indicates the correctness of the calibration constants. However, it is necessary to cross verify the calibration constants before continuing with the detailed tests, for which the 'centre-blocked tests' are carried out which is explained in the following sections.

3.6.3 Tests with the open source illuminating the whole detector plane

The open-bare ^{55}Fe source is placed at a height of about 30 cm from the detector plane such that it illuminates the entire geometric area of the detector. The data is acquired for about 30 minutes. The position of every photon on the detector plane is calculated using respective anode constants, corresponding to the anode on which the photon is incident. The position histogram is generated. Figure 3.23 shows the position histogram of few of the anodes in the detector. It can be seen that the counts registered at the ends of the anode are less compared to that at the central region. This is due to end-effects in the engineering model of SSM, which is minimized in the qualification model as discussed in section 2.10.6

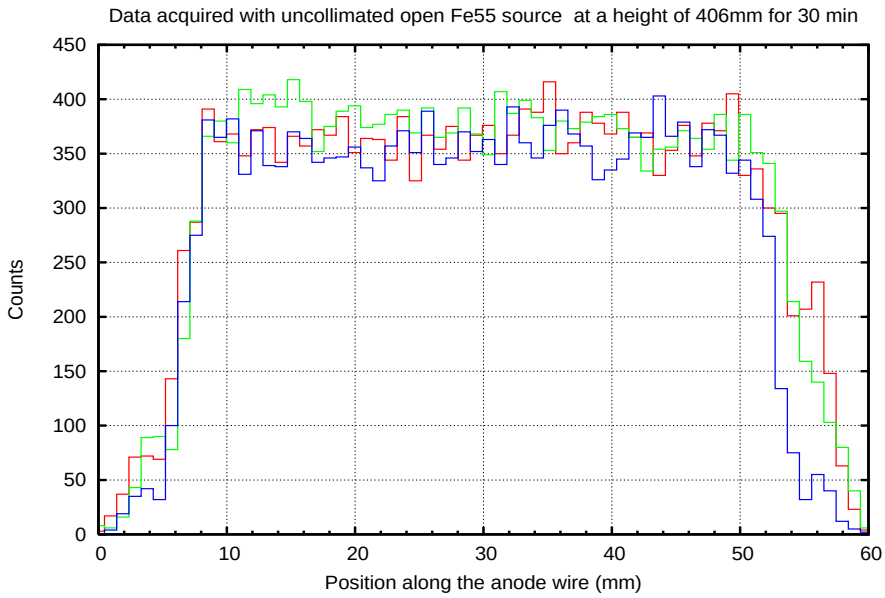

FIGURE 3.23: Position histogram of few anodes in the detector for the ^{55}Fe source illuminating the entire detector plane

of chapter 2. This test of illuminating the whole detector plane is done so that the position histogram from this data can be compared with that got from centre-blocked tests (which is discussed in section 3.6.4) for the central shadowed region.

3.6.4 Centre-blocked tests

The central 20 mm of the detector is blocked with iron bar such that X-ray photons will not be incident on this central 20 mm of the detector. Figure 3.24 shows the schematic picture of the detector plane blocked at the centre. The open-bare ^{55}Fe source is placed at a height of about 30 cm from the detector plane such that it illuminates the entire geometric area of the detector. The data is acquired for about half an hour and the position of every photon incident on the detector plane is calculated using the respective anode calibration constants and the position histogram is generated. The shadow pattern derived with this experimental set-up is shown in figure 3.25. Figure 3.26 shows the 3D view of the position histogram derived from the centre-blocked tests. The central 20mm are shadowed as expected, indicating that the calibration constants are correct.

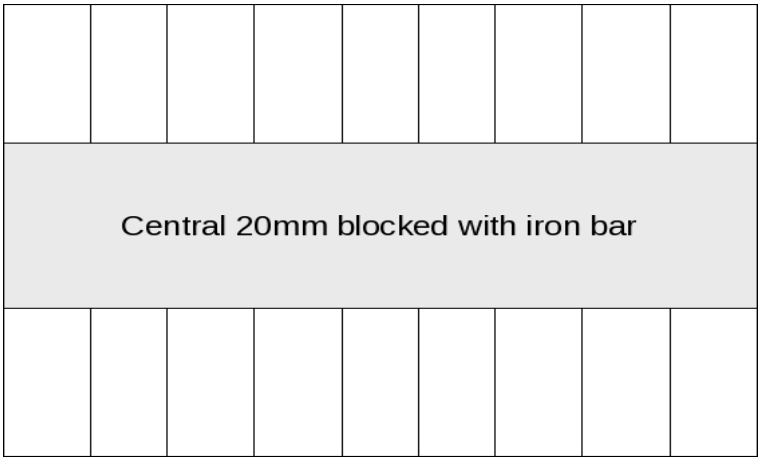

FIGURE 3.24: Schematic picture of the detector plane with the central 20 mm blocked with iron bar.

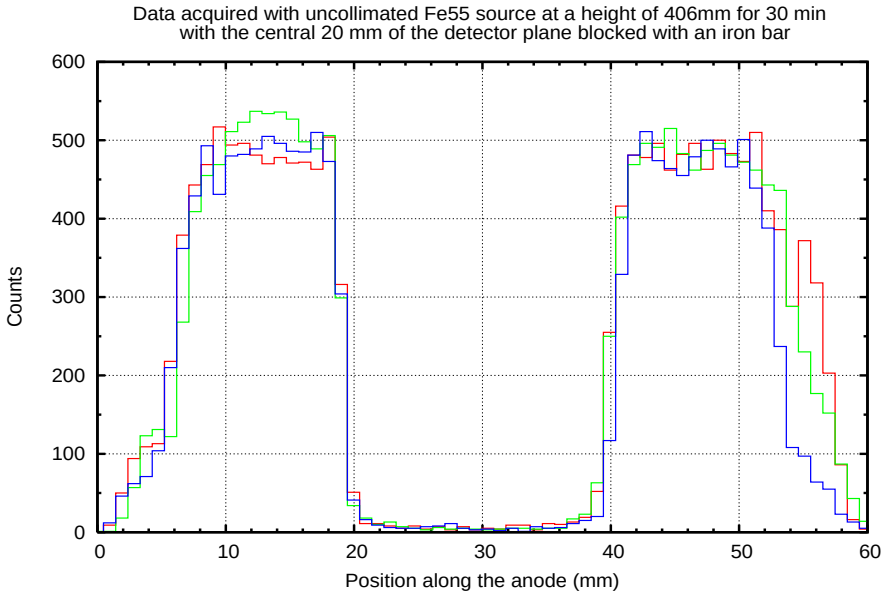

FIGURE 3.25: Position histogram from centre-blocked test

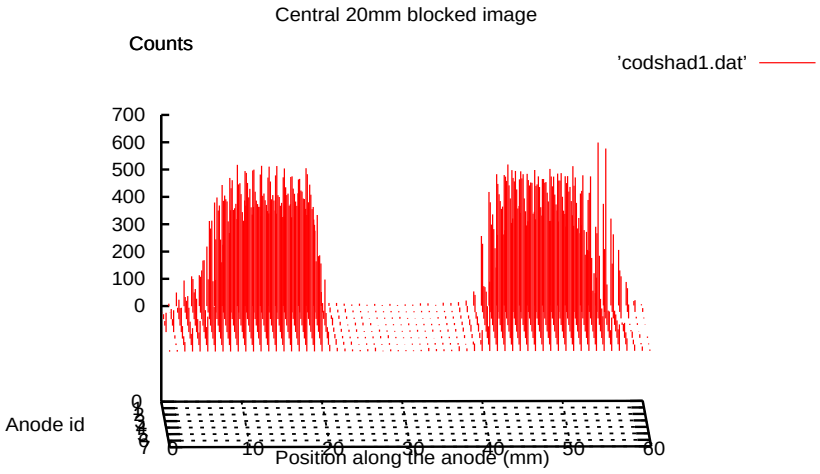

FIGURE 3.26: 3D view of the position histogram from centre-blocked test

3.6.5 Tests with a single mask pattern

Similar to the "centre-blocked test" experiment with the central 20 mm of the detector plane blocked, tests are conducted to get the shadow pattern of a single mask, which is one of the six mask patterns used in the coded-mask for SSM. The mask plate is placed on the detector plane and the X-ray source ^{55}Fe is placed at a height of 50 cm above the detector plane, so as to illuminate the entire geometric area of the detector plane. Figure 3.27 shows the experimental set-up where a single mask plate is placed on the detector plane. Data is acquired for about half an hour in this set-up. The data is processed to derive the shadow pattern of the mask placed on the detector plane. Figure 3.28 shows the shadow pattern of the mask pattern, which is compared with the actual mask pattern with the divergence factor (which is calculated from the ratio of the distances between the detector plane and the source and the source and the mask plate) included in it, which corresponds to the height of the diverging open-bare ^{55}Fe source that was placed at a height of 50 cm above the detector plane. The blue dotted histogram shows the close and open elements of the mask pattern and the red line shows the position histogram which is the shadow of the mask pattern cast on the detector plane. It can be seen in figure 3.28 that the shadow pattern matches with the mask pattern. The open elements of the mask pattern match with the high counts in the position histogram whereas the closed elements match with the relatively less counts in the position histogram. This provides an added proof of verification to the derived anode calibration constants.

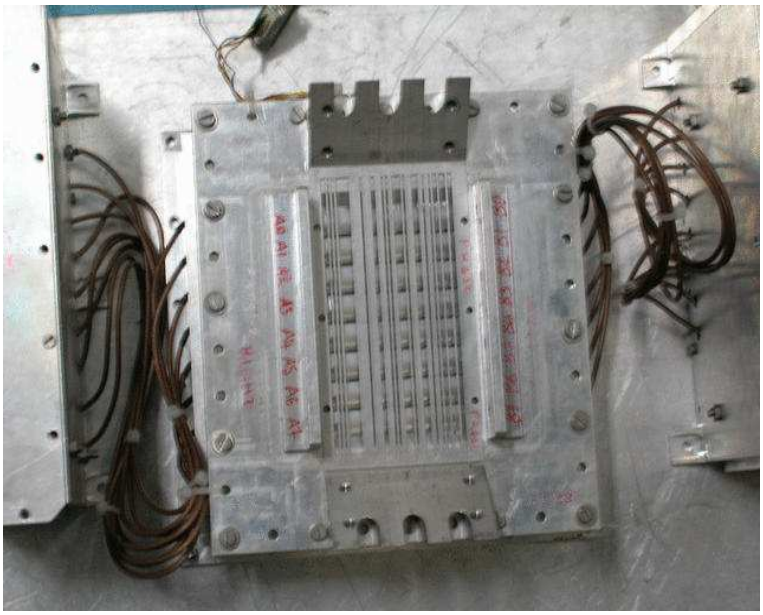

FIGURE 3.27: Single mask plate placed on the detector plane

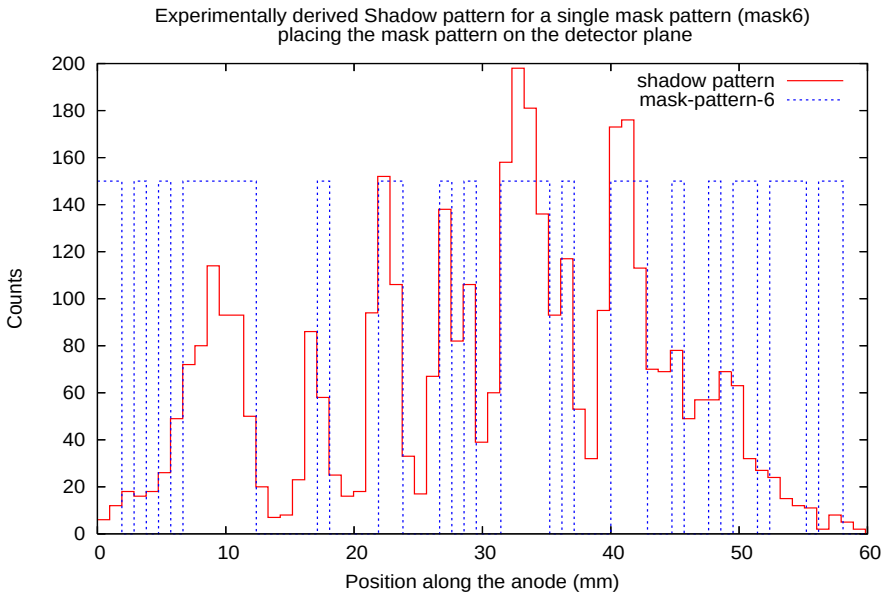

FIGURE 3.28: Shadow of the mask pattern along with the actual mask pattern with the divergence factor included in it.

3.7 Tests to derive the position of the X-ray source

The detector is now calibrated and the verification of the calibration is done by the experiments discussed in section 3.6.2. The prime objective of this instrument is to derive the location of the X-ray source in the sky. In the laboratory, experiments are done with a single X-ray source (an X-ray gun) at a certain position (the centre of the FOV) within the field of view of the instrument. Data acquired is analysed to derive the position of this source.

3.7.1 Experiment to derive the position of source in FOV of SSM

This experiment includes the coded-mask with the collimator placed on SSM detector as shown in figure 3.29. The collimator with the coded-mask which has six unique mask patterns is placed on the detector. The X-ray source (here it is the X-ray gun with high intensity compared to ^{55}Fe radioactive source) is placed at a height of about 2 m. This height is preferred for this experiment, as it is required to have the divergence factor of the source as minimum as possible. The requirement for having a low divergence factor is due to the fact that, as per the principle of coded-mask imaging discussed in section 3.1.3, the complete basic pattern of one of the six patterns of the coded-mask is required for reconstructing the image of the source plane with less coding noise. The X-ray gun which is used as the X-ray source here, gives a spectrum of X-rays and is not a monochromatic source. The current and voltage settings of the X-ray gun are 10 kV and 20 microAmp, so that it produces a continuum spectra of X-rays. The energy range of the continuum is found to be 6 to 10 keV at the SSM detector. Most of the low energy photons in the X-ray spectrum are absorbed due to the 2 m column of atmosphere. Figure 3.29 shows the test set-up with coded-mask and the source held at a height of about 2 m above the detector plane with the help of a pole.

Data is acquired for about half an hour. Position of every photon incident on the detector plane is calculated using the anode calibration constants as discussed in section 3.4. Position histogram is derived for the data.

The arrangement of the six mask patterns above the detector in SSM is such that the detector plane sees half of mask pattern-C and half of mask pattern-D, which are right above it. Therefore, the diverging source of X-rays, the X-ray gun, placed at about the centre of the field of view of the instrument, casts the shadows of the two central mask patterns on the detector plane. The first four anodes (named A_0, A_1, A_2 and A_3) have

FIGURE 3.29: Experimental set-up showing the detector with the coded-mask and the source held at a certain height with a pole

the shadow cast by mask pattern-C, and the next four anodes (named A_4, A_5, A_6 and A_7) have the shadow cast by the mask pattern-D. The shadow of these mask patterns have a divergence factor of 1.18 included in them, as the X-ray source used is a diverging beam of X-rays. The divergence factor is calculated as distance of source from detector plane divided by distance of the source from the mask plate. The X-ray gun is placed at a height of 2029 mm and 1719 mm from the detector plane and the mask plate respectively. The ratio of these two values give the divergence factor, which is 1.18. Figure 3.30 shows the shadow pattern as recorded in the detector plane compared with the actual mask pattern shown in black histogram. Figure 3.31 shows the shadow pattern recorded in the detector with the mask pattern after including the divergence factor. Thus the actual mask pattern with the divergence factor included in it is found to match with the recorded shadow pattern.

Figure 3.32 and 3.33 gives a different view of the shadow pattern on anodes A_0, A_1, A_2 and A_3 along with the mask pattern 3 (aka C) and that on anodes A_4, A_5, A_6 and A_7 along with the mask pattern 4 (aka D) respectively, with the divergence factor included in the mask pattern, for the X-ray source at a height of about 2 m.

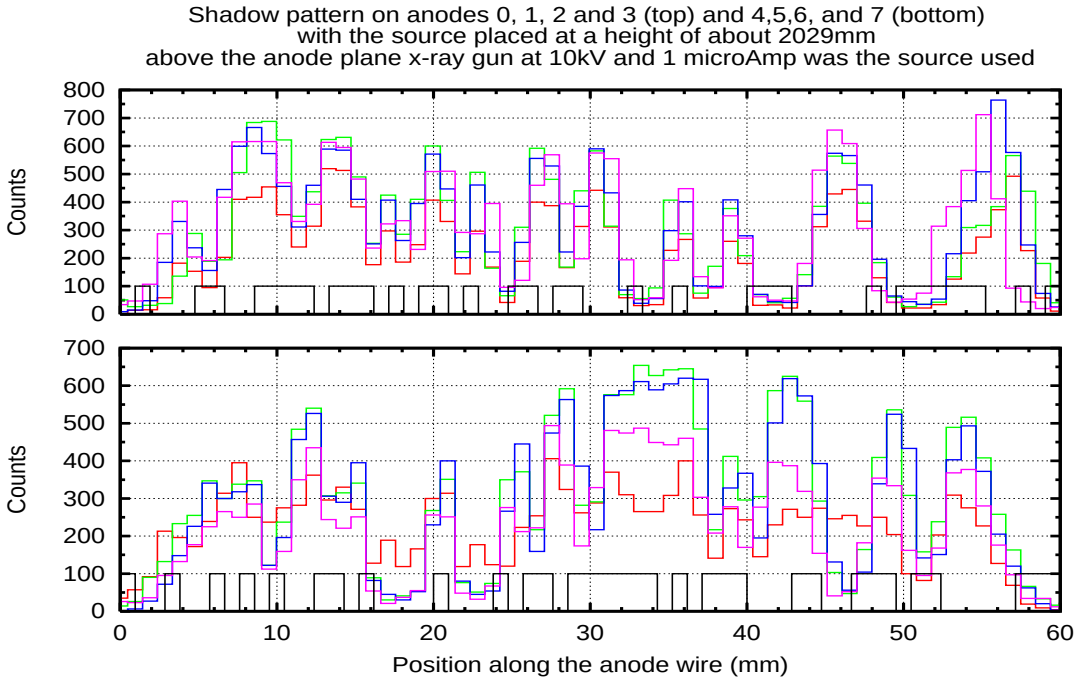

FIGURE 3.30: Shadow of the mask patterns 3 on anodes A_0, A_1, A_2 and A_3 and shadow of the mask pattern 4 on anodes A_4, A_5, A_6 and A_7; the black histogram in the figure is the actual mask pattern.

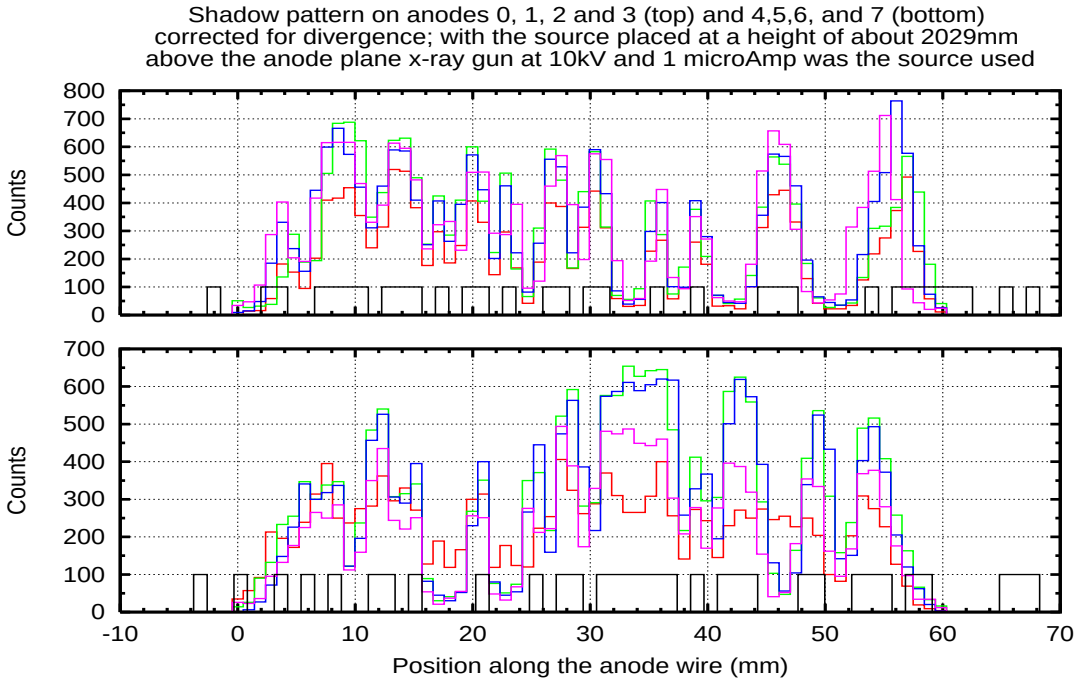

FIGURE 3.31: Shadow of the mask patterns 3 on anodes A_0, A_1, A_2 and A_3 (top panel) and shadow of the mask pattern 4 on anodes A_4, A_5, A_6 and A_7 (bottom panel); the black line in the figure shows the mask pattern with the divergence factor included in it.

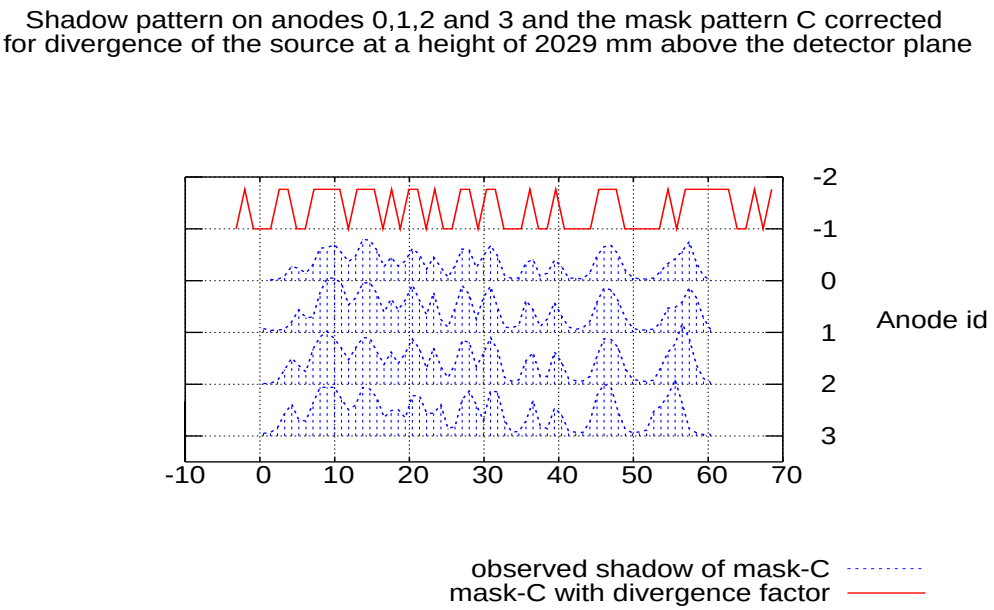

FIGURE 3.32: Shadow of the mask pattern C on anodes A_0, A_1, A_2 and A_3 with the divergence included in it for the X-ray source placed at a height of about 2 m.

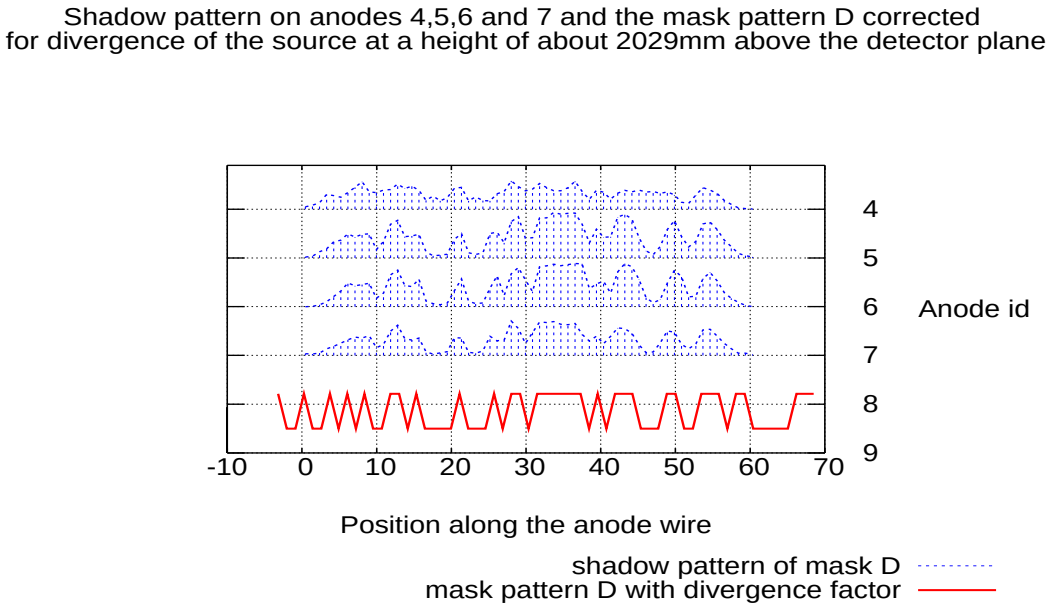

FIGURE 3.33: Shadow of the mask pattern D on anodes A_4, A_5, A_6 and A_7 with the divergence factor included in it, for the X-ray source placed at a height of about 2 m.

The shadow pattern or the position histograms of all the anodes due to a single source at the centre of the FOV of the detector is got in the above mentioned procedure. The ideal requirement is a source which gives a parallel beam of X-rays so that it produces the shadow of the whole mask pattern on the detector plane. Since getting a parallel source of X-rays is difficult, the source is placed at a sufficiently larger distance (about 2 m) from the detector plane, so that the divergence be small enough that almost the whole shadow of the mask pattern is cast on the detector plane.

3.7.2 Deriving the source position

The position histograms derived experimentally are fitted with the simulated position histograms for a single source in the FOV, but for different locations. The data is run through iterative auto-correlation to correlate the experimentally observed position histogram and the simulated position histogram for the source at different locations in the FOV of the detector. The best fit gives the location of the source in the FOV of the detector and thus the position of the source is derived. The algorithm used is "Richardson Lucy Algorithm" to do an iterative fit to the position histogram to get the source position. The details of this algorithm is not discussed here, as it is outside the purview of this work.

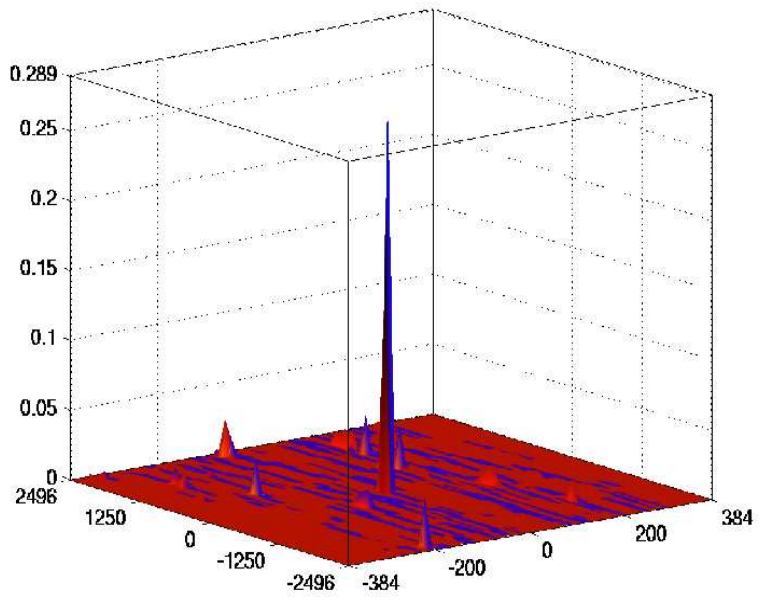

FIGURE 3.34: Surface plot of X-ray sources in the field of view of the detector for the X-ray source placed at a height of about 2 m

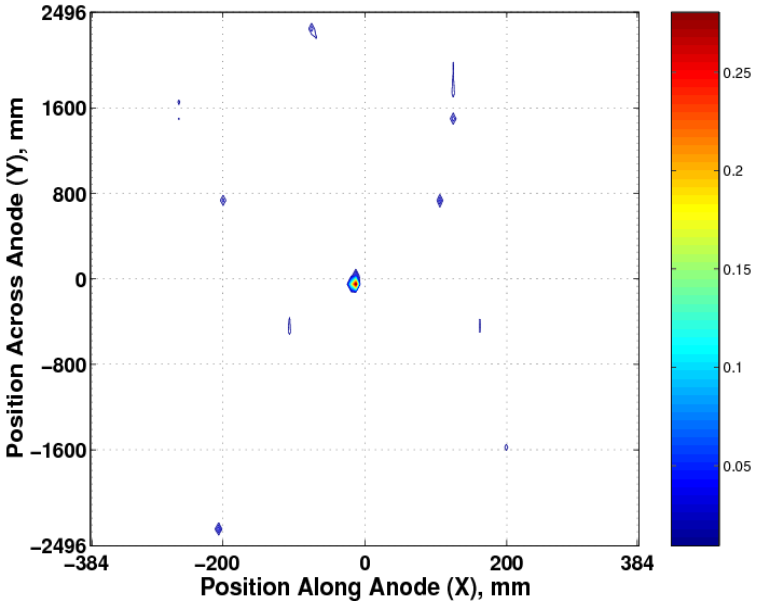

FIGURE 3.35: Contour plot of X-ray sources in the field of view of the detector, contour of the surface plot shown in figure 3.34

Figure 3.34 shows the surface plot of the sources in the field of view of the detector, for the source placed at a height of about 2 m and figure 3.35 shows the contour plot of the field of view for the same source. These two figures give the sources in the field of view of SSM detector. The image plane at a height of 2 m from the detector plane is divided into a number of pixels There are 125 pixels along X (i.e. along anode) and 55 pixels along Y (across anodes). The size of pixel along X is 6.2mm and 78.54mm across anode (Y). On the detector the binning is done at 63bins/anode (i.e. 0.95mm is the pixel-width along X, this is equivalent to the smallest element of the coded-mask). The pixel-width along Y, on the detector is the spacing between the anode wires which is 12mm. The images show the presence of a single dominant source at the centre of the FOV, as expected. The experiment was carried out with the X-ray gun at the centre of the FOV of SSM detector. It can be seen that the surface plot of the sources for the source placed at a height of about 2 m has a single dominant peak at the centre of the FOV (with a slight deviation in the source position from the centre of FOV, which is within the error limit) for the single source, along with small spurious peaks around it. These unwanted spurious peaks present in the surface plot could be due to the error in the divergence factor considered as well as due to small errors in the calibration constants etc. It is also true that due to the divergence factor of the X-ray source, the shadow of the whole mask pattern is not cast on the detector, which can be seen clearly in figures 3.32 and 3.33, where the experimentally derived position histograms do have the entire pattern of the mask. Hence, the auto-correlation of the shadow with the

mask pattern does not yield a single peak function corresponding to the single X-ray source in the field of view as per the principle of coded-mask imaging.

A parallel beam of X-rays will produce a single peak for a single source in the field of view of the detector, as it will cast the shadow of the whole mask pattern on the detector plane. While SSM is on-board, every source it observes, except extended sources like SNRs, Cluster of Galaxies etc., will produce a parallel beam incident on it, and hence the shadow of every mask pattern will be a complete pattern. Therefore, the auto-correlation of the observed position histograms or the shadow pattern and the simulated shadow pattern will give the positions of the X-ray sources in the field of view of SSM with a low coding noise. Thus the position of X-ray sources are derived.

3.8 SSM Background spectrum

It is equally important to study the background spectrum of the detector. The background spectrum is of two components, one is the external background seen by the detector and the other is the internal background generated by the detector in response to the incident spectrum. The background rejection is done by the principle of anti-coincidence logic in SSM. The veto layer which is beneath the anode layer and at the sides of the anode layer acts as the anti-coincidence unit in SSM. A charged particle incident on the detector will produce charges on the top anode layer as well as in the bottom veto layer, and hence will be rejected by the coincidence logic unit. Simultaneously output pulses from the veto layer and any one of the anodes in the anode layer is rejected. Also any highly energetic X-ray photon of energy greater than 10 keV is rejected as it will produce output pulses of amplitude greater than 5 V, which is above the ULD level for SSM or it can be detected by the veto layer and get rejected.

Experiments are done to estimate the efficiency of veto logic in SSM. The X-ray background in the laboratory is acquired for half an hour under two conditions: 1) with the veto-logic enabled to reject the background counts, 2) with the veto logic disabled so that the anodes in the SSM detector detect the background counts and the data is considered as valid counts and processed without rejecting the events. Figure 3.36 shows the lab background spectrum acquired by SSM detector with the veto-logic enabled and with the veto logic disabled, in which case the anti-coincidence logic is disabled and there is no rejection of any output pulse due to anti-coincidence. The ratio of the integrated counts from both the spectra gives the efficiency of the veto logic in SSM. The ratio of integrated counts of the background spectra acquired with veto-enabled condition to that of veto-disabled condition

is found to be 70%. Experiments have been conducted to increase the efficiency of veto further. When the end-to-end gain (ratio of the output of veto to the input to the CSPA of the veto unit) of veto unit is about half of the anode unit the vetoing efficiency is about 70%. It has been observed that with an increase in the post amplifier gain of the veto unit the efficiency improved. However, for higher end-to-end gain of the veto, the frequency of the saturated pulses in the output of the veto for charged particle hits is high enough to induce noise in the anode output channels. Hence, an increase in the gain of the veto to improve the veto efficiency along with added noise at the anode signals was not preferred. Therefore, the veto efficiency for SSM is 70%.

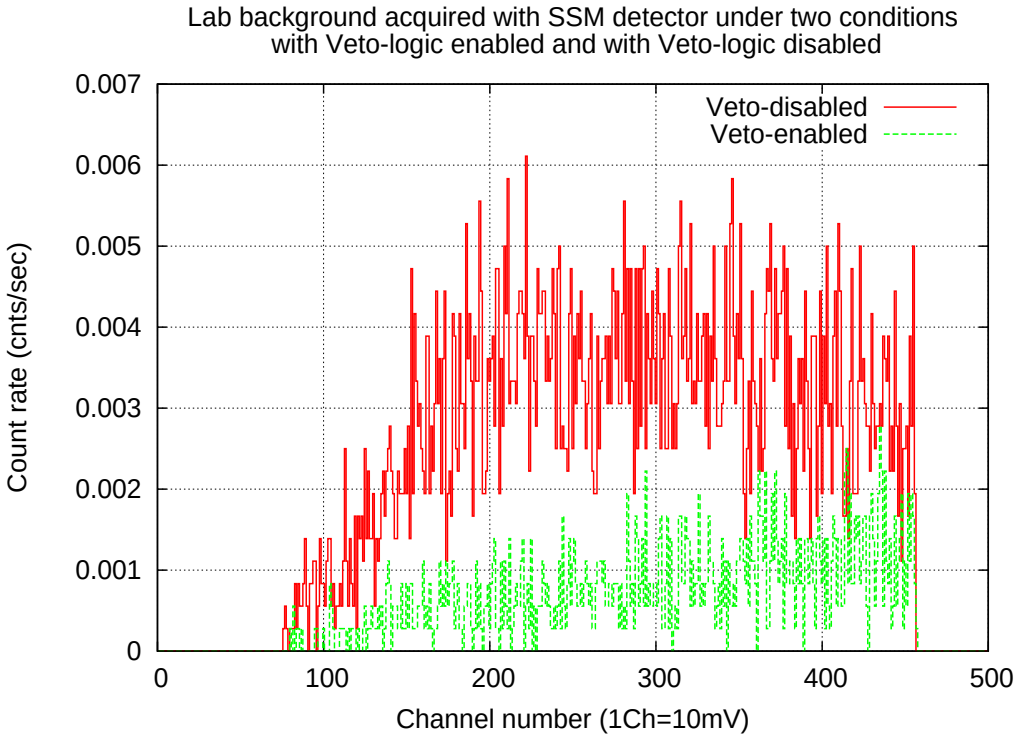

FIGURE 3.36: Plot showing the vetoing efficiency of SSM

3.8.1 Lab-background spectrum

The X-ray background in the lab is mainly that of the cosmic ray spectrum at sea level. Primary cosmic rays are particles with very high energies whose origins in the cosmos are still largely unknown. They consist of energetic protons, electrons, positrons and heavy nuclei. It is believed that these energetic particles are produced during supernovae and solar flares.

In the laboratory, charged particle background is very less. This is due to muons and highly energetic electrons, which form a part of the constituents of cosmic rays. The background count rate seen by detectors at sea level due to incidence of muons is given by equation 3.5 (MIT-report (2006) and references therein).

$$S = 2\pi * A * D * \rho * I_{\nu} \tag{3.5}$$

Here, A is the area of the detector, D is the thickness of the detection medium, ρ is the density of the detection medium and I_{ν} is the intensity of the penetrating particles at sea level given as 0.83×10^{-2} cm^{-2} s^{-1} str^{-1} (MIT-report, 2006)(Rossi, 1948). The background count rate as seen by the SSM detectors in the lab calculated using equation 3.5 is $\sim$0.02139 counts per sq-cm per sec in 180 ° FOV. Figure 3.36 shows the lab background spectrum acquired with SSM with the veto logic disabled so that there is no rejection of any background event happening. There is a cut off at 4.6 Volts due to the ULD settings which cuts off the high energy charge deposition.

The integrated count rate in the background spectrum acquired with the veto logic disabled is 1.128 cnts/sec. Therefore the background counts detected by SSM per unit area per sec is 0.023 cnts/s/cm^2, which agrees with the value calculated theoretically.

3.8.2 SSM background in-orbit

The background while SSM is in-orbit includes the local particle environment of the spacecraft (Charged particle background), induced radioactivity of the spacecraft due to the charged particle background, the cosmic diffuse x-ray background and the internal background of the detector due to the incident spectrum. Since SSM is a low energy X-ray detector, most of the charged particles produced by the spacecraft environment will be detected by the veto layer and will be rejected by anti-coincidence logic. Also, the induced radioactivity of the spacecraft due to charged particle background is likely to produce high energy gamma rays, which are beyond the energy range of operation of SSM and hence will be rejected by ULD threshold condition. The efficiency of background rejection for SSM is experimentally derived to be about 70%. This number will be valid for any calculations of the background count rate while SSM is on-board. This will help determine the errors on the flux detected from the sources while SSM is in-orbit.

3.9 Conclusions

In this chapter, the experiments carried out on SSM detector with the implementation of the design parameters discussed in chapter 2 are discussed. The results from all the experiments done to study different characteristics of SSM detector with reference to the objectives are successful. The working principle of SSM is briefly discussed. Different experiments to calibrate the SSM detector are done. The methodology to derive the position of the source, from which X-rays are incident on the SSM detector is discussed. The positional calibration on SSM detector gives the calibration constants which are required to derive the position of every incident photon on the detector. The steps involved in calibrating SSM detector are given in detail. Various experiments to verify the derived calibration constants are discussed. Experiment to derive the location of the source in the FOV of SSM is carried out and found successful. The background spectrum of SSM observed in the laboratory is studied and the background rejection efficiency of SSM is estimated. This will help understanding the background spectrum while SSM is on-board.

Chapter 4

Development of SSM response

4.1 Introduction

The output of SSM detectors not only give the information of the incidence of a photon, but also the energy of the incident photon, the position of incidence of the photon (which helps derive the position of the source), the intensity of source observed by the detector and the time dependent variabilities in the source observed. For a completely absorbed photon, the ionization in the detector produces charge which gives a measure of the energy of the incident photon. In proportional counters, the amplitude of the output pulse is proportional to the energy of the incident photon. Spectral response of an instrument is the probability that a photon of particular energy is detected in a particular channel number. The response of the detector is the product of the ancillary response file (which accounts for the effective area of the detector) and the redistribution matrix file (which accounts for the redistribution of the photon energy amongst the channels).

4.2 Effective Area of SSM

Effective area of a detector is defined as the geometric area times the detection efficiency. This is one of the factors determining the sensitivity of the detector. Larger the effective area of a detector better is its sensitivity. The effective area of SSM detector (one unit) is shown in figure 4.1 as a function of energy of the incident X-ray photon, for normal as well as 45deg oblique incidence.

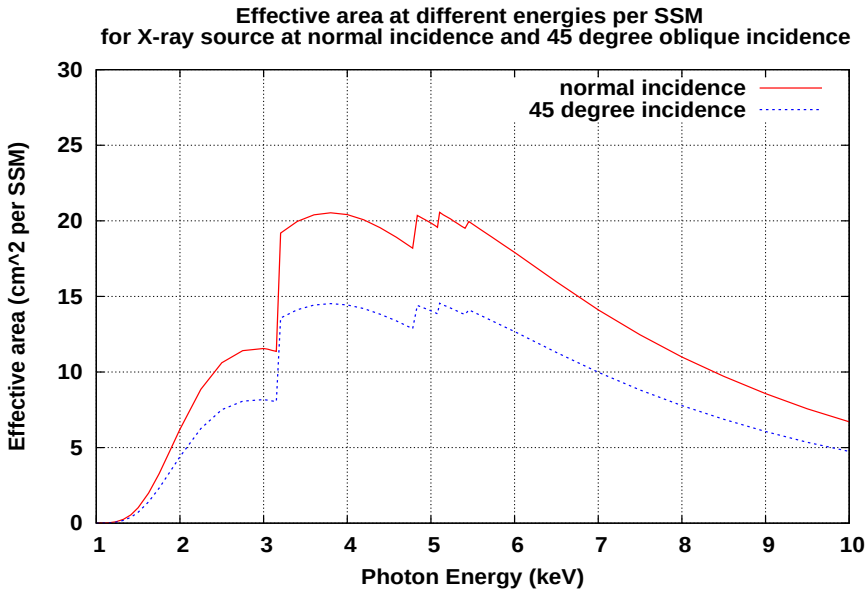

FIGURE 4.1: Effective area of single SSM for normal and oblique incidence

The maximum effective area of SSM is ∼20 cm^2 at a photon energy 4 keV at normal incidence. The effective area is ∼17 cm^2 at 6 keV for normal incidence. For oblique incidence at 45 ° in the direction along the coded-mask where the FOV is 90° at FWHM, the maximum effective area is ∼15 cm^2 at 4 keV.

4.3 Sensitivity of SSM

Sensitivity of an instrument is determined by its effective area, the background counts incident on it and the time of integration. The background seen by the instrument is of two types: the internal background of the detector and the diffuse cosmic X-ray sky background. The internal background of the detector is due to inadequate rejection of high energy γ rays and cosmic rays incident on it. This background intensity is given as B_1 t ϵ, where B_1 is the background counts in counts/s, t is the time of integration, ϵ is the detection efficiency of the detector. The diffuse cosmic X-ray background is that which exists as a background against the discrete sources in the sky. The spectrum of this background is given by

$$dN/dE = NE^{-\Gamma} \tag{4.1}$$

(Revnivtsev, 2003), where $\Gamma = 1.42 \pm 0.02$ (2-20 keV), is the spectral index and the normalization constant N = 9.8 ± 0.3 photons/s/cm^2/keV/sr. The spectral index given here is valid only for the energy range 2 to 20 keV, above which the spectrum becomes steeper.

This background intensity is given as B_2 and is calculated by integrating equation 4.1 for the energy range of interest of the instrument and given as B_2 Ω At ϵ, expressed in units of counts/cm^2/s/sr.

Signal to noise ratio of the instrument can be derived in the following way. Let Ω be the solid angle subtended by the detector in the sky, t be the integration time for which the source is observed, S be the flux density of the source in counts/s/cm^2, A be the area of the detector and ϵ be the detection efficiency of the detector. The number of photons detected from the source is given as SAtϵ. The internal background intensity of the detector due to cosmic rays incident on the detector is B_1tϵ and the number of photons due to the diffuse cosmic X-ray background is $B_2\Omega$Atϵ. The total background is the sum of these two backgrounds which is given by B=B_1 + B_2. The number of counts from a source in a detector depends on the detector area and its detection efficiency. With the exception of about a few hundred bright X-ray sources, majority of the X-ray sources are faint producing only few source counts/second above the background rate. This signal from the source has to be distinguished above the background noise, which is the statistical fluctuations in the number of background counts. Statistically, the fluctuations about the mean value N is just $N^{1/2}$. Therefore, the rms fluctuations in the background signal is given as

$$\Delta N \approx \sqrt{(B_1 + B_2\Omega A)t\epsilon} \tag{4.2}$$

Hence, signal to noise ratio (S/N) is given as

$$S.N.R = \frac{SAt\epsilon}{[(\frac{B_1}{A} + B_2\Omega)At\epsilon]^{1/2}} \tag{4.3}$$

Considering signal to be 3 times the noise, which is 3σ level of detection of the source, the above equation can be written as

$$S = 3\sqrt{\frac{(\frac{B_1}{A} + B_2\Omega)}{At\epsilon}} \tag{4.4}$$

Equation 4.4 gives the sensitivity (Longair, 1992) of the instrument which is a function of energy. The term B_2, which is the cosmic X-ray background and detection efficiency (ϵ) can be given as function of energy. Equation 4.4 can be rewritten as

$$S[E] = 3\sqrt{\frac{(\frac{B_1}{A} + B_2[E]\Omega)}{At\epsilon[E]}} \tag{4.5}$$

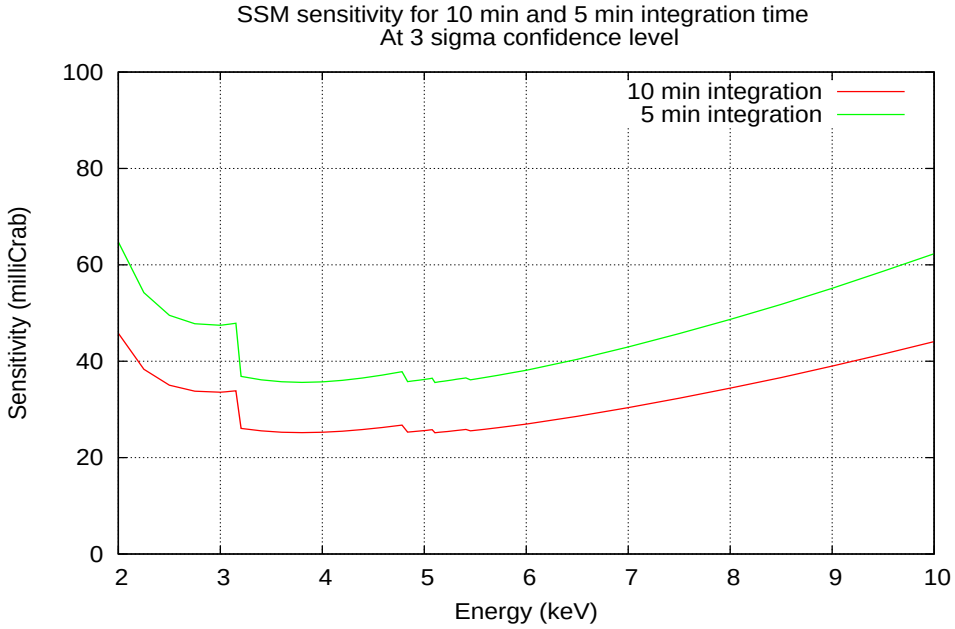

FIGURE 4.2: SSM sensitivity for two different integration times

The sensitivity calculations for an instrument with a coded-mask, like SSM, should include the following factors, in addition to the factors in the above equation 4.4: mask throughput (f), duty cycle of observation (h), correction factor for the source offset from the normal to the plane of observation (g) (Holt & Priedhorsky, 1987). Therefore, the equation for sensitivity for a scanning instrument can be given as,

$$S[E] = 3\sqrt{\frac{(\frac{B_1}{A} + B_2[E]\Omega)}{(gfA)(ht)\epsilon[E]}} \tag{4.6}$$

where, Ω is the solid angle subtended by each mask element on the detector plane.

The mask throughput (f) in SSM is 0.5, the duty cycle (h) is taken to be 1 and the correction factor (g) for the offset is taken as 1, which is the case for a normal incidence. The detection efficiency (ϵ) is a function of energy and varies with energy. The cosmic X-ray background (as given by equation 4.1) is calculated to be 8.57 photons/s/cm^2/keV/sr in the 2 to 10 keV range. The internal detector background will be much smaller than the diffuse cosmic X-ray background and hence negligible. The solid angle Ω is given by area of a single mask element divided by the square of the distance between the detector and the mask plate (which is 0.00122 sr for SSM). The sensitivity for SSM is calculated using equation 4.6 with all the above said parameter values. The sensitivity of SSM is about 30 milliCrab at 6 keV for an integration time of 10 minutes at 3σ. Figure 4.2 shows the sensitivity of SSM at different energies for 5 min and 10 min integration time with a 3 σ level of confidence.

4.4 Energy Calibration

It is necessary to calibrate the detector at different energies in the energy range of interest so that the energy response of the detector is well understood. The SSM detector is calibrated for spectral response at different energies in the range of interest. The energy range of interest for SSM is from 2 keV to 10 keV. The Front End electronics for SSM is devised such that the total output voltage range corresponding to the energy range of interest is 1 Volt to 5 Volts. Here, the total output is the sum of the amplitudes of the left and the right output pulses corresponding to a single photon event detected by an anode in the detector. For a 6 keV source (radioactive source Fe^{55}), the total output of SSM is 3.0 $\pm$ 0.23 Volts. It is required that the total output of the detector is stable over a period of time for a given energy of the X-ray photon. If there is any change in the total output, the HV can be stepped up or down appropriately within the available steps, so that the output is scaled up to the expected value. Thus the gas gain of the detector is maintained so that the energy-channel relation remains the same.

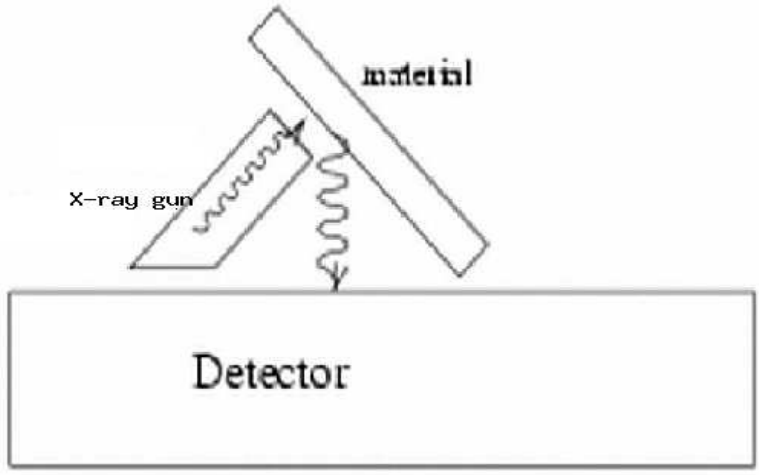

FIGURE 4.3: Experimental set-up to get low energy characteristic X-rays

The detector has to be calibrated at different energies to derive the Energy-vs-Channel relation, the Energy-vs-FWHM relation and the energy resolution at different energies. These relations are required to generate the response matrix of the detector. The position resolution at different energies is also estimated for SSM.

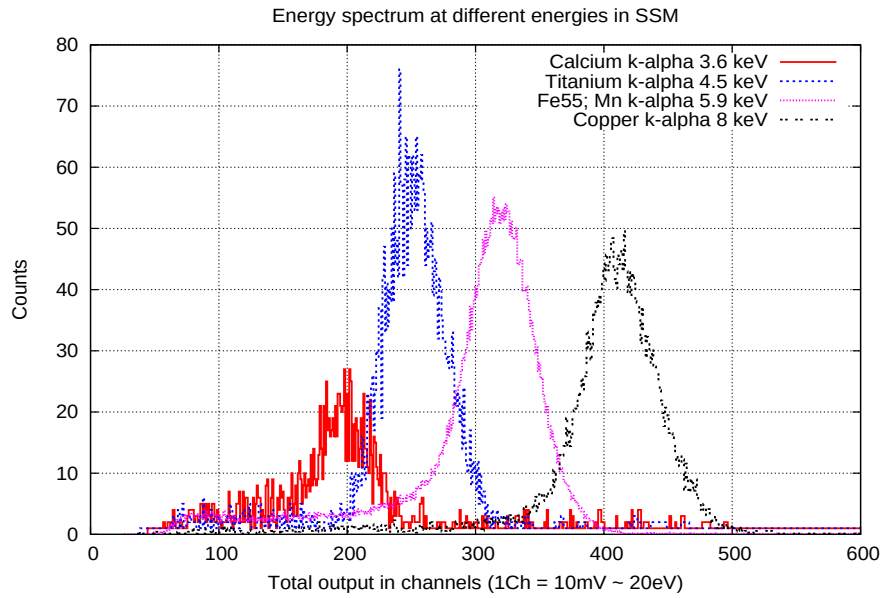

FIGURE 4.4: Energy spectra of different characteristic X-ray sources incident on the detector

4.4.1 Experimental tests at different energies

Radioactive source Fe^{55} gives X-rays of energy 5.9 keV (Mn K_α) and 6.4 keV (Mn K_β). These energies are detected under a single Gaussian in gas proportional counters as the energy resolution is not good enough to resolve the two lines. Characteristic X-rays are used to calibrate the detector at different energies. The photon energies used to calibrate the detector are Ca K_α (3.69 keV), Ti K_α (4.51 keV), Mn K_α (5.89 keV, Fe^{55} radioactive source) and Cu K_α (8.04 keV). The Ca K_α, Ti K_α and Cu K_α are produced by shining the continuum spectrum of an X-ray gun onto foils of respective materials to produce the characteristic X-rays. Thus, the detector is calibrated with four different X-ray sources within the energy range of interest. Figure 4.3 shows the experimental arrangement for the tests with characteristic X-rays within the energy range of interest.

The detector is tested at these energies and the energy spectra are plotted. Figure 4.4 shows the spectra for different energy sources incident on the detector. The peak channels corresponding to different energies are estimated using a Gaussian fit to these different energy spectra. The energy resolution at different energies is also estimated from these fits. Table 4.1 gives the values of FWHM and the centroid for different energies of X-ray sources incident on the detector. The relation between incident X-ray photon energy and

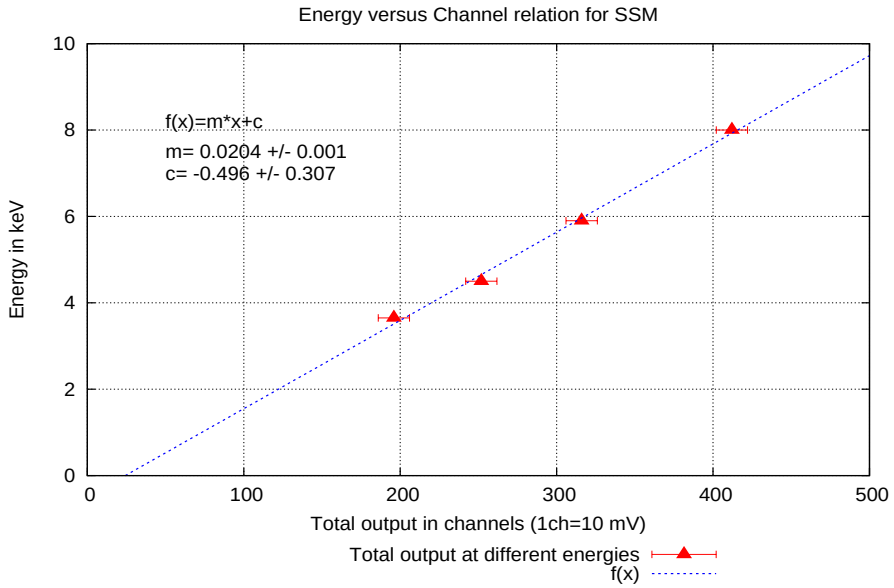

FIGURE 4.5: Plot showing the energy-channel relation for SSM

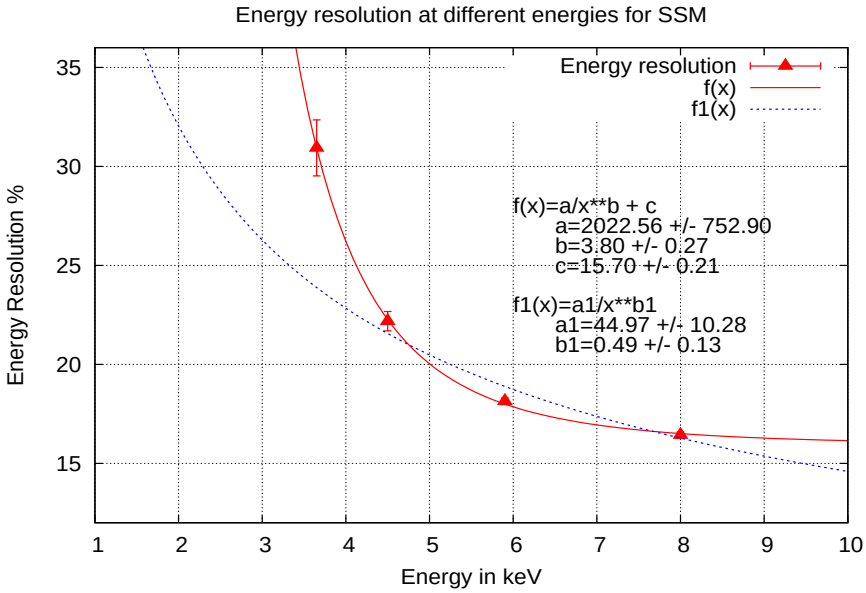

FIGURE 4.6: Plot showing the energy vs energy resolution for SSM

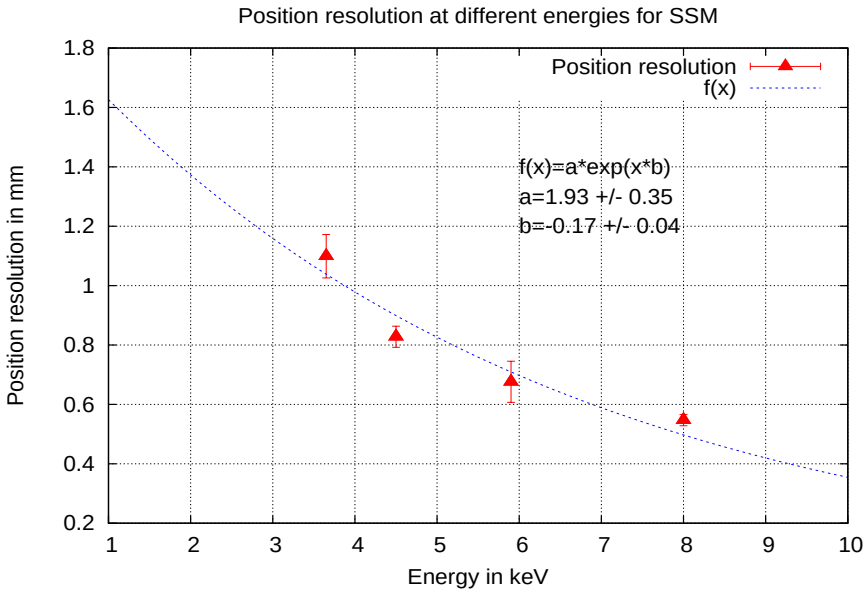

FIGURE 4.7: Plot showing position resolution as a function of energy for SSM

peak channel is derived using a linear fit to the data and is given by equation 4.7.

$$E = 0.020 \times Ch - 0.496 \tag{4.7}$$

where E is the Energy of the incident photon in units of keV and Ch is the channel number. Figure 4.5 shows the linearity between the total output (in channels) and energy of the incident photon. The relation between energy resolution and energy of the incident photon is derived by fitting a function f(x)=a/E^b+c to the data, where a=2022.56 $\pm$ 752.90, b=3.80$\pm$0.27 and c=15.70$\pm$0.21. Figure 4.6 shows the relation between energy and energy resolution at different energies for SSM. The dotted-blue line is the expected function for energy-vs-energy resolution and the observed fit is given by the red line. The fit to the data is found to deviate from the theoretical expectations at low energies. This deviation is attributed to the electronics noise which contributes substantially to the signal-to-noise ratio at low energies. These two relations, the relation between incident X-ray photon energy and the peak channel and the relation between incident photon energy and the FWHM are required as inputs to derive the response matrix for the detector. The details of response matrix for SSM are discussed in section 4.5.

The position resolution at different energies for SSM is also derived from this data. The position of every photon incident on one of the anodes is calculated with the respective anode-calibration constants and a position histogram is generated. The position spectra generated for various energies are fitted with Gaussian function. The FWHM of the fit

Energy (keV)	Centroid (Ch)	FWHM (Ch)	Resolution (%)
3.7	196.0 ± 1.1	60.6 ± 2.7	30.9 ± 1.4
4.5	251.9 ± 0.5	55.9 ± 1.2	22.2 ± 0.5
5.9	316.0 ± 0.3	59.1 ± 0.8	18.7 ± 0.4
8.0	412.0 ± 0.3	67.7 ± 0.6	16.4 ± 0.2

TABLE 4.1: Table giving the values of the centroid, FWHM and energy resolution at various energies for SSM

results give the position resolution at different energies. Figure 4.7 shows the position resolution as a function of energy for SSM.

Energy (keV)	FWHM-energy (keV)	Position-reso (mm)
3.65	1.13 ± 0.05	1.10 ± 0.07
4.51	1.00 ± 0.02	0.83 ± 0.03
5.89	1.10 ± 0.02	0.68 ± 0.07
8.04	1.31 ± 0.01	0.55 ± 0.02

TABLE 4.2: Table giving the values of energy resolution and position resolution at various energies for SSM

4.5 Detector Response

Detector response is proportional to the probability that an incident photon of a particular energy will be observed in a particular channel with respect to the instrument. One of the important properties of a radiation detector is its response to a monoenergetic source, which is called the response function of the detector at that energy. The response function is also called the "Spectral Redistribution Function (SRF)" where the probability of detection of a single energy photon is distributed over several channels in the pulse height spectrum. This SRF depends on the inherent characteristics of the detector such as the random fluctuations that occur during ionization which produces the charge for an incident photon, the noise of the electronics in the instrument and the fluctuations in the operating conditions of the detector. The SRF is modelled for different photon energies from the pulse height spectrum of the detector for the corresponding energies. In general, the SRF for a proportional counter has two elements, the escape peak and the photo peak, which are modelled with Gaussian functions.

4.5.1 Redistribution Matrix File

Detector response is a continuous function of E, while the detector output consists of discrete number of channels. The continuous function is converted to discrete function by creating a response matrix which is also called "Detector Redistribution Matrix" R_D(I,J), given by equation 4.8.

$$R_D(I,J) = \frac{\int_{E_{J-1}}^{E_J} R(I,E)dE}{(E_J - E_{J-1})} \tag{4.8}$$

where I is the detector channel number, J is the energy of the incident photon. Here R_D is the Redistribution Matrix as it describes how a photon of energy $E_{J-1} < E_J$ is redistributed into a number of detector output channels. The file which has the Redistribution Matrix is called the "Redistribution Matrix File" or RMF.

4.5.2 Ancillary Response File

The response of a detector not only depends on the spectral redistribution function, but also on the effective area (ie. the detection efficiency). Effective area of a detector is a function of energy of the incident X-ray photon. The effective area of SSM is discussed in section 4.2 of this chapter. The probability of detecting a photon of energy J in the detector channel I is given by the SRF and this probability is also affected by the effective area of the detector. The file that contains the effective area of the detector for the energy range of interest is called the "Ancillary Response File" or ARF. This file is a matrix with one column giving the effective area at different energy bins.

4.6 Detector Response Matrix for SSM

SSM detector is calibrated at different energies. The details of energy calibration of SSM are discussed in section 4.4. Energy-vs-channel relation and the FWHM at different energies are derived by fitting Gaussian function to the pulse height spectra, the details of which are discussed in section 4.4.1.

4.6.1 RMF for SSM

The pulse height spectra of different monochromatic X-ray sources are analysed and modelled for spectral redistribution function (SRF). SSM has a gas mixture of Ar and Xe as the

detection medium and hence the pulse height spectrum of a monochromatic X-ray source is modelled with three Gaussians: one for the photo peak of the incident X-ray photon, the second Gaussian for the escape peak of Argon for the energy of the incident photon, the third Gaussian for the escape peak of Xenon for the same energy of the X-ray photon. The pulse height spectrum is fitted with three Gaussians. The pulse height spectrum of Fe^{55} radioactive source modelled with three Gaussians is shown in figure 4.6.1. The fraction of the incident photons that contribute to the escape peaks in the pulse height spectrum is very less compared to that of the photo peak. Similarly, the other pulse height spectra are also modelled and the parameters of the Gaussians ie., the FWHM and the normalization values are derived as shown in table 4.3. The pulse height spectra of the sources Cu K_α, Ti K_α and Ca K_α are also shown in figure 4.6.1.

A data file containing the number of Gaussians and the parameters like the centroid value, FWHM and the percentage of counts under each Gaussian is created. This file is given as one of the inputs to the "genrsp", a routine to generate spectral response, which is one of the routines in ftools (A general package of softwares to handle FITS files containing X-ray data (http:heasarc.gsfc.nasa.govftools (Blackburn, 1995)). "Genrsp" is used to generate spectral response of a detector with a number of Gaussians. This routine can be used to generate response for proportional counters, as their energy spectrum consists of a number of Gaussians and there is no need to add any other functional form for the spectral redistribution function. The required inputs for creating the response matrix with 'genrsp' in ftools are

- Energy vs channel relation
- Energy vs FWHM
- the spectral redistribution accounting for the escape peaks.
- the Quantum efficiency as a function of energy

A zeroth order "Redistribution Matrix File" (RMF) for SSM is created with the first derived parameters (like centroid, FWHM and the percentage of photons that fall under the escape peaks) for the three Gaussians used to model the spectra at all the four different X-ray photon energies. The pulse height spectrum of SSM has 1 Channel = 10 mV, which is equivalent of $\sim$ 20 eV and the response is also generated for an energy binsize of 20 eV. The RMF generated using 'genrsp' is verified by simulating the pulse height spectrum for a monochromatic source incident on the detector, for all the four different energies. If there is any discrepancy found in the comparison between the simulated and experimental

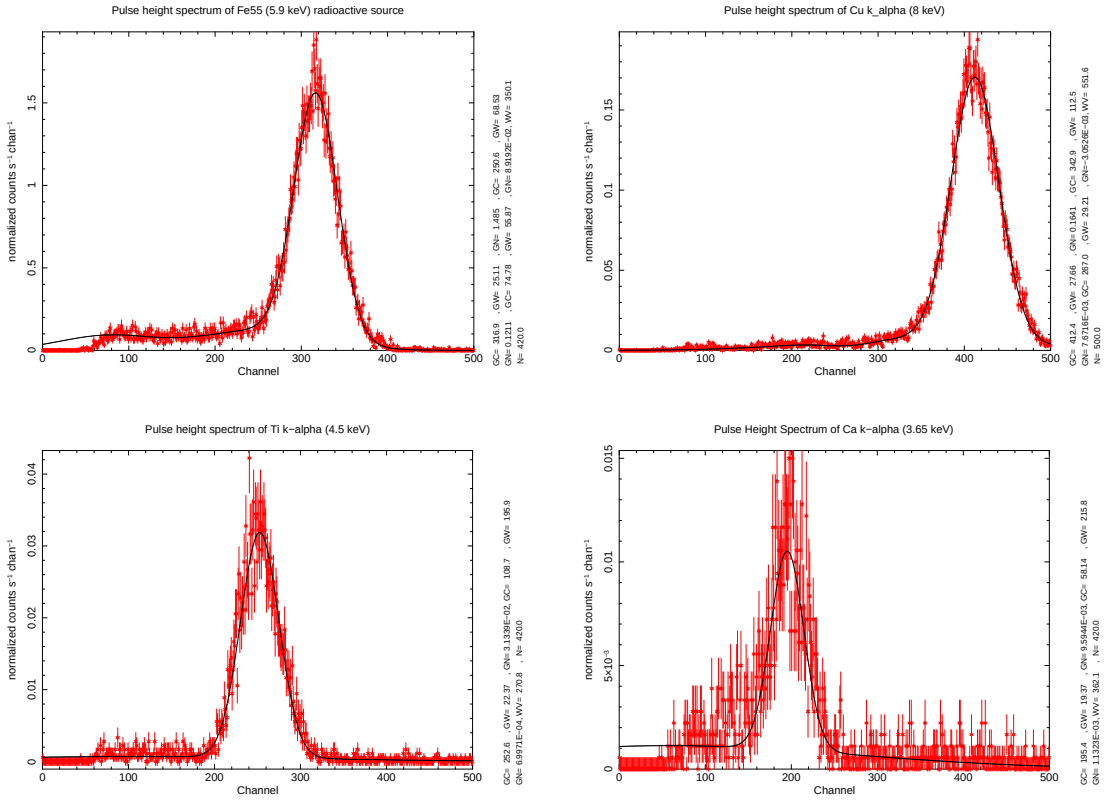

FIGURE 4.8: Pulse height spectrum of Fe^{55} radioactive source, Cu K_α source, Ti K_α source and Ca K_α source modelled with three Gaussians each

Energy	Photo-peak	Sigma	Norm	Ar Esc.Pk	Sigma	Norm	Xe Esc.Pk	Sigma	Norm
3.7	195.4	19.37	9.59e-03	58.14	215.8	1.13e-03	-	-	-
4.5	252.6	22.37	3.13e-02	108.7	195.9	7.0e-04	-	-	-
5.9	316.9	25.11.0	1.48	250.6	68.53	0.1211	74.78	55.87	0.09
8.0	412.4	27.66	0.16	342.9	112.5	7.67e-03	267.0	29.21	3.05e-03

TABLE 4.3: Values of different parameters of the pulse height spectra for four different X-ray photon energies shown in figure 4.6.1

spectra, the differences are noted and the corrections are done to the parameters of the pulse height spectra at the respective energies and these corrected parameters are given as input to 'genrsp' to create the new response file. For example, when the percentage of detected photons in the escape peak with respect to the photo peak in the simulated pulse height spectrum of a particular energy does not match with the observed pulse height spectrum, the correction factor is estimated and the corrected parameters are given as input to 'genrsp'. Thus a new RMF file is generated. A number of such iterations are carried out with respect to the pulse height spectra at different energies. The RMF file which produces the pulse height spectra that matches with the experimentally observed pulse height spectra at all the four energies, is considered as the correct RMF for SSM.

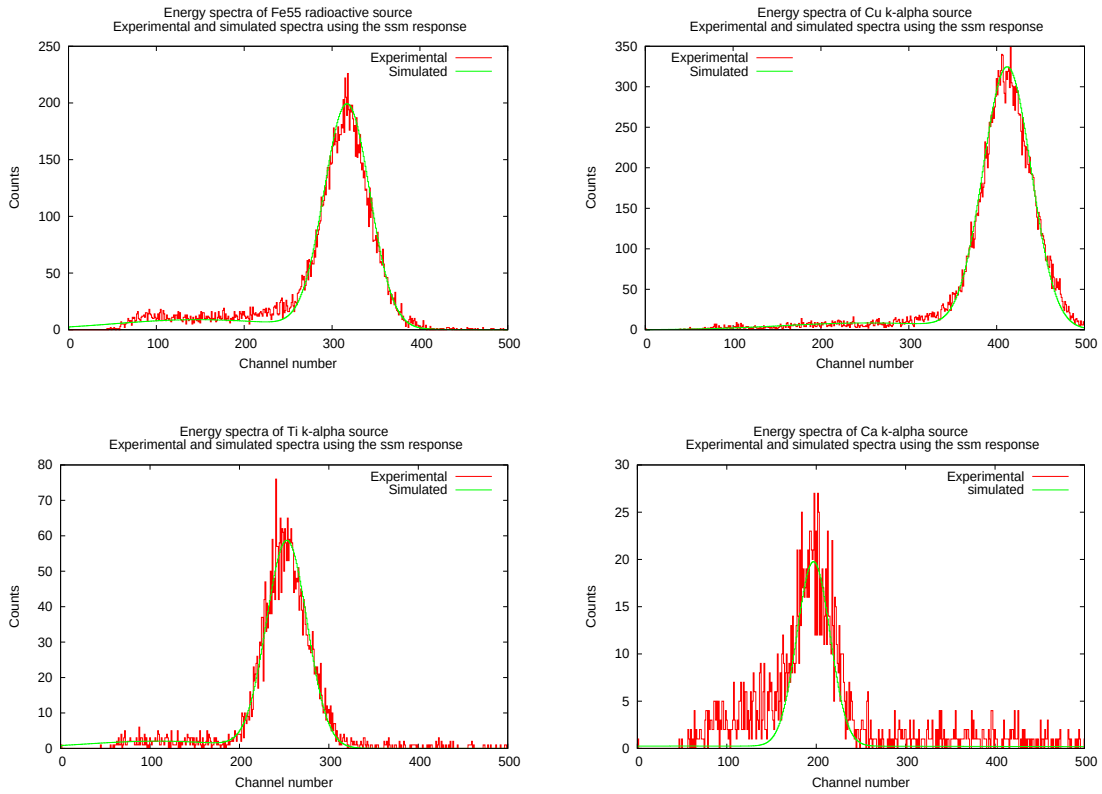

FIGURE 4.9: Pulse height spectrum of Fe^{55} radioactive source, Cu K_α source, Ti K_α source and Ca K_α source, both experimental and simulated using SSM response

The RMF thus created is verified for all the four different energy spectra as discussed in the following. The Energy-Channel relation for SSM is given by equation 4.7 as discussed in section 4.4.1 of this Chapter. The channel number corresponding to 5.9 keV photon energy is found to be at 316 channels. A delta function with the number of counts equal to the integrated counts in the pulse height spectrum, of SSM for Fe^{55} radioactive source, at the centroid channel of the pulse height spectrum is generated and written into a file with two columns: Channels and Counts. This function is convolved with the RMF of SSM to simulate the pulse height spectrum at 5.9 keV. The simulated pulse height spectrum is found to match with the experimentally observed pulse height spectrum at photon energy 5.9 keV. In this way, the pulse height spectra for other three energies are also simulated and compared with the experimentally observed pulse height spectra.

Figure 4.9 shows the experimental and simulated pulse height spectra for four different monochromatic sources. The experimental and simulated pulse-height spectra at all the energies are found to match with each other at the respective energies, except for a slight deviation in the Ca pulse height spectrum at low energies. The channels (< 160) in the pulse height spectrum of Ca K_α source where the simulated and experimental do not match

could be due to some impurities in the sample ($CaCO_3$) used to produce the Ca K_α line, as the channels corresponding to this region does not fall into any of the escape peaks.

4.6.2 ARF for SSM

The Ancillary Response File (ARF) for SSM is generated using the geometric area and the detection efficiency file. Detection efficiency file of SSM with the same energy bin size as that of the RMF is created. This file is multiplied with the geometric area of SSM to get the effective area for every energy bin within the energy range of interest. This gives the ARF for SSM. There is a provision in 'genrsp' to create the response matrix including the ARF also.

4.6.3 Spectral response for SSM

The RMF and ARF are combined to get the spectral response for SSM. This gives the spectral response including the effective area of detection at different energy bins. Figure 4.10 shows the spectral response for SSM detector in the energy range of interest.

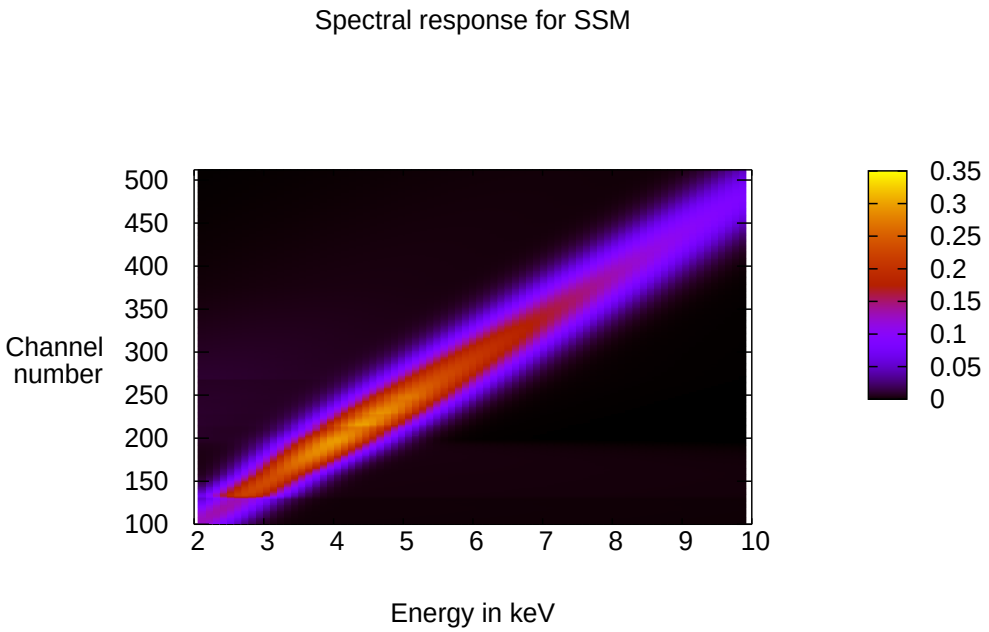

FIGURE 4.10: Spectral response for SSM

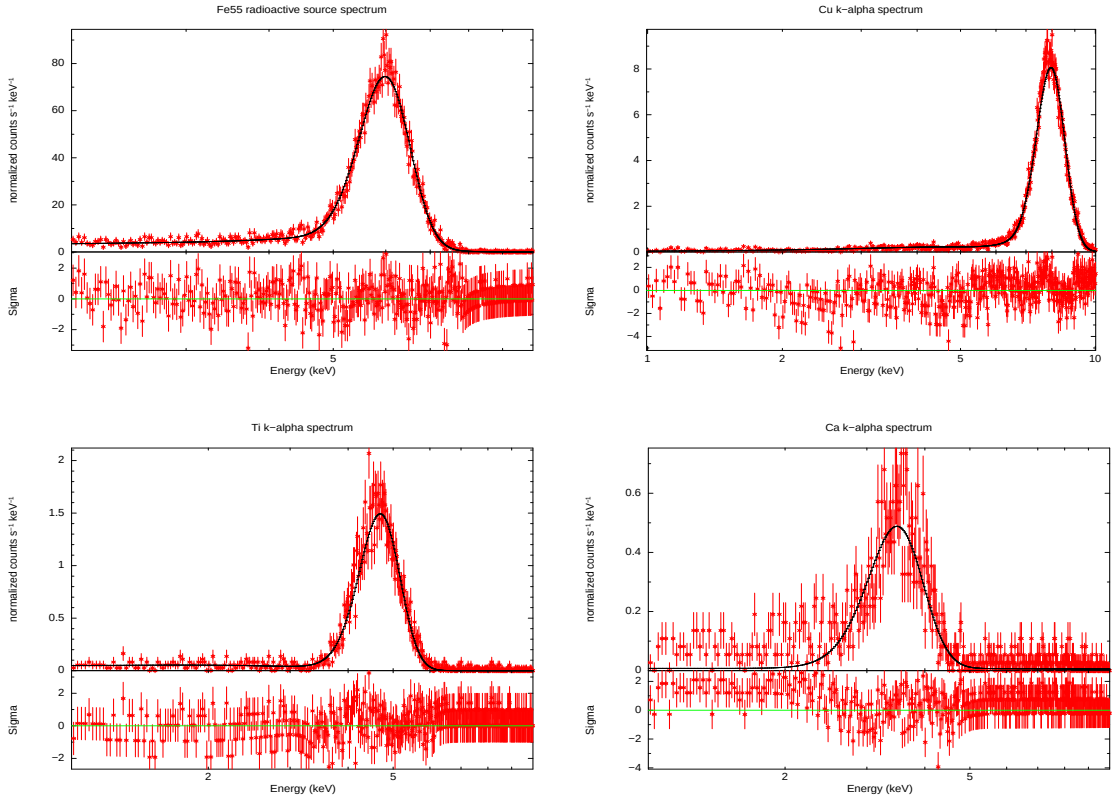

FIGURE 4.11: Energy spectra plotted using SSM response and fitted with Gaussian to get the centroid value of the energy peak

The spectral response is used to analyse the pulse height spectra obtained experimentally at four different energies to check for consistency of the response generated. XSPEC, an X-ray Spectral fitting package, which is used to analyse X-ray data is used here to analyse the pulse height spectra. The pulse height spectra in ascii format are converted to fits format using 'ascii2pha' a routine in ftools. This fits file is loaded in XSPEC along with the response file for SSM. The data is fitted with a Gaussian for the energy spectra of monochromatic source. Figure 4.11 shows the fits done to the energy spectra of all the four monochromatic sources.

The centroid value of the energy peaks are found to match with the incident energy spectra. The residuals of the fit are within 3σ variations. Table 4.4 gives the values of the parameters of the Gaussian fit done to the pulse height spectra at four different energies. The centroid values derived from the energy spectra for all the four X-ray sources are found to match with the incident X-ray photon energy within the error limits of the detector's spectral resolution.

X-ray Source	X-ray-Energy	Centroid Energy
Ca K_α	3.65	3.48 ± 0.02
Ti K_α	4.51	4.69 ± 0.01
Fe^{55} (Mn K_α)	5.89	6.00 ± 0.03
Cu K_α	8.04	7.96 ± 0.01

TABLE 4.4: Table giving the values of centroid energy peaks and error on it at different energies for the spectra generated using SSM response

4.7 On-board calibration

It is necessary that any instrument flown into space be calibrated once in a while to check for any change in its response and characteristics. Some instruments carry a radio-active source placed inside so that the photons from this radio-active source can be used for the calibration on-board. Some instruments use celestial sources for the calibration on-board. There is no radio-active source placed in SSM for on-board calibration. The advantage of having an on-board calibration source is that not only the gain calibration is carried out, but also the efficiency calibration at that particular energy is easily achieved. Here, in the case of SSM, we have to rely on the celestial sources for on-board calibration.

The Crab nebula is one of the standard sources which is used for calibration of instruments on-board. Since the intensity and the spectrum of Crab is constant in the given energy range over a long period, this is considered as an ideal candidate for on-board calibration for most of the instruments. The spectrum of the Crab nebula is given by

$$N = A\,E^{-\Gamma} \tag{4.9}$$

(Toor & Seward, 1974, Willingale et al., 2001) where A is the normalization constant which is equal to 9.7 ± 1.0, Γ is the photon index which is equal to 2.108 ± 0.006 (Toor & Seward, 1974, Willingale et al., 2001), E is the energy of the incident photon and N is the number of photons/s/sq_cm/keV. The integrated counts of the Crab spectrum given by equation 4.9 in the energy range 2 to 10 keV is 3.41 photons/s/sq_cm, which is equal to 2.156×10^{-8} ergs/s/sq_cm.

The Crab when observed by SSM is expected to have a constant count rate over the entire period of observation. The Crab count is estimated as discussed in the following sections for SSM. This count rate will be used as an on-board calibration parameter to calibrate the detection efficiency of SSM. Any change in the gas gain of the detector will reflect in the spectral index of the Crab energy spectrum and also in the hardness ratio, which is

the ratio between the counts in the energy range 5 to 10 keV and 3 to 5 keV. Hence by correcting for this, the gas gain corrections can be done on-board. Thus Crab can be used as an on-board calibration source for SSM.

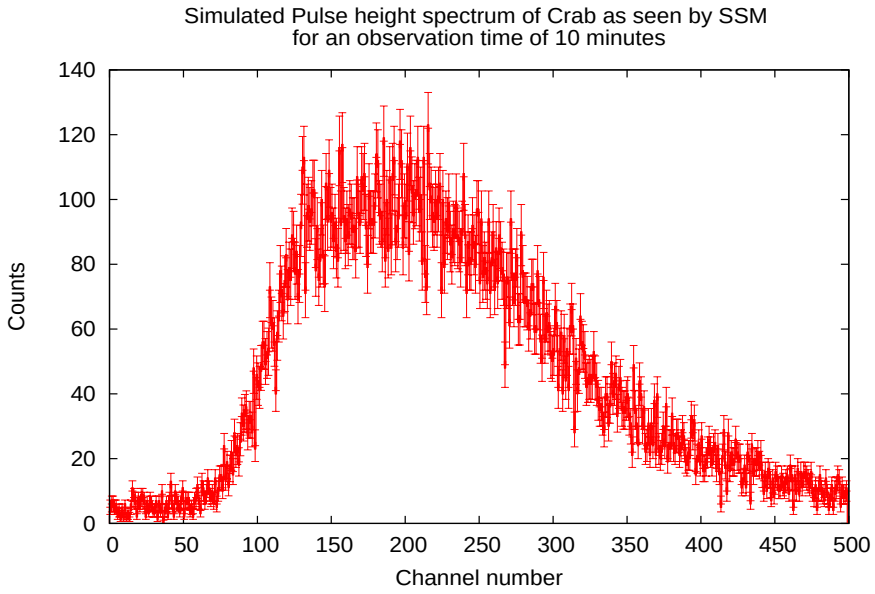

FIGURE 4.12: Simulated Pulse Height Spectrum of Crab in SSM

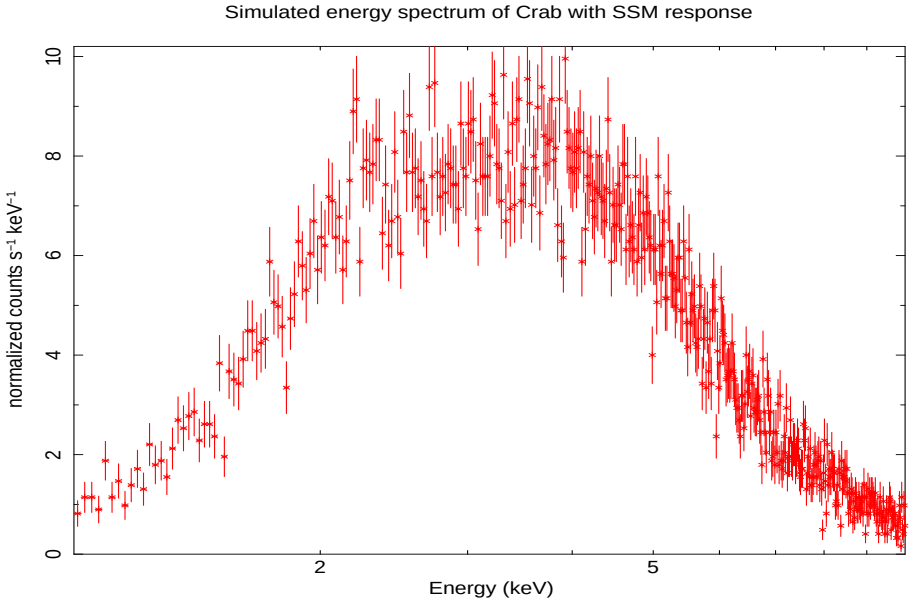

FIGURE 4.13: Simulated Crab spectrum as seen by SSM; photon absorption component is also included.

4.7.1 Simulated Crab spectrum for SSM

The spectrum of the Crab nebula is given by equation 4.9. The Crab spectrum as observed by SSM is derived by using a routine in ftools called "fakeit". This routine uses the spectral response of the instrument and convolves it with the specified model of the energy spectrum of the source and gives the spectrum of the source as seen by the instrument in channel space. Thus, the pulse height spectrum of the source that will be observed by the instrument is generated by this routine. In this way, the pulse height spectrum of Crab as seen by SSM is simulated and is shown in figure 4.12. The energy spectrum of Crab after the channel to energy conversion using the response is shown in figure 4.13.

The integrated counts in the Crab spectrum of SSM is 38.5 counts/sec/SSM. This gives the Crab count for SSM. Any variation in the gain of the SSM can reflect in the integrated counts of the Crab spectrum as well as the hardness ratio. The variation in the Crab count for SSM indicates the variation in its sensitivity. Therefore, SSM can be calibrated for its sensitivity by observing the Crab once in a while during the mission.

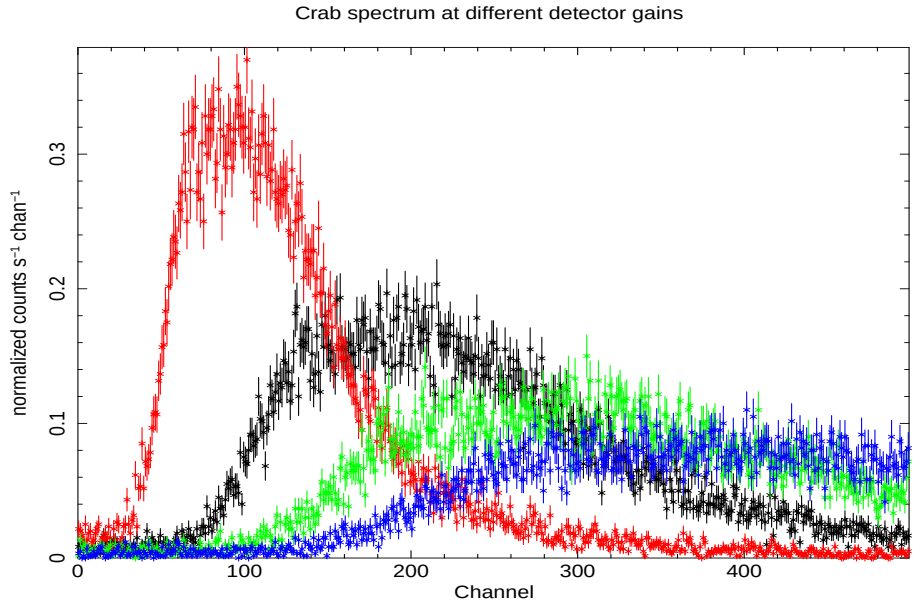

FIGURE 4.14: Simulated Crab spectrum as seen by SSM for different gas gains; black - nominal gain, red is at gain factor 0.5, green is at gain factor 1.5 and blue is at gain factor 2

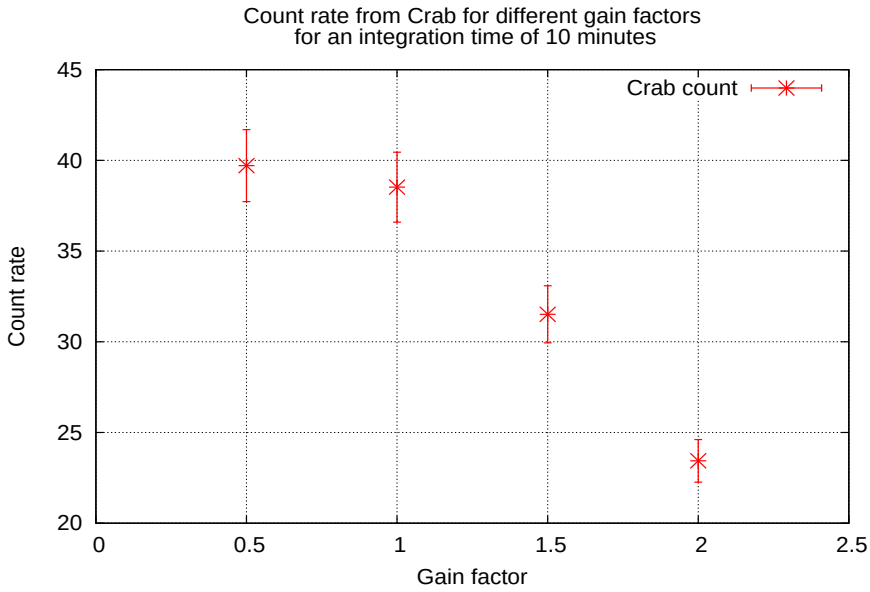

FIGURE 4.15: SSM Crab count for different gain factors

4.7.2 On-board gain calibration

It is also possible that the gain of the instrument changes during the mission period. The on-board gain calibration for SSM will be carried out using the Crab nebula. For any change in the gain, the energy-channel relation of the instrument changes. As the energy-channel relation changes, the spectral response also changes. Four different gains are considered here to study the variations in the observed spectrum of Crab. The gain factors which are the ratios of the nominal gain of SSM to the changed gain on-board (which could be due to contamination or leakage of gas) is taken as 0.5,1,1.5 and 2. These values indicate a variation of 50% decrease in the gain, the actual gain, 50% increase in the gain and 100% increase in the gain respectively. The spectral response for SSM is generated for these four different gains. Using these different responses, the pulse height spectrum of Crab is simulated as discussed in section 4.7.1. Figure 4.14 shows the pulse height spectrum of Crab for different gas gains.

It can be seen that the pulse height spectrum shifts for different gain factors. This shows that the integrated counts in a defined range of channels is changing for different gain factors. Figure 4.15 shows the variations in the Crab count for different gain factors. Thus, from the observed Crab count at different epoch of the mission, the sensitivity of SSM can be calibrated.

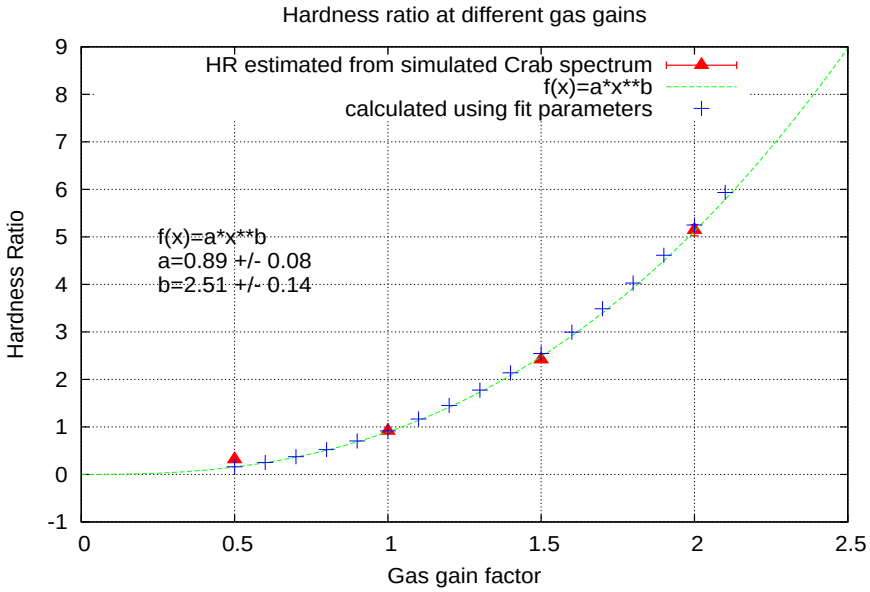

FIGURE 4.16: Hardness ratio as a function of gain; Variation in Hardness Ratio for every 10 percent variation in gas gain

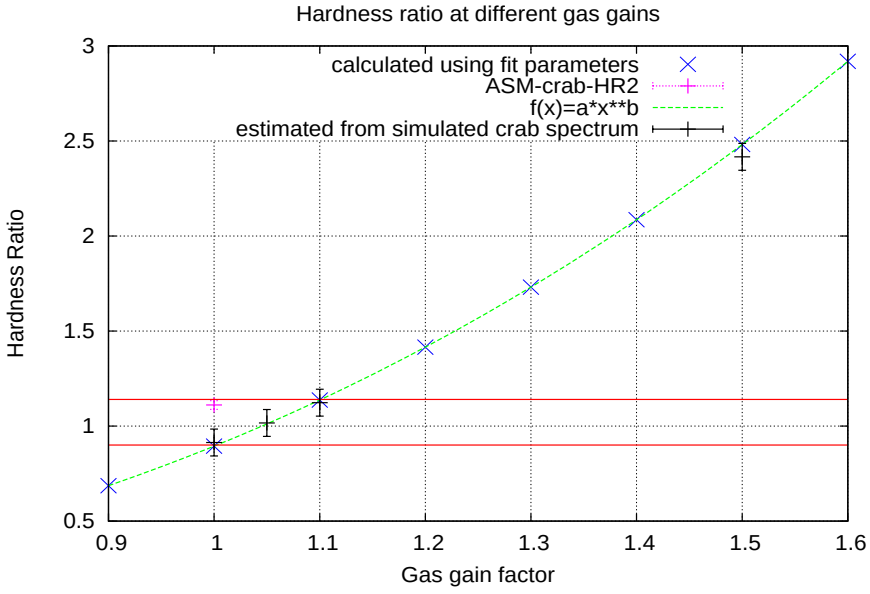

FIGURE 4.17: Hardness ratio as a function of gain shown at finer steps of gain factor along with the error bars for different error percentage

The hardness ratio (HR2), which is the ratio of the counts in one band (250 to 500 channels) to the other band (150 to 250 channels) also changes. This hardness ratio is equivalent to the ratio of the flux in the energy bands 5 to 10 keV and 3 to 5 keV. Figure 4.16 shows the variation in the hardness ratio as a function of gain factor. The fit to the data of hardness ratio as a function of gain factor is made using the function f(x)=a×x^b, where a = 0.895 ± 0.08 and b = 2.516 ± 0.14. Figure 4.17 shows that a 10% variation in the gas gain (ie. the gas factor is 1.1) can be detected from the variations in the hardness ratio calculated from observations of Crab nebula for an integration time of 10 minutes. Therefore, from the changes in the hardness ratio, the changes in the gain of the detector can be deduced.

Once the variation in the gain of the detector is estimated, the operating voltage of SSM can be tuned to bring it back to the nominally operating gain value. The HV for SSM are in steps of about 10 Volts around 1500 Volts, using which a 10% variation in the gain of the detector can be corrected. Figure 4.18 shows the variation in hardness ratio as a function of HV for SSM. The fit to the data of hardness ratio as a function of HV is made with the function f(x)= a×exp(x×b), where a = 2.33e-18 and b = 0.027. The points in the plot shown in figure 4.18 give the steps available for tuning the operating voltage of SSM on-board. Thus, by observations of the Crab nebula, SSM can be calibrated on-board over

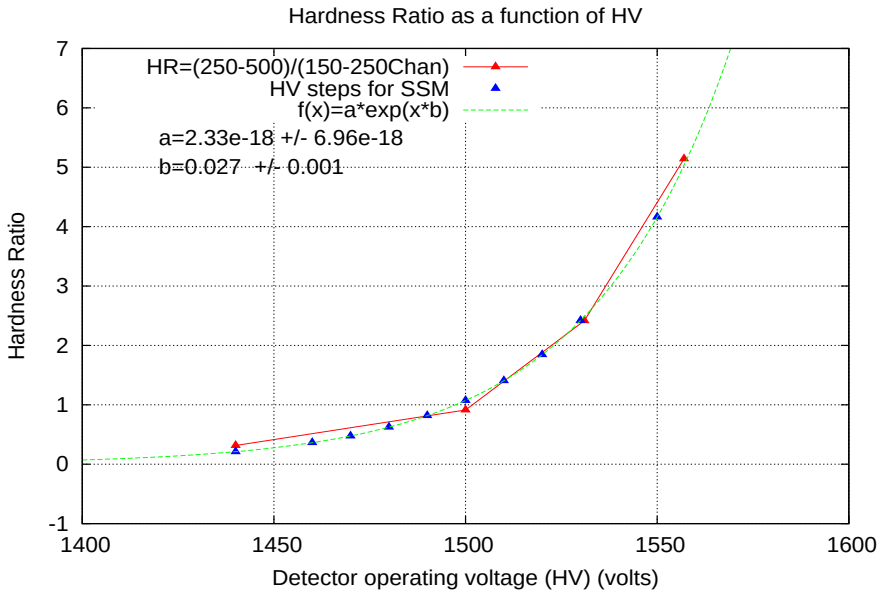

FIGURE 4.18: Hardness ratio as a function of operating voltage for SSM; the points indicate the available HV steps for SSM

a gain of ±50% about the nominal gain value, with the available small steps of HV, in the HV range 1440 to 1530 Volts. Beyond 1530 Volts, one more HV step is available which allows the gain increase by a factor of 2 from the nominal gain value.

4.8 Conclusions

In this chapter we have discussed in detail the response of SSM and the parameters that influence it. The effective area and sensitivity of SSM are estimated. Spectral calibration of SSM carried out with X-ray sources of different energies is discussed with the results. SSM is found to have a linear response in the energy range of interest. The energy and position resolution at different energies within the energy range of interest are derived for SSM. The spectral response for SSM is generated using the calibration data. The pulse height spectrum of SSM when it observes the Crab nebula is simulated using the derived spectral response. The sensitivity of SSM in terms of Crab count is defined. On-board calibration of SSM is planned to be done using the Crab nebula. The details of on-board calibration using the Crab nebula is discussed. The gain and sensitivity calibration of SSM can be done by observing the Crab nebula. Any variations in the gain, greater than 10% can be corrected by stepping the HV of SSM and for finer variations in the gas gain, correction factors can be applied to the data.

Chapter 5

X-ray data analysis of select X-ray transients

5.1 Overview

X-ray Sky Monitors are instruments that detect and locate any transient X-ray sources in the X-ray sky in addition to long term monitoring of the transient as well as persistent X-ray sources. These monitors give information of the position of the X-ray sources that show variabilities in the light curve. It is believed that these variabilities are due to some interesting physical processes occurring in these sources. In order to study the phenomena driving these variabilities, it is required to observe these sources with a pointed-mode instrument with much better sensitivity and a narrow field of view for longer duration. The data from these pointed-mode observations are analysed for spectral and timing study of these X-ray sources.

The work presented here discusses the spectral and timing analysis of two X-ray transient sources which are candidates, that are believed to host a stellar mass black hole as the compact star. Data from Rossi X-ray Timing Explorer (RXTE) mission is used for the analysis. The two sources studied are SLX 1746-331 and SWIFT J1753.5-0127. The study of these two sources is carried out using the data during an outburst of the respective sources. The compact objects in both the sources are estimated to be black hole candidates. Each source shows a varied sequence of physical processes causing the X-ray emission during the outbursts.

5.2 Rossi X-ray Timing Explorer

Rossi X-ray Timing Explorer (RXTE) is NASA's X-ray satellite mission launched on 30^{th} December in the year 1995. It has three instruments on-board which are the Proportional Counter Array (PCA), the High Energy X-ray Timing Experiment (HEXTE) and the All Sky Monitor (ASM).

The PCA is an array of five proportional counters with a total collecting area of 6500 cm^2. The energy range of PCA is 2-60 keV with energy resolution of ∼18% at 6 keV. The finest timing resolution is 1 microsecond. The field of view is 1° FWHM. A detailed discussion of PCA can be found in Jahoda et al. (1996).

The HEXTE consists of two clusters each containing four NaI/CsI phoswich scintillation detectors with a total area of 1600 cm^2. The energy range of HEXTE is 15 - 250 keV, with energy resolution of 9 keV at 60 keV. The timing resolution is 8 microsecond. The FOV of these detectors is 1° FWHM. A more detailed discussion of HEXTE can be found in Rothschild et al. (1998).

The ASM is an X-ray sky monitor consisting of three independent position-sensitive proportional counters mounted on a single platform which is rotated. Each detector has a one-dimensional coded-mask mounted on it. The energy range of ASM is 1.5 to 12 keV. This has a large field of view which is $6° \times 90°$ FWHM, for each detector. ASM scans 80% of the sky in one orbit. SSM on ASTROSAT is very similar to ASM. Details of ASM are discussed in Levine et al. (1996).

5.3 RXTE Data Reduction and Analysis

Data from observations of the X-ray sources can be got by downloading them from the High Energy Astrophysics Science Archive Research Center (HEASARC) website. The HEASARC is the primary archive for NASA missions that observe the extremely energetic phenomena. The data which is downloaded has to be processed by appropriate reduction procedures as given by the instrument team. These data reduction procedures are generally instrument specific. This includes selecting the good data out of the whole set by applying appropriate conditional checks, applying background corrections, generating the response of the instrument to be used during the analysis etc. Using the appropriate response for data analysis is very important so that there are no artifacts showing up in the data which is analysed.

5.3.1 RXTE Data Description

RXTE data provided for analysis consist of data from all the three instruments on it. The ASM data which give the light curve of the observed source is available on the website "http://xte.mit.edu". The data from PCA and HEXTE give the spectra at different energy bands and also the light curve for these energy bands. The data of these instruments can be downloaded from the HEASARC website. The data are of two types: Guest Observer facility (GOF) data and Target of Opportunity (TOO) data. The guest observer facility data are the data from observations done on the sources on the basis of the proposals for observations which have been proposed by guest observers. The TOO data are the data from observations done on the sources based on new discoveries or on occurrence of transient phenomena, without any proposal request under possible observation conditions. The data analysed and studied here in this chapter for two different sources are TOO data.

Each pointed mode observation has a unique observation ID, which is also called ObsId. The ObsId is in the format NNNNN-TT-VV-SSX, where 'NNNNN' is the five digit proposal number assigned by the GOF, 'TT' is the two digit target number assigned by the GOF, 'VV' is the two digit viewing number which tracks the number of scheduled stares at the target, 'SS' is a two digit sequence number used for identifying different pointings of the same observation and X is a special letter which if present indicates different types of observations like slew, scan, grid observations or observations with data gaps during long observations. The ObsId is the name of the directory which contains all the data corresponding to an observation. This directory contains the science data as well as the house-keeping data, which indicates the health of the instruments during the observations. The directory also contains space-craft related data on the attitude, power etc. of the satellite during the observation.

The science data for the two instruments, the PCA and the HEXTE consist of both event (every photon event information) data and binned (counts binned for an interval of time) data. The binning of the data is done on-board by the Electronic Data System (EDS) of RXTE. There are different modes of data as per the binning. One of the different modes of data for PCA is 'standard-2', which is a 16 second binned data and this is generally used for spectral analysis. There are few event mode data sets of different time-bins. The event mode data chosen for timing analysis can be 125 μs, which can be later rebinned to the time-bin of the user's choice to check for different frequencies in the power density spectra (PDS). Different modes of data are made available depending on the proposal of observation. HEXTE also has different modes of data and the standard mode is called the archive mode

which is a 16-second bin data and is binned spectrally into 64 channels. A detailed description of RXTE data and the data reduction procedures are given in "The ABC of RXTE", which is available online at "http://heasarc.gsfc.nasa.gov/docs/xte/abc/contents.html". In the thesis work presented here, standard-2 mode data of PCA and the archive-mode data of the HEXTE are used for spectral analysis. The 125 μs event mode data is used for timing analysis. RXTE data reduction involves certain standard routines which are provided along with "ftools", which is a standard tool to analyse X-ray data from the high energy missions.

5.3.2 Spectral Analysis

The X-ray energy spectrum is the plot of intensity of the X-ray source as a function of energy. The spectral analysis is basically the study of energy spectra to understand the physical processes in the X-ray sources giving rise to the emission of X-rays. There are different processes that give rise to the X-rays that are observed in these X-ray sources. The X-ray emission processes are discussed briefly in section 1.3 of chapter 1 . The energy spectra from the X-ray sources can be a combined spectra of different physical processes. A brief discussion on the energy spectra of black hole sources is given in 1.5.1 of chapter 1.

5.3.3 Timing Analysis

X-ray sources are highly variable with variability timescales ranging from milliseconds to years. Timing analysis is the study of the variabilities in the X-ray emission. The light curve which is the plot of intensity as a function of time is used for the timing analysis. If the variability is periodic, the period can sometimes be deduced from the light curve itself. Usually Fourier analysis is carried out on the light curve to find out if there is any frequency of X-ray emission present in the system. If $X(t_i)$ for i=1,2,...N, represents the time series data, the discrete Fourier transform of this series is given by $F_X(\omega)=\Sigma_j\ X(t_j)\exp(-i\omega\ t_j)$. Here the power at a frequency ω is given by $P_X(\omega)=[1/N][F_X(\omega)]^2$. The power density spectrum is generated to look for the frequencies which have high power and show above the continuum. The power spectrum is generated for small segments of the light curve and then co-added to increase the signal-to-noise ratio.

5.4 Black Hole Candidates

Black Hole Candidates are those binary systems where the mass of the compact object is indicated to be greater than 3 $M_{\odot}$, but yet not confirmed to be a black hole. The confirmation if the compact object is a black hole or not is done generally by optical observations of the companion star which helps derive the mass of the compact star. From the spectral analysis of the X-ray data alone, the mass of the compact object can only be estimated, thus giving these sources the name 'Black Hole Candidates (BHC)'. In the following sections, the study of two black hole candidates are presented. The physical processes taking place in these sources are studied from the spectral analysis.

Black Hole Candidates are known to undergo spectral state transitions between the different canonical states they enter during an outburst (Homan & Belloni, 2005, Remillard & McClintock, 2006). The different spectral states are discussed in section 1.5.1 of chapter 1. There is a subclass of x-ray transients, the Low/Hard state X-ray Transients (LHXTs) that undergo outbursts which are entirely in the low/hard state throughout the burst (Brocksopp et al., 2004). The accretion process during the low/hard state of the x-ray transients is still not well understood and requires an extensive study for which this subclass of x-ray transients showing low/hard state outbursts seem promising candidates. Swift J1753.5-0127 is one of the sources which has been observed to show this behaviour of Low/Hard state outburst, whereas SLX 1746-331 shows spectral state transitions similar to canonical systems. Also, from the spectral analysis of the X-ray data of these sources, the mass of these sources are estimated which indicate the sources to be black hole candidates.

The timing analysis adds to the understanding of the physics driving the outbursts in these sources. The study of the Quasi Periodic Oscillations (QPOs) in the power density spectra helps to derive the origin of X-ray emission. The following sections give the detailed spectral and timing study of the two black hole candidates in detail.

5.5 SLX 1746-331

SLX 1746-331 (aka. SLX 1746-311) is a black hole candidate which was discovered by Spacelab-2 in 1985 during an outburst (Skinner et al., 1990). The galactic plane survey-I by ROSAT reported the detection of the outburst in 1990 (Motch et al., 1998). This source was also detected by CHANDRA X-ray observatory during its quiescence(Wilson C., Patel, Sandeep, Kouveliotou Chryssaand Jonker, van der Klis, Lewin W., Belloni & Mndez, Wilson et al.). INTEGRAL, with its IBIS instrument, also detected this source during September

2003 with a flux of 5.4±0.2 mCrab (Revnivtsev et al., 2004). The bulge monitoring scans by RXTE-PCA report the detection of SLX 1746-311 at an intensity level of 40 mCrab in 3-25 keV on 5th April 2003 (Markwardt (2003) and references therein). The present work on the spectral analysis of this source during its outburst in April 2003 is discussed in detail in Narendranath et al. (2006).

5.5.1 Observations and Data Analysis

RXTE-PCA data of the outburst during April 2003 of this source constitute 40 pointed mode observations with the first PCA observation of this source on 7th April 2003. The burst was observed by the PCA till 2nd September 2003, which was towards the end of the decay phase. These data sets cover a period of about 100 days during the outburst. This data is analysed for the spectral and timing study of the source. The standard-2 data of PCU2 (Proportional Counter Unit 2) out of the five PCUs in the PCA instrument is used for the spectral analysis. The evolution of the spectral parameters is studied to understand the physics of the outburst and the nature of the source.

5.5.2 ASM-PCA light curve analysis

The observations of the source, SLX 1746-331 by ASM on RXTE from March 2003 to November 2003 is shown as the ASM light curve in figure 5.1. The profile of the light curve is found to be a Fast Rise and Exponential Decay (FRED). The rise time of the outburst is ∼13 days and the e-folding time (time when the flux becomes 1/e times the peak value) of the decay of the burst is ∼32 days. The peak of the outburst was on 14th April 2003. The flux during the peak of the outburst as seen in the ASM light curve is found to be 27.67 counts/sec, which is equivalent to 368.95 mCrab. The PCA light curve is shown in the top panel of figure 5.2. The maximum counts in the peak of the PCA light curve is ∼860 counts/s/PCU, as observed on 7th April 2003. However, the peak of the outburst as per the ASM light curve is found to be 14th April 2003. The ASM hardness ratio which is the ratio of the flux in the energy ranges 3-5 keV and 5-12 keV is shown at the bottom panel of figure 5.1. It can be seen that the hardness ratio is < 1 throughout, almost the entire burst, which shows that the spectra is soft during the entire burst and tends to become hard during the end of the decay phase.

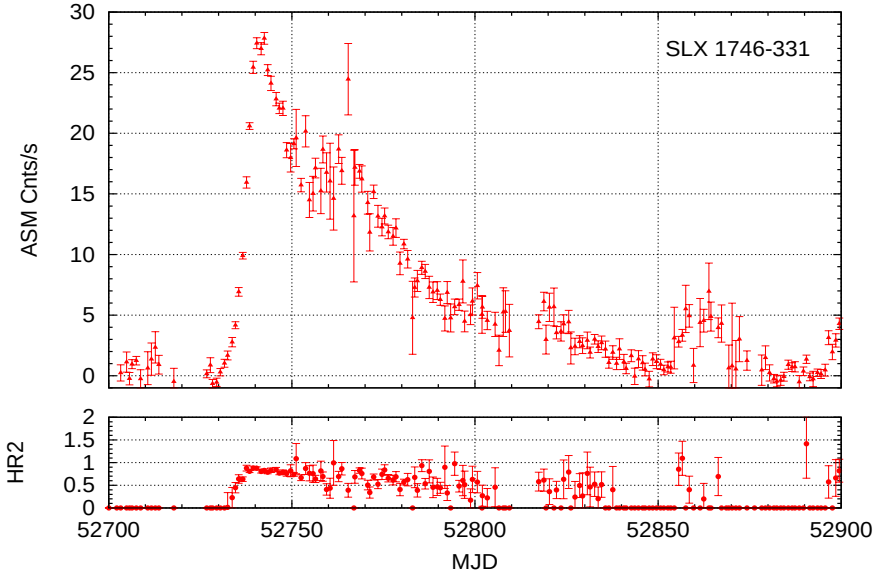

FIGURE 5.1: ASM light curve of SLX 1746-331 is shown in the top panel and the hardness (5-12 keV)/(3-5 keV) is shown in the bottom panel

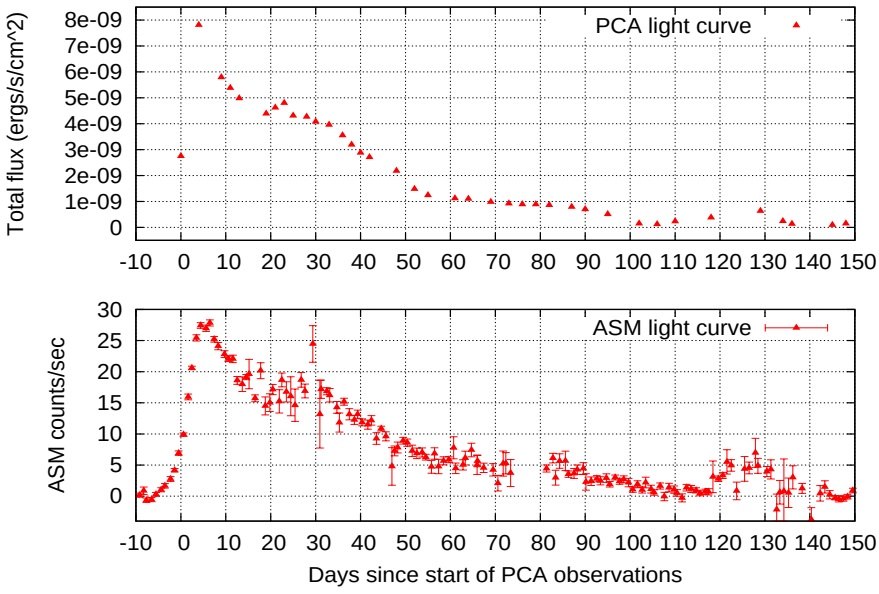

FIGURE 5.2: PCA light curve of SLX 1746-331 in the top panel and the ASM light curve in the bottom panel

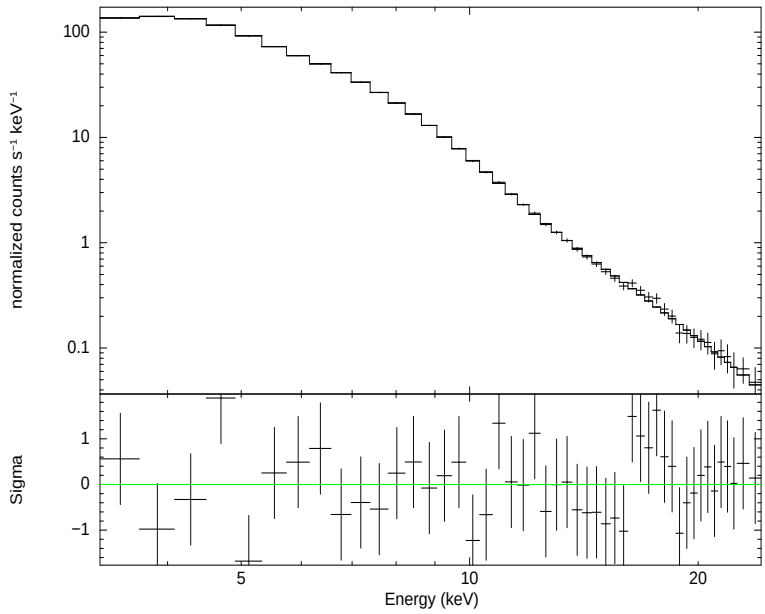

FIGURE 5.3: Spectral model with three components: (diskbb+gauss+pow) along with absorption component 'phabs' is fitted to the data, the obsid of which is 80138-02-08-00

5.5.3 Spectral analysis

The PCA standard-2 data, which has a time bin of 16s, is used to generate the energy spectra in the energy range 3-25 keV. Data from PCU2 (one of the proportional counter unit) of PCA is used for the spectral analysis. FTOOLS version V5.3.1 is used to extract the spectra from all the observations. A systematic error of 0.3% is taken into account in the energy spectra. XSPEC 11.3.1e is used for the spectral fits to the energy spectra of all the observations. The HEXTE data for this source is not studied as the whole outburst was found to be dominated by soft spectra.

The spectral model used to fit the energy spectra in the energy range 3-25 keV is a combination of three models: diskbb, which accounts for the accretion disk emission in the source, power law, which accounts for the non-thermal emission in the source and a Gaussian line to account for the Fe line emission from the accretion disk. Figure 5.3 shows one of the PCA observation data fitted with the combined model of 'disk black-body', a Gaussian for Fe line and a power law for the non-thermal component. The spectra are soft during the rise and decay of the outburst. The energy spectra during the peak of the burst are dominated by the thermal component, the 'diskbb'. The maximum flux observed in the PCA observations is found to be $7.81 \times 10^{-}9$ ergs/(s-cm^2). The PCA light curve is shown in the top panel of figure 5.2. The spectra is found to harden at a much later stage of the outburst, when it is almost reaching the quiescent state.

The evolution of the spectral parameters during the outburst are shown in figure 5.4. The temperature of the inner accretion disk is found to increase initially during the rise of the burst to a value of 1.6 keV and then decreases gradually with time in the decay phase of the outburst. This increase and decrease of the temperature of the accretion disk is normally observed in transient outbursts which are considered to have originated from the accretion disk. The energy spectra for the entire outburst is dominated by the disk emission. At the end of the decay phase of the outburst, that is beyond 100 days of the outburst, the energy spectra seems to be dominated by the non-thermal power law component.

The contribution of flux from different components in the spectra: the thermal component and non-thermal component is shown in figure 5.5. The ratio of the disk flux to the total and that of the power law component flux and the total are shown in figure 5.6. It can be seen that the disk emission dominates the energy spectra up to about 100 days of the outburst. After 100 days, when the outburst has reached the quiescence almost, the power law flux seems to dominate the energy spectra, indicating an emission mechanism different from that during the outburst.

The hardness ratio derived from the PCA data, which is the ratio of the flux in the energy bands 5-12 keV to 3-5 keV is shown in figure 5.7. It can be seen that for the initial 100 days of the outburst the hardness ratio is <1 and then the spectra is found to harden with a hardness ratio value of $\sim$1.5. This increase in the hardness ratio happens at the same time when there is an increase in the flux in the light curve of both ASM as well as PCA which can be seen in figure 5.2. This indicates a different emission mechanism that is different from the physical processes during the outburst. It can be considered like another short burst which has got triggered at the end of the decay phase of the previous outburst. However, this short burst seems to be dominated by non-thermal power law component indicating a hard outburst.

There are no QPOs found in the Power Density Spectra (PDS) during this outburst of the source.

5.5.4 On SLX 1746-311

The soft spectrum during the high/soft state of the source, SLX 1746-311 indicates the source to be a black hole system. The detection of a hard tail which is the non-thermal component (power law component) also supports this. During the high/soft state, the spectrum is dominated by the thermal component which indicates the presence of an optically

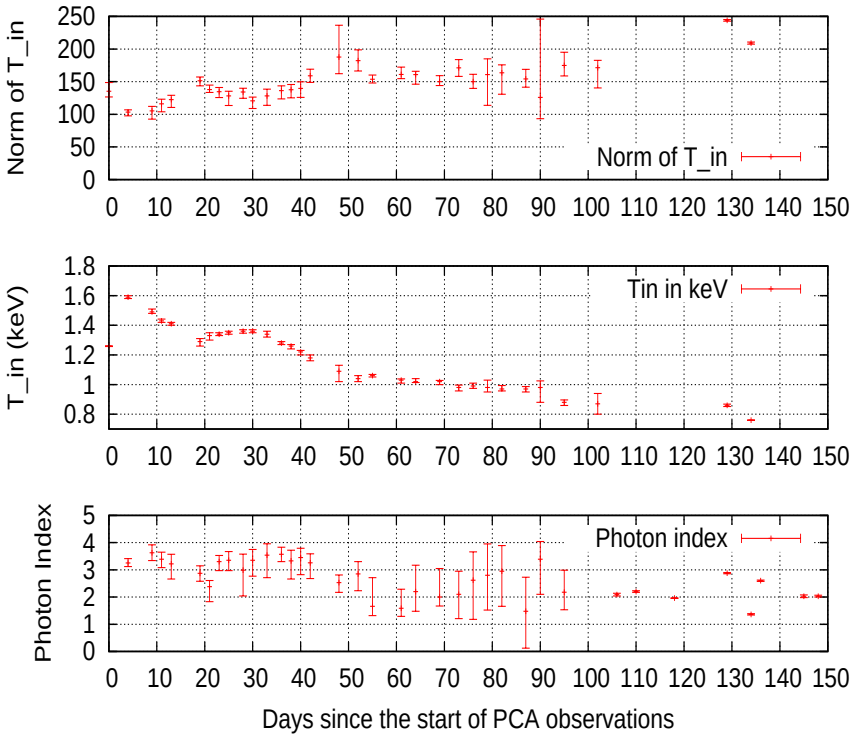

FIGURE 5.4: Evolution of different parameters of the spectra

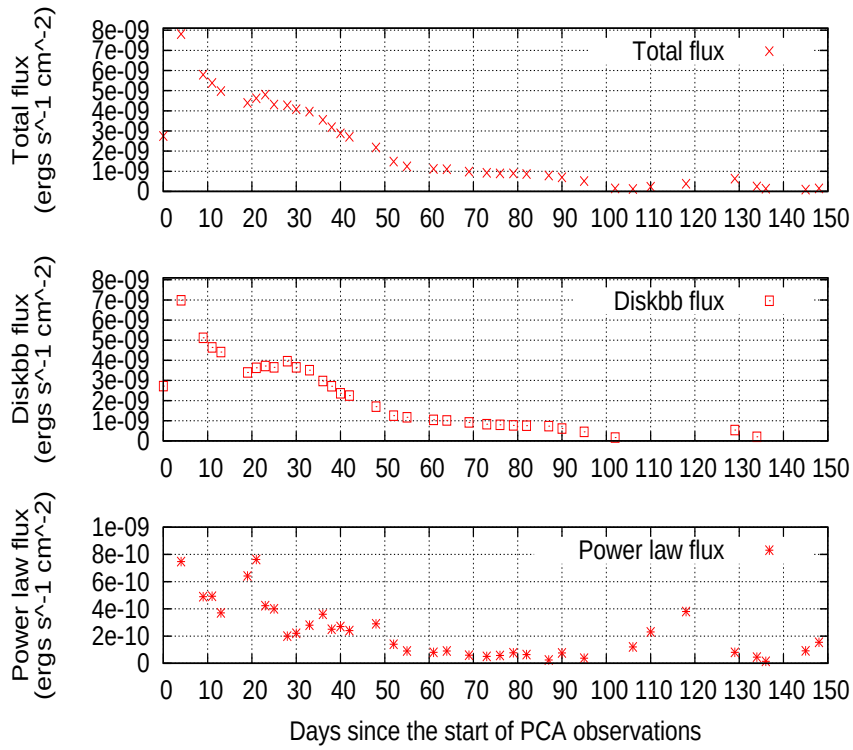

FIGURE 5.5: Varaitions in total flux,flux from disk component and power law component

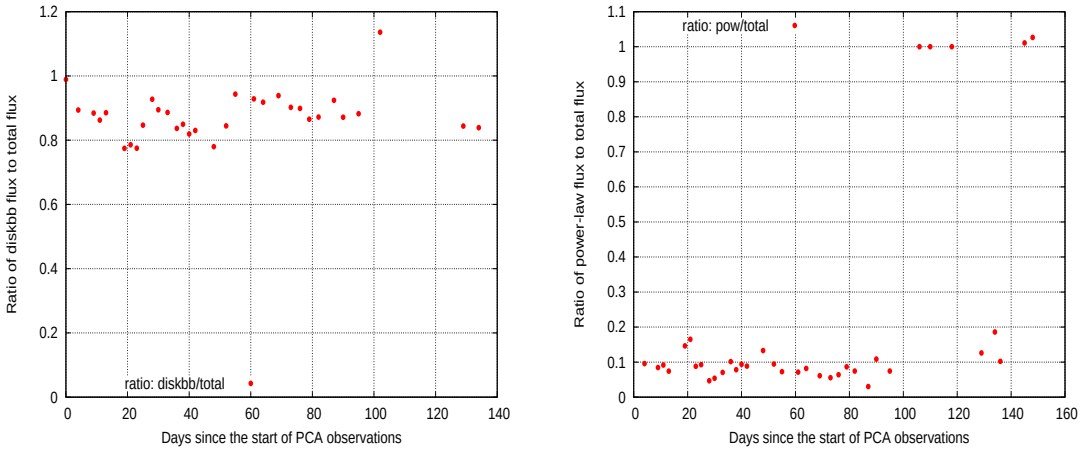

FIGURE 5.6: Ratio of disk flux to total is shown on the left and that of power law component flux to total flux is shown on the right

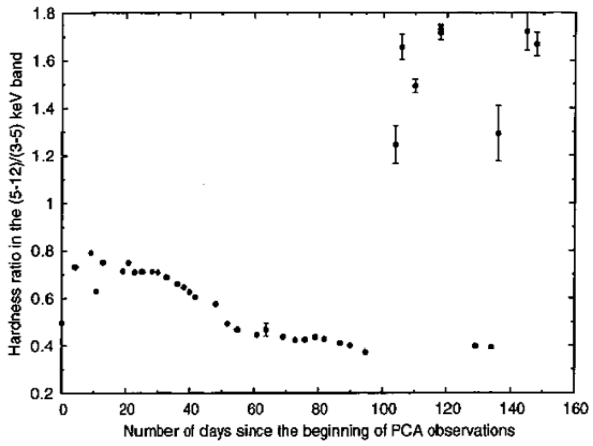

FIGURE 5.7: Variations in the Hardness Ratio (5-12 keV)/(3-5 keV) from PCA data

thick accretion disk (Shakura & Sunyaev, 1973). The spectrum of the source is soft during almost the entire burst and the state-transition to the hard state happens towards the end of the decay of the burst. During this state, the flux contribution from the thermal component is negligible and the spectrum can be fitted with just the power law component.

An estimate on the mass of the compact object in accreting systems can be made from the spectral parameters derived from the fits to the energy spectra during the peak of the outburst. The radius of the innermost stable circular orbit of the accretion disk R_{ISCO} is given as

$$R_{in} = R_{ISCO} = R_g = GM/c^2 \tag{5.1}$$

for a rotating Kerr Black Hole and is given as

$$R_{in} = R_{ISCO} = 6R_g = 6GM/c^2 \tag{5.2}$$

for a non-rotating Schwarzchild Black Hole (McClintock & Remillard, 2006). Here, R_g is the gravitational radius, G is the gravitational constant, M is the mass of the black hole and c is the velocity of light. The radius of the innermost stable circular orbit can be calculated from the normalization factor of the disk component in the spectra, during the peak of the burst using the equation 5.3 (Keith, Ben & Craig (Keith et al.) and references therein).

$$N = \left(\frac{r_{in}(km)}{D(10kpc)} \right)^2 cos\,\theta \tag{5.3}$$

Here, r_{in} is the 'apparent' inner radius of the accretion disk in units of km, D is the distance of the source in units of 10 kpc (kiloparsec) and θ is the inclination angle of the system to the line of sight of the observer. The inclination angle of the system is considered to be $\leq 65^\circ$ for this calculation as this system shows a FRED (Fast Rise Exponential Decay) like light curve (Narayan & Mclintock, 2003) and distance to the source is assumed to be 10 kpc. The apparent inner radius of the accretion disk is related to the true inner radius given by the relation

$$R_{in} = \kappa^2\, \zeta\, r_{in} \tag{5.4}$$

Where κ is the spectral hardening factor with value $\sim$ 1.7 to 2.0 (Shimura et al., 1995) and ζ is the correction factor for the inner boundary condition of the accretion disk given by ζ=0.41 (Kubota et al., 1998). The true inner radius of the accretion disk calculated using equation 5.4 is $\sim$26 km. The mass of the compact object is now calculated using equation 5.2 for a non-rotating Schwarschild black hole, using the estimated value of R_{in}. The estimate of the mass of the compact object in the system is found to be to be $\sim$ 3 $M_\odot$, which indicates it to be a black hole candidate. The spectral study and an estimate of the mass from the accretion disk component in the spectra indicate SLX 1746-331 to be a black hole candidate system. However, a more detailed multiwavelength observations of this source will help in confirming the nature of the compact object in this system. The study of this source SLX 1746-331 is discussed in our paper Narendranath et al. (2006).

5.6 Swift J1753-0127

SWIFT J1753.5-0127 was first detected by the BAT experiment on Swift satellite at RA (J2000) = $17^h\ 53^m\ 28^s.3$ and Dec (J2000) = -$01^o\ 27'\ 09.3''$, on June 30, 2005 (Palmer

et al., 2005). The other experiments of SWIFT also have observed this source. It was also observed by Swift-XRT (X-Ray Telescope) on July 1, 2005 and was found to be extremely bright (Burrows et al., 2005). Swift-UVOT (Ultra-Violet/Optical Telescope) observations do not indicate any temporal variability on 10-1000s timescale. The spectral fits to the ultra-violet spectra give a lower limit for the temperature of the accretion disk as 116,000 K (Still et al., 2005).

The optical observations of SWIFT J1753.5-0127 reveal the existence of a bright optical counterpart (Halpern, 2005). Optical spectroscopy of this source indicates the presence of a blue continuum with a broad-double-peaked H-alpha emission line (Torres et al., 2005). Infrared observations of the source indicated the presence of an IR point source at the same position as that of the optical counterpart (Torres et al., 2005). Radio observations of the source indicate the variability of the source and is found to be an extended (Fender et al., 2005). This could imply the presence of a jet, which is associated with the low/hard state of black hole candidates. However, this source does not follow the usual radio/X-ray correlation of X-ray binaries in the low/hard state (Cadolle Bel et al., 2007).

INTEGRAL observations of the source from August 10 to 12, 2005 indicate the spectrum to be typical of that of a BHC in the hard state (Cadolle Bel et al., 2007, 2005). The PDS of the RXTE-PCA observations of the source show a 0.6 Hz QPO with a shape typically seen in black hole candidates (Morgan et al., 2002). Simultaneous RXTE and XMM-Newton observations of this source on March 24, 2006, near the quiescent state of this source, by Miller et al. (2006) show the presence of an accretion disk in the low/hard state of this source. The present work on the detailed spectral and timing analysis of this source during its outburst in July 2005 is discussed in Ramadevi & Seetha (2007).

5.6.1 Observations and Data Analysis

RXTE TOO (Target of Opportunity) observations of this source span about 146 days and comprise of 58 observations. The observations date from July 6, 2005 to November 28, 2005. The data from ASM, PCA and HEXTE instruments on RXTE are analysed and discussed. The details of the light curve, the spectral analysis and timing analysis of the outburst are given in the following sections.

5.6.2 ASM-PCA Light Curve Analysis

The data from ASM of RXTE on this source date from July, 1, 2005 to November, 28, 2005. The light curve from the one-day averaged data of ASM is shown in figure 5.8. The profile of the light curve is a typical FRED (Fast Rise Exponential Decay). The peak of the ASM light curve of the burst corresponds to 200 mCrab. The rise time of the light curve is found to be 8 days. An exponential fit to the light curve gives an e-folding time of ∼30 days. The bottom panel of figure 5.8 shows the hardness ratio from ASM, the ratio between the count rates in the energy bands (5-12) keV and (3-5) keV. The hardness ratio is calculated from the three-day averaged count rate in the two different bands so that the evolution of it can be seen clearly. This hardness ratio is ∼1.0 at the start of the burst, increases to ∼1.5 and remains > 1.0 throughout the burst, which indicates that the source has not entered the high/soft state throughout the burst.

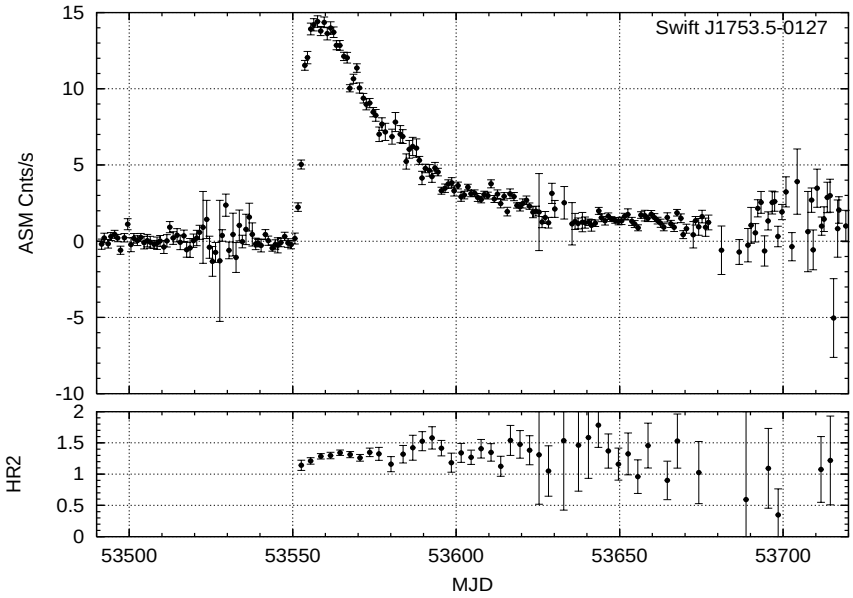

FIGURE 5.8: ASM light curve (top panel) and the hardness ratio (HR2) (5-12 keV)/(3-5 keV) (bottom panel); hardness ratio is calculated from the 3-day averaged count rate in the two energy bands.

5.6.3 Spectral analysis

The 3-25 keV energy spectra is extracted from the standard-2 data of the PCA instrument. The data from the PCU2 of the PCA is used for the spectral analysis. A systematic error of 1% is accounted for in the data. The spectra are extracted using FTOOLS V6.0. As

the hardness ratio of ASM indicates this source to be in the hard state during the entire outburst, the hard energy spectra from the HEXTE is also analysed and studied. The 20-180 keV energy spectra is extracted from the HEXTE instrument. The standard mode data (for which the spectral bins are in 64 channels with 16 s time bin) from one of the clusters, Cluster A is used for the spectral analysis. The energy spectra in the energy range 3-20 keV from the PCA and 20-180 keV from the HEXTE are combined together for the spectral analysis study of this source. In order to account for the uncertainties in the relative calibration of the PCA and HEXTE instruments, the normalization factor for the PCA data is frozen to 1 and that of the HEXTE data is allowed free for the fits to the combined data from both these instruments. The n_H value of the column density for interstellar absorption is fixed at 2.3×10^{21} atoms-cm^{-2} (Miller et al., 2006) for all the fits.

First, the energy spectra from the PCA data in the energy range 3-25 keV is used for the spectral fits. A simple power law model is used to fit the data and one such fit for the observation during the peak of the burst is shown in figure 5.9. The photon index is found to be 1.83 and the parameters are given in table 5.1. It can be seen in figure 5.9 that the fits to the data with just a simple power law show large residuals at low energies around 3 keV. A thermal component is added to the spectral model to account for this excess of soft photons in the spectrum. Different models for the thermal component like the multicolor disk blackbody (diskbb in Xspec), the blackbody component (bbody in Xspec) as well as the blackbody component corresponding to the boundary layer emission of a neutron star (bbodyrad in Xspec) are tried in the spectral fits. Here the 'diskbb' is a model to account for the X-ray emission from the accretion disk and the other two models 'bbody' and 'bbodyrad' are the models which account for X-ray emission from the surface of a neutron star with a single temperature for the blackbody emission. The fits with these different models for the thermal component do not show substantial difference. The 'diskbb' model out of the three thermal component models is chosen for further spectral fits. This is because the radius of the surface of emission, at the peak of the burst, as estimated using 'bbodyrad' model is $\sim$100 km for a distance of 8 kpc, which is unrealistic for a neutron star. After the inclusion of the thermal component, substantial residuals are still present around 7 keV. This is an indication of the presence of an Fe emission line along with an absorption feature. Inclusion of an absorption edge component and a Gaussian to the model removes the line feature but not the absorption feature completely. However, on the addition of the smedge component ("smedge" in Xspec (Ebisawa et al., 1994), which accounts for the absorption feature), the emission feature also disappears and the fits are found to improve substantially. The reduced chi-square value and the residuals at the high energy end from the fits indicate the need to fit the data with a high energy cutoff component to get a better fit. Hence the data

from both PCA and HEXTE are combined to get the energy spectra in the energy range 3-180 keV and spectral fits are done to the data.

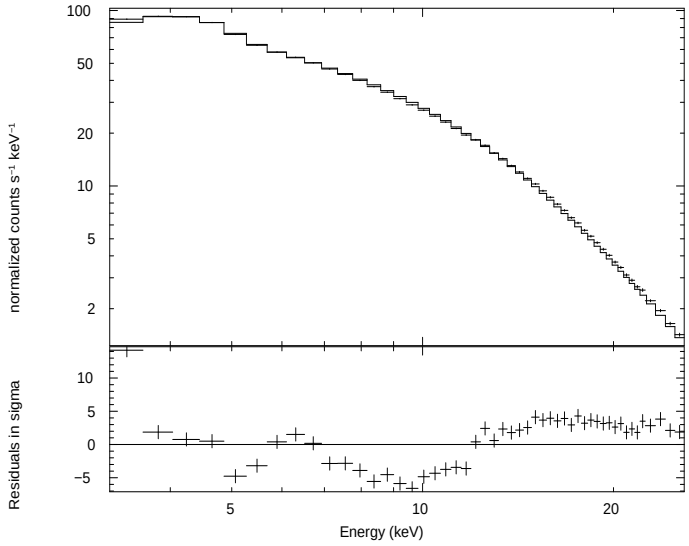

FIGURE 5.9: The spectrum from PCA data for one observation (obsid: 91423-01-01-04)fitted with a simple power law component is shown here. The residuals are shown in the bottom panel, in units of sigma.

The spectral model that is used is a combination of a simple power law, a smeared edge (smedge), a high energy cutoff, a diskbb component and a photon absorption parameter to account for the interstellar absorption. The spectral fit to the combined data from the PCA and the HEXTE data with this model is shown in figure 5.10. The parameters of the spectral fit to the combined spectra is given in table 5.1. The absorption edge derived from the smedge component is found to be at ∼7 keV and this does not vary throughout the burst. The power law component is the dominating factor in the spectra. The thermal component though necessary for the fit at low energies, contributes less than 2% to the total flux in the 3-25 keV range. The inclusion of thermal component and the high energy cutoff are required for the first 35 days of the observations, after which only the power law component and the smedge component are required. Eighty days after the peak of the burst, the smedge component also becomes insignificant. The data sets after this are therefore fitted with a simple power law and the absorption parameter.

In order to explain the underlying physics, the data is fitted with the comptonization model (compTT in Xspec) (Titarchuk, 1994), which describes the comptonization of the soft seed photons from the disk by the hot plasma. Though the uncertainties on the parameters are large, the fits to the complete set of observations indicate an average temperature of the

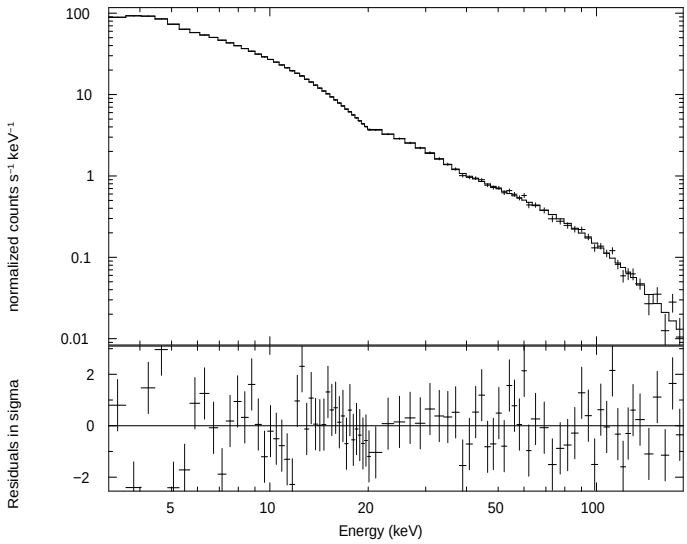

FIGURE 5.10: The spectrum from PCA and HEXTE data, for the observation (obsid: 91423-01-01-04) shown in figure 5.9, fitted with a combined model of simple power law, a smeared edge (smedge), high energy cutoff and diskbb components is shown here. The residuals in the bottom panel are in units of sigma.

TABLE 5.1: Table showing the fit parameters and the reduced chi-square for the fits to the PCA and HEXTE data for the observation (obsid: 91423-01-01-04) during the peak of the burst

Fits for PCA (3-25 keV) data							
Model	PI	T_{in} (keV)	E_{cut} (keV)	T_0 (keV)	KT_e (keV)	τ	reduced-chi-square
PL	1.831	-	-	-	-	-	15.38
PL+diskBB	1.744	1.096	-	-	-	-	5.68
PL*Smedge+diskBB	$1.78^{+0.006}_{-0.006}$	$0.38^{+0.079}_{-0.057}$	-	-	-	-	1.67
Fits for PCA+HEXTE (3-180 keV) data							
PL*Smedge*HEcut +diskBB	$1.76^{+0.012}_{-0.015}$	$0.42^{+0.086}_{-0.058}$	$38.2^{+9.8}_{-7.7}$	-	-	-	1.3
compTT*smedge +diskBB	-	0.43±0.04	-	0.6±0.13	44.6±8.7	1.08±0.23	1.33

Explanations for the abbreviations in the table are as follows:
PL - Power Law; HEcut - High Energy cutoff; PI - Photon Index of the power law;
T_{in} - Temperature of the disk; T_0 - Temperature of the disk which is the source of the seed photons; KT_e - Temperature of the plasma, ie. the corona; τ - optical depth of the plasma

hot corona to be $\sim$ 40 keV and the optical depth $\sim$ 1.4. Inspite of the caveats of the large errors, the average value of the temperature of the seed photons from the accretion disk derived from this model, which is $\sim$0.4 keV, matches the temperature of the accretion disk derived from the fits mentioned above. The fit parameters for the different models are given in table 5.1.

5.6.4 Timing analysis

Timing analysis is done using the event mode PCA data which has a time resolution of 125 μs. Power Density Spectrum (PDS) is generated for each observation using ftools. The power spectra are normalised such that their integral gives the squared rms fractional variability ((rms)**2/Hz), with the expected white noise level subtracted. The PDS thus obtained are fitted with a sum of Lorentzians. The power density spectrum obtained from the PCA data during the peak of the burst is shown in figure 5.11. A prominent low frequency QPO (LFQPO) at 0.891±0.008 Hz. with a Q-factor of 4, and an amplitude of ∼0.06 is observed. There are no kHz QPOs found in the PDS. The peaked noise and the band-limited noise are fitted with other Lorentzians. The total rms power of the PDS is found be 23% at the peak of the outburst. In order to determine the energy dependence

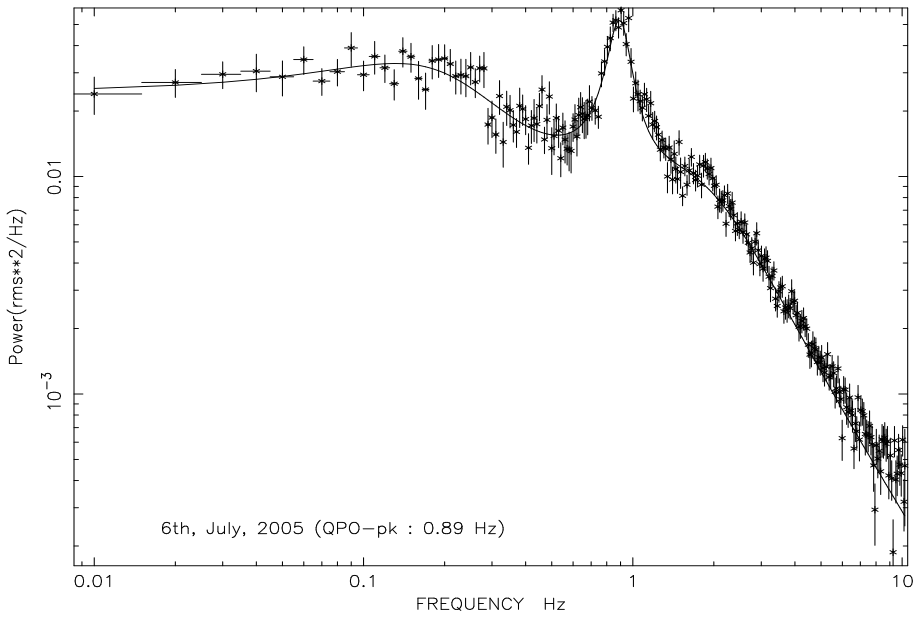

FIGURE 5.11: Power density spectrum showing the low frequency QPO, for the observation (obsid: 91423-01-01-04) at the peak of the burst.

of the LFQPO, we generated the PDS for different enegry bands. We find that the QPO is prominent in all the data sets in the energy range of 3-15 keV. Its presence at higher energies is evident only in few data sets.

5.6.5 Evolution of parameters

Different spectral and timing parameters and the observed flux are plotted as a function of MJD (Modified Julian Date) in figure 5.12. This figure shows the time evolution of various

parameters like the PCA count rate (in the energy range 3-25 keV), the photon index, the hardness ratio (the ratio of the PCA count rate in the energy bands (8.6 to 18.0) keV to (5. to 8.6) keV, as defined by Muno et al. (2002) and Remillard & McClintock (2006)), the low frequency QPO and the rms amplitude of the power density spectrum in the frequency range 0.1 to 10 Hz. It may be noted that the entire set of data available is from the peak to the decay of the burst.

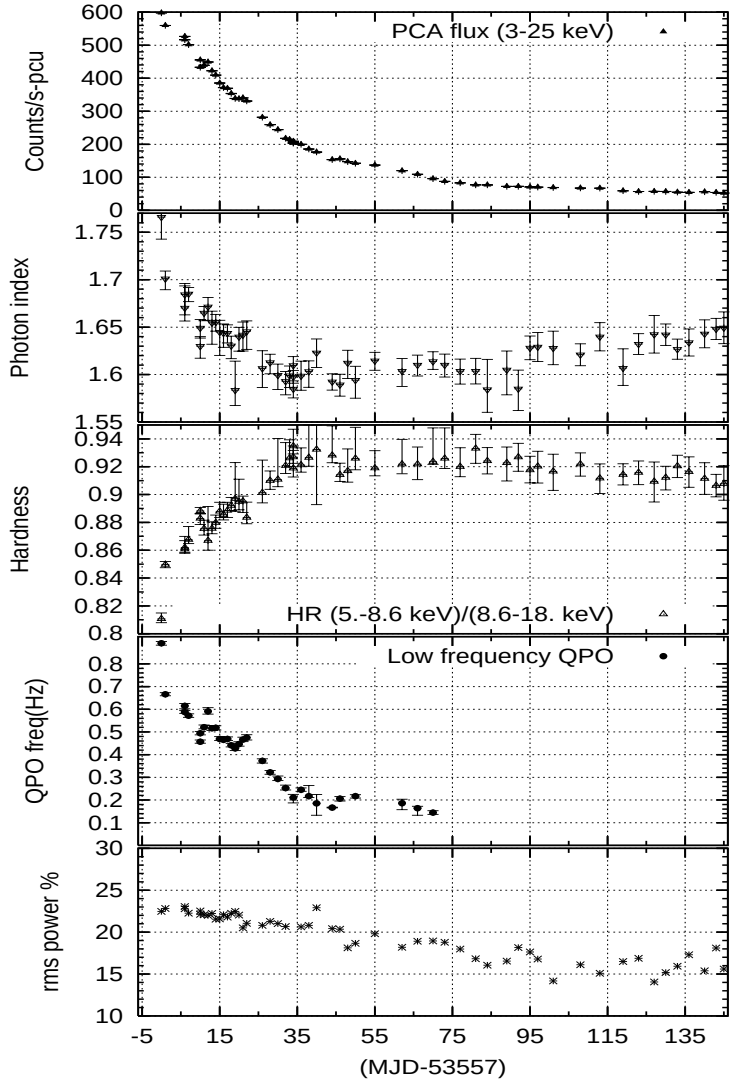

FIGURE 5.12: The time evolution of PCA count rate, photon index, hardness ratio, QPO and the rms power are shown from the top to the bottom panel respectively.

The power law component is dominant throughout the decay of the burst. The photon index is found to be 1.76 at the peak of the burst and decreases to 1.70 within a day although the flux decrease observed is within the level of 1σ. After this abrupt decrease the photon index of the power law further decreases almost linearly from 1.7 to 1.6 within a span of

30-35 days. Later the photon index hovers around 1.61 till about 90 days after which there is a slow trend of increase seen towards the end of the observations. The hardness ratio is also found to indicate a similar behaviour, with HR showing an abrupt increase from 0.81 to 0.85 within a day followed by an almost linear increase from 0.85 to 0.92 within 30-35 days and then leveling off at 0.92 till 90 days. The tendency for HR to decrease gradually after 90 days up to the end of the burst is also similar to the photon index. The spectral softening observed after 90 days is very gradual with time and continues till the end of the observations. This behavior of spectral softening is observed in few other sources like XTE J1550-564 (Belloni et al., 2002, Sturner & Shrader, 2005).

The centroid frequency of the QPO is found to be 0.891 Hz at the peak of the outburst and is found to decrease abruptly to 0.66 Hz within a day and then it decreases almost linearly from 0.66 Hz to 0.2 Hz within a span of about 35 days. Later, the QPO is visible only intermittently at lower values of about 0.2 Hz and is observed only till 70 days, after which it is not detectable. The rms power of the PDS (0.1 to 10.0 Hz) however exhibits a more uniform trend with a slow decrease from 23% to 15% till the end of the burst. This trend is also seen if the frequency range of the PDS is extended down to 0.01 Hz.

In order to study the variation of these parameters as a function of flux, the same parameters are plotted against flux as shown in figure 5.13. It may be noted that since the observations cover the decay portion of the burst, the time line in this figure goes from right to left. The softening of the spectra at low flux levels (towards the end of the burst) can be clearly seen in the top two panels of figure 5.13, which shows the photon index and the hardness ratio as a function of PCA flux. The QPO frequency follows a linear trend as a function of flux, which is seen in the third panel. The rms power of the PDS shows an abrupt decrease at low flux levels as shown in the bottom panel of the figure. The time evolution of the disk parameters like the temperature of the disk, the inner radius of the disk etc. are difficult to comment on as the uncertainties on these parameters are large. The high energy cutoff is found to be about 40 keV on an average and a straight line fit to the values during the entire outburst does not show any systematic change during the decay.

5.6.6 Discussions

The optical observations (Halpern, 2005) of the source reveal the presence of a bright optical counterpart with R$\sim$15.8 magnitude indicating the system to be a low mass x-ray binary (LMXB), with a reddened companion star. Spectral analysis of the source indicating the hard spectrum with a power law dominance and the timing analysis of the data indicating

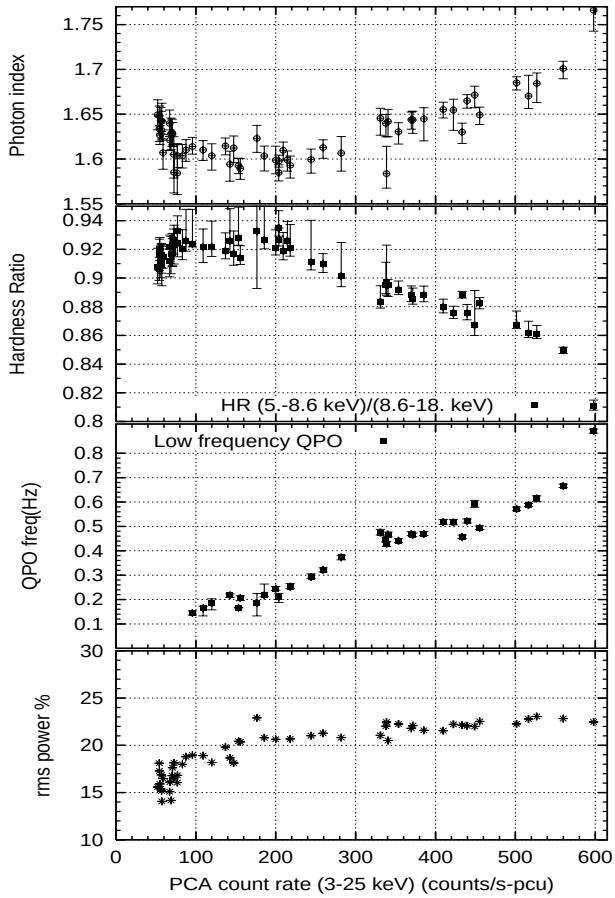

FIGURE 5.13: The photon index is shown at the top panel, the hardness ratio (8.6-5.0 keV)/(8.6-18.0 keV) derived from the PCA data in the second, the QPO frequency in the third and the rms power at the bottom.

the presence of low frequency QPOs at < 1 Hz are typical features observed in BHCs. There are no kHz QPOs found in the power spectrum. The fits to the thermal component in the spectra with a black body component ("bbodyrad" in Xspec) for a normalized surface area, corresponding to the boundary layer of a neutron star, gives an estimate of the radius of the compact object $\sim$100 km, for a typical distance of 8 kpc, at the peak of the burst and is found to be $>$20 km till the end of the outburst. From these points, it can be surmised that the probability for the compact object being a neutron star is almost negligible.

The low/hard spectral state of black hole candidates (BHC) is typified with a dominant power law component, contributing $> 80\%$ of the total flux in 2-20 keV range, having a spectral index between 1.4 and 2.1. The total rms power (r), in the power density spectrum, integrated over the frequency range 0.1-10 Hz is strong with r > 0.1 (Remillard & McClintock, 2006). From the spectral study of all the observations of the source, it is

clear that the power law component dominates the spectra throughout the burst with the spectral index decreasing from 1.76 to 1.6. Further, the thermal component, though present during the bright phases of the outburst, contributes only $< 2\%$ of the total flux in the 3-25 keV energy range. This, along with the presence of a low frequency QPOs <1 Hz and the rms power in the frequency range 0.1-10 Hz being $> 10\%$ (shown in figure 5.12), clearly indicates that the source is locked in the low/hard state throughout the outburst and never made it to the high/soft state.

In all the Low/Hard X-ray transient (LHXT) outbursts observed till date, the presence of a hot accretion disk component in spectra of the 3-25 keV energy range is not reported. Here, the presence of a cool accretion disk at an average temperature of 0.4 keV in addition the presence of a smedge component is clearly seen, which is usually attributed to be the disk reflection component. The inner radius of the disk (estimated from the normalization factor of diskbb component) turns out to be $\leq 4R_g$ for a black hole of mass 10 $M_\odot$. It is found that the contribution of the disk component is seen only till day 35 and the smedge component is seen till 80 days after the peak of the outburst. The reason for the lack of a thermal component in the later part of the burst in the 3-25 keV range could be due to the reduced sensitivity of the RXTE-PCA instrument at energies below 3 keV and that, the accretion disk still continues to exist even towards the end of the burst. The presence of the accretion disk during the low/hard state approaching quiescence for this source, SWIFT J1753.5-0127, was strongly suggested by Miller et al. (2006), with simultaneous RXTE and XMM-Newton observations, after about 118 days from the last observation of the outburst studied here in this work. The fits to the XMM-Newton data by Miller et al. (2006) imply the presence of an accretion disk extending near to the inner stable circular orbit with an $R_{in} \leq 6R_g$ for a black hole of mass 10 $M_\odot$. All these provide the evidence for the presence of the inner accretion disk in a low/hard state x-ray outburst.

Fits to all the RXTE data sets of the outburst of the source, SWIFT J1753.5-0127, show that the spectrum is however, dominated by the power law component, which can be described by the inverse Comptonization of seed photons from the accretion disk by a hot plasma near the central compact object. This picture is supported by modeling the data using the Comptonization model ("compTT" in Xspec), the results of which show an accretion disk of temperature $\sim$0.4 keV and a hot corona of temperature $\sim$40 keV with an optical depth $\sim$1.4. This Comptonization region could be a corona, a Compton cloud or a post shock region as referred in the literature (Titarchuk, 1994).

Low frequency QPOs less than 1 Hz are observed up to about 35 days. The QPOs seen in the PDS of all the observations are found to be from photons predominantly in the

energy range 3-15 keV. Simple Keplerian inflow of matter predicts higher frequencies for a 10 $M_{\odot}$ black hole. The centroid frequency decreases with time and appears to be linearly correlated with the flux (figure 5.13). This correlation does not favour the global normal disk oscillation model (Titarchuk & Osherovich, 2000) for the origin of QPOs in this source, as also indicated by Zhang et al. (2007). The trend of photon index and QPO correlation as seen in figure 5.14 is similar to that predicted by the transition layer model of Titarchuk & Fiorito (2004). The optical depth (τ) of the transition layer, is estimated to be $\sim$1.8 from

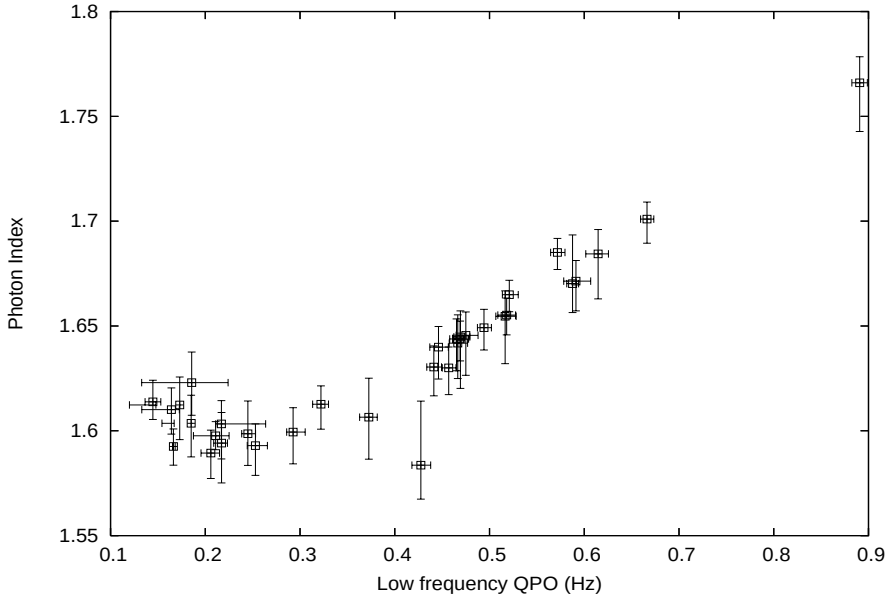

FIGURE 5.14: Photon index as a function of low frequency QPO

the figure 6 of Titarchuk & Fiorito (2004) for a photon index of 1.7. This is comparable to the value of 1.4 for the optical depth of the corona derived from the CompTT model as applied to these observations studied here in this work. Using figure 4 of Titarchuk & Fiorito (2004), which relates LFQPO frequency to the outer radius of the transition layer (TL), the 0.9 to 0.7 QPO frequency decrease observed in this data corresponds to $\sim$20 to 25 R_s, which translates to 600-750 km for a 10 $M_{\odot}$ black hole. This size of TL is much larger than the estimated R_{in} (estimated using the apparent inner radius of the accretion disk as given in equation 5.3 and 5.4) from the diskbb model which is of the order of 150 km. Therefore, the current observations can match the size of the transition layer only if the QPO-vs-TL size relationship can be proportionally reduced for a lower mass black hole, of the order of 3 $M_{\odot}$ black hole. However, the estimated mass from the value of R_{in} using equation 5.2 turns out to be about 16.8 $M_{\odot}$. Although, the range of spectral index predicted by the transition layer theory for low/hard state ($\Gamma = 1.6 \pm 0.2$) applies to these observations, the observed dependence of spectral index on flux is not predicted by

the model. In addition, this model predicts that the the low frequency and high frequency QPOs are correlated. There is no high frequency QPO observed in the PDS for this source. Zurita et al. (2008) give the study of optical observations of the source Swift J1753.5-0127, in which the mass estimate for this source is given to be ~ 12 $M_{\odot}$.

The profile of the light curve of this source, SWIFT J1753.5-0127, is of a FRED (Fast Rise Exponential Decay) type. FRED type light curves of the x-ray outbursts are supposed to be originating due to the instabilities in accretion disk (Chen et al., 1997). This can be explained either by the Disk Instability Model (DIM) (Lasota, 2001) or due to the disk diffusion propogation model (Wood et al., 2001). The correlation of QPO frequency with source flux as seen in figure 5.13 does not favour the disk diffusion propogation model (Wood et al., 2001). Since the profile of the light curve is a FRED, which is associated with the disk, it can be considered that the outburst could have been triggered due to some instability in the disk. It may be noted that the e-folding decay time of this outburst (31 days) is also associated with similar timescales on which several spectral parameters show a change in behavior indicating a strong correlation between the spectral and light curve characteristics. The disk probably starts receding with the abrupt decrease in the spectral index within a day, and by the end of 35 days it cools to the extent that it is not detectable in the 3-25 keV region. This change is indicated by the increase in hardness and decrease in the QPO frequency within a day of the outburst.

A similar FRED profile has been seen in the 40-150 keV light curve of GRO J0422+32 during its 1992 low/hard state x-ray outburst detected by BATSE on CGRO (Burst And Transient Source Experiment on Compton Gamma Ray Observatory) (Van der Hooft et al., 1999). Since there was no soft x-ray coverage during the early stages of the burst, it could not be proved that an ultrasoft disk component existed or not (Pietsch et al., 1993).

The light curves of most of the x-ray outbursts in the low/hard state of the sources observed in the 2-10 keV energy range are found to be of triangular shape with or without a plateau. None of these outbursts are found to be reported with an ultrasoft component associated with an accretion disk in their spectra. However, the presence of a cool outer disk can be found implicitly, from the reflection components in the spectra. Whether a common instability model with difference in parameters can explain both the FRED profile and the triangular profile for low/hard X-ray outbursts is still an open question.

5.6.7 On the possible explanations for a low/hard state x-ray outburst

While Brocksopp et al. (2004) try to look for a possibility of explaining the behavior of these LHXTs as part of the outburst mechanisms associated with other canonical SXTs, Meyer-Hofmeister (2004) gives an explanation in terms of short orbital periods, which result in less mass accumulation in a smaller accretion disk giving rise to relatively low peak luminosities during the outbursts.

It is stated (Meyer-Hofmeister, 2004) that for low peak luminosities, ie. low mass flow rate in the disk, coronal evaporation truncates the thin disk even in the outburst and an advection-dominated accretion flow (ADAF) occurs resulting in a spectrum that remains hard. Also the evaporation efficiency is stated to be proportional to the mass of the compact object and larger the mass, larger is the truncation radius of the inner disk (Meyer-Hofmeister, 2004). The behavior of SWIFT J1753.5-0127 can also be explained by the ADAF model, if the compact object is a less massive black hole, resulting in lesser evaporation efficiency allowing the disk to extend near the inner stable circular orbit accounting for the thermal component, while having a contribution of evaporation of the disk to give rise to the overwhelming hard state of the outburst. We also see a softening towards the end of the burst which is seen in figure 5.12 and more clearly seen in figure 5.13. Spectral softening at low luminosities is predicted by ADAF model (Esin et al., 1997). This could imply that it is possibly ADAF which is being observed at the low flux levels of the burst approaching quiescence.

There are some sources which have been observed only in low/hard state outbursts. They are GRO J0422+32 (Van der Hooft et al., 1999), GRS 1716-249 (Hjellming et al., 1996), GS 2023+338, 1E1740.7-2942 and GRS 1758-258, amongst which the last two have been reported to be persistent sources (Cui et al., 1997, Grebenev et al., 1996). The reason for a source to show low/hard state x-ray outbursts only and not having any canonical outbursts could be something to do with the orbital parameters of the system as such. Such systems can be classified as Low/Hard state X-ray Transients (LHXTs), as mentioned by Brocksopp et al. (2004). There are also sources, which have had state transitions in canonical outbursts, at times showing low/hard state outbursts. A few of them are XTE J1118+480, XTE J1550-564, GX 339-4, Cyg X-1 etc. The low/hard state x-ray outbursts shown by these sources can be classified as "failed outbursts" in the canonical SXTs, which could be due to low mass accretion rate or due to discrete accretion events.

While there are many models to explain the varied outbursts from different sources, whether a common model will be able to explain all these different natures of the outbursts or not, is still an open question.

5.6.8 On SWIFT J1753.5-0127

Spectral and timing analysis of RXTE observations of the source, SWIFT J1753.5-0127, show that the source was in the low/hard state throughout the outburst. The physical picture of the burst is explained by the Comptonization of the seed photons by the hot corona near the compact object. The FRED profile of the light curve, usually uncommon in low/hard x-ray outbursts and the presence of a multicolor black body component in the fits to the spectra imply a likely association of the burst with the instabilities in the accretion disk. The low frequency QPOs <1 Hz and the rms power between 10 and 30 %, along with the spectral behavior of the source with an optical counterpart of magnitude R$\sim$15.8 indicates this source to be a LMXB with a stellar mass black hole, most likely, as the compact object. Thereby, this source falls in the category of SXTs that show low/hard state x-ray outbursts.

The QPO frequency observed during the first 35 days after the peak of outburst is almost linearly correlated with the flux and the photon index. During the same period a spectral hardening and diminishing contribution of disk are also found. These factors rule out some of the current models for outbursts. There is also a softening of spectrum seen towards the end of the burst, accompanied with very small change in source flux. While the transition layer model and the ADAF model can explain some of the observed features, both the models indicate that the compact object in this system is most probably a low mass black hole.

5.7 Conclusions

Two X-ray transient sources, SLX 1746-331 and Swift J1753.5-0127, during their first observed outburst are studied in detail in this chapter. The nature of these sources are discussed. The spectral and timing analysis of these indicate that they are black hole candidates. The physics of the outburst in these sources are also discussed. Both these analyses are published in two different papers Narendranath et al. (2006) and Ramadevi & Seetha (2007). Study of spectral and timing of such new transients help in finding out the nature of the compact object in X-ray binary systems and the physics driving the outbursts.

Chapter 6

Summary

6.1 Introduction

All Sky Monitor is one of the important instruments in an Astronomy mission as a large area of the sky is scanned within few hours to look for any X-ray transients sources in the sky. Once an X-ray transient is detected and located, this information is given to other observatories to do further observations for detailed spectral and timing studies of the X-ray source, to understand the source in detail. Scanning Sky Monitor (SSM) on-board ASTROSAT is designed for detection and location of transient X-ray sources. The present work is on the design optimization and calibration of position-sensitive proportional counters for SSM on ASTROSAT. Along with this, the detailed study of two X-ray transients observed by the RXTE is also undertaken and discussed.

SSM comprises of three identical units of position-sensitive proportional counters which are design optimized with certain parameters for better performance. SSM detectors are characterized after implementation of the optimised parameters, in order to meet the science objectives, through various experiments. These detectors are tested and calibrated for positional and spectral response. The methodology of detecting and locating the X-ray sources in the field of view of the detector is devised, implemented and experimentally verified.

The two X-ray transient sources studied here are found to be black hole candidates. The spectral and timing studies of these sources are carried out in detail to understand the physical processes of X-ray emission that have resulted in the outburst. The nature of the compact object in both these sources is also discussed.

This chapter brings out the salient features of the present work and the important results obtained are summarised in the following sections. The scope of future work is also discussed. A brief note on the design for future X-ray sky monitor is also discussed.

6.2 Brief summary of the present work

6.2.1 Design optimisation of SSM

In chapter 2 we discussed the characteristics and design optimisation of different parameters of the SSM-detectors, like cell size, gas mixture, gas pressure and operating voltage, which in turn control the detection efficiency and gas gain of the detector. Simulation softwares like GARFIELD and MAXWELL are used for this study. GARFIELD is used to simulate the SSM cell and study the electric field inside the cells. The electric field inside the wire-walled cell of SSM is estimated to be 62596 V/cm at a distance of three times the anode radius from the centre of the cell. The value of 'Er' which is the electric field potential at regions around the anode where the gas multiplication takes place is found to be constant at distances, few times the anode radius around the anode. The gas gains are calculated using Diethorn formula using the electric field values for different cell sizes. The gas gain as a function of cell size is studied. The gas gain for SSM cell with an anode of diameter 25 microns at an operating voltage of 1500 Volts is found to be 8675 for P-10 gas and 13690 for the gas mixture of 20%Xe+80%P-10, at a gas pressure of 1 atm. The cell size was optimized by choosing an optimum gas gain of about 10000. The cell size for SSM is chosen to be 1.2 $\times$ 1.25 cm^2. The maximum parallax error for the chosen cell size for the oblique incidence of photon at angles $\pm 5^\circ$ is estimated as 0.52 mm at higher energies, the probability of occurrence of which is $\leq$20%. Therefore, parallax errors in position determination can be ignored.

The gas mixture for SSM is chosen in view of better detection efficiency and sufficient gas gain. From the perspective of detection efficiency, Xe + a quench gas will be preferred as the gas mixture for SSM, as Xenon has better detection efficiency because of its relatively high atomic number as compared to Argon. However, Xe is easily prone to contamination (Ramsey & Agrawal, 1988) and hence, a mixture of Xe and Ar along with a quench gas is chosen for SSM. It is observed from our study that the gas mixture of 25%Xe+75%P-10 gives better detection efficiency than P-10. This also gives a detection efficiency >20% at extreme ends of the energy range of interest, ie. at 2 keV and at 10 keV. It is also required that this gas mixture gives the required gas gain of about 10000 at an operating voltage of

1500 Volts for SSM cell configuration. It has been shown in earlier literature that the gas gain increases with the addition of Xenon with Argon up to about 10% concentration of Xenon and then decreases (Fuzesy, 1972). The gas gain of 0%Xe concentration (ie. P-10) equals the gas gain of the gas mixture with 27%Xe with P-10 (Fuzesy, 1972). Three different gas mixtures which are P-10 (90%Ar+10%CH4), 20%Xe+80%P-10 and 25%Xe+75%P-10 are experimentally studied for gas gain at different operating voltages. It is found that the gas gains of the gas mixtures which have 20% or 25% concentration of Xe along with P-10 are higher than that of P-10. The ratio of the gas gains of the gas mixture of 20%Xe + 80%P-10 to that of P10, from the theoretical and experimental measures are 1.76 and 1.93 $\pm$ 0.08 respectively, for an anode of diameter 25 microns, at an operating voltage of 1500 Volts. The gas gain of gas mixture of 25%Xe + 75%P-10 is greater by about 1.5 times than that of pure P-10 for an operating voltage of 1500 Volts, for an anode of diameter 25 microns. Amongst the two gas mixtures 20%Xe+80%P-10 and 25%Xe+75%P-10, the gas mixture with higher Xe concentration gives better detection efficiency. Considering these parameters, the gas mixture for SSM detectors is chosen to be 25%Xe+75%P-10.

The quench gas for SSM is chosen to be methane. Methane serves as a better quench gas with Xenon rather than with Argon from the perspective of better energy resolution Ramsey & Agrawal (1988). We have experimentally found that the energy resolution for the gas mixture 25% Xe + 75% P-10 is about 17-18% at 5.9 keV, which is better than that from P-10 which is about 19-20% at the same energy. It is to be noted that here it is a mixture of Ar and Xe with methane which is compared to that of pure P-10, which is a mixture of Ar and methane. It is the addition of 25% Xe to P-10 which has enhanced the energy resolution by about 1-2% at 5.9 keV.

The gas pressure is optimized such that the detection efficiency is greater than 20% at all energies in the energy range of interest for the given gas mixture and detection depth (which is 1.25 cm). It is also considered that the window that is bulged out is not at the risk of breaking. The pressure at which the gas mixture for SSM detectors is filled is 800 torr.

The anode wires for SSM are resistive wires so as to help position sensing by charge division method. Anode wires which are carbon-quoted-quartz of diameter 25 microns and graphite wires of diameter 10 microns are studied for their characteristics to decide on the anode wire for SSM. It is required that the resistance per unit length be of the order of kΩ to get position resolution of sub-millimeters. Graphite wires have a low value of resistance per unit length which is about 100Ω/mm. Hence graphite wires of short lengths (here, 60 mm) are not preferred for position sensing by charge division method. The anodes for SSM

are chosen to be carbon-coated quartz wire of diameter 25 microns and resistance per unit length of 8 kΩ/mm. The aging effects of these wires are also experimentally observed.

The window for SSM detectors is chosen to be Aluminized-Mylar of thickness 25 microns. Although, Be windows give a better transmission probability and hence better detection efficiency at low energies, getting micro-pore free Be windows of large areas (as large as few thousands of sq-cm) is quite difficult. Hence, aluminized Mylar of thickness 25 microns is chosen for SSM detectors. End-effects in SSM detectors are studied experimentally. Simulation study of end-effects are done using MAXWELL-2D software, for the SSM cell configuration. It is found that by using kel-F insulator protruded into the cell, the high gas gain at the ends of the cell is reduced. Simulations are done with different kel-F protrusions inside the SSM cell and a 4 mm protrusion of kel-F insulator is found to minimize the end-effects in SSM. It is also experimentally verified that a 4 mm protrusion minimizes the end-effects.

6.2.2 Characterisation of SSM detector

Chapter 3 discusses the experimental results of SSM detector with all the design parameters implemented as discussed in chapter 2. The details of the SSM detector with the electronics and the coded-mask on it is discussed in this chapter. The principle of operation for measurement of energy and position of the incident photon is discussed. The characteristics of the detector such as stability of the output for a given energy of the incident photon, detection efficiency in the energy range of interest, gas gain at different operating voltage, energy resolution, position resolution etc. are experimentally studied and results are discussed. The stability of the total output of one of the SSM detectors is studied for more than two and a half years. It has been found that the total output varies within ±2% typically (Seetha et al., 2006), for the collimated ^{55}Fe source placed at the same position and tested every time. However, the variations of the total output at different positions along the anode wire is found to be about ±5%, which are within the threshold for variation.

Detection efficiency of SSM is compared with that of SiPIN to estimate the experimental value of detection efficiency at 5.9 keV. The detection efficiency of SSM at 6 keV is estimated experimentally to be 60%, which matches with the theoretically estimated value.

SSM detectors are tested at different HV values. A high voltage of 1500 Volts fed to the anodes produces an output of 3 V (300 channels) at 6 keV. The output voltage range for SSM is chosen to be 1 to 5 Volt for the energy range 2 to 10 keV.

SSM detectors are not for spectroscopic study as the energy resolution is poorer compared to semiconductor detectors. Energy resolution of SSM is experimentally measured to be 18% at 6 keV. The position resolution of SSM detectors is expected to be of sub-millimeter in the energy range of interest. Position resolution of SSM is experimentally measured to be 0.68 ± 0.07 mm at 6 keV.

The variations in the total output for a monochromatic source of X-rays at different positions along the anode wire are found to be ±5% (Seetha et al., 2006). These variations are found to be within the limits of the energy resolution of the output for a photon of particular energy.

6.2.3 Methodology to derive the position of the incident photon and the source in the FOV of SSM

Chapter 3 also discusses the working principle of SSM and the methodology of deriving the position of the photon incident on the detector. The importance of calibrating the detector to deduce the electrical start and end point of the anodes in the detector for deriving the correct position of the incident photon is explained. Positional calibration of SSM detectors are discussed in detail in this chapter. The anodes in the detector are calibrated to derive the anode calibration constants which are used to calculate the position of incidence of a photon on the anode wire. Position resolution at different positions along the anode wire for collimated ^{55}Fe placed at different positions is estimated.

Various experiments are done to verify the derived anode calibration constants. Experiments like the 'centre-blocked tests', tests with a single mask pattern on the detector plane are done to cross check the calibration constants of the anodes. Experiments with the coded-mask mounted on the detector to derive the position of the sources in the FOV of SSM are carried out. Experiments carried out are discussed in detail and the results are also shown. It has been shown that for a single source in the FOV, the source plane image derived from the data also contains a single source in the expected location.

The background spectrum for SSM in the laboratory is studied. The experimentally estimated background counts as detected by SSM is found to match with the theoretically calculated counts. Also, the efficiency of the veto layer of SSM to reject charge particle background is also studied. The efficiency of veto layer of SSM is estimated to be 70%. This information will be used to estimate the errors on the flux observed by SSM when flown on-board the satellite.

6.2.4 Development of SSM response

Chapter 4 discusses the details of response of SSM detectors. Effective area of SSM in the energy range of interest is estimated using the detection efficiency and the geometric area of SSM. The effective area of SSM is 20 cm^2 at 4 keV. Sensitivity of SSM in the energy range of interest is also calculated. SSM is found to have a sensitivity of ∼30 milliCrab for an integration time of 10 minutes with a 3σ confidence.

Energy calibration of SSM detector using different energy X-ray sources are presented in this chapter. Energy resolution and position resolution at different energies are estimated for four different energies in the energy range of interest. The energy resolution of SSM is 18% at 6 keV and the position resolution is 0.68 ± 0.07 mm at 6 keV. The detector is calibrated at different energies in the energy range of interest. The pulse height spectrum of SSM for a monochromatic source of X-rays is modelled using three Gaussians, one for the photopeak of the incident X-rays and the other two for the escape peaks corresponding to Argon and Xenon in the SSM gas mixture. Therefore, the Spectral Redistribution Function (SRF) for SSM consists of three Gaussians at each energy. In this way, the pulse height spectra at four different X-ray energies in the energy range of interest are modelled using the SRF. The response matrix for SSM is generated using the calibration data, using 'genrsp' a routine in ftools to generate response. The response matrix generated in this way is cross checked with the pulse height spectra acquired from four different X-ray energy sources.

6.2.5 On-board calibration procedure for SSM

Chapter 4 also discusses the on-board calibration procedure for SSM. On-board calibration of SSM is planned to be done by observing the Crab nebula which is considered to be an X-ray source with constant spectrum and constant intensity given by $dN/dE=9.7E^{-2.1}$. The simulation of pulse height spectrum of the Crab nebula as seen by SSM is done using the SSM response. The integrated counts of the pulse height spectrum of the Crab nebula as observed by SSM gives the Crab count for SSM. The Crab count for SSM is estimated to be 38.5 counts/second. The Crab count is used to calibrate the sensitivity of SSM on-board.

The gas gain of SSM is likely to vary on-board due to various reasons. It is required to correct for the gain variations if any, on-board. The spectrum of Crab nebula is simulated for different gain factors of SSM. The integrated counts from the Crab nebula for different gain factors are estimated. It is also shown that the hardness ratio (HR) which is the ratio of the intensity in the energy range 5 to 10 keV to intensity in the energy range 3 to 5 keV

is a function of the gas gain of the detector. Therefore, any variation in the hardness ratio is an indicator of change of gain in the detector. Knowing the variation in the hardness ratio and hence the variation in the gain, the operating voltage of the detector can be tuned to bring the detector back to its original gain value. It is shown that a 10% variation in the gain can be be corrected on-board by stepping the HV value to the available steps in SSM. Any variation in the gain, finer than 10% can be estimated from the variations in the hardness ratio and can be corrected in the data using correction factors.

6.2.6 Spectral and timing study of select X-ray transient sources

As SSM is an instrument to detect and locate transient X-ray sources, it is not designed to do spectroscopy or timing observations (with time resolution of the order of microseconds) of the sources. However, SSM will be the first instrument to trigger such detailed observations of these sources, as a first hand information of an outburst is given to other instruments to do these detailed observations of the source. Chapter 5 discusses the X-ray data analysis of two X-ray transient sources which are observed by RXTE in these outbursts. The spectral and timing study of these two sources are discussed in detail in this chapter. The detailed spectral and timing analysis show that the two X-ray transients (one of them, Swift J1753.5-0127, is a newly discovered source) are X-ray binary systems which have a stellar mass black hole as the compact object. The mass estimate for the compact object in the source SLX 1746-331 is found to be ~ 3 $M_{\odot}$, which is close to the lower mass limit for black holes. The mass estimate for the compact object in the source Swift J1753.5-0127 is found to be ~ 16.8 $M_{\odot}$ derived from the innermost stable circular orbit which is estimated from the 'diskbb' component of the energy spectra. However, the statistics of the disk flux in the energy spectra is very low to consider this mass estimate. The mass estimate of the black hole for this source, using the Transition Layer model turns out to be ~ 3 $M_{\odot}$, which is close to the mass limit for black holes. Zurita et al. (2008) give the study of multiwavelength observations of the source Swift J1753.5-0127, in which the mass estimate for this source is given to be ~ 12 $M_{\odot}$. The detailed analysis of these sources SLX 1746-331 and Swift J1753.5-0127 are discussed in the respective publications of ours, which are Narendranath et al. (2006) and Ramadevi & Seetha (2007).

One of the sources Swift J1753.5-0127 is found to be in the low/hard state throughout the outburst. This behaviour is different from the canonical outbursts of X-ray transient sources. Study of this class of sources which show outbursts which are only in the low/hard state can be done to understand these systems in details.

6.3 Future work for a more detailed study

There are few things in this thesis work which can be studied in a more detailed way. One such study is the simulation of end-effects in SSM detectors, which can be simulated more realistically with MAXWELL 3D software, where the electric field for a given geometry is simulated considering the 3D geometry. This work is planned for the near future using MAXWELL 3D software.

A more detailed estimation of the anode calibration constants by doing non-linear function fits to the position-vs-charge ratio data is to be conducted, so that the errors on position determination of the source will be minimised. Such a detailed study will be carried out in the near future for the flight model detectors of SSM.

Detection efficiency for SSM is derived experimentally for the energy 6 keV using ^{55}Fe radioactive source and compared with the theoretical value, in this thesis work. It is desired that the detection efficiency be estimated experimentally for the entire energy range of interest, which is 2 to 10 keV. This can be done using a continuum spectrum from an X-ray gun, shined on to SSM and SiPIN. The cross calibration of SSM can be done with SiPIN to estimate the detection efficiencies in the energy range of interest.

Experiments to derive the location of the sources in the FOV of SSM have been done with a single source in the FOV. The image of the source plane derived from the data acquired from the experiments showed a single source in the FOV at the expected source position. It is also required that the experiments be carried out with two or more sources in the FOV of SSM and the image of the source plane be derived to find out the location of the sources in it. Since the X-ray sources used for this experiment have to be placed at a height of about 2 m or more from the detector plane, radioactive source ^{55}Fe cannot be used, as the 6 keV X-ray photons will be absorbed in the atmospheric column of 2 m. Hence X-ray gun which produces a continuum is used for such experiments. It is planned to test the SSM flight model detectors with two such sources in the FOV and look for the location of the sources in the image of the source plane constructed from the data.

6.4 Future Scope

This section gives a brief discussion on the future sky monitors with an attempt to give a design for future All Sky Monitors based on the knowledge gained from this thesis work.

Also, the scope of studying the X-ray transients which show low/hard state outbursts are also discussed in brief.

6.4.1 Future Sky Monitors

Scanning sky monitors are required for an astronomy mission to detect interesting variabilities happening in the X-ray sky. All-sky X-ray monitoring is needed for several reasons which are discussed in detail in chapter 1. A new sky monitor with a better sensitivity is required to extend the already existing catalog of the X-ray sources, with new discoveries, to generate complete light curves of almost all the outbursts of transient sources including the rising phase of the outbursts, to study long term variations of the flaring stars, to catch unexpected transient phenomena etc. Future sky monitors can be designed in such a way that they have large field of view and can scan the sky effectively, with a higher duty cycle, higher sensitivity and higher angular resolution with a wider energy range of operation. Till today, many of the transients are studied in spectral and timing domain only after they reach the peak of an outburst till the decay phase. If the sky monitors can give alert notification during the start of an outburst or start of the variabilities observed in these X-ray sources, the detailed observations of the entire outburst can give a better understanding of the physical picture of these sources. Therefore, it is worthwhile to devise such an instrument in the future. A detailed study of All Sky Monitors can be found in (Holt & Priedhorsky, 1987).

Semiconductor detectors have better detection efficiency compared to proportional counters. Hence, a semiconductor detector with a coded-mask on top of it can serve the purpose of a sky monitor with better sensitivity compared to proportional counters. Si-based detectors are largely used for soft X-ray detection in the energy range 1 to 30 keV. The detection efficiency of a Si-based detector of thickness 500 μ with a half mil Be window is $\geq$20% at the 1 and 30 keV and is almost 100% in the energy range 5 to 10 keV. CdZnTe (CZT) detectors are largely used for hard X-ray detection in the energy range 20 to 300 keV. The detection efficiency of a 1 mm thick CZT detector is found to be >80% up to 100 keV and >30% up to 250 keV. The hard X-ray detection range can be increased to 600 keV if the thickness of the CZT is about 5 mm. A sky monitor with both these types of detectors (ie. a 0.5 mm thick Si-based detector and a 1 mm thick CZT detector) in it will span the energy range from 1 to 300 keV. Considering the mask pixel to be about 1 mm $\times$ 1 mm, the 2D coded-mask should be at a height of about 60 cm to produce an angular resolution of about 6 arcmin $\times$ 6 arcmin.

Amongst the known Si-based detectors, a new type of detector which is Silicon Drift Detector (SDD) is capable of handling high photon count rates of about 100 kcps, without any degradation effects in its performance, at an operating temperature of -20° C. These type of detectors can be used for an All Sky Monitor, as there can be high photon count rates from different sources in the large FOV of the ASM. There are two types of SDDs: cylindrical and linear. Amongst these two, cylindrical SDD are available at a minimum area of 5 mm^2 which give a pixel size of 1.4 mm. Large areas of tens of sq-cm can be made from an array of such SDDs. The linear SDDs provide better position resolution with pixel size of the order of 50 to 100 microns. These linear SDD detectors are available in large areas of about 4×4 cm^2, that are developed by the Max Planck Institute at Germany. SDDs are also available commercially at different companies. Similarly, pixellated CZT detectors are also available in large areas with custom-made read out electronics. The pixel sizes of the order of about 300 microns in a 1 mm thick CZT detectors are available, which are good enough for achieving an angular resolution of about few arcminutes.

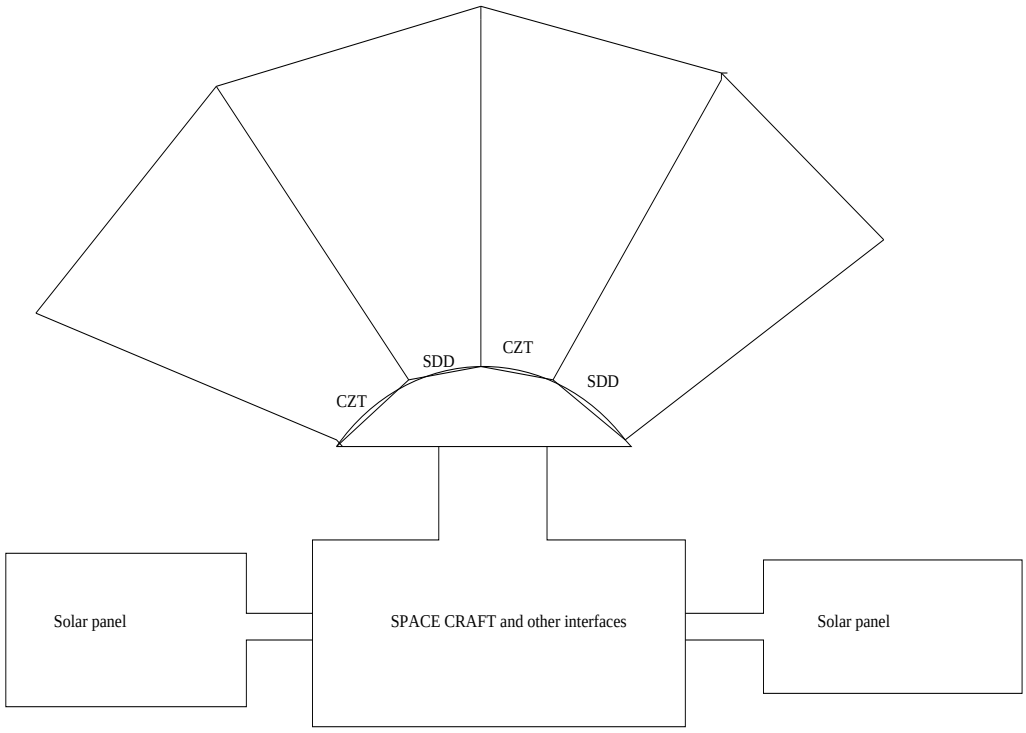

FIGURE 6.1: Schematic configuration of a future All Sky Monitor

An all sky monitor with these two detectors can span the energy range from 1 keV to 300 keV. Given the pixel sizes of the two detectors which are ∼100 microns for SDD and 300 microns for CZT, a coded mask with the smallest mask element size of 1 mm can be designed. As large areas of SDD and CZTs of 4 × 4 sq-cm each are available, the ASM can be made out of an array of such units to make the effective area for photon detection. Therefore, four such units to make a 2 × 2 array of SDD detectors make an area 64 cm^2 and similarly a 2 × 2 array of CZT forms an area of 64 cm^2. Each detector of area 16 × 16 cm^2 (ie. 64 cm^2) with a coded-mask area of 32 × 32 cm^2 (ie. 1024 cm^2) at a height of 60 cm from the detector plane defines an FOV of ∼40 ×40 sq-degrees. Four such units, two SDD units and two CZT units, placed alternatively in a curved structure as shown in figure 6.1, collectively gives an FOV of 40°× 160°. The geometric area of SDDs and CZTs available for detecting the photons is 128 cm^2 for each type of detector and hence the entire area for detection is 256 cm^2.

Considering the mask element to be 1 mm, the angular resolution for the ASM is ∼ 6 arcmin. For the given area of one SDD unit which is 64 cm^2, with a detection efficiency of 99% and a mask throughput of 0.5, the sensitivity is calculated to be ∼ 10 milliCrab, for an integration time of 10 minutes, at 6 keV. An integration time of an hour gives a sensitivity of ∼ 4 milliCrab. Similar sensitivity is achieved with the CZT detectors at high energies. Given the large effective FOV of 40°×160°, this All Sky Monitor can scan the entire sky in few hours.

The coded-mask has to be suitably designed to meet these requirements. The collimator material should be chosen such that it stops incoming photons of energy 300 keV incident from a direction beyond the FOV of the detector.

Thus a design for future sky monitors which can add many more sources to the existing catalogue of X-ray sources, with it high sensitivity is discussed.

6.4.2 Study of LHXTs

The archival data analysis of two X-ray transients presented in this work shows that they are black hole candidates. One of the sources studied here, Swift J1753.5-0127 is found to be in an outburst which does not show any state transitions but remains in the low/hard state, throughout the bursts. This behaviour is different from the canonical outbursts of X-ray transient sources. Study of this class of sources which show outbursts which are only in the low/hard state would likely unravel a new class of X-ray transient sources, probably a subset of X-ray transients.

Study of such new X-ray transients will help discover many more black hole sources in the galaxy and hence know more about the black hole population in the universe.

6.5 Conclusions

This chapter briefly summarizes the thesis work which is discussed in detail in various chapters. The results of various studies carried out in this thesis work are quantitatively mentioned here in this chapter. The future scope of designing a new future All Sky Monitor with a better sensitivity is discussed here. This sky monitor with a better sensitivity can discover faint sources and increase the number of sources in the already existing catalog of X-ray sources.

Bibliography

Agrawal P.C. 2004, Progress of Theoretical Physics Supplement, 155, 305

Agrawal P.C. 2006, Advances in Space Research, 38, 2989

Agrawal P.C. Sreekantan B. V., Bhandari N., 2007, Current Science, 93, 12

Belian R. D., Conner J. P., Evans W. D., 1976, ApJ, 206, L135

Belloni T., Psaltis D., Van der Klis M., 2002, ApJ, 572, 392

Blackburn J. K., 1995 Vol. 77 of ASP Conference Series, Astronomical data analysis software and systems. San Francisco, p. 367

Blinov V., 2001, in International Workshop on aging phenomenon Influence of materials and sense wire surface quality on aging with dme and other gases. Desy

Brocksopp C., Bandyopadhyay R. M., Fender R. P., 2004, New Astronomy, 9, 249

Burrows D. N., Racusin J., Morris D. C., Roming P., Chester M., La Verghetta R., Markwardt C. B., Barthelmy S. D., 2005, ATel, 547

Cadolle Bel M., Ribo M., Rodriguez J., Chaty S., Corbel S., Goldwurm A., Frontera F., Farinelli R., D'Avanzo P., Tarana A., Ubertini P., Laurent P., Goldoni P., Mirabel I. F., 2007, ApJ, 659, 549

Cadolle Bel M., Rodriguez J., Goldwurm A., Goldoni P., Laurent P., Ubertini P., Mereghetti S., 2005, ATel, 574

Charles P. A., Coe M. J., 2006, Optical, ultraviolet and infrared observations of X-ray Binaries in Compact Stellar X-ray Sources. Cambridge Astrophysics Series 39, Cambridge University Press

Charles P. A., Seward F. D., 1995, Exploring the X-ray Universe. Cambridge University Press

Charpak G., Bouclier R., Bressani T., Favier J., Zupancic C., 1968, Nuclear Instruments and Methods, 62, 235

Chen W., Shrader C. R., Livio M., 1997, ApJ, 491, 312

Cockroft A. L., Curran S. C., 1951, Rev. Sci. Instr., 22, 37

Cornelisse R., Heise J., Kuulkers E., Verbunt F.and in't Zand J. J. M., 2000, A&A, 357, L21

Cui W., Heindi W. A., Swank J. H., Smith D. M., Morgan E. H., Remillard R., Marshall F. E., 1997, ApJ, 487, L73

Doty J. P., 1988, SPIE - X-Ray Instrumentation in Astronomy II, San Diego, CA, 982, 164

Ebisawa K., Ogawa M., Takashi A., Tadayasu D., Takizawa M., Tanaka Y., Yoshida K., Miyamoto S., Iga S., Hayashida K., Kitamoto S., Terada K., 1994, PASJ, 46, 375

Esin A. A., McClintock J. E., Narayan R., 1997, ApJ, 489, 865

Fender R., Garrington S., Muxlow T., 2005, ATel, 558

Fischer J., Kuhne M., Wende B., 1986, NIMA, 246, 404

Forman W., Jones C., Cominsky L., Julien P., Murray S., Peters G., Tananbaum H., Giacconi R., 1978, ApJS, 38, 357

Frank J., King A., Raine D., 2002, Accretion Power in Astrophysics, third edn. Cambridge University Press

Fraser G. W., 1989, X-ray detectors in astronomy. Cambridge Astrophysics Series, Cambridge University Press

Fuzesy R. Z., 1972, NIM, 100, 267

Ghosh P., Lamb F. K., 1979, ApJ, 234, 296

Giacconi R., Branduardi G., Briel U., Epstein A., Fabricant D., Feigelson E., Forman W., Gorenstein P., Grindlay J., Gursky H., co authors ., 1979, ApJ, 230, 540

Giacconi R., Gursky H., 1974, X-ray Astronomy. Reidel Publishing Company

Giacconi R., Gursky H., Kellogg E., Schreier E., Tananbaum H., 1971a, ApJ, 167, L67

Giacconi R., Gursky H., Kellogg E., Schreier E., Tananbaum H., 1971b, ApJ, 167

Giacconi R., Gursky H., Paolini F. R., Rossi B. B., 1962, Phy. Rev. Lett, 9, 439

Gierlinski M., Andrzej A. Z., Juri P., Coppi P. S., Ebisawa K., Johnson N., 1999, MNRAS, 309, 496

Grebenev S. A., Pavlinsky M. N., Sunyaev R. A., 1996, in Proceedings 2nd INTEGRAL Workshop The transparent universe. St. Malo, France, pp SP–382

Grindlay J., Gursky H., Schnopper H., Parsignault D. R., Heise J., Brinkman A. C., Schrijver J., 1976, ApJ, 205, L127

Halpern J. P., 2005, ATel, 549

Hamburg D., ed. 2001, Summary and Outlook of the international workshop on aging phenomena in gaseous detectors

Heiberg S. A., 1968, NIM, 63, 71

Heise J., Jean in't Z., 2006, Chapter 6 in Compact Stellar X-ray sources, Cambridge University Press, Cambridge Astrophysics Series 39

Hjellming R. M., Rupen M. P., Shrader C. R., D. C.-W., Hunstead R. W., McKay D. J., 1996, ApJ, 470, L105

Holt S., Priedhorsky W., 1987, Space Science Reviews, 45, 269

Homan J., Belloni T., 2005, Astrophysics and Space Science, 300, 107

Jager R., Mels W. A., Brinkman A. C., Galama M. Y., Goulooze H., Heise J., Lowes P., Muller J. M., Naber A., Rook A., Schuurhof R., Schuurmans J. J., Wiersma G., 1997, A&AS, 125, 557

Jahoda K., Swank J. H., Giles A. B., Stark M. J., Strohmayer T., Zhang W., Morgan E. H., 1996, Proc. SPIE, 59, 2808

Keith A., Ben D., Craig G., , XSPEC, An X-ray Spectral Fitting Package. http://heasarc.nasa.gov/docs/xanadu/xspec/manual/manual.html

King A. R., 2006, Accretion in compact binaries, in Compact Stellar X-ray Sources. Cambridge Astrophysics Series 39, Cambridge University Press

Knoll G. F., 2000, Radiation detection and measurement. John Wiley & Sons

Kubota A., Tanaka Y., Makishima K., Ueda Yoshihiroand Dotani T., Inoue H., Yamaoka K., 1998, PASJ, 50, 667

Lasota J. P., 2001, New Astron. Rev., 45, 449

Leahy D. A., Darbro W., Elsner R. F., Weisskopf M. C., Kahn S., Sutherland P. G., Grindlay J. E., 1983, ApJ, 266, 160

Levine A. M., Bradt H., Cui W., Jernigan J. G., Morgan Edward H., Ronald R., Shirey Robert E., Smith Donald A., 1996, ApJ, 469, L33

Lewin W. H. G., Paradijs J. V., Edward P. J. V. D. H., 1995, X-ray Binaries. Cambridge University Press

Lewin W. H. G., Paradijs J. V., Taam R. E., 1995, X-ray Bursts in X-ray Binaries. Cambridge University Press

Longair M. S., 1992, High Energy Astrophysics, second edition edn. Vol. 1, Cambridge University Press

Longair M. S., 1994, High Energy Astrophysics, second edition edn. Vol. Vol. 2, Cambridge University Press

McClintock J. E., Remillard R. A., 2006, Black Hole Binaries in Compact Stellar X-ray Sources. Cambridge Astrophysics Series 39, Cambridge University Press

Makino F., 1987, Research Note 326. Institute of Space and Astronautical Science, Tokyo

Markwardt C. B., 2003, ATel, 143

Matsuoka M., Kawasaki K., Ueno S., Tomida H., Kohama M., Suzuki M., Adachi Y., Ishikawa M., Mihara T., Sugizaki M., co authors ., 2009, PASJ

Mertz L., 1968, Proc. Symp. on Modern Optics. Brooklyn:Polytechnic Press

Meyer-Hofmeister E., 2004, A&A, 423, 321

Miller J. M., 2007, ARAA, 45, 441

Miller J. M., Homan J., Miniutti G., 2006, ApJ, 652, L113

MIT-report D. o. P., 2006, Report on experiments to study muons, The Speed and Decay of Cosmic-Ray Muons: Experiments in Relativistic Kinematics - The Universal Speed Limit and Time Dilation. MIT, Department of Physics

Morgan E., Swank J., Markwardt C., Gehrels N., 2002, ATel, 550

Motch C., Guillout P., Haberl F., Krautter J., Pakull M. W., Pietsh W., Reinsch K., Voges W., Zickgraf F. J., 1998, A&AS, 132, 341

Muno M. P., Remillard R. A., Chakrabarty D., 2002, ApJ, 568, L35

Narayan R., Mclintock J. E., 2003, ApJ, 623, 1017

Narendranath K. C. S., Ramadevi M. C., Sudhakar M., Bhattacharya D., Sreekumar P., Seetha S., 2006, Advances in Space Research, 38, 2788

Negoro H., 2009, Proc. of Astrophys. with All-Sky X-ray Obs. - 3rd MAXI Inter. WS, p. 60

Palmer D. M., Barthelmey S. D., Cummings J. R., Gehrels N., Krimm H. A., Markwardt C. B., Sakamoto T., Tueller J., 2005, ATel, 546

Pfeffermann 2008, The Universe in X-rays. Springer Berlin Heidelberg

Pietsch W., Haberl F., Gehrels N., Petre R., 1993, A&A, 273, L11

Psaltis D., 2006, Accreting Neutron Stars and Black Holes, Chapter 1 in Compact Stellar X-ray Sources. Cambridge Astrophysics Series 39, Cambridge University Press

Ramadevi M. C., Seetha S., 2007, MNRAS, 378, 182

Ramadevi M. C., Seetha S., Babu V. C., Ashoka B. N., Sreekumar P., 2006, Advances in Space Research, 38, 3002

Ramsey B. D., Agrawal P. C., 1988, SPIE, 982, 258

Remillard R. A., McClintock J. E., 2006, ARA&A, 44, 49

Remillard R. A., McClintock J. E., 2006, ARAA, 44, 49

Revnivtsev 2003, A&A, 411, 329

Revnivtsev M. G., Sunyaev R. A., Varshalovich D. A., Zheleznyakov V. V., Cherepashchuk A. M., Lutovinov A. A. C. E. M. G. S. A. G. M. R., 2004, AstL, 30, 382

Rossi B., 1948, Rev Modern Physics, 20, 537

Rothschild R. E., Blanco P. R., Gruber D. E., Heindl W. A., MacDonald D. R., Marsden D. C., Pelling M. R., Wayne L. R., Hink P. L., 1998, ApJ, 496, 538

Sandage A., Osmer P., Giacconi R., Gorenstein P., Gursky H., Waters J., Bradt H., Garmire G., Sreekantan B. V., Oda M., coauthors ., 1966, ApJ, 146, 316

Sauli F., 1977, Principles of operation of MWPC-Lectures-CERN-1977, CERN

Schartel N., Parmar A., 2008, ESA Bull., 134, 2

Schnopper H. W., Thompson R. I., Watt S., 1980, Sp. Sc. Rev., 8, 534

Schwartz D. A., 2004, Int. J. Mod. Phys., D13, 1239

Seetha S., Ramadevi M. C., Babu V. C., Sharma M. R., Murthy N. S. R., Ashoka B. N., Shyama K. C., Kulkarni R., Meena G., Sreekumar P., 2006, Advances in Space Research, 38, 2995

Seetha S. 2003, BASI, 31, 485

Shakura N. I., Sunyaev R. A., 1973, A&A, 24, 337

Shimura Toshiya Takahara Fumio 1995, ApJ, 445, 780

Skinner G. K., Foster A. J., Willmore A. P., Eyles C. J., 1990, MNRAS, 243, 72

Still M., Roming P., Brocksopp C., Markwardt C. B., 2005, ATel, 553

Strohmayer T., Bildsten L., 2006, New views of thermonuclear bursts, Chapter 3 in Compact Stellar X-ray Sources. Cambridge Astrophysics Series 39, Cambridge University Press

Strohmayer T. E., Zhang W., Swank J. H., Smale A., Titarchuk L., Day C., Lee U., 1996, ApJ, 469, L9

Sturner S. J., Shrader C. R., 2005, ApJ, 625, 923

Sunyaev R. A., 1973, Soviet Astronomy, 16, 941

Tanaka Y., Lewin W. H. G., 1995, X-ray Binaries, Cambridge University Press

Tanaka Y., Shibazaki N., 1996, ARAA, 34, 607

Terada Y., Terada Y., Hayashi T., Ishida M., Mukai K., Dotani T., Okada S., Nakamura R., Naik S., Bamba A., Makishima K., 2008, PASJ, 60, 387

Titarchuk L., 1994, ApJ, 434, 313

Titarchuk L., Fiorito 2004, ApJ, 612, 988

Titarchuk L., Osherovich V., 2000, ApJ, 542, 111

Toor A., Seward F. D., 1974, The Astronomical Journal, 79, 995

Torres M. A. P., Steeghs D., Blake C., Jonker P. G., Garcia M. R., McClintock J. E., Miller J. M., Zhao P., Calkins M., Berlind P., Falco E., Bloom J., Callanan P., Rodriguez-Gil P., 2005, ATel, 566

Torres M. A. P., Steeghs D., Garcia M. R., McClintock J. E., Miller J. M., Jonker P. G., Callanan P. J., Zhao P., Huchra J., Vivian U., Hutcheson C., 2005, ATel, 551

Truemper J., 1992, QJRAS, 33, 165

Tsoulfanidis N., 1995, Measurement and Detection of Radiation, second edn. Taylor and Francis

Turner M. J. L., Thomas H. D., Patchett B. E., Reading D. H., Makishima K., Ohashi T., Dotani T., Hayashida K., Inoue H., Kondo H., Koyama K., Mitsusa K., Ogawara Y., Takano S., Awaki H., Tawara Y., Nakamura N., 1989, PASJ, 41, 345

Van der Hooft F., Kouveliotou C., Van Paradijs J. andPaciesas W. S., Lewin W. H. G., der Klis M. V., Crary D. J., Finger M. H., Harmon B. A., Zhang S. N., 1999, ApJ, 513, 477

van der Klis M., 1995, Rapid X-ray Variability in "X-ray Binaries". Cambridge University Press

van der Klis M., 2006, Rapid X-ray Variability in Compact Stellar X-ray Sources. Cambridge Astrophysics Series 39, Cambridge University Press

van der Klis M., Swank J. H., Zhang W., Jahoda K., Morgan E. H., Lewin W. H. G., Vaughan B., van Paradijs J., 1996, ApJ, 469, L1

Van Paradijs J., McClintock J. E., 1995, Optical and ultraviolet observations of X-ray Binaries in X-ray Binaries. Cambridge Astrophysics Series 26, Cambridge University Press

Veenhoff R., 1984, http://cern.ch/garfield/

Weisskopf M. andWeisskopf M. C., Brinkman B., Canizares C., Garmire G., Murray S., Van Speybroeck L. P., 2002, PASP, 114, 1

White N. E., Peacock A., 1988, Memor. Soc. Astron. Ital., 59, 7

Willingale R., Aschenbach B., Griffiths R. G., Sembay S., Warwick R. S., Becker W., Abbey A. F., Bonnet-Bidaud J. M., 2001, A&A, 365, L212

Wilson C. A., Patel Sandeep K., Kouveliotou Chryssaand Jonker P. G., van der Klis M., Lewin W. H. G., Belloni T., Mndez M.,

Wood K. S., Meekins J. F., Yentis D. J., Smathers H. W., McNutt D. P., Bleach R. D., Byram E. T., Chubb T. A., Friedman H., 1984, ApJ Supplement Series, 56, 507

Wood K. S., Titarchuk L., Ray P. S., Wolff M. T., Lovellette M. N., Bandyopadhyay R. M., 2001, ApJ, 563, 246

Zand J. i., 1992, PhD thesis, University of Utrecht, Netherlands

Zhang G. B., Qu J. L., Zhang S., Zhang C. M., Zhang F., Chen W., Song L. M., Yang S. P., 2007, ApJ, 659, 1511

Zurita C., Durant M., Torres M. A. P., Shahbaz T., Casares J., Steeghs D., 2008, ApJ, 681, 1458